TECHNISCHE UNIVERSITÄT MÜNCHEN

Walter Schottky Institut

Zentralinstitut für physikalische Grundlagen der Halbleiterelektronik

Electronic properties of electrolyte-gated diamond FETs for bioelectronic applications

Markus Raimar Dankerl

Vollständiger Abdruck der von der Fakultät für Physik der Technischen Universität München zur Erlangung des akademischen Grades eines

Doktors der Naturwissenschaften

(Dr. rer. nat.)

genehmigten Dissertation.

Vorsitzender:	Univ.-Prof. Dr. P. Vogl
Prüfer der Dissertation:	
	1. Priv.-Doz. Dr. J. A. Garrido Ariza
	2. Univ.-Prof. Dr. F. Simmel

Die Dissertation wurde am 03.08.2012 bei der Technischen Universität München eingereicht und durch die Fakultät für Physik am 06.11.2012 angenommen.

Contents

Chapter 1

Introduction

The advent of microelectronics with the invention of the transistor has created a new type of complex system next to nature's biological systems. Direct communication between these systems has proved difficult, as the communication in one is electronic, and ionic in the other. Communication across this interface between electronic and biological systems is the field of bioelectronics. Bioelectronics promises to deliver treatments to a number of diseases via implantable prosthetic devices e.g. for the ear or eye [Cla09, Vel08]. A significant challenge in this field is the aqueous environment, that deteriorates the material systems most successfully employed for electronic systems, namely those based on silicon. Bioelectronics, thus, requires materials with the chemical and electrochemical stability to operate in an aqueous environment. The demands placed on a suitable material for bioelectronics or, more generally, biosensing, have been tried to be satisfied by a number of materials. Among the semiconductors, diamond shows an exceptional stability in aqueous environments [Stu06]. The scarcity of natural diamond and its expense is an immediate disadvantage that comes to mind. However, while the de Beers company has controlled the natural diamond trade for decades ([Dow08]), methods of producing artificial diamonds have become available. First with the high-pressure and high-temperature (HPHT) method in the fifties, followed by chemical vapor deposition (CVD) in the eighties [Sus09]. The advancement of these methods for the production of artificial diamond has not only been important for financial reasons. The CVD of diamond also allows the fabrication of very high quality, pure artificial diamonds that are thus also suited for electronic applications. The renewed interest in the material and the research which it spawned led also to the discovery of a further very special material property. Beyond the exceptional bulk properties of diamond, the termination of the surface bonds with hydrogen facilitates a p-type surface conductivity in intrinsic

diamond [Mai00]. This surface conductivity allows the manufacture of field effect transistors by controlling the hole accumulation at the diamond surface with a gate. Due to the electrochemical stability of diamond, the gate may be an electrolyte solution with a reference electrode, thus creating solution gate field effect transistors (SGFETs) [Kaw01]. These SGFETs are sensitive to changes in the potential across the diamond/electrolyte interface. Thus the electronic sensing capability was added to the chemical stability of diamond, making diamond a strong contender as a material for biosensor and bioelectronic applications.

The first diamond sensors in aqueous environments were based on boron doped diamond [Foo09], utilizing the large potential window and electrochemical stability of the material. These are amperometric sensors, whose operating principle requires only a conductive material. With the discovery of the surface conductivity of intrinsic hydrogen-terminated diamond [Lan89], another avenue was opened for diamond sensors. Thus, the surface conductivity was utilized in the development of diamond SGFETs, presenting a diamond biosensor with attractive properties applicable for operation in aqueous environments, as already implied above.

Soon after, the diamond SGFETs were investigated as pH sensors [Kaw01, Gar05]. However, as the origin of the surface conductivity as well as the principle of the diamond SGFET were only partly understood at the time, the pH sensitivity was qualitatively and quantitatively hotly debated [Son06, Neb06, Rez07, Dan08].

Meanwhile other aspects of the diamond technology directly related to sensing applications were advancing, e.g. the functionalization of the diamond surface. Protocols were developed to functionalize both the oxygen- as well as the hydrogen-terminated diamond surface, and these covalent functionalizations were shown to be exceptionally stable [Yan02]. Thus a novel technological tool kit was made available from which various diamond biosensors could be assembled.

Largely prior to the development of diamond devices for biosensing and bioelectronics the cell-transistor coupling was studied with devices based on silicon. The transduction of action potentials from living cells as well as their stimulation was accomplished [Fro91] [Kau04]. Theoretical models for the signal transduction between cells and transistors were developed around the same time [Reg89, Fro03]. These initial achievements using silicon began to be reproduced with other material systems better suited to the operation in electrolytes, such as wide bandgap semiconductors [Ste05]. This is the starting point for the work presented here.

This thesis set out to deepen the fundamental understanding of the diamond SGFETs and advance the technological capabilities of these devices. All these efforts are di-

rected towards diamond as a material for bioelectronics and biosensing, and more specifically the signal transduction from living cells. This goal requires advancements on a number of fronts which are partly interdependent, and thus a number of different issues ranging from electronic transport to surface functionalization are covered in this thesis. So does, for example, the capability for defined oxidation of the surface allow the study of the effect of an inhomogeneous hydrogenation on the electronic transport. The possibility of functionalization of the diamond surface, for instance, aids the growth of cells.

However, the main focus of this thesis is the study of fundamental aspects of the interface between diamond and water or aqueous electrolytes. Especially the interfacial capacitance is of primary importance, as the sensitivity of the diamond SGFETs is directly proportional to it. As shown in this thesis, the hydrophobic nature of the hydrogen-terminated diamond surface is a parameter that considerably alters this interfacial capacitance. These issues are also relevant for other hydrophobic materials which are currently being used in biosensing or bioelectronics, such as graphene or organic semiconductors [Dan10, Rob08]. Aside from the desired signal transduction the nature of the interface can also influence adsorption properties, or be a source of charge carrier scattering through interface charges.

In one form or another this interface is relevant in all chapters of this thesis. Concretely, the thesis is structured as follows:

Chapter 2 summarizes the advancements made in this thesis towards controlling and investigating the composition of the diamond surface. Initially, diamond as a material and the diamond surface are introduced, and the status quo regarding the surface conductivity of hydrogen-terminated diamond is presented. Building on this, technological advancements made in several areas controlling the termination and functionalization of the surface are discussed, namely the hydrogen-termination, a controlled partial oxidation, and the functionalization of both oxygen- and hydrogen-terminated diamond surfaces. Results from the investigation of the composition of the hydrogen-terminated diamond surface with XPS are shown and considered in light of the proposed water layer adsorbed on this surface. As suits the intended application, the electrochemical stability of the hydrogen-termination under operation and over time is explored.

Chapter 3, the central chapter of this thesis, describes the charge accumulation and the electronic transport at the diamond/electrolyte interface investigated with in-liquid Hall effect measurements. The first section explains the solution gate field effect transistor (SGFET) model as largely understood at the outset of this work.

To obtain a fundamental understanding of the operation of the diamond SGFETs, a large number of in-liquid Hall effect measurements under potential control on various hydrogen-terminated diamond samples have been performed. The results are presented in the second section, which discusses the charge accumulation at the diamond/electrolyte interface. Parameters systematically influencing the interfacial capacitance are extracted, where the difference in the interfacial capacitance between the (100) and the (111) surface orientation is particularly interesting. Simulations of the charge accumulation at this interface were carried out with the nextnano software using the isotropic effective mass approximation as well as calculating the effective masses according to the kp method. The comparison between experimental and simulation results reveals that the hydrophobic nature of the surface is decisive to quantitatively understand charge accumulation in diamond SGFETs. The third section of chapter 3 deals with the electronic transport, that is the hole mobility, at the diamond/electrolyte interface. Experimental results include not only the mobility of the measurements discussed before, but also specific experiments to elucidate the transport mechanisms in the accumulation channel. Clear differences are observed between electronic grade and optical grade samples and again between the two surface orientations studied. Interesting is the lack of any effect of the composition of the electrolyte, such as pH, ionic strength or ion adsorption, on the electronic transport. While the phenomenological findings are very clear, their theoretical explanation is less straightforward and requires further research. For each sample category transport mechanisms that are compatible with the experimental results are presented and discussed, though often more than one mechanism is applicable.

A number of applications of diamond SGFETs are studied and developed in Chapter 4. The first explored application deals with the use of the diamond SGFET as a pH sensor, where a correct interpretation of the data resolves a controversy over the sign and value of the pH sensitivity. The second application extends the diamond SGFET to solid electrolytes in the form of a polyethylene oxide based electrolyte and presents a solid FET device with potential applications in electronic transport studies and quantum computing. Lastly, the SGFET principle is applied to graphene, to fabricate graphene SGFETs, whose characteristics are competitive and whose operation principles are similar to diamond SGFETs.

Chapter 5 demonstrates the use of diamond SGFETs to record the electrical activity of living cells, and thus taking the first experimental steps to bioelectronics based on diamond. Two types of cells were grown on the diamond SGFET gate area, showing

the biocompatibility of the material. The first recordings of the electric signals from single cells was accomplished with a patch clamp setup. The recorded signals can be well explained with the so-called point contact model for the cell-transistor coupling. A short summary is finally presented in Chapter 6. The outlook given in Chapter 7 outlines the various loose ends of this work and possible routes to explore these issues. The appendix contains various practical information relevant to this work.
This thesis deals with the fundamental properties of diamond SGFET and exemplary applications in biosensing and bioelectronics. It explores the operating principles of diamond SGFETs, firstly the effect of hydrophobicity on the interfacial capacitance, which can be applied to other material systems and secondly the electronic transport in surface conducting diamond, laying the groundwork for a deeper understanding of the scattering mechanisms. The demonstrated recording of the electrical activity of cells with diamond SGFETs is a step on the path towards the goal of communication between electronic and biological systems.

Chapter 2

Diamond and its surface

The work presented in this thesis deals almost exclusively with effects of or at the diamond surface. Accordingly, this chapter begins by introducing diamond, especially the diamond surface, its technologically most relevant surface terminations, and the surface conductivity of hydrogen-terminated diamond.

2.1 Bulk diamond

Diamond is a sp^3 bonded allotrope of carbon that forms a face centered cubic lattice. The lattice base consists of two atoms, whereby the second atom is shifted along the body diagonal by a quarter lattice constant, giving both atoms the positions (0,0,0) and ($\frac{1}{4}$, $\frac{1}{4}$, $\frac{1}{4}$) in the lattice respectively (see Figure 2.1). While graphite is the most stable allotrope of carbon, diamond is metastable, with a high activation energy between the two phases. This structural arrangement and the strength of the covalent carbon-carbon bonds leads to a number of outstanding properties. A selection of these physical properties is summarized in Table 2.1.

The remarkable stability of diamond extends to its chemical properties, where the material is inert to chemical attack of various kinds. This chemical stability is likely to contribute to the bioinertness of diamond, which has also been reported [Kal08] [Gar09].

All these exceptional properties should warrant a host of applications. Indeed diamond has been used industrially. A number of applications make use of diamond's hardness for mechanical applications such as drilling, cutting and polishing. Further products include high performance heat sinks, UV transparent windows, or radiation detectors. Electronic applications, however, have been rare. This is mostly due to the difficulty in the doping of diamond. The most efficient dopant in diamond

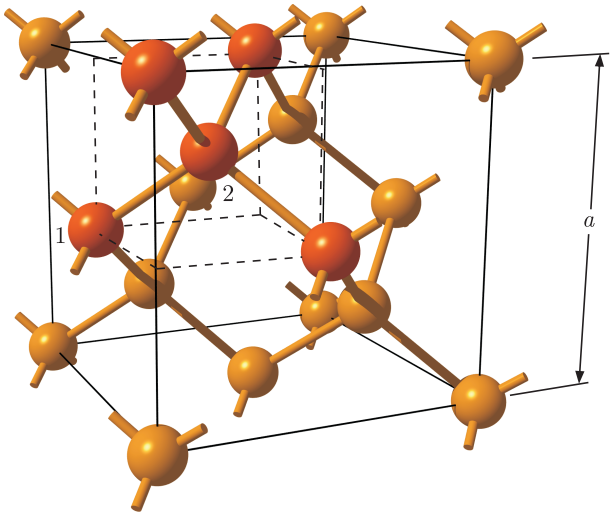

Figure 2.1: *Cubic unit cell of the diamond crystal structure showing the face centered cubic lattice with an edge length of a. The tetrahedral coordination is indicated by the atoms colored in red. Atoms 1 and 2 are an example for the base of the lattice.*

is boron resulting in p-type doping with an activation energy of 0.37 eV. Efficient n-type doping has so far been elusive with phosphorous being the most "efficient donor" with an activation energy of 0.6 eV, which is too deep for most practical purposes. The relative small size of the carbon atoms combined with the close packing in the diamond crystal structure makes the incorporation of impurities of many elements difficult. A further barrier to a wider range of applications is, of course, the high price of the material. However, this is being overcome with continuous developments in the synthesis of artificial diamond and, to a lesser degree, the increase of mined diamonds after the end of the cold war. Industrial diamond production began with the high temperature high pressure (HTHP) method, which enables the preparation of diamonds of significant size and quality, but with impurities intrinsic to this production process.

Since the 1980s diamond can be grown homoepitaxially and heteroepitaxially with chemical vapor deposition (CVD). Currently, high quality single crystalline homoepitaxial CVD grown diamonds can be produced reproducibly with dimensions in the range of several millimeters. Polycrystalline and nanocrystalline diamond films can also be grown heteroepitaxially on a large variety of substrates, enabling large area deposition. During this thesis CVD grown diamonds became readily available on a commercial basis, first at low quality and low price, and later in electronic grade quality as well. While it is unlikely that diamond will ever be as cheap as silicon,

Table 2.1: *Selected physical properties of diamond*

Property	**Value**	**Unit**	**Comments**	**Reference**
lattice constant	3.567	Å		[Rös02]
enthalpy of crystal formation	730-1060	kJ/mol	@2150-2300K zero pressure	[Rös02]
bond length	1.54	Å		[Dav09]
hardness	10	on Mohs scale		[Rös02]
heat conductivity	6-20	W cm^{-1} K^{-1}		[Iof11]
density	3.515	g cm^{-3}		[Iof11]
dielectric constant	5.66	As/Vm		[Rös02]
band gap E_{gap}	5.46-5.48	eV		[Rös02]
electronic state of nitrogen impurities	1.7	eV	other states exist	[Iof11]
electronic state of boron impurities	0.37	eV		[Iof11]
electron mobility	2200	cm^2 V^{-1} s^{-1}		[Iof11]
hole mobility	1800	cm^2 V^{-1} s^{-1}		[Iof11]
intrinsic electrical resistivity	10^{16}	Ohm cm	type IIa	[Isb09]

for example, the price of the material itself should be less and less of an obstacle for new applications. Already, these include e.g. industrial applications such as electrochemical reactors for wastewater treatment.

2.2 The diamond surface

For many applications in biosensing, health care, bioelectronics or in aqueous environments in general, its surface rather than its bulk properties make diamond particularly attractive.

The most technologically relevant surface orientations of diamond are the (100) and the (111) surface, although diamond can be grown and finished more easily and with higher quality in the (100) orientation. On the unterminated diamond (100) surface each carbon atom at the surface is left with two dangling bonds, which bind together

and thereby the surface reconstructs to a 2x1 geometry. The same is true for the (111) surface, although the reconstruction is more complicated in this case [Ris06]. However, the diamond surface is usually terminated by atomic adsorbates. The most important termination for this work, and the as-grown state of CVD diamonds, is the hydrogen termination. During CVD growth, hydrogen radicals saturate the dangling bonds of the surface carbons, leaving the surface in a hydrogen-terminated state. Furthermore, diamond samples with a different initial termination can be hydrogen-terminated by treatment with a microwave assisted hydrogen plasma (see Section 2.2.2), for instance. For the (100) surface, surface hydrogenation also leads to a 2x1:2H reconstruction with two hydrogen atoms per unit cell and one hydrogen atom per surface carbon atom (see Figure 2.2). The hydrogen atoms are arranged in dimer rows and the C-H bond is tilted with respect to the surface normal by 25° [Fur96]. In the case of the (111) surface, the hydrogen termination stabilizes the bulk terminated surface into a 1x1:H reconstruction, typically with one hydrogen atom per topmost surface carbon atom. Here, the C-H bonds are parallel to the surface normal. The density of surface carbon atoms and therefore C-H bonds is 1.57×10^{15} cm^{-2} and 1.81×10^{15} cm^{-2} for the (100) and (111) surfaces, respectively [Cui98] [Mai01].

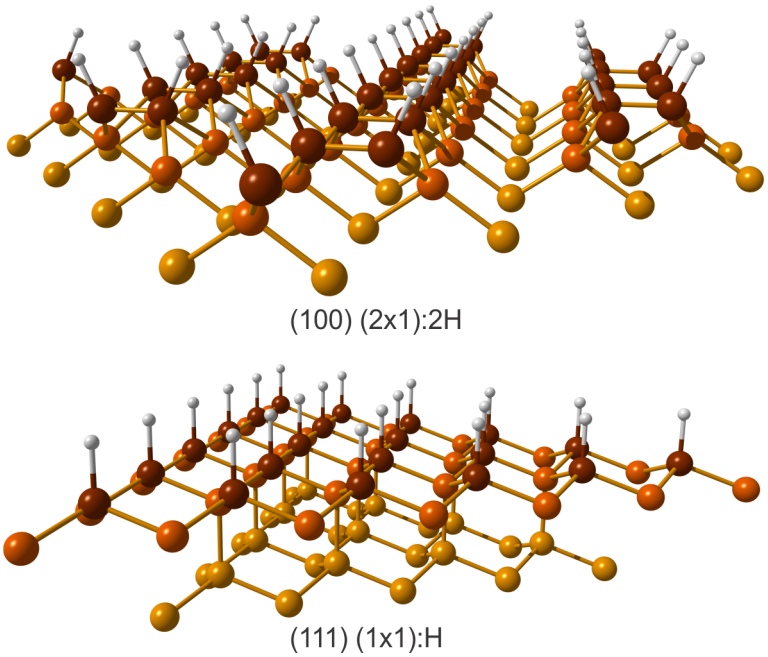

Figure 2.2: *Hydrogen-terminated diamond (100) (2x1):2H (top) and (111) (1x1):H (bottom) surface. The three topmost carbon atom layers are shown (brown, orange, and yellow from surface to bulk).*

The other important atomic adsorbate at diamond surfaces is oxygen. Untreated diamonds (except CVD grown diamonds) are assumed to be oxygen-terminated in some form. In contrast to hydrogen, the two available valence electrons of oxygen allow for a larger variety in the surface bond structure. One oxygen atom can either form a double bond with each surface carbon atom, or can bridge two carbon atoms forming a single bond with each. Both cases result in a 1x1:O reconstruction for the (100) surface and a 2x1:O reconstruction for the (111) surface [Ris06]. Another possibility for the O-termination is the formation of hydroxyl groups bonding to the surface with single bonds. The hydrogen- as well as the oxygen termination of the diamond surface are stable at ambient conditions and in electrolytes within their respective potential windows. The termination of the diamond surface leads to surface bonds with dipole moments, which depend on the difference in electronegativity between the carbon and the terminating atoms. As these dipole moments have a component perpendicular to the surface, a potential step is induced across the interface, which depends on the surface dipole density and the dipole strength. This potential step changes the electron affinity of the surface. As carbon is more electronegative than hydrogen, the electron affinity is lowered by hydrogen-termination of the surface to a negative value of χ=-1.3 eV. In contrast, carbon is less electronegative than oxygen, and the electron affinity is increased by oxygen termination to a value of χ=+1.7 eV. A negative electron affinity of the surface means that the conduction band minimum E_C is above the vacuum level E_{VAC} and therefore, there is no potential barrier for electrons in the conduction band to leave the diamond surface. Even more important for the surface conductivity of hydrogen-terminated diamond however, is the influence on the position of the valence band maximum E_V. As $\chi = E_{VAC} - E_C$, the negative χ leads to a value of the valence band maximum closer to E_{VAC}, which has important consequences for the electronic properties of hydrogen-terminated surfaces, as will be described in more detail in Section 2.2.1.

2.2.1 Surface conductivity of hydrogen-terminated diamond

Intrinsic diamond with its large band gap is an insulator. However, intrinsic diamond terminated with hydrogen was discovered to show a p-type surface conductivity in atmospheric conditions [Lan89]. After a number of years and some controversy this surface conductivity is understood considering surface transfer doping ([Gi95], [Gi99], [Mai00], [Cha07], [Zha08]). A well-written summary of the development of the transfer doping theory up to 2008 can be found in [Ley09]. In principle, the

transfer doping model proposes that electrons from the diamond valence band are transferred to adsorbed acceptors on the diamond surface, thereby leaving a two-dimensional surface conductive hole channel behind.
This model assumes that the surface acceptors are provided by the adsorbed water layer at the hydrogen-terminated diamond surface. This water layer contains redox couples such as H_3O^+/H_2, which is related to the hydronium reduction

$$2H_3O^+ + 2e^- \rightleftharpoons H_2 + 2H_2O\ , \tag{2.1}$$

or O_2/H_2O, related to the oxygen reduction

$$O_2 + 4H^+ + 4e^- \rightleftharpoons 2H_2O\ . \tag{2.2}$$

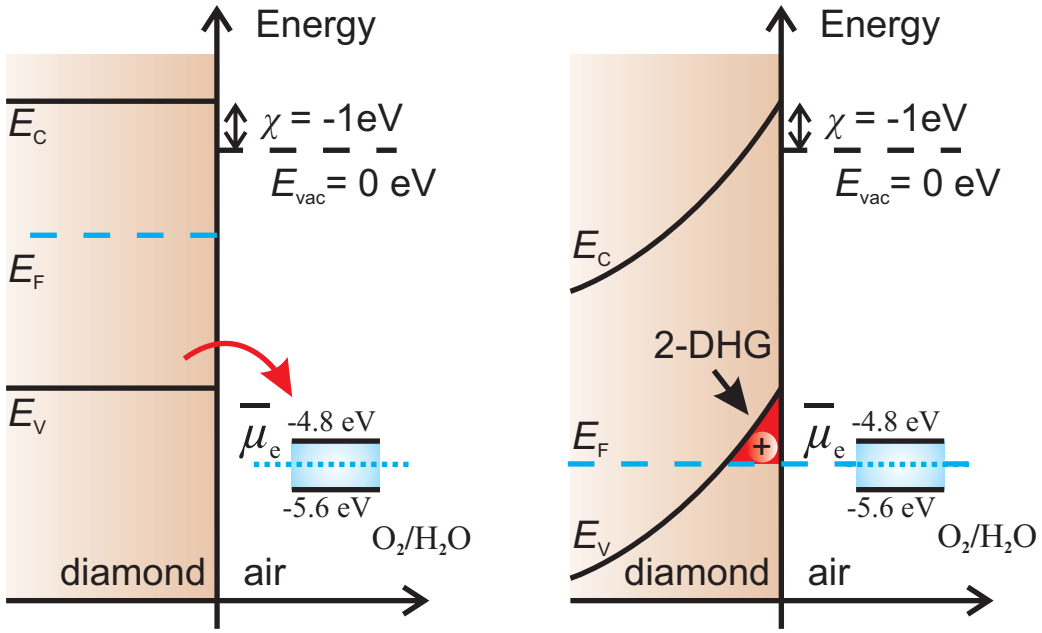

Figure 2.3: *Band alignment and charge transfer according to the transfer doping model with the oxygen redox couple as electron acceptor. The potential of the oxygen redox couple varies within the indicated range (blue shadow) with the pH. left: The energy levels are shown before equilibrium is established between the electrons in the diamond and those associated with the redox couple. right: Energy levels after equilibrium is established, with the Fermi level in the diamond at the same energy position as the redox potential of the oxygen couple. The electron transfer from the diamond to the redox couple results in the charge accumulation in the diamond, band bending, and establishes the quasi two-dimensional hole gas (2DHG).*

The reactants of these chemical reactions are provided by dissolved atmospheric gases (H_2, O_2) and potentially the autoprotolysis of water. From a thermodynamic point of view, the electrochemical potential of electrons in the diamond and the electrochemical potential associated with the described redox reactions, have a tendency to equilibrate. As the hydrogen termination leads to a negative electron affinity (see Section 2.2), the valence band and the Fermi level of diamond are close to and above, respectively, of the adsorbate-related redox levels. This enables the transfer of electrons from the diamond valence band into the redox acceptors at the diamond surface. This removal of electrons leads in turn to the accumulation of holes at the diamond surface, giving rise to an electric field and spatially varying electric potential, which induces an upward band bending (see Figure 2.3). The Fermi level is eventually lowered below the valence band edge, resulting in the accumulation of holes in a two-dimensional hole gas (2DHG) close to the surface. The hole accumulation provides the observed p-type surface conductivity. Figure 2.3 illustrates this transfer doping process. The transfer doping of diamond has also been observed in the absence of the proposed water layer in vacuum, after the adsorption of other electron acceptors such as fullerenes [Str04]. The net transfer of electrons stops when the electrochemical potential of electrons in the diamond and those in the acceptors are in thermodynamic equilibrium. The electrochemical potential $\bar{\mu}$ of the redox couples, the acceptors, is determined by the ratio of the concentrations of the oxidized and reduced species in the reaction

$$\mathrm{nOx} + \mathrm{ze}^- \rightleftharpoons \mathrm{mRed} \tag{2.3}$$

according to Nernst:

$$\bar{\mu} = \bar{\mu}_s - \frac{k_B T}{z} \ln[\frac{([Ox]/[Ox]_s)^n}{([Red]/[Red]_s)^m}] \; . \tag{2.4}$$

n, m, and z are the number of participating molecules and the number of exchanged electrons, respectively. The index s refers to standard conditions (1 mol/kg for species in solution and 1 bar partial pressure for gaseous species in equilibrium with the electrolyte) and the square brackets denote concentrations. Whereas the electrochemical potential on the acceptor side remains almost constant if the atmospheric reservoir is big enough, the accumulation of charge in the diamond lowers its electrochemical potential and brings it in line with that of the acceptor states. The electrochemical potential corresponds to the Fermi level in the diamond for a temperature of 0 K. For this transfer of electrons to be viable, a difference in the electrochemical potentials is not sufficient. The highest occupied state in the diamond, the valence band edge, must also be higher, or within the thermal energy kT,

than the lowest unoccupied state of the adsorbed electron acceptors. In the case of hydrogen-terminated diamond, the negative electron affinity of $\chi = -1.0$ eV [Gar08] lifts the valence band above or close to the levels of the adsorbed electron acceptors, even when considering the large diamond band gap. Finally, to establish the surface conductivity, the generated holes need to be mobile, requiring an absence (or very low concentration) of electronic traps in the material.

The transfer doping model explaining the observed surface conductivity of hydrogen-terminated diamond was first developed quantitatively by Maier et al. [Mai00] after the idea of a transfer of electrons outside the diamond was first articulated by Ri et al. [Gi95]. It was observed that the surface conductivity could only be established in atmospheric conditions, leading to the conclusion, that it is facilitated by the redox reaction of hydrogen (Equation 2.1). For this reaction H_3O^+ is provided by the autoprotolysis of water, and H_2 is a trace gas in atmosphere. The solvation of atmospheric CO_2 produces H_2CO_3 which lowers the pH and thus the redox potential of Equation 2.1. The charge of the holes in diamond was proposed to be compensated by an equal countercharge provided by the remaining HCO_3^- ions. In this way, the residual surface conductivity observed well above 100°C can be explained by the hard-to-desorb HCO_3^- ions. With a water layer on the hydrogen-terminated diamond, the negative electron affinity provided by the C-H dipoles of the surface termination, was then proposed to be lowered from the vacuum value of $\chi = -1.3$ eV to a value of -1.0 eV, as a result of screening by the water molecules. Any change of the electron affinity affects, of course, the final position of the Fermi level in diamond with respect to the valence band and, therefore, the free carrier concentration achieved by transfer doping. As an alternative to the originally proposed reaction, also the reaction of oxygen (Equation 2.2) was proposed by Angus et al. as an electron acceptor [Cha07]. Ristein et al. finally showed that both reactions contribute as electron acceptors and the resulting electrochemical potential is determined by the potential of each reaction adjusted for by the reaction speed [Zha08]. This reaction speed is $2 * 10^8$ cm^{-2} s^{-1}, which means that the surface conductivity establishes in a matter of hours to a day [Zha08]. The contribution of both of these reactions in an adsorbed water layer at the diamond surface and an electron affinity of $\chi = -1$ eV is now the generally accepted explanation for the surface conductivity of hydrogen-terminated diamond.

2.2.2 Hydrogen-termination of diamond

As already mentioned, the hydrogen-termination of the diamond surface is part of the CVD growth process of diamond. In this process, a mixture of hydrogen and methane, which provides the carbon atoms for building up the diamond crystal, is used. Hydrogen and methane molecules are split in the microwave-assisted plasma and can then react as radicals with the surface carbon atoms of diamond. The hydrogen is necessary, as it saturates the dangling bonds of the surface carbon atoms preventing the formation of other carbon forms during growth. The addition or removal of methyl/methane on the diamond surface determines the growth or etching rate of the process [Sch09]. In order to terminate the diamond surface with hydrogen, independent of the source of the diamond sample (CVD, HPHT, or naturally formed), the same method is applied without the addition of methane. Termination of the surface with hydrogen without or little etching is achieved by choosing the reaction parameters, notably temperature, accordingly.

After a vacuum is provided to minimize contaminants, pure H_2 gas is microwave-activated to form a hydrogen plasma. The hydrogen radicals diffuse to the diamond surface and form the desired C-H bonds. To enable this endothermic process, the sample is heated. In order to keep the diamond surface hydrogen-terminated while switching to atmospheric conditions, the sample is cooled in hydrogen atmosphere after the plasma shut-down. Alternatively to the microwave activation, the hydrogen molecules can also be split with a hot filament [Uch01]. For the hydrogen-termination in this work, an ASTEX microwave-assisted plasma reactor (AX5010, 1.5kW; Seki Technotron Corp.) was used. The parameters for the process are listed in Table 2.2. The base pressure of the chamber is below 1×10^{-6} mbar, and the base pressure achieved with the rotary pump during the process is 2×10^{-3} mbar. The hydrogen gas used has a purity of "5.0"=99.9990 volume %.

Besides the gas phase hydrogen termination described here, an electrochemical method for hydrogen termination was developed recently [Hof10]. It is, however, limited in its application as it requires conductive diamond samples, therefore excluding the intrinsic diamond material mostly used in this work.

The quality of the hydrogen-termination can be assessed by the lack of surface oxygen with XPS (see Section 2.2.4), by the surface conductivity measured in ambient conditions (see Section 2.2.1), and by the hydrophobicity of the hydrogen-terminated diamond surface. The oxygen terminated surface is generally hydrophilic with water contact angles down to 10°, depending also on the dominating oxygen groups at the surface. In contrast, the hydrogen-terminated surface is rather hydrophobic,

	Power	H_2 pressure	H_2 flux	Process time	Temperature
H-termination process	750 W	50 mbar	100 sccm	15 min	700 °C
Soft shut-down	230 W	50 mbar	100 sccm	10 min	ends at <400°C
Cool down	0 W	50 mbar	100 sccm	30 min	ends at <50°C

Table 2.2: *Reaction parameters for the microwave plasma assisted hydrogen-termination of diamond. The process is performed in a ASTEX microwave reactor (AX5010).*

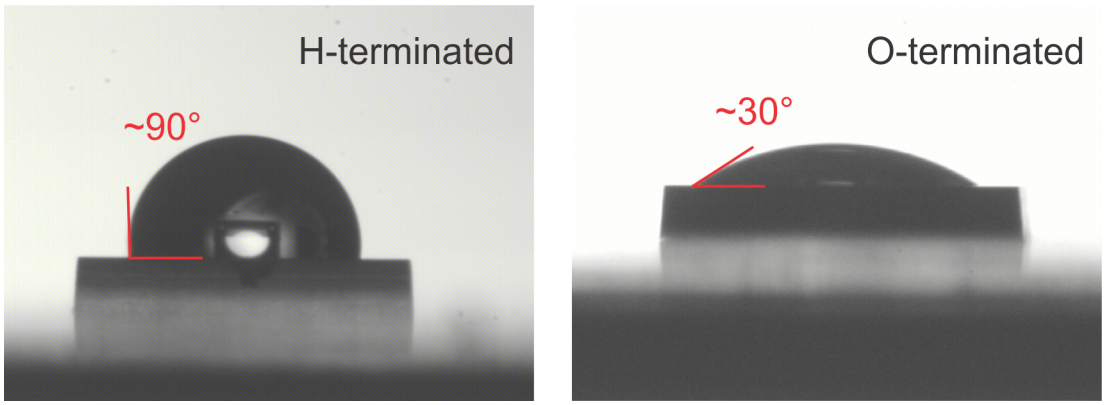

Figure 2.4: *Water contact angle of a hydrogen- (left) and an oxygen- (right) terminated diamond surface, evidencing the hydrophobicity of the hydrogen-terminated surface, and the hydrophilicity of the oxygen-terminated surface.*

exhibiting contact angles around 90°. The diamond hydrophobicity was determined by measuring the water contact angle of the surface. For this, 3 μL of deionized water are manually dropped onto the sample surface. From the image of the resulting droplet along the sample plane, the angle at which the water meets the surface plane can be obtained (see Figure 2.4). The accuracy of this method is estimated at $\pm$ 5°. However, while general agreement exists that hydrogen-terminated diamond is hydrophobic with a contact angle of up to e.g. 90° for single crystal samples, the values measured over the course of this work have deviated significantly and seemingly arbitrarily to lower values. As well as contact angles of around 90°, values of down to 70° to 80° have been routinely measured, although no correlation could be found with e.g. results for the surface conductivity. Nonetheless, the contact angle of hydrogen-terminated surfaces is always markedly larger than that of oxygen-terminated surfaces. It is therefore still a fast and easy method to qualita-

tively determine the surface termination of diamond.

2.2.3 Controlled oxidation of diamond

While for most applications the complete termination of the surface with either hydrogen or oxygen is desired, the controlled increase of the fraction of oxygen-terminated surface carbons can be advantageous to tune the surface properties to a state between the extremes. Such a controlled oxidation of the hydrogen-terminated surface can be achieved with ozone as a slow and, therefore, controllable oxidizing agent [Sak03]. In our case, the ozone was generated with UV light (5 W, Heraeus Noblelight GmbH, Germany; mercury lamp with wavelengths of 185 and 254 nm) in an oxygen atmosphere. The sample rests in the reaction chamber where the generated ozone slowly oxidizes the hydrogen-terminated surface. Once the chosen time is reached, the UV light is turned off and the generated ozone flushed out with nitrogen.

Before measuring the effect of this partial oxidation on e.g. the conductivity, the surface conductivity needs time to equilibrate before reaching its new equilibrium value. This effect can be attributed to the mechanism initially responsible for the surface conductivity, i.e. the surface transfer doping [Rie04]. The samples were therefore left in ambient condition overnight, before taking measurements. The samples used for this study were prepared as to have a hydrogen-terminated area between two contacts. The effect of the ozone on the exposed hydrogen terminated area could then be conveniently recorded by measuring the conductivity of the sample before and after the ozone exposure. As the hydrogen-terminated area is contacted before ozone exposure, thereby covering the contact area, the contact resistance can be assumed to remain unchanged, in a first approximation.

As expected, the conductivity decreases with increasing exposure time to the UV light in oxygen atmosphere. The conductivity decrease exhibits a linear rather than exponential dependence with time, as shown in Figure 2.5. It should be noted here, that the time is measured from the switching on of the UV lamp. Therefore, a steady state ozone concentration needs to be established initially. This is expected to result in a time lag between the start of the UV lamp and the steady-state rate for the conductivity decrease. The conductivity decrease shown in Figure 2.5 is appropriate for the purpose of a rough control of the oxidized fraction of the surface. A complete surface oxidation requires a longer UV exposure. Such an experiment is shown in Figure 2.6, where the surface of a sample was successively oxidized over a total

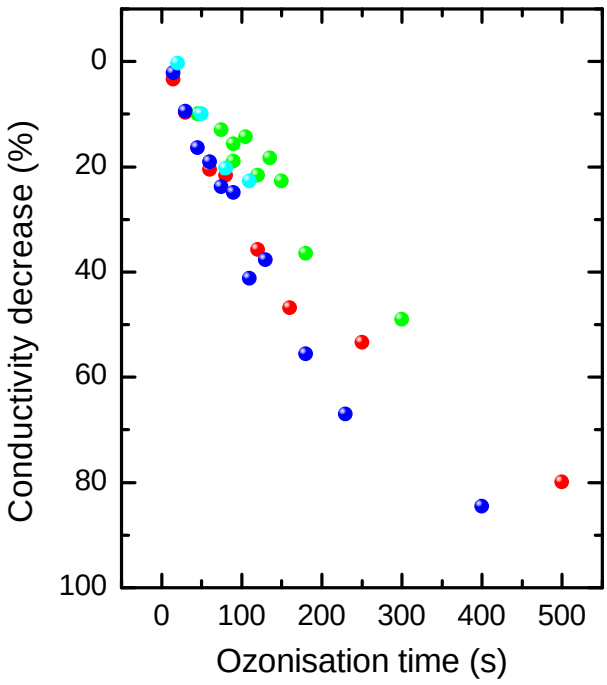

Figure 2.5: *Conductivity decrease of hydrogen-terminated diamond surfaces versus time exposed to UV-produced ozone. After the ozonisation, the sample was left to equilibrate over night before the conductivity was measured. Each data point represents the ozonisation of one sample with a particular initial, absolute conductivity. Different colors represent different data series composed of a number of samples.*

time of 9.2 hours until the conductivity reached the same value as for a completely oxidized (with O_2 plasma) sample, within the sensitivity limit of the current meter. As before, the conductivities were measured after letting the sample equilibrate over night after each oxidation step. In a linear plot, all of these current-voltage curves show linear behavior, with only minor and not systematic deviations from linearity observed as the conductivity decreases and the signal gets smaller. The sample conductance (calculated from the slope of the current-voltage curves) is shown in Figure 2.6 in a semi-logarithmic plot versus the ozonisation time. Notwithstanding the scattering in the data, the dependence of the conductivity decrease on the ozone exposure time can be described as exponential. The first three data points (starting at zero ozonisation time) seem to follow different kinetics. However, further experiments are required to verify this. The data, starting from two hours of ozonisation, can be fitted assuming first order kinetics, yielding a rate constant of -0.7 h^{-1}. The exponential dependence as compared to the linear dependence in Figure 2.5 can be attributed to the belated onset of oxidation due to the concentration

buildup of ozone, which affects only the shorter oxidation times significantly, as discussed above. This is supported by the data points above 350 s in Figure 2.5, which show a deviation from the linear behavior. A logarithmic behavior dependence with a decreasing rate of conductivity decrease with a decreasing absolute conductivity is plausible. Even while the probability of oxidation of a single hydrogen-carbon bond by an ozone molecule may remain constant, the absolute number of hydrogen-carbon bonds and therefore the total probability of encounters with ozone molecules decreases with the absolute conductivity. This is a standard situation in which to expect first order kinetics.

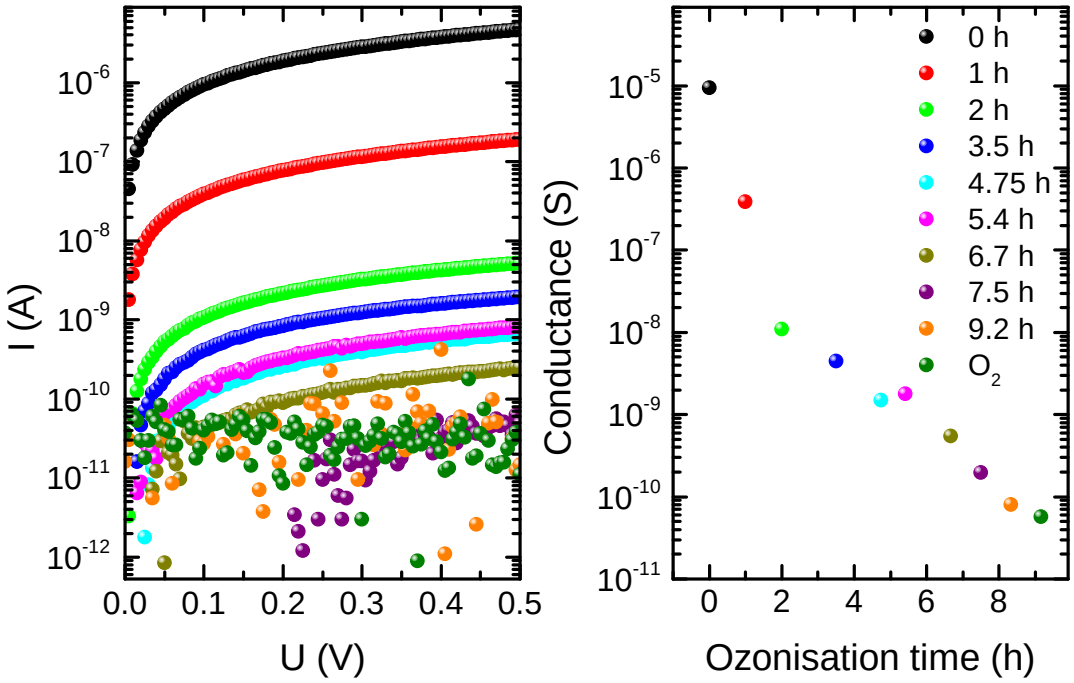

Figure 2.6: *left: Current-voltage curves recorded after consecutive ozone-induced oxidation steps (indicated times give the total accumulated oxidation time). After 9.2 hours, once the conductivity cannot be resolved anymore with the current meter, the sample is oxidized with oxygen plasma, known to result in a complete oxygen-termination of the diamond surface. The color code is identical to the figure on the right. right: Conductances calculated from the data on the left, shown in a semi-logarithmic plot over the accumulated oxidation time.*

Overall, the presented method allows for the controlled oxidation of a hydrogen-terminated surface and, with it, of the properties associated with the degree of hydrogenation or oxidation of the diamond surface.

2.2.4 XPS characterization of diamond surfaces

While the hydrogen-termination of the diamond surface is a standard process and its quality can be indirectly assessed via the established surface conductivity, the direct investigation of the elements present on the surface via a surface sensitive method such as X-ray photoelectron spectroscopy (XPS) can provide additional information. The X-ray source used here was a synchrotron, where the monochromatic radiation is generated by the deflection of electrons in an accelerator ring (beamline 11.0.2 of the Advanced Light Source (ALS) at Lawrence Berkeley National Laboratory). The X-rays are used to induce photoemission from the sample material. The kinetic energy of the emitted electrons can be measured and, as the X-ray energy is known, the original binding energy of the electrons can be calculated. Even for high energy X-rays, only photoexcited electrons from approximately the top 10 nm are emitted. Electrons generated deeper in the sample are recaptured or trapped in excited states. XPS is thus a surface sensitive technique. In order to detect all emitted electrons and prevent their adsorption before reaching the detector, XPS requires ultrahigh vacuum (UHV) conditions.

The hydrogen-terminated samples were placed in an UHV chamber after prolonged exposure to ambient conditions. In order to avoid charging of the surface as much as possible, the samples were grounded. In addition to the predominant carbon peak (nominally at 284 eV; [Fra95]), the initially recorded spectra showed a small oxygen peak (nominally at 532 eV; [Mak03]) (see Figure 2.7). As will be discussed later, adsorbed water on the diamond surface is believed to contribute to the oxygen signal in the XPS spectrum (Section 2.2.5). Furthermore, adsorbed hydrocarbons on the surface are expected to contribute to the carbon peak. Therefore an annealing of the surface to remove both adsorbed water and hydrocarbons is necessary to investigate the true composition of the diamond surface. After heating the samples to approximately 725 °K and cooling down, the carbon peak is significantly sharper and the oxygen peak relatively smaller (see Figure 2.7 and also Figures 2.8 and 2.9). The diamond samples investigated exhibit peaks at the corresponding binding energies of carbon (Figure 2.8) and oxygen (Figure 2.9). We fitted the C1s carbon peak with four components with slightly different peak positions, one for the bulk carbon (around 284 eV [Wu93] [Gra94] [Kla10] [Gho10]), one for the hydrogen-bonded carbon (Δ E=+0.75 eV; [Gra98]), one for the oxygen-bonded carbon (Δ E=+1.5 eV for the (100) surface and Δ E=+1.8 eV for the (111) surface; [Mak03]), and one for the reconstructed π bonded carbon (Δ E=-1.0 eV; [Gra98]). For the hydrogen-terminated diamond surface, contributions from the bulk carbon and hydrogen-

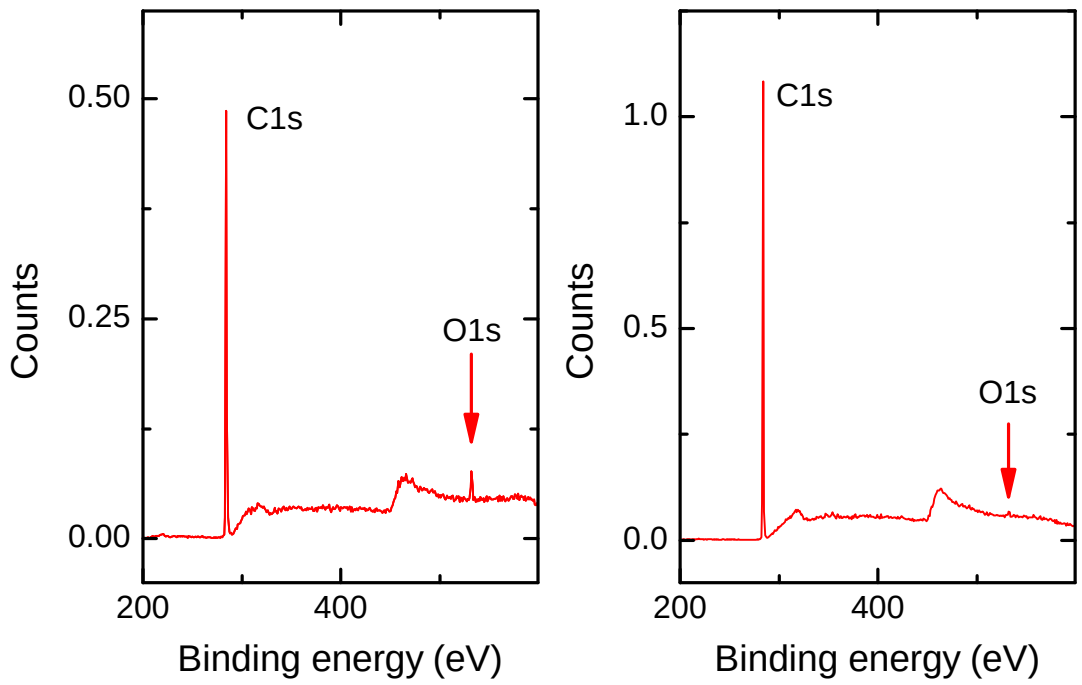

Figure 2.7: *XPS survey spectra of hydrogen-terminated diamond without any pre-treatment (left) and after annealing at 725 K (right), revealing the C1s carbon peak (≈ 284 eV) and the O1s oxygen peak (≈ 532 eV). The O1s peak is greatly diminished after annealing.*

bonded carbon are obviously expected. The recorded O1s oxygen peak and the fact that a component for the oxygen-bonded carbon is necessary to fit the overall carbon peak both point to an imperfect hydrogenation. The contribution from reconstructed π bonded carbon is less obvious and would point to surface carbon not terminated at all or even sp^2 hybridized carbon residues. This component is very small and the influence of its inclusion in the fit on the other components negligible. However, as it does consistently improve the overall residual of the fit and is frequently observed in literature it was nevertheless included. The combination of these four components is therefore expected for an imperfectly hydrogen-terminated diamond surface. Over all spectra this combination results in a consistently decent fit. The constrictions imposed on the fitting parameters are shown in Table 2.3.

In some cases, none of these restrictions where actually needed, while in most cases only one of the restrictions was required to fit the spectra with the four components in a physically meaningful way. Before the fitting procedure the spectra were shifted with the bulk carbon peak assigned to its expected binding energy value of 284 eV. This is necessary due to charging of the surface from the photo-generated electrons.

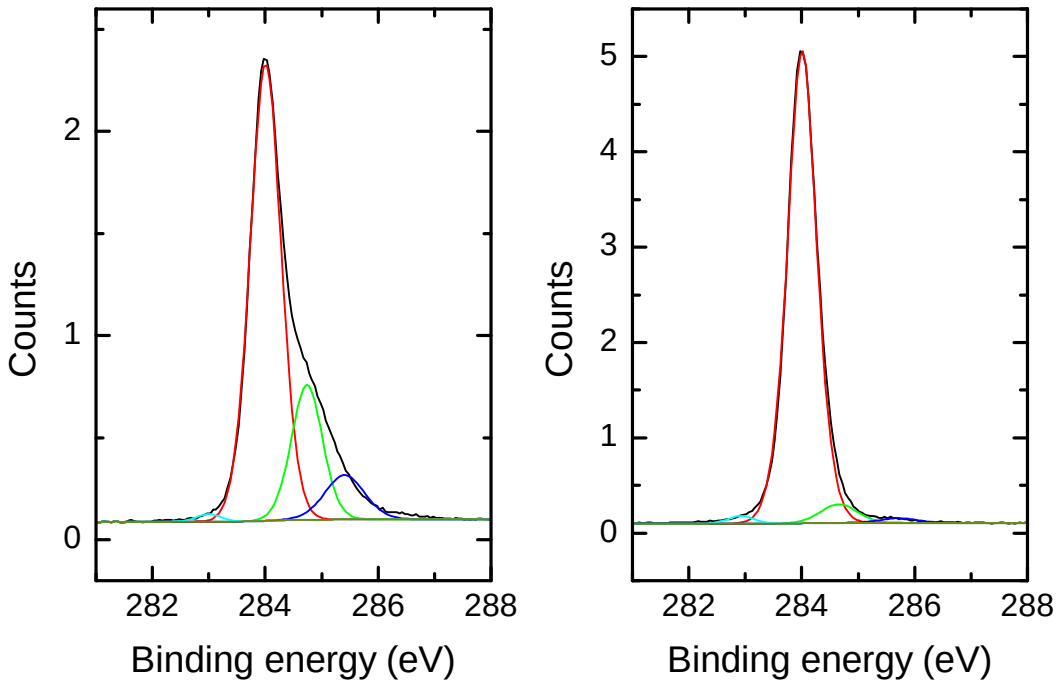

Figure 2.8: *XPS spectra of the C1s carbon peak, fitted with four components for the bulk carbon (red curve), the hydrogen-bonded carbon (green curve), the oxygen-bonded carbon (blue curve), and the π-bonded carbon (cyan curve). left: The spectrum was recorded without any pre-treatment. right: The spectrum was recorded after in-situ annealing at 725 K.*

It is worth recalling that the surface conductivity of the hydrogen-terminated diamond strongly decreases after annealing in UHV conditions (see Section 2.2.1). The biggest uncertainty of the fit of the C1s carbon peak results from assigning the contribution of the C-H and the bulk carbon component. Small shifts in the position of the C-H component significantly change its overall area and consequently also the area of the carbon-oxygen component. As a result, the ratio of the oxygen versus the hydrogen-terminated surface regions cannot be determined from the components of the carbon peak alone. The O1s oxygen peak provides a more direct and quantitatively accurate measure for the oxygen content of the surface. After annealing in UHV, the oxygen peak was fitted with one component, representing chemisorbed oxygen on the surface with a binding energy of 532 eV (see Figure 2.9). The calculation of the oxygen surface coverage of the nominally hydrogen-terminated diamond substrate is described in Appendix A.1, where we estimate a monolayer coverage of oxygen of 3% for the best hydrogen-terminated sample.

The XPS results discussed above allow to draw two conclusions. First, the surface is

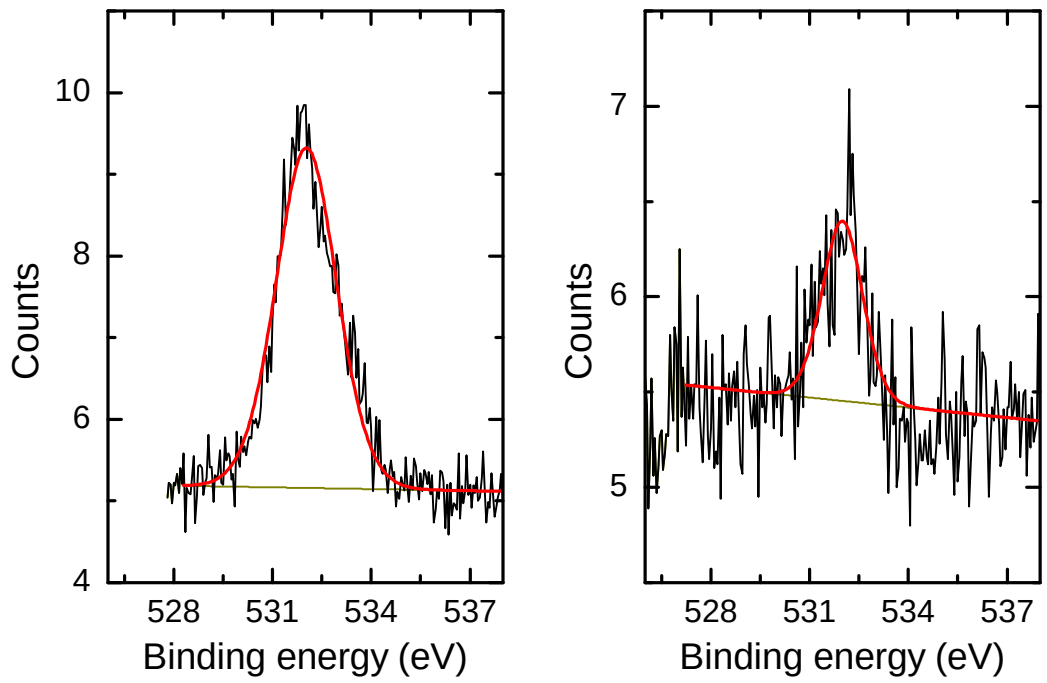

Figure 2.9: *XPS spectra of the O1s oxygen peak, fitted with one component (red). left: The spectrum was recorded without any pre-treatment. right: The spectrum was recorded after in-situ annealing at 725 K.*

C1s	C bulk	C-H	C-O	C-C π
line shape	GL(50)	GL(30)	GL(30)	GL(30)
fwhm constr. [eV]	0.6-0.8	0.6-0.8	0.6-0.8	-
position constr. [eV]	284	284+0.75 $\pm$ 0.1	284+1.5 $\pm$ 0.1 for (100) 284+1.8 $\pm$ 0.1 for (111)	-
background	shirley			

Table 2.3: *Constraints used for the fitting parameters of the C1s carbon peak XPS spectra. The values for the lineshape refer to the contribution ratio between a gauss and a lorentz shape.*

indeed hydrogen-terminated with only a small oxygen content. Second, even without subjecting the surface to annealing, there are little to no contaminations from elements other than carbon, hydrogen and oxygen. Even the sample, which had undergone processing for the gold contacts, showed additionally only a small silicon peak before annealing, which we attribute to contaminations picked up during pro-

cessing as silicon is a widely used material in the relevant rooms and equipment.

2.2.5 Water on hydrophobic diamond

The surface conductivity of hydrogen-terminated diamond has been explained [Mai00] based on the presence of a layer of adsorbed water on the surface and, yet, the surface is considered hydrophobic with a contact angle of around 90°. This apparent contradiction is the motivation to investigate the adsorption of water on the hydrogen-terminated diamond surface in ambient conditions.
Initially, we have studied the effect of water on the establishment of the surface conductivity. For this purpose, the presumed water on the surface was initially removed by annealing in vacuum, followed by a selective reintroduction of water vapor into the vacuum chamber, all while continuously monitoring the surface conductivity of the sample in situ. Experimentally, this was implemented by placing a hydrogen-terminated diamond sample with processed gold contacts on a heater in a vacuum chamber, where a leak valve to a water reservoir containing deionized and degased water was installed.

Figure 2.10 shows the time-dependent current recorded in a surface conductive diamond sample. The start (”1”) and end (”8”) points were both measured under ambient conditions. During the heating phase (”2” to ”5”) from room temperature to around 740 K, the conductivity drops by six orders of magnitude, only to be reestablished by the stepwise increase of the water vapor pressure in the chamber (”5” to ”8”). The base pressure of the chamber was approximately 5×10^{-7} mbar.

Going through the steps one by one, the conductivity already drops while pumping down the vacuum chamber (”1” to ”2”). In order to further remove the water, the heater temperature is increased from point ”2” (RT) to point ”3” (740 K). This leads initially to an increase in conductivity, followed by a decrease. When the heater is turned off again (after point ”3”), the conductivity further decreases (until point ”4”). As the temperature decrease begins to slow down (”4” to ”5”) the current rises again to a low steady state value. After the leak valve is opened (point ”5”), thereby introducing water vapor into the chamber, the conductivity rises again, but to a higher value than before (”5” to ”6”). Each subsequent increase in the water vapor pressure is immediately followed by an increase in the conductivity (”6” to ”7” to ”8”). Finally, the sample is again exposed to ambient conditions (after point ”8”),

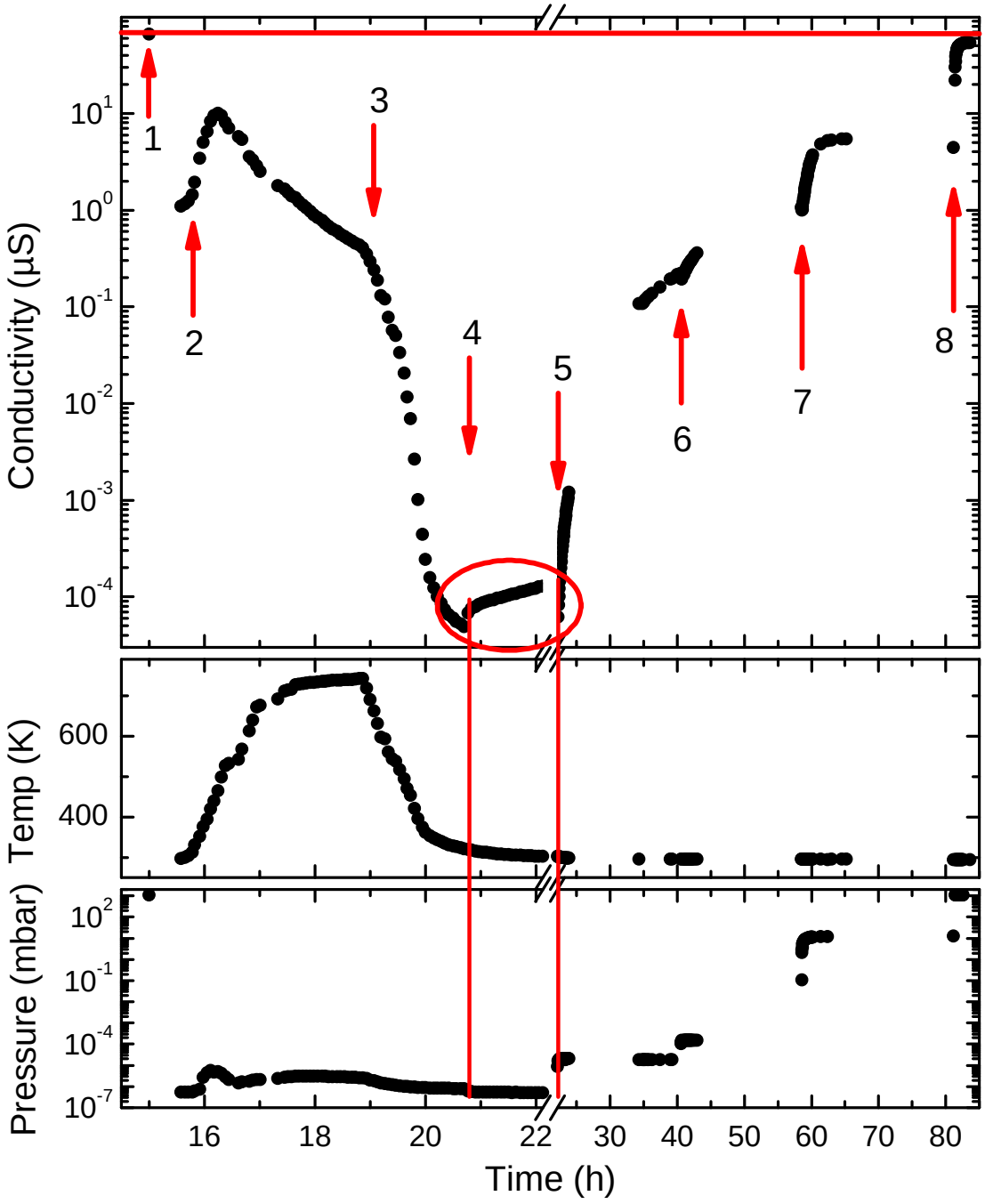

Figure 2.10: *In-situ surface conductivity of a hydrogen-terminated diamond sample during water removal and subsequent readsorption. The pressure increases in the bottom graph are the result of water vapor dosing through a leak valve. After step 8, the vacuum chamber was opened to ambient conditions (as for the very first data point). The gaps in the manually recorded data points correspond to the sleep cycle of the experimenter. Note the broken x-axis at 22 h.*

resulting in a conductivity almost equal to the value before the experiment.

In light of the current understanding of the mechanism of the surface conductivity of hydrogen-terminated diamond, we interpret the results in Figure 2.10 as follows. In this experiment there are several processes at work, related to temperature and the partial pressure of various gases, which influence the surface conductivity. As described in Section 2.2.1, the transfer doping mechanism in diamond establishes the equilibrium between the electrochemical potential of the electrons in the diamond and those of two redox couples, described by Equations 2.1 and 2.2. By establishing a vacuum, the partial pressure of the reactants and therefore their concentration in the adsorbed water layer changes. However, as hydrogen is relatively much more prevalent in high vacuum than in air, the ratios of the reactants of Equation 2.1 and 2.2 changes as well. Furthermore, the sample is heated, but not the whole vacuum chamber. This means, that water is expected to specifically desorb form the sample surface, while at the same time the water vapor pressure in the chamber stays almost constant. A lack of water constitutes a lack of electron acceptors as e.g. the hydronium ion cannot exist independently, which is part of Equation 2.1 and 2.2. Therefore the conductivity decreases during the heating phase. Finally, the conductivity that is established can be susceptible to thermal activation, which could possibly explain the rise in conductivity during the first part of the heating phase. After the heating phase, when the sample has cooled down again, residual water vapor in the vacuum chamber can readsorb on the surface and provide once again electron acceptors for transfer doping. This could be at the origin of the current increase between points ”4” and ”5”. The subsequent injection of water vapor through the leak valve increases the water vapor pressure, allowing for more adsorption (more electron acceptors) and thus a further increase of the measured current. That indeed the water vapor pressure is increased above all other constituents of the atmosphere after water dosing, can be seen from the mass spectrometer data shown in Figure 2.11. The water vapor pressure (atomic mass 18) is a factor of twenty higher than the nitrogen pressure (atomic mass 28) as the second most common constituent, not counting hydrogen (atomic mass 2), which is always disproportionately abundant in high vacuum.

The increase of the conductivity observed after each increase of water vapor pressure has an exponential component, though the dependence is not the same for each increase of water vapor pressure. The addition of water constitutes a fresh supply

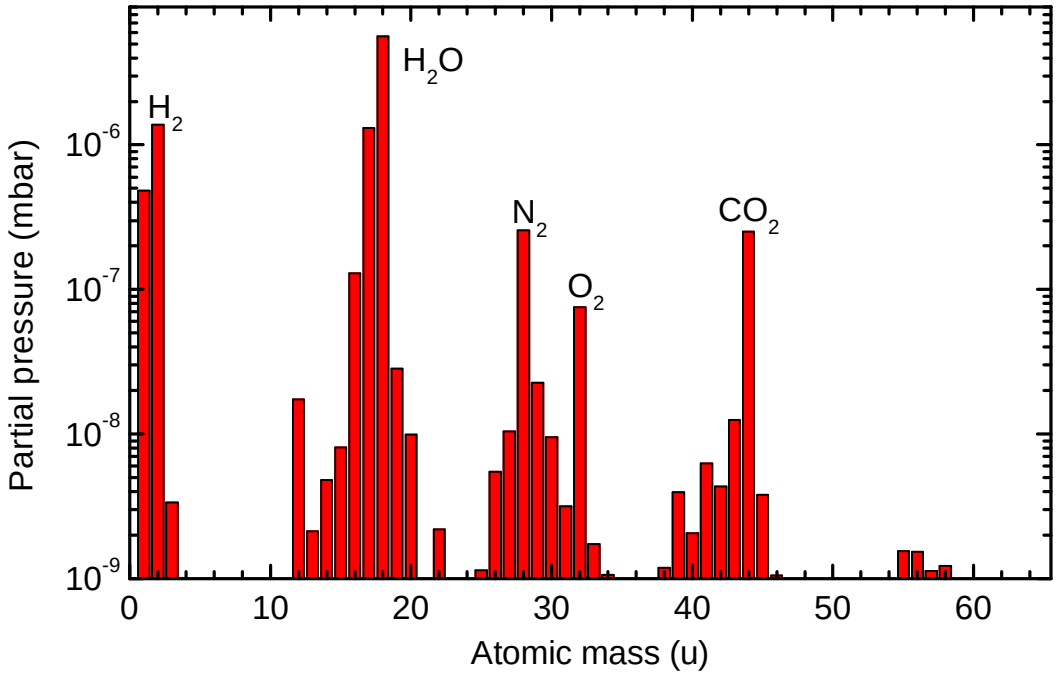

Figure 2.11: *Mass spectrometer recording obtained after the addition of water vapor resulting in a total pressure of 1.4* 10^{-5} *mbar corresponding to step 5 in Figure 2.10. The water vapor pressure (atomic mass 18) is a factor of twenty higher than the nitrogen pressure (atomic mass 28).*

of reactants, providing electron acceptors and thereby also changing the electrochemical potential of the acceptor redox couples. An exponential dependence of the current increase can then be explained either by assuming corresponding adsorption kinetics for the reactants, or by the reaction kinetics. While the adsorption kinetics are not known, the reaction kinetics do add an exponential component to the observed current increase. As a fresh supply of reactants is added with each water vapor increase, the electrochemical potential of the electrons in the diamond and in the acceptor redox couples are not in equilibrium anymore. Therefore electron transfer from the diamond into the adsorbed acceptors will take place, until the new equilibrium is reached. As a result, the number of accumulated holes in the diamond increases, leading to the observed current increase. The rate or exchange current across the diamond/acceptor interface in such a situation, can be described by the Butler-Volmer equation, which describes the exchange current as a function of the overpotential beyond the equilibrium potential (e.g. [Zha08]).

$$j = j_0 \left[\exp\left(\frac{(1-\alpha)ze}{k_B T}(E - E_{eq}) \right) - \exp\left(\frac{\alpha ze}{k_B T}(E - E_{eq}) \right) \right] \tag{2.5}$$

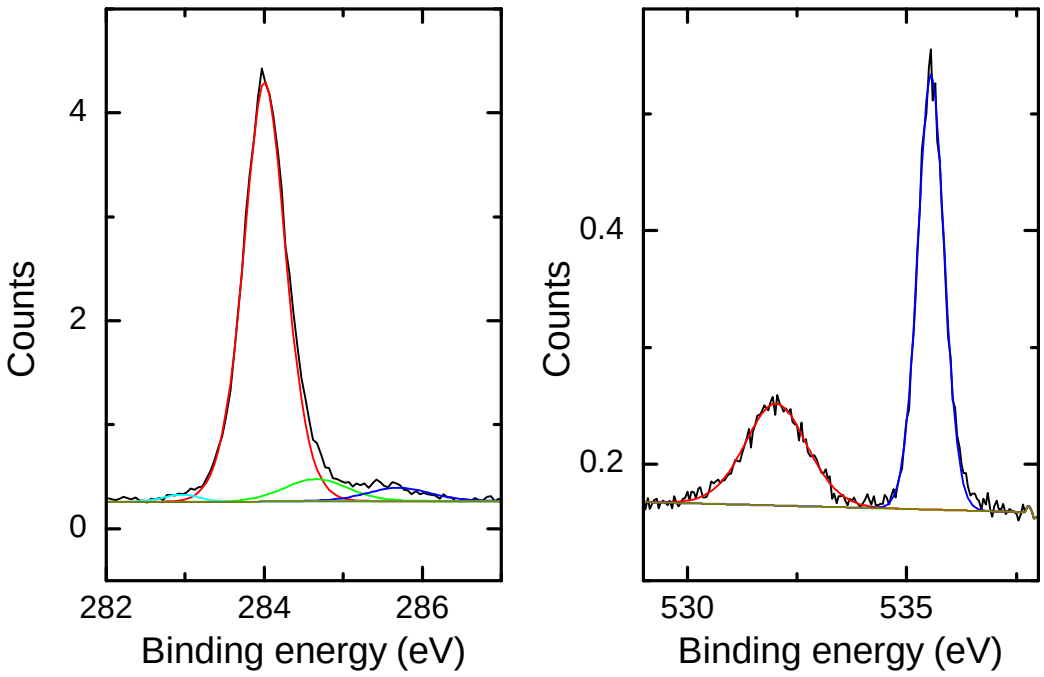

Figure 2.12: *XPS spectra of the C1s carbon peak and the O1s oxygen peak after dosing water into the chamber (pressure 1.5 mbar). left: The C1s peak is fitted with four components for the bulk carbon (red curve), the hydrogen-bonded carbon (green curve), the oxygen-bonded carbon (blue curve), and the π-bonded carbon (cyan curve). right: The O1s peak is fitted with two components for the adsorbed oxygen (red), and the oxygen of the water vapor in the vicinity of the surface (blue).*

j and j_0 describe the current and exchange current density respectively. α denotes the charge transfer coefficient, e the elementary charge, k_B the Boltzmann constant, T the temperature, and z the number of electrons involved in one reaction. E_{eq} and E are in the case discussed here, the equilibrium potential of the redox couple at the present conditions and the electrochemical potential of the electrons in diamond, the Fermi level, respectively. The difference between E_{eq} and E is the overpotential. As the conductivity of Figure 2.10 is dependent on the number of charge carriers and therefore on the derivative of the exchange current over the interface, it inherits the exponential dependence from the Butler-Volmer equation. Additional kinetic effects, such as the above mentioned adsorption of the reactants at the surface will further contribute to the overall kinetics.

Despite the complexity of the detailed behavior of the surface conductivity of the described experiment, the basic conclusion remains clear. Once the surface conductivity is removed by desorption of the surface acceptors, water is a necessary

prerequisite to reestablish this surface conductivity, as only the water concentration is limited during the annealing and only the water concentration changes significantly during the dosing in of water into the chamber. This does not exclude the contribution from other reactants (such as O_2 and H_2) to the surface conductivity.

This preliminary experiment was followed by a XPS investigation of the presence of water on the hydrogen-terminated diamond surface, using the same synchrotron beamline described above (see Section 2.2.4). For these experiments an important and unique feature of this XPS setup was used. Traditionally XPS spectra are recorded in vacuum conditions, as the electrons need to travel a significant distance from the sample to the detector, and would be adsorbed by the gas molecules at higher pressures. In ambient pressure XPS, this limitation is overcome by creating an evacuated pathway for the emitted electrons while the chamber itself is at high pressure. This is achieved with a very small opening of this evacuated pathway to the chamber directly above the sample surface. The opening is big enough to capture most electrons, but so small that the gas flow entering this pathway can be evacuated with powerful pumps. This differentiated pumping is repeated three times to reach satisfactory low pressures at the detector stage. An excellent overview over this technique is given by H. Bluhm [Blu10].

Following the initial recording of the XPS spectra, the sample was annealed (as described in Section 2.2.4) and new XPS spectra were recorded, then water was dosed into the chamber via a leak valve and spectra were recorded once again (see Figure 2.12). Within the available beam time, it was possible for only one sample to continue the experiment. This sample was cooled, to increase the relative humidity, and spectra were recorded. Finally, the cycle was completed by annealing the sample a second time and recording the spectra of the once more water-free sample surface. Each of these spectra was fitted as described before (Section 2.2.4). In the spectra of the O1s peak recorded at high water vapor pressure, a second oxygen peak at higher binding energies (approx. +3 eV) is visible (see Figure 2.12). This peak has been attributed to the photoelectrons emitted from the oxygen in the water vapor in the vicinity of the surface, which are also detected [Blu10],[Ver07]. As this is not adsorbed water, we do not include this peak area into the calculations of the oxygen peak.

Table 2.4 and Figure 2.13 show the ratio of the O1s oxygen peak area to the C1s peak area for the investigated samples for different experimental conditions. A calculation of the surface coverage does not seem to be prudent as it involves the oxygen in the water layer on top of the partially oxidized diamond surface. The ratio of the O1s

experimental steps	peak area ratio sample S17 (100)	peak area ratio sample S30 (111)	peak area ratio sample S33 (100)
after annealing to 725 K	0.035	0.005	0.014
after water dosing to 1.5 mbar at 295 K $\equiv$ 6.4 % RH	0.068	0.040	0.021
after water dosing to 1.5 mbar at 273 K $\equiv$ 28 % RH	0.073	-	-
after annealing to 725 K	0.039	-	-

Table 2.4: *Ratio of peak areas from the O1s and the C1s peak. The relative humidity (RH) is calculated according to [Den08]:* $p/p_v(T) \times 100 = RH$*, with* p *and* $p_v(T)$ *the water vapor pressure and the equilibrium vapor pressure of water at the temperature* T*, respectively.*

oxygen peak area to the C1s peak area increases for all samples when dosing water into the chamber. It increases further for the sample cooled to approximately 275 K, in line with a higher relative humidity. Finally the oxygen content is restored to almost its original value after heating the sample to 725 K. These results show that water or O_2 is indeed adsorbed on the hydrogen-terminated diamond surface. The surface is not oxidized during the water dosing experiment, as its oxygen content can be restored to its previous value through annealing. The annealing temperature is high enough to remove adsorbed water, but not high enough to remove chemisorbed oxygen. These observations are in agreement with similar experiments in literature [Lai04], [Akh10].

From these experiments we conclude that water is indeed adsorbed on the hydrophobic hydrogen-terminated diamond surface. This is even the case at humidities below ambient conditions. Furthermore, this water is a prerequisite for the surface conductivity of hydrogen-terminated diamond. As the hydrogen-terminated diamond surface is hydrophobic, this leaves us with an apparent contradiction, namely "hydrophobic water". It is beyond the scope of this work to resolve this contradiction. However, it should be noted that such phenomenons have been previously discussed. The group of P-G. de Gennes has calculated thermodynamically situations in which a drop forms on a liquid of the same material [Bro91]. Similarly, in the Stranski-Krastanov growth mode in molecular beam epitaxy, initial growth in complete layers is followed by further growth of islands on the same material. Furthermore, the behavior of water is strongly influenced by its ability to form hydrogen bonds [Cha05].

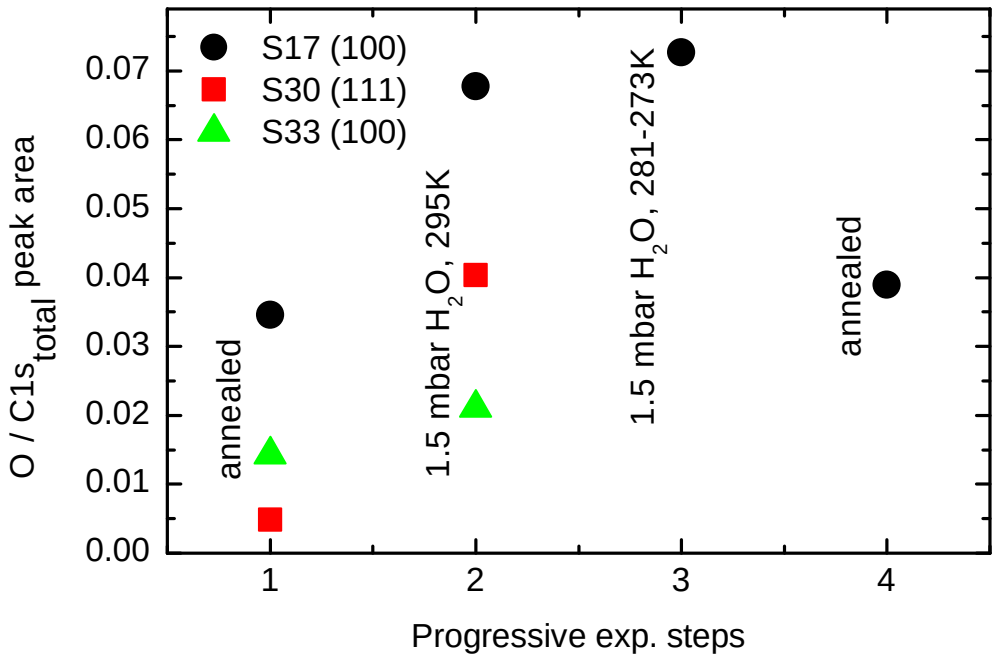

Figure 2.13: *Ratio of peak areas from the O1s and the C1s peak during the progressive experimental steps described in the text. The relative humidity corresponds to 6.4 % in step 2 and 28 % in step 3 (see Table 2.4).*

The hydrophobicity of surfaces is to some extent a result of the ability or inability of water molecules to keep the hydrogen bond network intact at the interface to such surfaces. Water molecules may also be oriented close to surfaces [Sed08], which in turn reduces their ability to be incorporated in the hydrogen bond network. These considerations make it plausible that the water adsorbed on the hydrogen-terminated diamond surface has not the same characteristics as bulk water and therefore might appear hydrophobic.

2.2.6 Functionalization of diamond surfaces

The development of diamond as a material for biosensors or bioelectronic devices necessitates control of the surface and more specifically surface-functionalization capabilities. In this context, the functionalization of diamond surfaces was developed as an enabling capability in the course of this work.

The so-called functionalization of surfaces refers to their chemical modification with molecular groups, that give the surface a desired property. Very often the goal is to prepare the surface in such a way as to further covalently graft to the surface

molecules such as e.g. fluorescence dyes or proteins to promote or inhibit cell growth. In a sense, the termination of diamond with O- and H- atoms is already a functionalization of the surface, as e.g. the hydrophobicity changes drastically. Further, simple plasma or gas assisted terminations of the diamond surface are possible, e.g. with F, Cl or NH_2 [Fre90] [Fre94] [Mil96]. A number of further functionalization pathways for larger molecules have been developed. They use either hydrogen- or oxygen-terminated diamond as their starting point. The reactions between the H- or O-terminated diamond surfaces and these molecules are either photochemical, electrochemical or simply chemical in nature. Two of these reactions, the functionalization of the H-terminated diamond with alkene molecules and the binding of silanes on the O-terminated surface, are of greater importance for this work. The photochemical modification of the H-terminated diamond surface was first developed and its mechanism described by the Hamers group [Yan02] [Nic06]. This process uses UV light to excite electrons from the diamond into the solution, activating the terminal double bond of the alkene molecule, which subsequently reacts with the surface to form a covalent C-C bond. The molecule used for the functionalization was trifluoroacetamide-protected 10-aminodec-1-ene (TFAAD), which exhibits an amine group after deprotection (see Appendix A.5.4). The silanisation of oxygen-terminated diamond surfaces depends on the reactivity of hydroxyl groups at the surface [Ulm96]. Silanes are believed to react to silanols with water adsorbed on the diamond surface and then form covalent bonds with the hydroxyl groups on the diamond surface. This silane chemistry is a standard process applied to non-diamond surfaces with hydroxyl groups as well [Ulm96]. A common silane also used for the functionalization of diamond is 3-aminopropyltriethoxysilane (APTES). For details of the chemicals involved and protocols regarding these functionalizations see Appendix A.5.4.

Functionalization of new molecules

Proteins are in many cases the type of molecules to tether to the surface. And one of the most common functional groups present in almost any protein is the amine group. As the functional end group of the TFAAD molecule is also an amine group, a crosslinker is necessary to bind proteins to the TFAAD functionalized surface. It is therefore desirable to use different molecules with other functional end groups to avoid crosslinkers and bind e.g. proteins more directly to the surface. Undecylenic acid (UA) is a molecule which differs only in its carboxyl end group from TFAAD. This carboxyl group can directly bind to amine groups to form the so-called peptide bond. The undecylenic acid molecule contains the same C-C double bond as

the TFAAD molecule, therefore the same protocol than for the functionalization of TFAAD molecules ([Yan02], [Har04], [Zho07], [Hau08]) was employed. Fluorescence microscope images (see Figure 2.14) show that undecylenic acid could be functionalized on the surface and that the carboxyl group which binds to the dye remains active. The bright regions were functionalized with undecylenic acid and thus bind to the dye, whereas the dark regions are oxygen-terminated and therefore not functionalized. The fluorescence dye used was Alexa Fluor 594 cadaverine (Invitrogen) with an excitation wavelength of 590 nm and an emission wavelength of 617 nm [Her08].

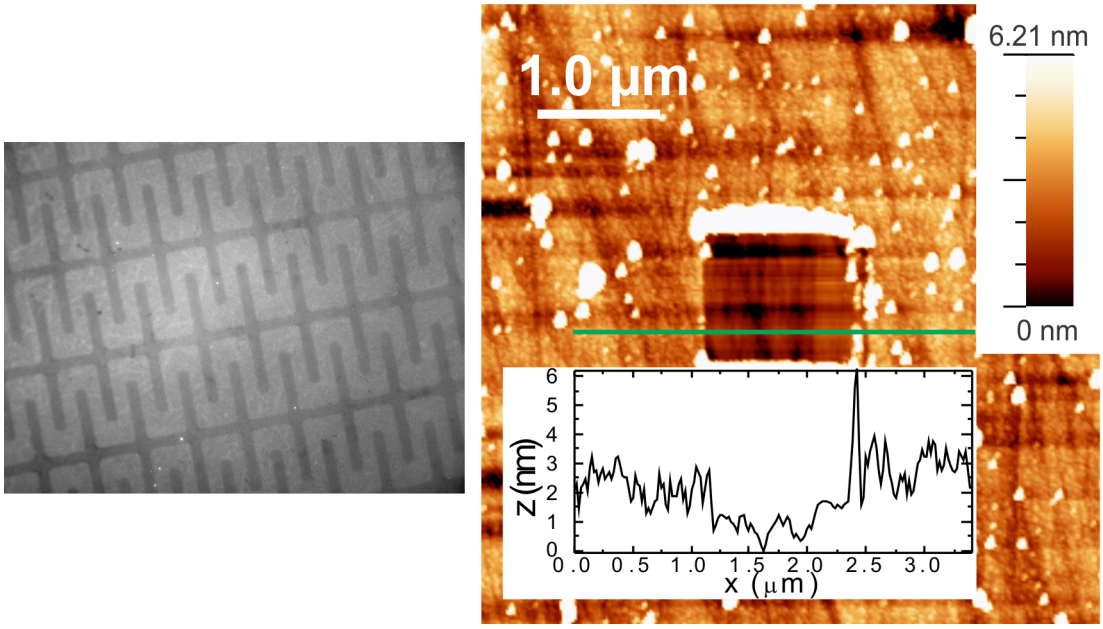

Figure 2.14: *left: Fluorescence image of undecylenic acid functionalized diamond surface using the Alexa Fluor 594 cadaverine dye to label the carboxyl groups. The bright regions correspond to the functionalized part of the surface, whereas the dark regions are oxygen-terminated and therefore not functionalized. right: AFM image of undecylenic acid functionalized diamond surface. The central square was scratched in contact mode, while the image was recorded in tapping mode. The insets show the z-scale and an example profile across the scratched region (indicated by green line). The height difference between the scratched and the unscratched areas is approx. 0.8 nm after averaging several profiles.*

Monolayer functionalization

While a large amount of work exists on functionalization of different biosensor surfaces including diamond, the emphasis is often, though not always, on the proof of a

successful functionalization and not on the functionalization of a monolayer. Building on previous work of the functionalization of the TFAAD molecule ([Yan02], [Har04]) and the undecylenic acid molecule, the thickness of the layer resulting from the used functionalization protocol was investigated with an AFM. The functionalized surface is scratched with an AFM tip in contact mode, followed by a scan of the scratched area and its surroundings in tapping mode (see Figure 2.14). The functionalization protocol was adjusted at a UV exposure time of 2 hours. The resulting image is shown in Figure 2.14 with depth profiles of, on average, 0.8 nm, which roughly corresponds to 1 monolayer. Analogue procedures for the TFAAD molecule resulted in a layer thickness of 2.2 nm, corresponding to roughly 2 monolayers. When judging the monolayer coverage from the thickness of the functionalized layer, a stretched molecule is assumed. Further optimization of this coverage would require improving the homogenity of the functionalization and the measurement techniques for the coverage.

Aside from chemically attached material, functionalized multilayers could also arise from physisorption. In order to remove physisorbed material suitable cleaning procedures have to be employed. This is especially important when functionalizing surfaces in a pattern as in Figure 2.14, because the functionalizing molecule can also physisorb on the nominally unfunctionalized parts thus destroying the desired contrast [Hau08]. This is especially true for oxygen-terminated surface parts, which are much more prone to adsorption of organic molecules than hydrogen-terminated surfaces. Obviously the cleaning procedure to remove excess material and physisorbed molecules has to be tailored to the solvents and functionalization molecules used. For the photochemical attachment of undecylenic acid, shown in Figure 2.14, and TFAAD, the samples were cleaned with chloroform, methanol and isopropanol (see Appendix A.5.4). Besides excess material from the functionalization, contaminations from dirty solvents, dirty reaction containers, and ambient reaction conditions can result in agglomerates on the surface (see Figure 2.15). Independently of the functionalization process, these agglomerates can be effectively removed by cleaning the sample with diluted (5%) acetic acid solution in an ultrasound bath (see Figure 2.15).

Discriminating functionalization

Surface functionalization usually refers to the chemical modification of the whole surface. However, for a number of applications it is useful to pattern the surface with different terminations and, therefore, properties on different parts of the surface. The diamond surface naturally shows a great versatility in this respect, as it

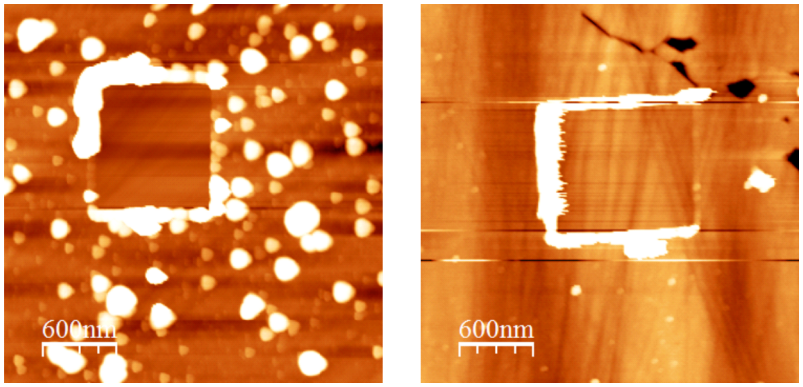

Figure 2.15: *AFM image of APTES functionalized diamond surface. left: The sample was cleaned with toluene and isopropanol for 20 min each in an ultrasonic bath. right: This sample was cleaned additionally with 5 % acetic acid for 30 min in an ultrasound bath.*

can be oxygen- as well as hydrogen-terminated. Variation of functionalization on the same surface is more challenging however. Several combinations of surface functionalizations with different backgrounds - e.g. non-functionalized parts - have been achieved (see Table 2.5). For any combination involving an oxygen-terminated part on the final surface, this is simply accomplished by patterning the fully functionalized surface with photoresist, oxidizing the required parts and finally removing the photoresist. A surface pattern relying wholly on a hydrogen-terminated surface is more challenging. Figure 2.16 depicts a fluorescence image of a pattern composed of TFAAD functionalized parts, which are based on a hydrogen-terminated surface, with a background, which is still hydrogen-terminated but not functionalized.[1] The pattern depicted in Figure 2.16 was achieved by first processing a gold pattern protecting the background area and dissolving the gold after functionalization with a KI/I_2 solution. Seemingly less challenging, but yet unsuccessful, is the a surface pattern with a functionalization with APTES and a hydrogen-terminated background. The problem here is the accumulation of presumably physisorbed APTES on the hydrogen-terminated surface. A solution to this problem could be a cleaning procedure particularly suited to this functionalization.

[1]Masks which shield the UV light required for this functionalization from the background area first come to mind to achieve such a pattern. However, their lateral resolution is not high enough if the mask is simply laid on the sample surface. A pattern made of photoresist is equally unsuitable as the UV light and the functionalization solution damages the resist.

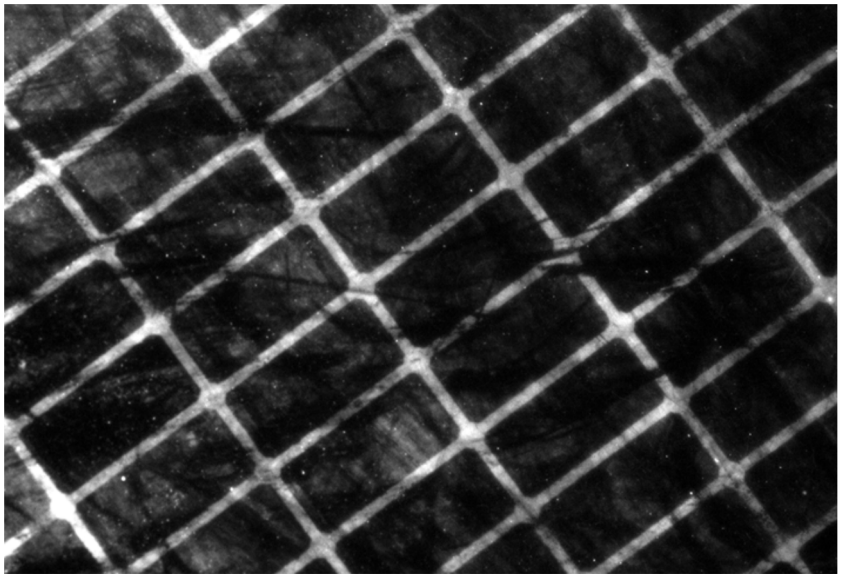

Figure 2.16: *Fluorescence image of a hydrogen-terminated diamond surface with a pattern of TFAAD-functionalized, 4 μm wide lines (bright areas) on the hydrogen-terminated background (dark areas). To achieve this pattern, the hydrogen-terminated diamond surface was patterned with gold, the not-covered areas functionalized with TFAAD, and the gold etched away with a KI/I_2 solution.*

pattern	success	process
H vs. O	yes	H-term.; photoresist mask; O_2 plasma
TFAAD vs. O	yes	TFAAD funct.; photoresist mask; O_2 plasma
TFAAD vs. H	yes	H-term.; Au mask; TFAAD funct.; Au etching
APTES vs. O	yes	APTES funct.; photoresist mask; O_2 plasma
APTES vs. H	no	H-term.; photoresist mask; O_2 plasma; APTES funct. probl.: APTES accumulates on H-term. areas

Table 2.5: *Different combinations of functionalizations and backgrounds with the basic processing steps necessary to achieve these combinations. See Appendix A.5.4 for details regarding the functionalizations.*

2.2.7 Electrochemical stability of the diamond hydrogen-termination

One of the big advantages of the diamond surface over other materials for biosensors is its chemical and electrochemical stability. This work, however, deals with hydrogen-terminated diamond and for any application that relies on this surface termination its stability is equally important. Two fundamental dependences can

be differentiated when investigating the degradation of the hydrogen-termination for bio-applications in electrolyte. One is the degradation with time, which would be due to chemical reactions of electrolyte components with the hydrogen-terminated surface. The second is the degradation resulting from the operation of the device: when changing its electrochemical potential, electrochemical reactions can be accelerated. Such reactions are, of course, very much dependent on the potential of the electrode. The potentials beyond whose either the electrode or the electrolyte decompose mark the limits of the "potential window" of an electrode-electrolyte combination. However, a number of electrochemical reactions (e.g. from impurities in the electrode or the electrolyte) do take place within the potential window and long-term operation within the potential window might still lead to electrode degradation. We therefore look into degradation within the potential window of hydrogen-terminated diamond [Shi05] [Neb07].

In order to assess the stability of the hydrogen-termination in electrolyte over time, the samples were kept in electrolyte under ambient conditions and their conductivity measured irregularly every couple of days. Since the surface conductivity directly depends on the hydrogen termination, any oxidation results in an immediate decrease of the conductivity. The samples were kept in a phosphate based electrolyte buffer solution of pH 7, 10 mM phosphate and adjusted to an ionic strength of 100 mM with KCl. For measuring the conductivity, a three electrode setup with a potentiostat (BANK, POS2) was used to set the electrode potential and an automated current meter and voltage source (Keithley 2400) to measure the conductivity. The use of a potentiostat is prudent for such an experiment, since the conductivity is dependent on the electrode potential (see Section 3.1) and only with a potentiostat a defined potential can be guaranteed (see Appendix A.4).

The results over a period of 50 days can be seen in Figure 2.17. For some samples very limited degradation is observed over this time period (S09), while for other samples the degradation is significant (S11f). Furthermore, in the first few days an increase in conductivity can be observed for some samples (S43, S09). From these observations, we initially concluded that it is at least possible to achieve very limited degradation over such a time period. This conclusion is supported by similar measurements (see Figure 2.17) in a two-electrode configuration, that does not use a potentiostat (see Appendix A.4). The samples show no continuous degradation - at least over the shorter time span investigated. Thus, we investigated the possible degradation during the device operation.

For the investigation of the stability of the hydrogen termination while operating the

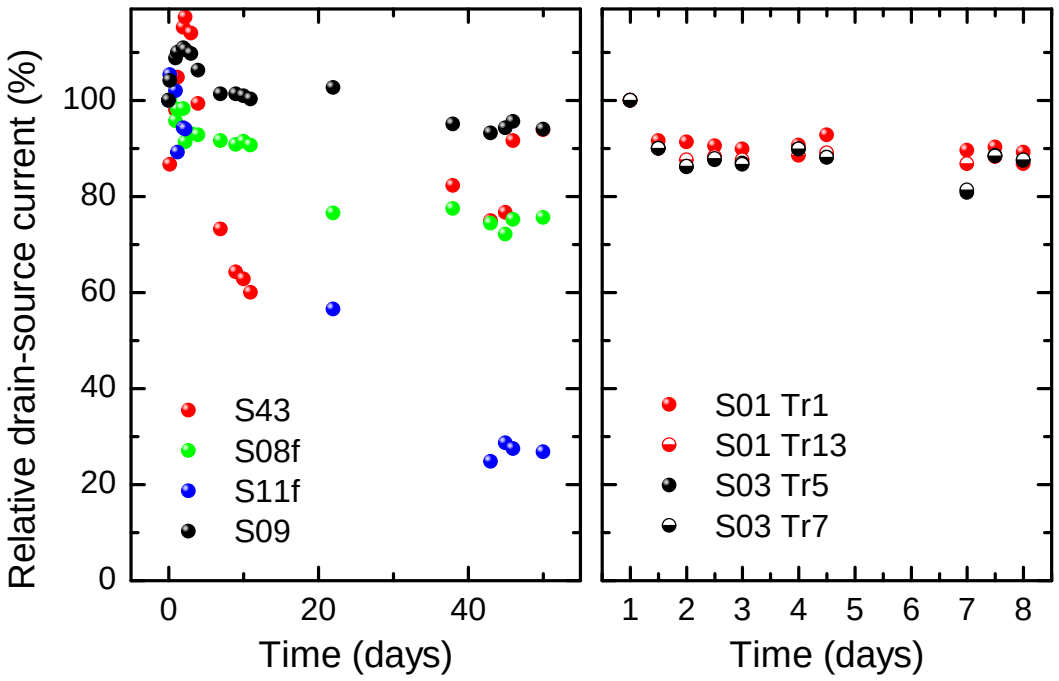

Figure 2.17: *left: Recordings of the surface conductivity over time for several diamond samples stored in electrolyte. The samples were under potential control, using a potentiostat, only during the measurements. right: Analog recordings for two samples with two devices each. The setup for these measurements did not use a potentiostat, but a standard voltage source to control the diamond electrode potential with respect to the reference electrode.*

device, the conductivity of the device was measured over eight hours while constantly changing the electrode potential. Figure 2.18 shows a plot of the conductivity at the same potential over the number of consecutive measurements. The conductivity changes less than 1% over this period. The sample was operated within the potential window considered as "safe" - from -0.1 V to +0.4 V vs. Ag/AgCl.

Previous experience has shown that any electric switching can cause significant potential peaks exceeding the potential window of the hydrogen-termination by far. This has been investigated as shown in Figure 2.18 (*right*), where the conductivity over the number of consecutive measurements is shown, similarly to Figure 2.18 (*left*), but with switching the potentiostat off and on after every ten measurements. The data shows clearly, that the on/off switching of the potentiostat causes a significant and yet erratic degradation of the sample conductivity, which is not caused by e.g. continuous changing of the electrode potential. Measurements with an oscilloscope confirmed that the on/off switching of the potentiostat causes voltage

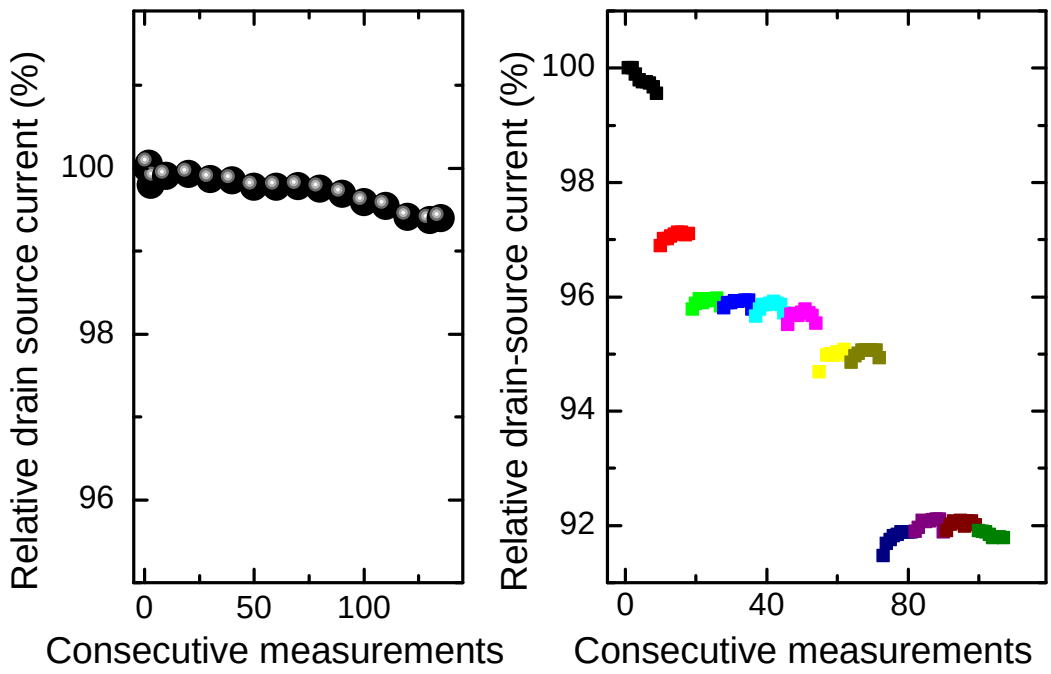

Figure 2.18: *Recordings of the surface conductivity over a number of consecutive measurements consisting of sweeps of the gate voltage from -0.1V to +0.4V and of the drain source voltage from 0V to -0.5V. The total measurement time was approximately eight hours. left: The samples stayed under potential control continuously. right: After every ten measurements the potentiostat controlling the gate potential was switched off and on again (each set of ten measurements has one color).*

peaks exceeding 2 V, significantly outside the potential window of the hydrogen-termination.

The combined experiments discussed above are interpreted as follows: Continuous operation in electrolyte causes only minor degradation of the surface conductivity (see Figure 2.18 *left*), while on/off switching, e.g. of the potentiostat, can cause significant degradation by oxidizing the hydrogen-terminated diamond surface (Figure 2.18 *right*). Considering this, the degradation observed for some samples in Figure 2.17 (*left*) is most likely due to the on/off switching of the potentiostat. The fact that some samples show only very limited degradation supports this, as any purely chemical oxidation should affect all samples roughly equally. Furthermore, stability measurements over a shorter time on a different setup, as shown in Figure 2.17 (*right*), reveal no continuous degradation, suggesting, that the chemical oxidation is very limited at most. Another indication of the chemical stability of the hydrogen-termination is its stability in air under ambient conditions, where the sur-

face conductivity is preserved for months. The initial rise in conductivity observed for some samples in Figure 2.17 could result from changes of the surface charge of the diamond, resulting from adsorbants as samples were stored in ambient conditions. Overall, the hydrogen-termination shows a high stability over time and under operation in electrolyte, considering the minimum degradation over time (Figure 2.17) and the minimal degradation under operation (Figure 2.18 *left*). Furthermore, the results show the importance of controlling the potential peaks, which occur when switching electric equipment on and off. This has led to a new procedure for turning on the potentiostat (see Appendix A.4.2), which disconnects the sample during the switching.

In order to further investigate the stability of the hydrogen-termination, it appears advisable to safeguard the sample from overpotentials even more. This could be achieved by relinquishing the use of a potentiostat, operating in a two-electrode configuration and using a battery powered voltage source to further avoid peaks resulting from grid fluctuations. Such precautions might limit the degradation caused by electrochemical oxidation with overpotentials and thus enable to detect any degradation solely based on chemical reactions or on electrochemical oxidation within the potential range now considered ”safe”.

Chapter 3

Charge accumulation and transport at the diamond/electrolyte interface

3.1 Diamond solution gate field effect transistors (SGFETs)

Diamond solution gate field effect transistors (SGFETs) based on the surface conductivity of diamond (Section 2.2.1) were first developed by the group of H. Kawarada [Kaw01]. For these devices, the metal gate of earlier diamond surface-conductive FETs [Kaw94, Tsu99] was replaced with an electrolyte solution and a reference electrode was used to control the gate voltage. The use of electrolytic gates for FETs instead of metal gates has long been established [Ber70] [Ber03] and first applied to silicon FETs. Such devices are often referred to as ion-sensitive field effect transistors (ISFETs), although they are usually not sensitive to any particular ion, but to the ionic strength.

For diamond SGFETs two metal contacts are placed on the surface of intrinsic diamond, contacting the hydrogen-terminated diamond area. Once immersed in an electrolyte, a potential can be applied between a reference electrode (RE) and a contact on the hydrogen-terminated diamond (see Figure 3.1). This potential applied across the diamond/electrolyte interface determines the position of the Fermi level, i.e. the electrochemical potential of electrons, in the diamond [Boc98]. By adjusting the gate potential, the Fermi level can thus be pushed below the valence band maximum, allowing the accumulation of holes beneath the diamond surface. The charge

is injected through the metal contacts and the potential drop leads to upward band bending and the formation of a quasi two-dimensional hole gas (2DHG) beneath the surface. Thereby the amount of charge carriers, and therefore the surface conductivity, can be generated, adjusted, and removed by varying the potential applied across the diamond/electrolyte interface. As the Fermi level corresponds to the electrochemical potential of the diamond electrons, any change in the electrical potential of the diamond is immediately reflected in its position. The positive charge that accumulates consequently in the diamond is balanced by negative ions on the electrolyte side as counter charge. Figure 3.2 visualizes the operating principle behind the diamond SGFET.

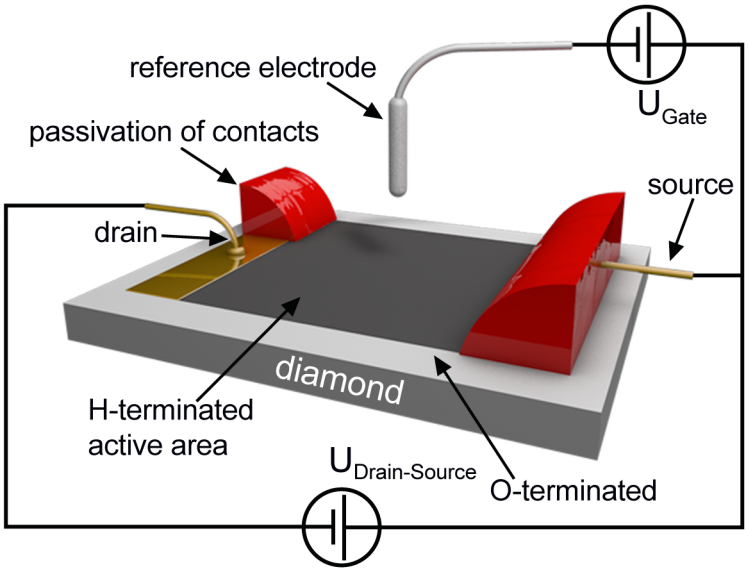

Figure 3.1: *Diagram of a diamond SGFET. The hydrogen-terminated part of the diamond sample is conductive and contacted by the Au drain and source contacts. The contacts are passivated with a silicone glue to avoid contact with the electrolyte. The conductivity of the hydrogen-terminated part exposed to the electrolyte can be modified by applying a potential between the reference electrode in the electrolyte and the source contact, which thus acts as a working electrode. The oxygen termination of the remaining diamond surface avoids a short circuit via sample areas not exposed to the electrolyte and, thus, not controlled by the electrolyte gate.*

The importance of the hydrogen termination of the diamond surface lies again in the shift of the valence band edge it produces (see Section 2.2.1). As a result of the negative electron affinity of $\chi = -1.0$ eV, the valence band edge is shifted from -6.75 eV versus the vacuum level E_{vac} for oxygen-terminated diamond to -4.45 eV versus E_{vac}

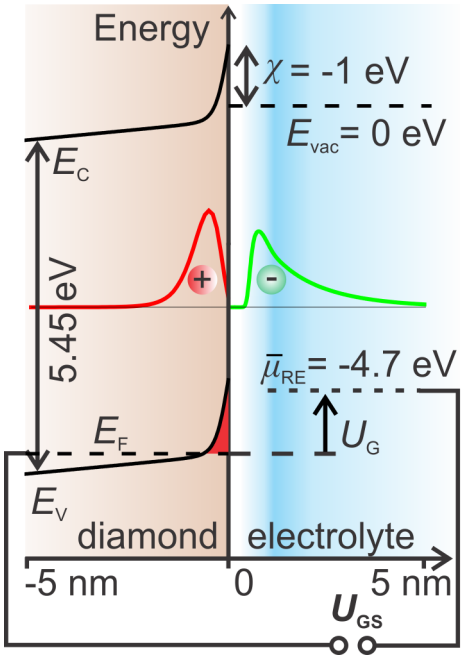

Figure 3.2: *Simulated band diagram of the hydrogen-terminated diamond/electrolyte interface. The Fermi level E_F can be shifted below the valence band edge E_V at -4.45 eV with a gate potential U_G applied between the reference electrode $\bar{\mu}_{RE}$ and a contact on the diamond. In the resulting potential well carriers accumulate in a two-dimensional hole gas (2-DHG, red area), leading to band bending at the surface. The hole density is mirrored by a net negative ion density on the electrolyte side (qualitatively indicated by red and green curve).*

for hydrogen-terminated diamond. For diamond SGFETs this means that much less positive potentials need to be applied in order to push the Fermi level below the valence band edge, and thus to accumulate holes and open the transistor channel. Due to the limited potential window of diamond in aqueous electrolyte ([Gra99] [Gra00] [Neb07]), the diamond SGFET can be operated only for hydrogen-terminated surfaces. A second crucial aspect of the hydrogen termination is its intrinsic surface conductivity under ambient conditions. Somehow an electrical contact needs to be established between the metal contact and the surface-conductive region of the diamond. For diamond SGFETs this is easily accomplished by an overlap of the metal contact onto the hydrogen-terminated and thus surface-conductive area. As the whole hydrogen-terminated area is already conductive, the potential applied to the diamond electrode reaches the whole surface and can control the carrier accumula-

tion.[1]

The surface conductivity of the diamond SGFET can also be influenced by the pH and the ionic strength of the electrolyte solution [Har07]. The basic mechanism behind this is the presence of surface charge adsorbed on the electrolyte side of the diamond surface. Any charge on the hydrogen-terminated diamond surface changes the effective gate potential applied to the diamond SGFET and therefore its conductivity. The pH changes this surface charge either by charging hydroxyl groups left due to imperfect hydrogen termination (as described by the so-called site-binding model [Dav78]) or by preferential adsorption of hydroxyl or hydronium ions. Further, any surface charge present can then be screened by the electrolyte ions more or less effectively depending on the ionic strength, adding another sensitivity to the diamond SGFET and giving some justification to the description as "ISFET".

It is important not to confuse the operation of diamond SGFETs with the transfer doping model, which explains the surface conductivity in ambient conditions. The transfer doping model explains the accumulation of conducting holes beneath the surface by the transfer of electrons from the diamond valence band to electron acceptors outside the diamond, such as redox couples (see Section 2.2.1), until electrochemical equilibrium is reached. In the SGFET case the charge is provided by injection through the metal contacts contacting the hydrogen-terminated surface, without any charge transfer across the surface. Furthermore, an equilibrium situation is most likely never reached in the SGFET configuration, as the position of the Fermi level is set and kept at a certain level by the potential between the diamond and the reference electrode. In a SGFET configuration, with the gate potential and therefore the Fermi level and the hole concentration set, the transfer doping mechanisms will still result in a transfer of charge. However, not the Fermi level of the diamond will adjust to the electrochemical potential of the redox couples in the electrolyte, but conversely the composition of the electrolyte will change with the charge provided by the voltage source, keeping the diamond/reference electrode potential constant.

[1] For an oxygen-terminated surface this contact would have to be just at the border between the metal contact and the diamond surface, with a surface conductivity yet to be established at this border line by pushing the Fermi level low enough. Necessarily the metal contact would have to be exposed to the electrolyte, facilitating a multitude of electrochemical reactions including electrolyte decomposition.

The field of possible applications for the diamond SGFET is that of biosensors and bioelectronic devices. One of the fundamental characteristics of this device is the change in the amount of accumulated charge as a result of a given gate potential change. This should be directly proportional to the change in conductivity assuming a constant mobility. The interfacial capacitance therefore determines the sensitivity of the device. For diamond SGFETs, this interfacial capacitance is high compared to other materials. The reason for this lies in the absence of an insulator between gate and conducting channel, which is required in traditional field effect transistors to prevent electrochemical reactions at the bare semiconductor surface. The large electrochemical potential window of diamond enables the direct polarization of the diamond/electrolyte interface without the need of an insulating layer. Furthermore, the diamond crystal is stable against the penetration of ions from the electrolyte, avoiding drift of the device characteristics typical of e.g. Si-FETs in electrolytes. The use of an ion containing solution, the electrolyte, as gate is then in principle also the difference of SGFETs to e.g. MOSFETs. Accordingly, they could more accurately be described as electrolyte gate field effect transistors (EGFETs)[2].
The design analogy to MOSFETs extends also to the electrical characteristics of

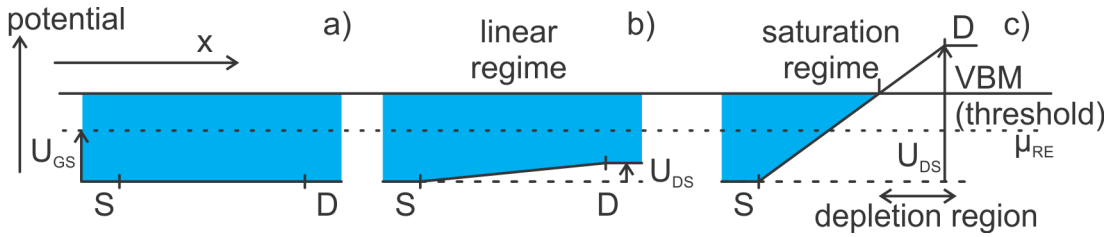

Figure 3.3: *Operating principle of the diamond SGFET. a) The gate potential U_{GS} determines the position of the source contact potential S relative to the reference electrode potential μ_{RE}. A source contact potential below the valence band maximum (VBM), results in hole accumulation (blue region). b) A drain-source potential U_{DS} shifts the drain contact potential D relative to the source contact potential. c) The drain-source potential shifts the drain contact potential above the VBM (the threshold for hole accumulation), thus creating a depletion region with no hole accumulation. This depletion region limits the drain-source current.*

diamond SGFETs. The conductivity of the conducting channel between the drain and source contacts is modulated by the relative potential of the gate contact. In an

[2]The acronym "EGFET" is already in use for extended gate field effect transistors.

open state, both drain and source potential are far from the threshold (see Figure 3.3). A small drain-source voltage U_{DS} gives rise to a drain-source current I_{DS}, and since neither contact is brought close to the threshold by this small potential change, the $I_{DS} - U_{DS}$ dependence is linear. If the drain-source voltage is increased, so that the drain contact is brought close to or over the threshold by the potential change, a depletion region is created, and the drain-source current saturates with respect to the drain-source voltage. Both contacts are shifted with respect to the threshold by the gate potential, which therefore determines the onset of saturation. In the diamond SGFET case, the threshold corresponds to the potential, when the Fermi level at the source contact reaches the valence band edge. The drain-source voltage then shifts the Fermi level at the point of the drain contact with respect to the source.

In the linear regime the drain-source current I_{DS} can be described by [Sze07, p.305]:

$$I_{DS} = \mu C \frac{W}{L} \left[- \left(U_{GS} - U_{th} \right) U_{DS} + \frac{1}{2} U_{DS}^2 \right] \tag{3.1}$$

μ and C are the mobility of the holes and interfacial capacitance, respectively. W and L are the width and length of the conducting channel. U_{th} is the threshold voltage, U_{DS} the drain-source voltage, and U_{GS} the gate-source voltage. On the other hand, the saturation regime is described by [Sze07, p.306]:

$$I_{DS} = -\frac{1}{2} \mu C \frac{W}{L} \left(U_{GS} - U_{th} \right)^2 \tag{3.2}$$

The threshold voltage depends on the negative electron affinity χ, the band gap E_{gap}, any surface charge at the diamond/electrolyte interface, and the reference electrode potential (see Figure 3.2).

While diamond SGFETs have been around for a number of years and the processing technology is generally available, the interfacing of living cells as part of a bio-electronic application requires transistors with gate areas on a scale of μm. Such dimensions require a processing technology that is completely compatible with photolithography. The biggest challenge in this respect is the passivation of the metal contacts. The passivation material needs to be stable in electrolyte and yet allow photolithographic processing. SU8, a negative photoresist from MicroChem Corp., fulfills these requirements. A reliable technology for the fabrication of diamond SGFETs of 10-20 μm dimension was established during this thesis (see Figure 3.4; see Appendix A.5.1 for processing protocols) [Rei08]. Figure 3.5 shows typical transistor characteristics of the diamond SGFETs used in this work. The conductivity can be varied 3-4 orders of magnitude and the leakage current for a closed channel is

in the range of a few nA. The conductivity has a slope of 0.05 μS mV^{-1} in its linear part, which should correspond to the product μC of Equation 3.1. A good agreement is found considering values of around 50 cm^2 V^{-1} s^{-1} for the mobility and 2 μF cm^{-2} for the capacitance. Small discrepancies can be partly explained by taking into account the contribution to the total conductivity of the fraction of the surface conductive channel beneath the SU8 passivation, and thus not under electrolyte control [Hau10]. This is the so-called access region, which diminishes the amount by which the total conductivity (of the electrolyte exposed and the SU8-covered parts) can be varied. The effective ratio of exposed to SU8-covered channel length is about 1:1 in the devices of Figure 3.5. For devices in the mm range, the SU8-covered part of the channel corresponds to a negligible fraction of the total channel length. Indeed, the slope of the conductivity has been recorded to be around 0.1 μS mV^{-1} for such devices. The threshold voltage of this particular device, +220 mV, is a typical value. However, as shown below, the threshold voltage is one of the most variable parameters between devices. This parameter is affected by the quality of the hydrogen termination, as well as by the surface charge. Assuming a value of 200 mV for the threshold voltage, one would expect a negative electron affinity of χ=-1.0 eV corresponding well to measured values [Gar08]. As already mentioned, the transconductance maximum of approx. 20 μS at around U$_G$=-200 mV is directly proportional to the interfacial capacitance and the carrier mobility, which are therefore fundamental for the sensitivity of the device. For a maximum device sensitivity, the device should be operated at the maximum of the transconductance .

Regarding the stability in electrolytes the diamond SGFET has obvious advantages over the standard silicon technology. In order to achieve comparable stability for silicon devices a much more complex and sophisticated processing technology is necessary. However, diamond SGFETs need to also live up to other sensor performance characteristics. The signal to noise level of current, not yet optimized, diamond SGFETs compares already well with silicon devices [Hau10].

A general weakness of SGFET devices, independent of the material technology, is the need for a reference electrode. A proper reference electrode requires a chemical equilibrium with the solution to establish its potential. This requires the analyte solution to keep a constant concentration of the relevant ion species, which could be problematic for implanted devices.

The picture presented above shows the diamond SGFET as a MOSFET equivalent, where the conductivity is regulated via the electrolytic gate control of the carrier concentration. While the device characteristics are in accordance with this picture,

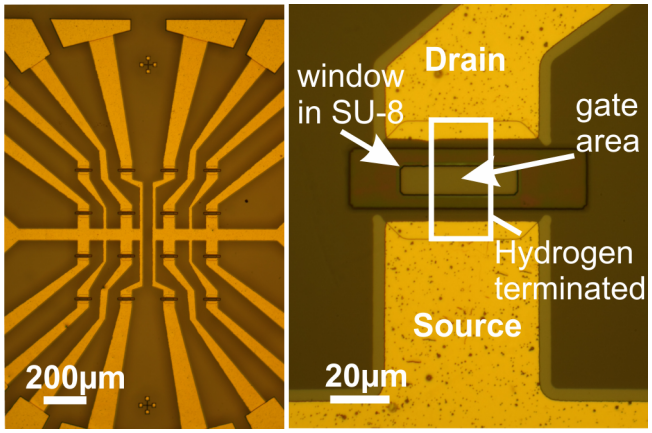

Figure 3.4: *left: Micrograph of a 4x4 diamond SGFET array with leads to the bond pads including SU-8 passivation. right: Image of a single transistor with Ti/Au drain and source contacts. The intersection between the opening in the SU-8 passivation layer and the hydrogen-terminated area of the diamond (not visible, but indicated) represents the gate area.*

it needs further verification through the determination of the carrier concentration for different gate potentials. Aside from the charge accumulation, the transport at the diamond/electrolyte interface is of interest to determine the limitations to the mobility of the conducting holes. Based on the mobilities in bulk diamond (see Section 2.1), there is a big discrepancy between the expected high mobilities in diamond, and the initial estimate of 50 cm^2/Vs based on the slope of the conductivity. As the conducting channel is directly beneath the surface, the influence of the electrolyte gate on both the charge accumulation and the electronic transport is of special interest here. To this end, we have developed a system capable of combined Hall effect and resistivity measurements in electrolyte, which enables the determination of both carrier concentration and mobility independently (see Appendix A.2 for experimental details regarding the setup).

3.2 Charge accumulation at the diamond/electrolyte interface

This section deals with the charge accumulation at the diamond/electrolyte interface according to the diamond SGFET model described in Section 3.1. Initially, the experimentally observed carrier concentrations from Hall effect measurements are presented and discussed. Finally, the experimental data is compared to simulations,

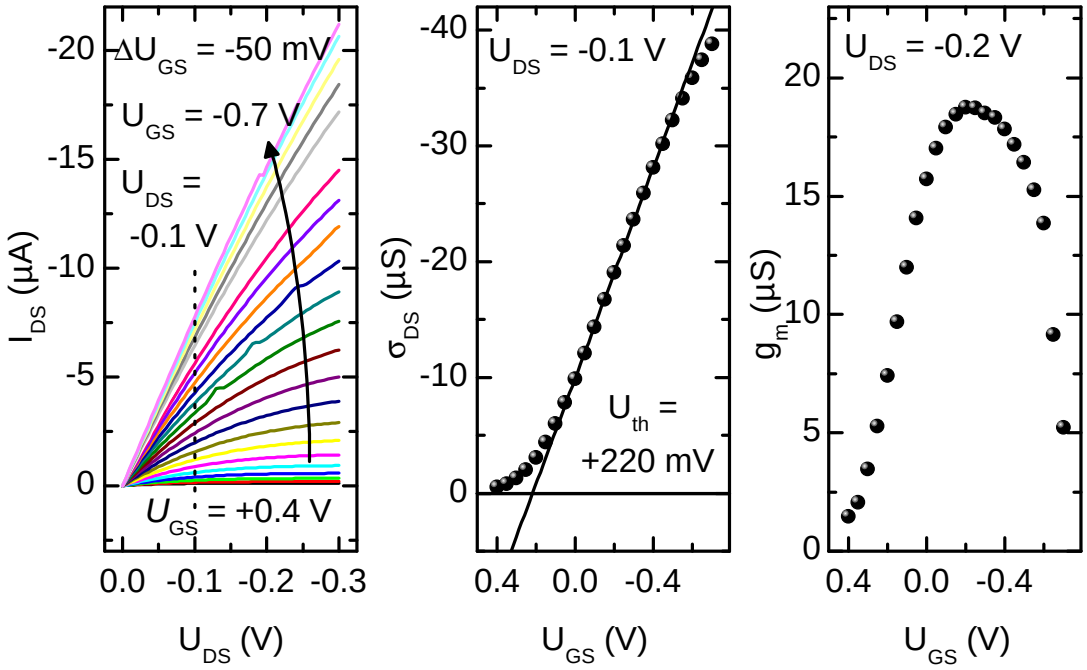

Figure 3.5: *Transistor curves of a typical diamond SGFET (40x20 μm^2). left: Recordings of the drain-source current for drain-source voltages up to -0.3 V, at gate potentials between U_{GS}= 0.4 V and U_{GS}= -0.7 V in steps of 50 mV. middle: Conductivity σ_{DS} of the two-dimensional transistor channel measured at U_{DS}= -100 mV. The slope above the threshold voltage U_{th} is 0.05 μS mV^{-1}. right: Transconductance g_m of the transistor at U_{DS}= -200 mV. For this device, the working point with the highest sensitivity is around U_{GS}= -0.22 V.*

performed using the software nextnano, to further elucidate the mechanisms of the charge accumulation at the diamond/electrolyte interface.

3.2.1 Experimental sheet conductivity and sheet carrier density

Figure 3.6 and 3.7 show the sheet conductivity and sheet carrier density as a function of the gate voltage of hydrogen-terminated diamond samples. The data are from Hall measurements in the van der Pauw configuration and encompass a large number of samples with variations in a number of parameters (surface orientation, nitrogen impurity content, surface roughness, hydrogenation quality, ...). Figure 3.8 shows a subset of the data in Figures 3.6 and 3.7 that exemplarily illustrates the behavior for the most important categories of samples: optical grade samples with (100) and

(111) orientation, and electronic grade samples with (100) orientation. The sheet conductivity shows the behavior long observed for the SGFET configuration. The continuous accumulation of holes with increasingly negative gate voltage validates the model, that predicts charge accumulation as the Fermi level is pushed further below the valence band edge. As will be shown in Section 3.3 the mobility also plays a role in the conductivity change with gate voltage. However, this is highly dependent on the diamond crystal quality and surface orientation. Therefore the SGFET model adequately describes the behavior of the diamond surface conductivity in electrolyte under potential control. For all samples the carrier density increases linearly with the gate voltage after the initial slower rise, as shown in Figure 3.7. A linear fit on that part, extrapolated to zero carrier concentration yields the threshold voltage. The variation (approx. between -0.2 V and 0.45 V) in threshold voltages over the different samples is significant. In principle the threshold voltage should be mostly dependent on the quality of the hydrogen termination (Section 3.1). Additionally, variations in the surface charge are effectively changing the threshold voltage. The amount of surface charge is itself dependent on the hydrogen termination, since it is partially influenced by the density of hydroxyl groups at the surface [Har07].

As discussed in Section 3.1, the slope of the carrier density with respect to the gate voltage is the interfacial capacitance. At higher gate potentials the interfacial capacitance is dominated by the double layer capacitance and therefore constant, as will be discussed in more detail later (see Section 3.2.3 and Figure 3.19). However, the slope of the conductivity and carrier concentration are sometimes observed to decrease with increasing gate voltage at very high (negative) gate voltages (see Figure 3.7 sample "S37b 100"). This decreasing interfacial capacitance can be understood by considering that the gated region of the hydrogen-terminated surface is always contacted by a non-gated access region, which is covered under passivation (see Section 3.1). When approaching high carrier concentrations, the gated areas become more conductive than the non-gated ones, and the overall conductivity is increasingly limited by the non-gated region [Hau10].

Figure 3.9 visualizes the dependence of the interfacial capacitance and the threshold voltage on the surface orientation and the nitrogen impurity content for all investigated samples (see Figure 3.7). The corresponding numerical values are summarized in Table A.2 in the appendix. Over the wide variety and large number of samples the capacitance is highly homogeneous in the "linear" part of the carrier density curve. A systematic difference is observed, however, between the (100) and (111) surface orientations. The average value of the interfacial capacitance for the (100) surface

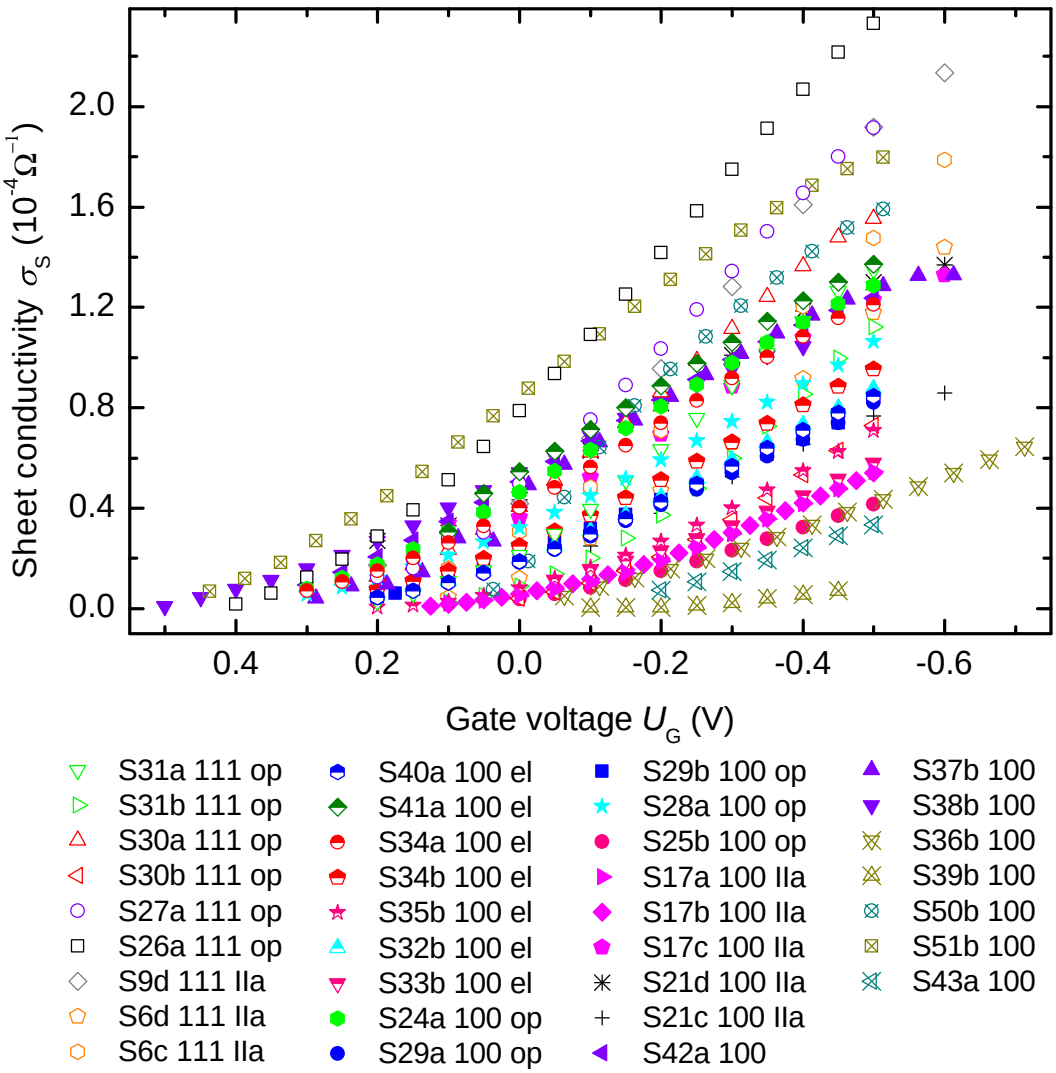

Figure 3.6: *Sheet conductivity versus gate voltage of all investigated diamond samples. Solid symbols represent optical grade samples with a (100) orientation, open symbols depict optical grade samples with a (111) orientation. Half-solid symbols are for electronic grade samples, all of which have a (100) orientation. Open crossed symbols correspond to samples that fall in neither category.*

is 2.45 ± 0.53 μF cm^{-2} and the value for the (111) surface is 4.29 ± 0.31 μF cm^{-2}. A slight difference in the average capacitance depending on the nitrogen impurity level can also be observed. The values are 2.12 ± 0.62 μF cm^{-2} for electronic grade samples and 2.65 ± 0.37 μF cm^{-2} for optical and natural IIa grade samples. However, considering the scattering of the data, this difference would need to be further verified in order to be statistically significant. As for the threshold voltage, a clear difference depending on the surface orientation can not be observed. The threshold

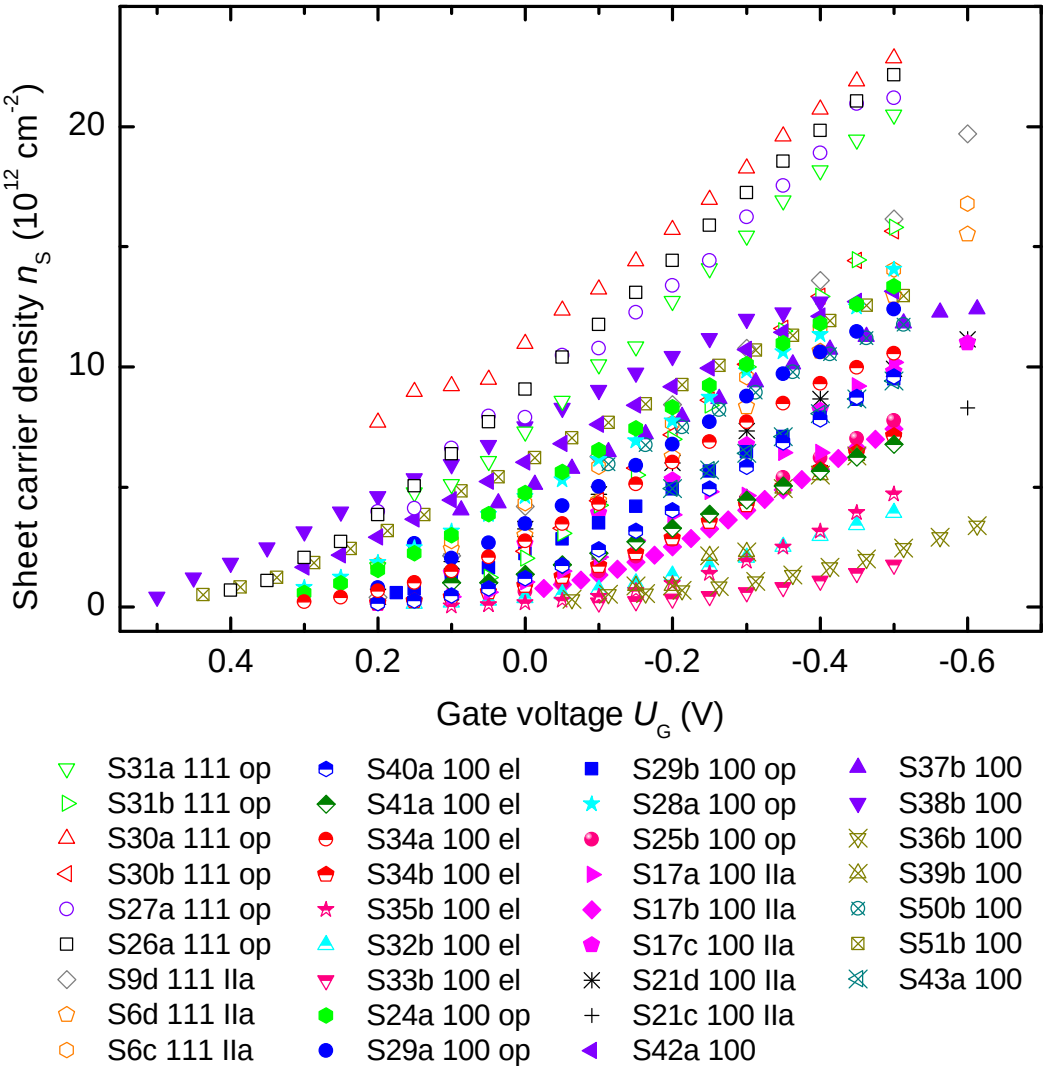

Figure 3.7: *Sheet carrier density versus gate voltage of all investigated diamond samples. Solid symbols represent optical grade samples with a (100) orientation, open symbols depict optical grade samples with a (111) orientation. Half-solid symbols are for electronic grade samples, all of which have a (100) orientation. Open crossed symbols correspond to samples that fall in neither category.*

voltage does seem to depend however, on the nitrogen impurity with an average of -36 ± 155 mV vs. Ag/AgCl for electronic grade samples and 181 ± 181 mV vs. Ag/AgCl for optical and natural IIa grade samples. Again, the scattering in the data is significant.

Complementary to the values derived from the Hall effect measurements, the interfacial capacitance can also be obtained by electrochemical techniques such as cyclic voltammetry (CV) and electrochemical impedance spectroscopy (EIS). Both

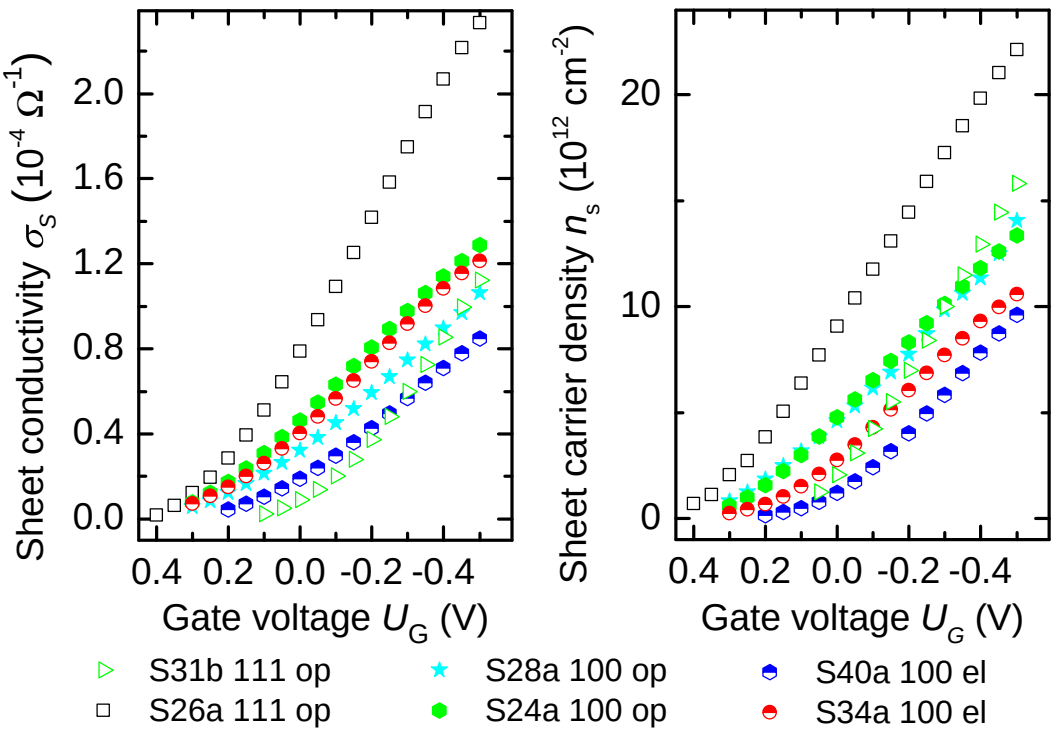

Figure 3.8: *Subset of the data in Figures 3.6 and 3.7 that exemplarily illustrates the behavior for the most important categories of samples: optical grade samples with (100) and (111) orientation, and electronic grade samples with (100) orientation.*

techniques in effect measure the current flow to the electrode/electrolyte interface that follows a change in gate potential [Bar01]. This has been done for a selection of samples and the interfacial capacitance calculated. The results are presented in Table 3.1 together with the interfacial capacitances obtained from Hall effect measurements. While the independently obtained capacitance values are of the same order, they do deviate by a margin not readily explained by experimental errors. This deviation could be explained by taking the Hall factor into account and assuming the capacitance values measured with EIS to be correct. As a consequence of Equation A.14, the carrier density n_H measured with the Hall effect differs from the carrier density n_{EIS} measured with EIS by the Hall factor r_H:

$$n_H = \frac{1}{r_H} n_{EIS} \;\Rightarrow\; r_H = \frac{C_{EIS}}{C_H} \tag{3.3}$$

The Hall factor can thus be calculated from the ratio of the capacitances C_{EIS} and C_H derived from EIS and Hall effect measurements respectively (see Table 3.1). The Hall factors calculated are different for (100)-oriented optical grade samples (0.7), (111)-oriented optical grade samples (0.5), and (100)-oriented electronic grade

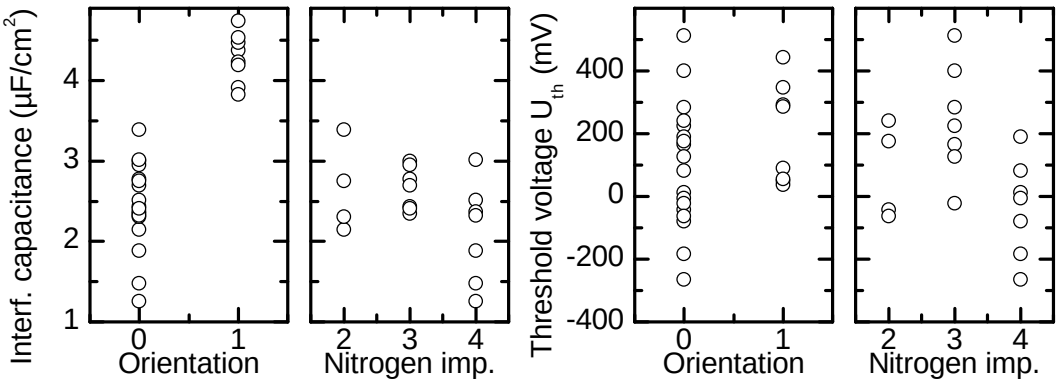

Figure 3.9: *Graphical evaluation of the interfacial capacitance and threshold voltage of the diamond samples in Figure 3.7 (see Table A.2 for numerical values). The labels of the x-axis are to be read as follows: "0" as (100) orientation, "1" as (111) orientation, "2" as IIa grade, "3" as optical grade, "4" as electronic grade. The evaluation of the surface orientation dependence of the interfacial capacitance and the threshold voltage contains samples of IIa grade, optical grade, and electronic grade. The evaluation of the nitrogen impurity concentration dependence of the interfacial capacitance and the threshold voltage contains only the (100)-oriented samples.*

samples (1.0). As the Hall factor is also dependent on the scattering mechanism, this could indicate different scattering mechanisms for these sample categories, which will be discussed in Section 3.3.3.

Table 3.1: *Interfacial capacitances obtained by Hall effect measurements (see Table A.2) and electrochemical impedance spectroscopy (EIS). The Hall factor is given as well, assuming the capacitance values measured with EIS are correct.*

sample name	surface orientation	impurity grade	$C_H \left[\frac{\mu F}{cm^2}\right]$	$C_{EIS} \left[\frac{\mu F}{cm^2}\right]$	Hall factor r
S17b	(100)	IIa	2.74	2.07	0.76
S25b	(100)	op	2.69	1.72	0.64
S29b	(100)	op	2.40	1.78	0.74
S34b	(100)	el	2.32	1.97	0.85
S35b	(100)	el	2.37	2.57	1.08
S30b	(111)	op	4.53	2.29	0.51
S31b	(111)	op	4.74	2.33	0.49

3.2.2 nextnano^3

nextnano^3 is a software tool intended to simulate electronic and optical properties of nanostructures in semiconductors [Bir07] [Bir]. To this end the Poisson and Schrödinger equation are solved numerically and self-consistently. The equations describing the semiconductor structure are discretized on a grid according to the finite differences method. They are then solved iteratively with a Newton-Raphson algorithm until the convergence criteria are fulfilled. The solution provides the electrostatic potential, the band structure and the carrier density in one, two or three dimensions. Additionally the situation in the device under the application of external potentials across the device can be simulated. Furthermore, nextnano^3 is also capable of simulating an electrolyte phase as part of the semiconductor device, thus making it highly suitable for the simulation of the diamond solution gate field effect transistor. Accordingly, the carrier density of the diamond SGFETs can be simulated depending on the applied gate voltage, providing a theoretical reference to the experimentally observed results, as well as allowing further insights into the charge and potential distributions governing the diamond SGFETs.
The potential in the diamond SGFET and charge accumulation associated with it are governed by the Poisson equation:

$$\epsilon_0 \epsilon_r \Delta\varphi(z) = -\rho(z) \tag{3.4}$$

Here, ϵ_0 and ϵ_r are the dielectric constant in vacuum and the material respectively, $\varphi(z)$ is the electrostatic potential, and $\rho(z)$ the charge density at position z. Additionally, the potential and the charge density are linked via the Schrödinger equation. In the present case, in order to fully describe the accumulation of holes at the diamond interface, the Schrödinger equation needs to be set up and solved. Similarly, the electron accumulation in silicon inversion layers was originally calculated based on self-consistent solutions of the Poisson and Schrödinger equations [Ste67] [Ste72] [Fan66] [And82]. Here, a potential well was assumed, which depends only on z. The motion parallel to the surface is thus largely unperturbed and the motion perpendicular to the surface is very limited, a problem, which can be solved using an effective one-dimensional Schrödinger equation. This leads to a situation in which the eigenstates generated by the confining potential well perpendicular to the surface correspond to the ground states of subbands for states parallel to the interface, which are not confined. The occupation of these subbands gives the charge density. It was assumed, that the wavefunction in z direction (so-called envelope function) vanishes at the surface, and that the effect of any charge at the surface can be modeled by

an equivalent electric field [Ste72]. A more general treatment of two-dimensional systems can be found in the book of Davies [Dav98]. The effective one-dimensional Schrödinger equation can be written as [Ste72]:

$$-\frac{\hbar^2}{2m^*}\frac{d^2\zeta_i(z)}{dz^2} - e\varphi(z)\zeta_i(z) = E_i^0\zeta_i(z)\ , \tag{3.5}$$

where m^* is the isotropic effective mass, $\zeta_i(z)$ the wavefunction describing the motion in z-direction in the ith subband, e is the elementary charge, and E_i^0 is the bottom level of the ith subband. The total charge is the sum over the charges of all subbands [Ste67]:

$$\rho(z) = e\sum_i |\zeta_i(z)|^2 N_i, \tag{3.6}$$

where N_i is the occupation number of the ith subband and given by [Ste67] [Ste72]:

$$N_i = g_{subband} g_s \frac{kTm_{dos}}{2\pi\hbar^2} F_0\left(\frac{E_F - E_{ik}^0}{kT}\right) \tag{3.7}$$

$g_{subband}$ is the degeneracy of the subbands (with lowest energy E_{ik}^0), g_s is the spin degeneracy, m_{dos} is the density of states effective mass per subband, $F_0(x) = \ln(1 + e^x)$ is the Fermi-Dirac integral with exponent zero, and $E_{ik}^0 = E_i^0 + \frac{\hbar^2k^2}{2m^*}$ is the subband energy including the motion parallel to the interface. The total number of carriers amounts to $n_s = \sum_i N_i$, and in this two-dimensional system the Fermi wavevector is given by $k_F = \sqrt{2\pi n_s}$.

As is evident from the equations, the Schrödinger and Poisson equations are coupled via the electrostatic potential and the total charge density, and therefore have to be solved numerically. In order to achieve this, an approximation serves as starting point. For the presented case an approximation was developed by Fang and Howard [Fan66] [Ste72]. With the presented approach the charge density in the diamond can be calculated.

In the case of the diamond SGFET the device contains an electrolyte phase, thus requiring an alternative description of the potential-charge interdependence in this part of the device. The electrolyte, consisting of mobile ions in the solvent, can be described by the Poisson-Boltzmann equation. The Poisson equation relates the electrostatic potential with the charge density. The charge density, which in the electrolyte is the net density of the positive minus the negative ionic charge, is governed by a Boltzmann distribution [Ham98]:

$$\rho(z) = e\sum_i z_i n_i^0 \exp\left(-\frac{z_i e}{kT}(\varphi(z) - \varphi_l)\right) \tag{3.8}$$

n_i^0 is the total charge density of ions i with z_i being their valency. φ_l is the potential in the bulk of the electrolyte. The Poisson-Boltzmann equation describes then the situation in the electrolyte phase:

$$\epsilon_0 \nabla_z \cdot (\epsilon(z) \nabla_z \varphi(z)) = -e \sum_i z_i n_i^0 \exp\left(-\frac{z_i e}{kT}(\varphi(z) - \varphi_l)\right) \tag{3.9}$$

The equation is given here with a spatially varying dielectric constant $\epsilon(z)$, which will be shown to be relevant for aqueous electrolytes, as will be discussed in detail later (see Section 3.2.3).
In summary, the Poisson equation links the electrostatic potential to the charge density in the complete device, whereas the charge density is calculated using the Schrödinger equation in the diamond part and the Boltzmann distribution in the electrolyte part of the diamond SGFET.

In order to solve the Poisson equation, boundary conditions have to be provided. They can be either Dirichlet boundary conditions, where a specific value is assigned to the potential at the boundary, such as $\varphi = const.$, or Neumann boundary conditions where a specific value is assigned to the derivative of the potential at the boundary such as $\frac{\partial \varphi}{\partial z} = const.$. In the case of diamond SGFETs, a Neumann boundary condition is chosen for the bulk diamond boundary with a value of zero for the derivative of the potential. This constant potential corresponds to a situation where the valence and conduction bands are flat and the Fermi level is determined by any electronic states in the band gap related to trace impurities. For the electrolyte side a Dirichlet boundary condition is chosen, giving the electrostatic potential a specific value in the bulk electrolyte. This boundary condition reflects the effect of the gate potential applied versus the reference electrode. It is important to clarify that this boundary condition value does *not* correspond to the physical value of the electrostatic potential in the bulk electrolyte without any gate potential applied - such a value is experimentally unaccessible [Boc98]. The fact that the gate potential used (the set value of the boundary condition for the electrostatic potential) in the nextnano simulations corresponds roughly with the experimental gate potentials when using a Ag/AgCl reference electrode is coincidental. The zero point of the experimental gate potentials is the reference electrode potential which in the case of the Ag/AgCl electrode lies 200-300 mV below the valence band edge of hydrogen-terminated diamond in electrolytes [Gar08]. For the nextnano simulations, the zero point is always set at the position of the Fermi level and the Dirichlet boundary condition in the electrolyte is set relative to the Fermi level. For the experimentally

relevant charge accumulation range, this results in a zero point for the simulations, which is also a few hundred millivolts below the valence band edge.

The Poisson-Boltzmann distribution has long been recognized as being insufficient to model the electrolyte behavior at interfaces [Boc02]. The ions have a finite size and therefore cannot get infinitively close to the surface. In addition, solvated ions are surrounded by a solvation shell of water molecules further increasing their effective size. This was recognized by Helmholtz in 1879 who modeled the interface with two planes of ions at different distances from the surface. The inner Helmholtz plane, comprised of adsorbed ions, which lost their hydration shell and can therefore get closer to the surface, and the outer Helmholtz plane farther from the surface, corresponding to the closest approach of hydrated ions. This picture was further refined by Stern in 1924, who combined the two Helmholtz planes with the Gouy-Chapman region (Gouy in 1909 and Chapman 1913), representing a diffuse layer corresponding to a Poisson-Boltzmann distribution.

Beyond the approach of the ions to the interface, the assumption of a non-varying dielectric constant of bulk water up to the interface has been challenged. Especially for hydrophobic surfaces, the orientation of water molecules at surfaces and fluctuations in the density of water were predicted and experimentally shown [Pra77] [Ton94] [Hum98] [Cha05]. A spatially varying dielectric constant in the immediate vicinity of the interface is therefore to be expected.
With the availability of molecular dynamics simulations it becomes possible to simulate these effects and infer quantitatively any fluctuation of the density of water and the forces acting upon ions near surfaces. We take the results from such calculations and incorporate them in the Poisson-Boltzmann model.

The fit-functions obtained from atomistic molecular dynamic simulations by Schwierz et al. [Sch10] result in water density profiles for hydrophobic and hydrophilic surfaces (see Figure 3.10) as a function of the distance z from the surface. The hydrophobicity of the surface was modeled by self-assembled monolayers ($C_{20}H_{40}$) with CH_3 and CH_2OH endgroups for the hydrophobic and the hydrophilic surface respectively [Sch10]. It is interesting to note, that even for the hydrophilic surface, the water density shows fluctuations and decreases very close to the surface [Sch10]. For the nextnano simulations we assume the dielectric constant to be directly proportional

to the water density, according to [Sch10]:

$$\epsilon(z) = \epsilon_{vac} + \frac{\rho(z)}{\rho_0}(\epsilon_{bulk} - \epsilon_{vac}), \tag{3.10}$$

where $\epsilon_{vac} = 1$ is the dielectric constant in vacuum, $\epsilon_{bulk} = 78$ is the dielectric constant of bulk water, $\rho(z)$ is the water density profile as calculated from molecular dynamics simulations, and ρ_0 is the bulk density of water. The resulting dielectric constant is shown in Figure 3.10. Additionally to the water density profile, the force

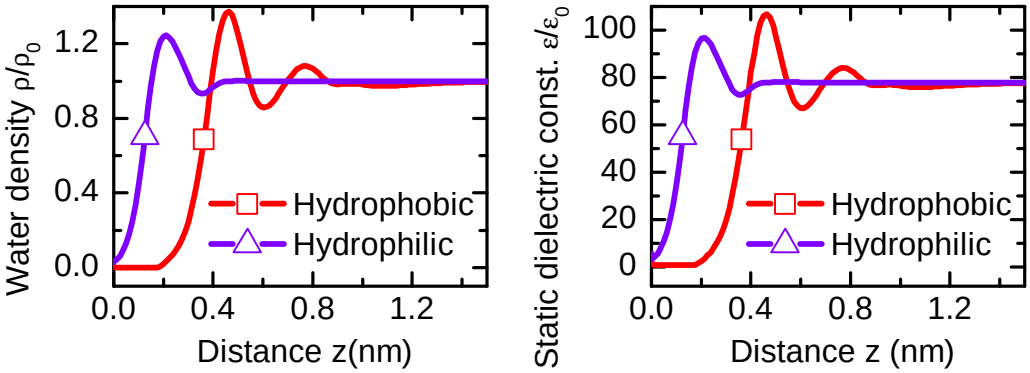

Figure 3.10: *left: Water density profile at a hydrophobic and hydrophilic surface obtained from molecular dynamics simulations [Sch10]. right: Dielectric constant as a linear function of the water density for the same surface. The parameters for the calculations were taken from [Sch10].*

between specific ions and the surface has been investigated with molecular dynamics simulations, resulting in the potential of mean force (PMF) for ions in the electrolyte [Sch10]. For two common ions, Na^+ and Cl^-, also used as salts in the electrolytes of this work, the PMF is illustrated in Figure 3.11. As can be seen, the potential rises sharply for both ions around 0.6 nm from the surface, and consequently the ions cannot approach the surface infinitely close.

The spatially varying dielectric constant and the potentials of mean force for the ions are both incorporated into the original Poisson-Boltzmann description of the electrolyte, yielding an extended-Poisson-Boltzmann model (ePB). Equation 3.9 changes therefore to:

$$\epsilon_0 \nabla_z(\epsilon(z)\nabla_z\varphi(z)) = -e\sum_i z_i n_i^0 \exp\left(-\frac{1}{kT}(\varphi_i^{PMF}(z) + z_i e(\varphi(z) - \varphi_l))\right), \tag{3.11}$$

where $\epsilon(z)$ is the position dependent dielectric constant, and $\varphi_i^{PMF}(z)$ is the potential of mean force for the ion i.

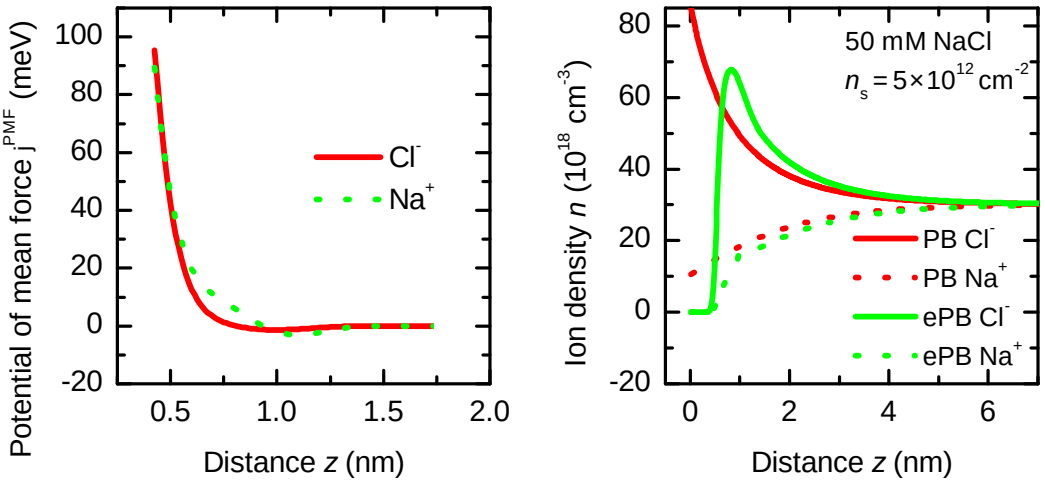

Figure 3.11: *left: Potentials of mean force (PMF) for sodium and chloride ions at a hydrophobic interface, taken from [Sch10]. right: Ion distributions at the diamond/electrolyte interface for the conventional Poisson-Boltzmann (PB) model and the extended Poisson-Boltzmann (ePB) model with the potentials of mean force, calculated assuming no surface charge. The PMF prevent the ions from approaching the surface infinitely close.*

The difference of the ion density profile at the interface between a plain Poisson-Boltzmann model and the extended Poisson-Boltzmann model is illustrated in Figure 3.11. In the PB model, the electrolyte ions can get infinitely close to the interface, according to the Boltzmann distribution. This close approach is prevented in the ePB model with the potentials of mean force for the ions. Before the PMFs become dominant in the ePB model (at distances from the surface smaller than 2 nm), the ratio of the positive to negative ion species corresponds roughly to that from the Boltzmann distribution.

In the nextnano model discussed so far, isotropic effective masses were assumed. Accordingly, the simulated charge accumulation is independent of the crystallographic direction along which the potential is applied, and thus independent of the diamond surface orientation. This is in contrast to the experimentally observed differences between the different surface orientations (see Figure 3.7). In order to further refine the model and to include the directional dependence in the calculations of the diamond crystal, the simplification of isotropy of the effective masses is dropped. The so-called "**k·p**" method allows the calculation of effective masses according to the band structure [Yu05, p.69]. The effective masses thus calculated are not isotropic

and should result in a more realistic model.

The **k·p** method can be derived using the Bloch-function as a solution to the one-electron Schrödinger equation, which then reads [Yu05, p.69]:

$$\left(\frac{p^2}{2m} + \frac{\hbar\vec{k}\cdot\vec{p}}{m} + \frac{\hbar^2k^2}{2m} + V\right) u_{n\vec{k}} = E_{n\vec{k}} u_{n\vec{k}} \tag{3.12}$$

The wavefunction $u_{n\vec{k}}$ has the periodicity of the lattice, n is the band index, and $\vec{k}$ lies within the first Brillouin zone. Initially this equation is solved for the case of $\vec{k_0} = (0,0,0)$. Once the solution for this case is known, the terms $\hbar\vec{k}\cdot\vec{p}/m$ and $\hbar^2k^2/(2m)$, which dropped out from Equation 3.12 by solving it at $\vec{k_0} = (0,0,0)$, can be included as perturbations to the initial situation.

This leads to a solution for the energy eigenvalues $E_{n\vec{k}}$ in the form of

$$E_{n\vec{k}} = E_{n\vec{0}} + \frac{\hbar^2k^2}{2m^*}, \tag{3.13}$$

with m^* called the effective mass of the band, which is

$$\frac{1}{m^*} = \frac{1}{m} + \frac{2}{m^2k^2}\sum_{n'\neq n} \frac{\left|\left\langle u_{n\vec{0}} \left| \vec{k}\vec{p} \right| u_{n'\vec{0}} \right\rangle\right|^2}{E_{n\vec{0}} - E_{n'\vec{0}}}. \tag{3.14}$$

As the perturbation used is proportional to k, this method is ideally employed for small k, but can be expanded over the whole Brillouin zone. For details of the method see e.g. the book of Yu and Cardona [Yu05] or Davies [Dav98]. When applying the **k·p** method to calculate the band dispersion, the valence bands can be characterized by so-called Luttinger parameters. Thus, the effective masses and energy eigenstates can be determined using these Luttinger parameters [Yu05]. For the **k·p** calculations performed by nextnano a 6x6 **k·p** Hamiltonian is used [Bir].

For the Luttinger parameters, which serve as an input to the nextnano **k·p** calculations, several sets can be found in literature ([Rau61] [Rau62] [Law71] [Reg83] [Bas81] [Ere91] [Kon93] [Wil94] [Ghe99] - and partly references therein). Sadly, even though diamond is an elemental semiconductor and has obviously been available for some time, these Luttinger parameter sets all disagree among each other and much less do the values converge toward a single, generally agreed result over the course of the years. This is true for experimental as well as theoretically derived sets. C.J. Rauch presented the first values for effective masses [Rau61] [Rau62], experimentally determined by cyclotron resonance. The most recent contribution is from M.

Willatzen, M. Cardona, and N.E. Christensen, a theoretical work [Wil94].

In this situation we have calculated the energy dispersion for a number of these Luttinger parameter sets (see [Bir11]). Some of these (e.g. [Bas81] [Ere91] [Kon93]) show an upward curvature of the energy dispersion, which we deem unrealistic. Among those is e.g. the parameter set reported by Kono et al. [Kon93], who employed the cyclotron resonance technique just as Rauch, and claim that Rauch misinterpreted the results. However, the unrealistic energy dispersion derived from their values casts instead doubt on their results and their conclusions.

In this situation we focus on two sets of Luttinger parameters (see Table 3.2), the first experimental one by Rauch and the most recent theoretical one by Willatzen et al. This is done in the full knowledge, that the "true" Luttinger parameters might eventually turn out to differ from either of these two sets. However, having compared a range of parameter sets, it is clear that at least some qualitative conclusions can be obtained. The initial experiments by Rauch employed straightforward cyclotron resonance with a variation of the crystallographic orientation [Rau62]. The values could not be credibly refuted since then and, actually, are one of the few experimental parameter sets not leading to an upward curvature of the energy dispersion. Furthermore, Rauch correctly predicts the value of the low split off energy of 6 meV. The theoretically calculated (with some experimental input values) sets by Willatzen et al. are the most recent addition in literature. This enables the authors to use the latest methods (linear muffin-tin-orbital and $\mathbf{k}\cdot\mathbf{p}$ calculations). Furthermore, the results correspond reasonably well to band structure results obtained by a different method (tight binding) [Bir11]. The energy dispersion for both parameter sets and different crystallographic directions are illustrated in Figure 3.12. The energy dispersion for the Rauch parameters is very isotropic in concurrence with his experimental findings. The Willatzen parameters, however, do lead to an anisotropy, where there is a larger effective mass for the heavy and light holes in the (111) direction versus the (100) direction. Comparing the energy dispersions for both sets, it is apparent, that especially the heavy hole band from Rauch corresponds to a larger effective mass as compared to the Willatzen results. Table 3.2 shows the Luttinger parameters and isotropic effective masses according to both Rauch and Willatzen.

In order to efficiently assess the effect of various parameters on the hole accumulations, isotropic effective masses were used for a number of simulations instead of $\mathbf{k}\cdot\mathbf{p}$ calculated effective masses. In these cases the effective masses were taken from

Rauch.

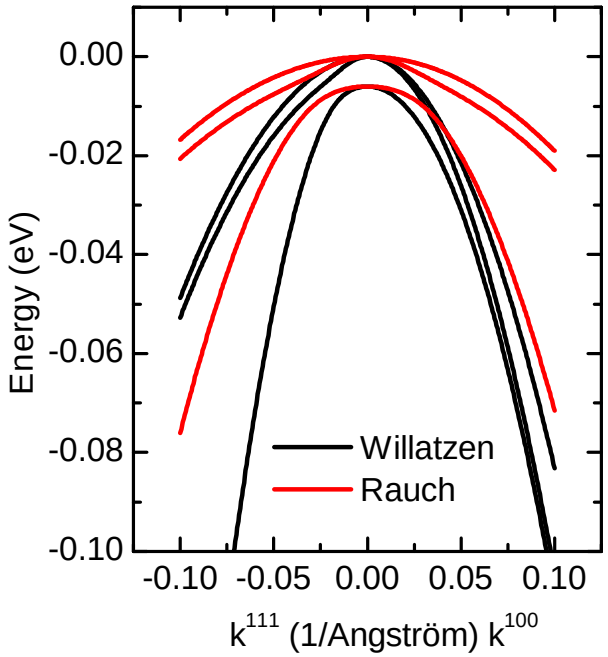

Figure 3.12: *Bulk valence band energy dispersion of diamond for the (100) and the (111) directions according to the parameters by Rauch and Willatzen.*

Table 3.2: *Luttinger parameter sets for* $\boldsymbol{k}\cdot\boldsymbol{p}$ *calculations as well as isotropic effective masses (from [Rau62], [Ghe99], and [Wil94]).*

	Rauch	Willatzen
γ_1	0.94	2.54
γ_2	0.22	-0.10
γ_3	0.25	0.63
κ	-0.58	-0.95
m_{hh}	2.21	0.287
m_{lh}	0.70	0.629
m_{so}	1.06	0.394

3.2.3 Simulated results and comparison to experimental values

The detailed electronic structure of the diamond hole accumulation layer and the interface with the electrolyte as simulated with nextnano will be presented in the following. The results are compared to experimentally obtained results, if these are available. For most of the results, there is no qualitative difference between the calculations for the Luttinger parameter sets of Rauch and Willatzen discussed in the last section. In these cases only the results for calculations with the Rauch parameters are presented. If there is a qualitative difference, the results for the Willatzen parameters are presented as well.

Figure 3.13 depicts the simulated diamond conduction and valence band at the interface to the electrolyte for a charge accumulation of 1.3 $\times 10^{13}$ cm^{-2} (gate voltage $U_G = -0.9$ V). This charge accumulation corresponds to the maximum experimentally observed charge accumulation for the (100) surface orientation. The electrostatic potential associated to the charge distribution at the interface is shown as well. The conduction band is shown at the X point. For the valence band the three valleys heavy hole (hh), light hole (lh), and split-off hole (so) are shown, whereby the split-off hole lies 6 meV beneath the energetically equal heavy- and light-hole bands. The indirect band gap is, of course, 5.46 eV. In all nextnano simulations, the Fermi level E_F is set at 0 eV (gray line) and all other energies are depicted relative to this level. As suggested earlier (see Section 3.1), the valence and conduction bands bend upwards and the Fermi level rests below the valence band edge at the surface. Accordingly, holes are accumulated in a quasi two-dimensional conducting channel beneath the surface. For a hole accumulation of 1.3 $\times 10^{13}$ cm^{-2} as shown, the lowest four eigenstates contain 97 % of the charge in case of the Rauch parameters. For the Willatzen parameters the lowest six eigenstates contain 99.8 % of the charge. Figure 3.14 depicts the probability distribution for these first eigenstates shifted by their eigenvalues. Respectively two of these eigenvalues and eigenstates always have the same energy and probability density because of spin (Figure 3.14 shows only one eigenvalue of each set). The lowest four eigenvalues for the Rauch parameters have energies of -0.017 eV and -0.021 eV, while the lowest six eigenvalues for the Willatzen parameters have energies of -0.007 eV, -0.032 eV, and -0.036 eV.

The spatial distribution of the hole density can be seen in Figure 3.15. The densities plotted correspond to the simulated gate potentials between $U_G = -0.9$ V and $U_G = -0.2$ V for the (100) orientation. The maximum of the density shifts about

0.3 nm between these two gate potentials. This result contradicts earlier calculations, which predicted a significant shift of the charge density towards the surface with increasing charge density [Hei04]. In the surface-conductive channel the vast majority of carriers is located within a region of 1 nm. For a sheet carrier density of 1×10^{13} cm^{-2} to 5×10^{11} cm^{-2} this corresponds to a volume density of 1×10^{20} cm^{-3} to 5×10^{18} cm^{-3}. Overall, 99.9 % of the hole density is accumulated over the first four nanometers from the interface. Therefore, the size of the region, where the charge distribution is calculated quantum mechanically is sufficiently large with 10 nm.

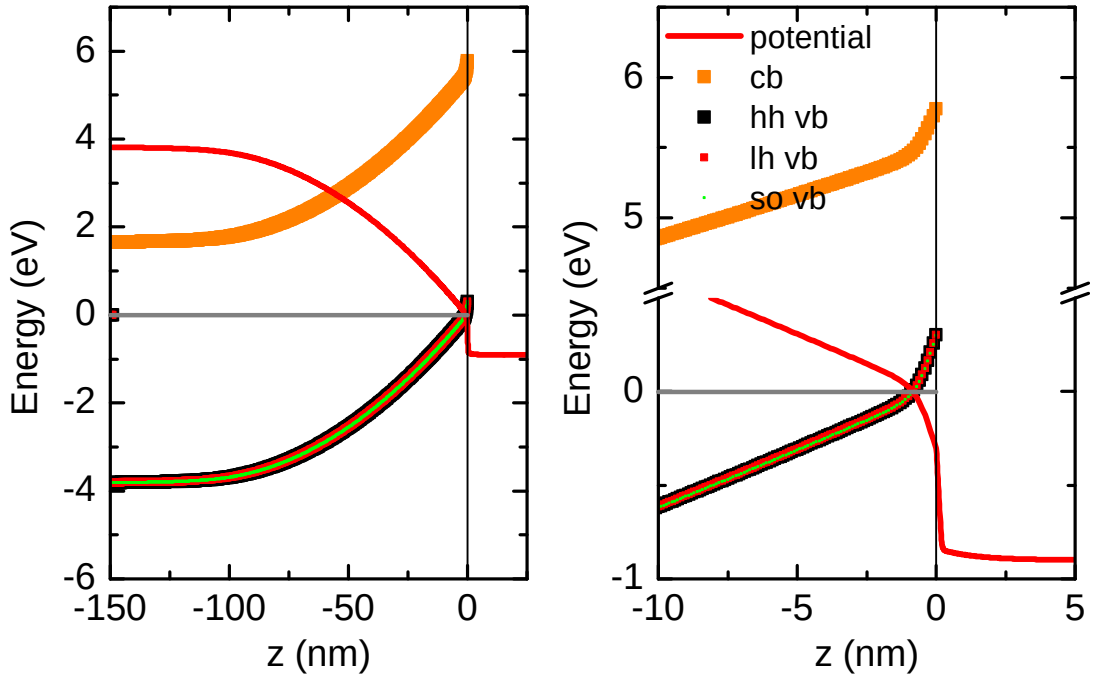

Figure 3.13: *Simulated conduction and valence band edge at a charge density of* 1.3×10^{13} *cm*$^{-2}$ *shown for the complete diamond slab (left) and the surface region only (right). The electrostatic potential in the diamond and across the interface is shown as well.*

The hole density distribution in the $k_{parallel}$ plane (parallel to the diamond surface) for a charge accumulation of 1.3×10^{13} cm^{-2} is illustrated in Figure 3.16 for the (100) orientation. This shows the contribution to the overall hole density from each $k_{parallel}$ point. Integrating over the whole plane in k space yields the total hole density. The density distribution is very spherical for Rauch parameters, but less so for the Willatzen parameters. The hole density distribution also shows, that only k-values up to approximately $k = 0.1$ nm^{-1} are relevant. According to Figure 3.12

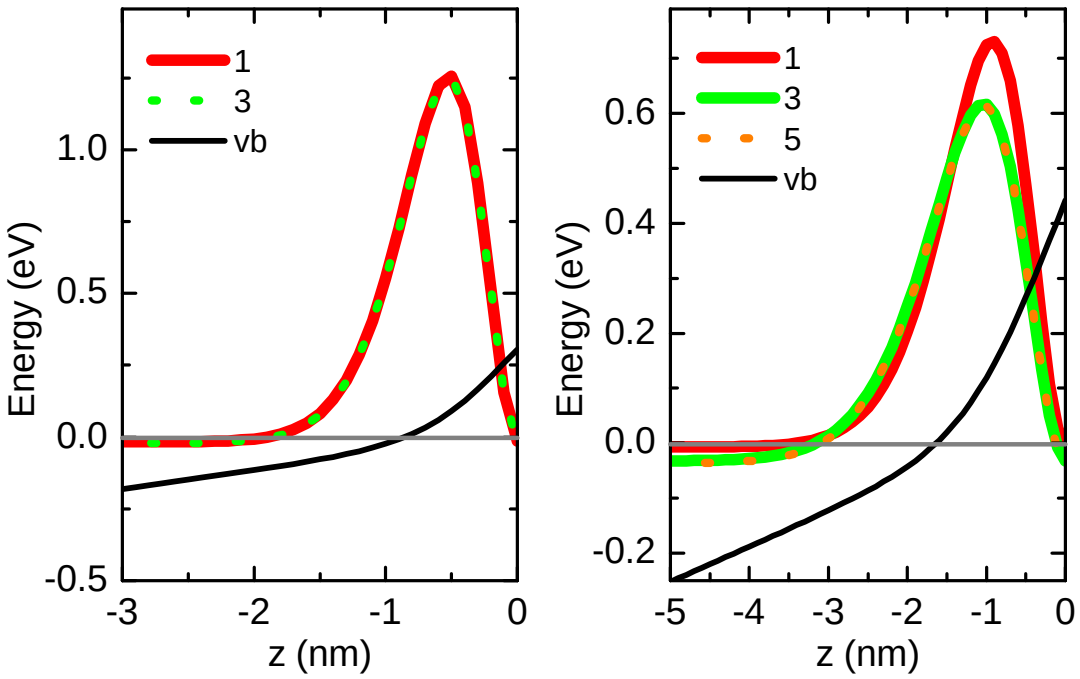

Figure 3.14: *The lowest eigenstates (square of the wavefunction shifted by its eigenvalue) for the (100) direction at a charge density of* 1.3×10^{13} *cm*$^{-2}$ *containing 97 % and 99.8 % of the charge for the Rauch (left) and Willatzen (right) parameters, respectively. The valence band edge and the Fermi level (at 0 eV) are depicted as well.*

this corresponds to energies no more than approximately 100 meV below the valence band edge.

In the simulation shown in Figure 3.13, an impurity concentration of nitrogen states of 0.18 $\times 10^{18}$ cm^{-3} (corresponding to a concentration of 1 ppm) was included throughout the diamond slab. Most natural and all CVD grown diamond samples of optical grade have a nitrogen impurity concentration of that range. The level of the electronic state created in the lattice by the substitutional nitrogen is 1.7 eV below the conduction band [Far69]. The effect of including this nitrogen impurity can be seen in Figure 3.13, in which the Fermi level in the bulk diamond comes to rest in the band gap at 1.7 eV below the conduction band. Furthermore, the total hole density is reduced by the amount of ionized nitrogen donors. This effect is demonstrated in Figure 3.17 by comparing the total hole accumulation for an optical grade sample (5 ppm nitrogen impurity concentration) with an electronic grade sample (5 ppb nitrogen impurity concentration). The increased nitrogen concentration

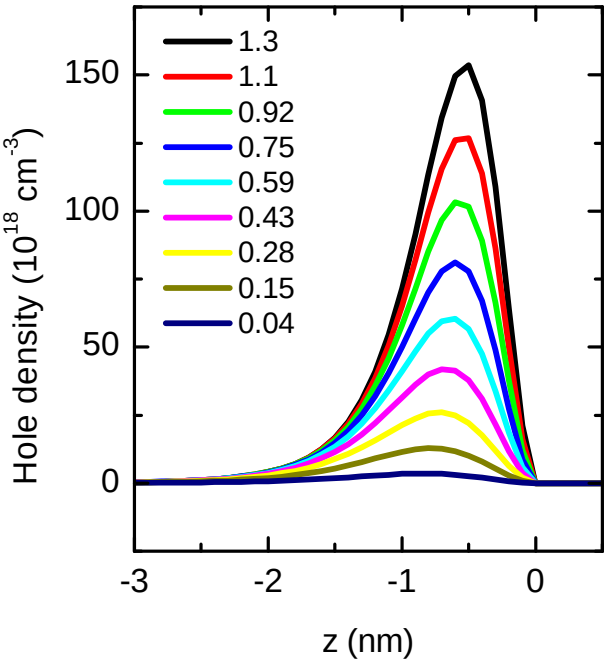

Figure 3.15: *Distribution of the hole density in z-direction at different integrated hole densities, calculated for Rauch's Luttinger parameters and a (100) orientation. The values of the legend represent the integrated areal hole density in units of* 10^{13} cm^{-2}.

effectively shifts the threshold voltage, as the nitrogen donors are compensated by holes. Comparing the average experimentally observed threshold voltages for groups of samples with different nitrogen impurity content (see Figure 3.9), this effect is supported, though the dispersion of the data is significant. If the density of nitrogen donors becomes too large, the hole density decreases accordingly and the surface conductivity vanishes [Ris02]. This may happen either in samples with a naturally high density of nitrogen impurities or in samples treated with nitrogen ion beam implantation to create nitrogen-vacancy (NV) centers [Hau11]. Reversely, the hole density compensates the electrons from the nitrogen donors and as more holes are generated at higher gate potentials, more nitrogen donors are compensated. This effect can also be used to compensate the NV centers. In effect, the charge state of the NV centers can be switched by controlling the gate voltage of the diamond SGFET accordingly [Hau11].

The positive charge in the diamond is balanced by a net negative charge in the electrolyte. The ion distribution can be seen in Figure 3.18. While in the bulk

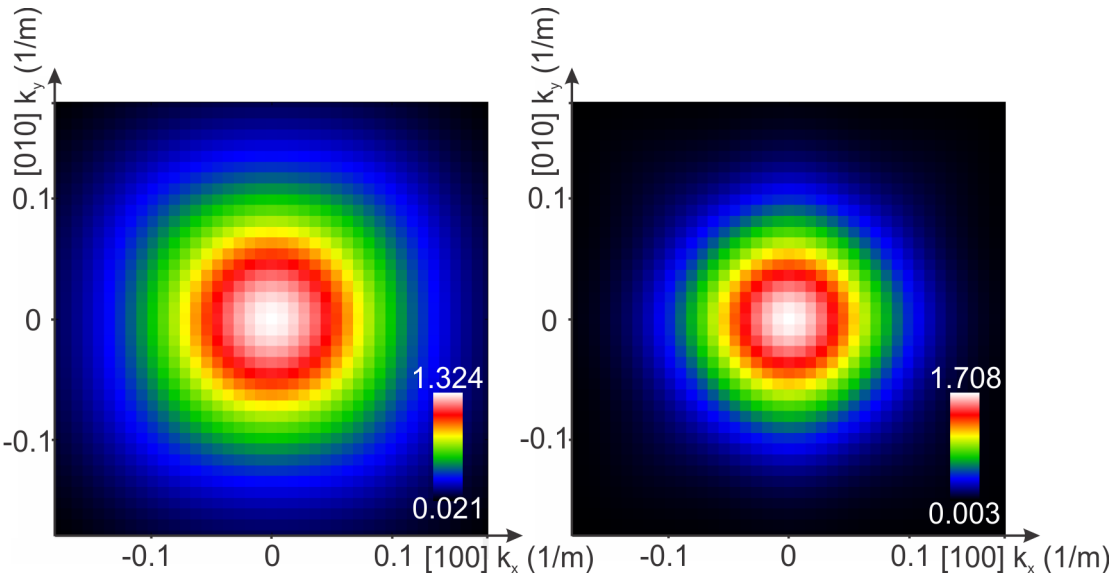

Figure 3.16: *Hole density distribution in the $k_{parallel}$ plane for a (100) orientation at a carrier concentration of 1.3×10^{13} cm^{-2} - left: for Rauch parameters and right: for Willatzen parameters.*

electrolyte negative and positive ions compensate each other, in the vicinity of the interface a net surplus of negative ionic charge compensates the positive charge of the holes in the diamond. The positive charge in the diamond is not completely compensated by the ions, as some of the hole charge is compensated by nitrogen impurities distributed over the whole diamond slab and ionized closer to the interface. The maximum of the ion distribution is at 0.76 nm from the surface (at a simulated charge density of 1.3×10^{13} cm^{-2}). The ion distribution illustrated by Figure 3.18 shows the total positive and negative ion density, which is mostly composed of the base salt of the electrolyte such as sodium and chloride. The anions in the electrolyte compensate the charge of the accumulated holes in the diamond. The total ion concentration (cation concentration minus anion concentration) is therefore negative in this region. The buffer ions are also subject to the electrostatics in the vicinity of the interface. As a consequence, the different charge states of the buffer ions show different concentrations depending on the distance from the surface and, consequently, the local pH should be affected (data not shown).

For the calculations of Figure 3.18 no surface charges were taken into account. At pH 7 negative surface charges are expected to be at the diamond surface [Har07]. In principle, the presence of surface charges shifts the effective gate potential, and consequently the threshold voltage. Indeed, the simulations predict such a shift in

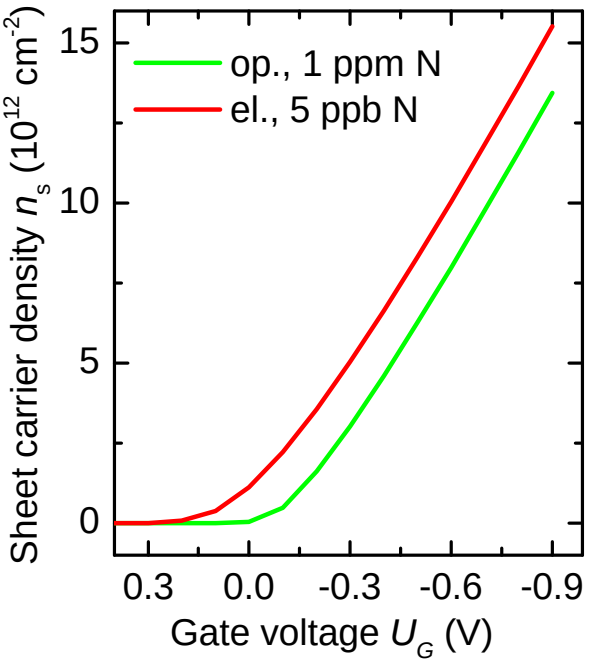

Figure 3.17: *Gate potential dependent carrier accumulation for two typical nitrogen impurity contents: 1 ppm (optical grade samples) and 5 ppb (electronic grade samples).*

threshold voltage, of approximately +200 mV for an additional surface charge of 5 $\times 10^{12}$ cm^{-2} (data not shown).

The basic effect of the extended Poisson-Boltzmann (ePB) as compared to the conventional Poisson-Boltzmann (PB) model discussed in Section 3.2.2 is that it creates a gap between the diamond surface and the electrolyte in the hydrophobic case. The effect on the potential drop at the interface from the difference between the hydrophobic ePB model and the conventional PB model is illustrated in Figure 3.19. The potential drop in the electrolyte is much larger for the hydrophobic ePB model due to the presence of a region (about 0.25 nm thick) with a dielectric constant of about 1 (see Figure 3.10 and Equation 3.10). Accordingly, for the same gate bias conditions, the potential drop in the diamond is smaller for the hydrophobic ePB model, allowing less charge carriers to accumulate at the interface. The electric field corresponding to the potential drop between the diamond surface and the onset of the water density, corresponds to 87 mV/Å between 0 nm and 0.2 nm. In the intermediate region between 0.2 nm and 0.34 nm the average field (note that the potential drop is not linear here) is 11 mV/Å . The potential drop in the diamond

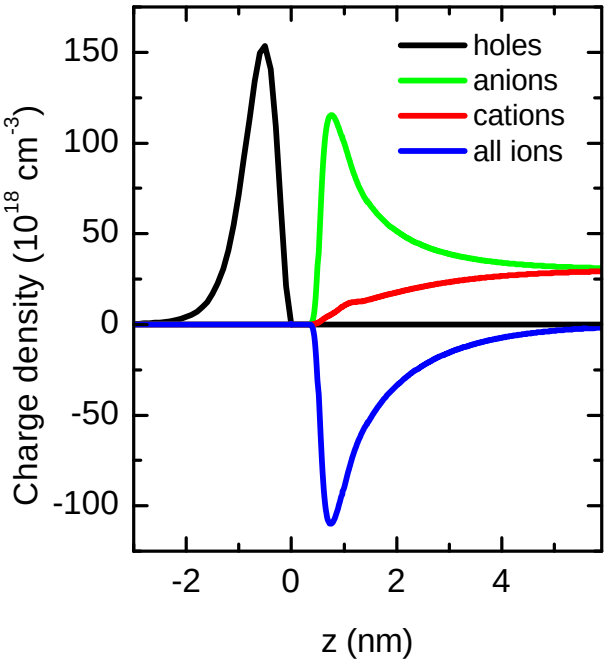

Figure 3.18: *Ion density profile in the vicinity of the surface for a hole accumulation of* 1.3×10^{13} cm^{-2}. *The anions (predominantly chloride ions) compensate the charge of the accumulated holes in the diamond. The total ion density (cation concentration minus anion concentration) is therefore negative in this region.*

provides the extra energy that is required for filling the quantum well at the surface with holes, defining the so-called the "quantum capacitance" of the two-dimensional hole gas [Lur88]. The quantum capacitance C_Q can be calculated as:

$$C_Q = \frac{\partial n_S}{\partial (E_V - E_F)/e} \tag{3.15}$$

Therefore, the total interfacial capacitance is the serial combination of the quantum capacitance and the capacitance of the electrolytic double layer formed by the holes in the diamond and the ions in the electrolyte (see Figure 3.19). At low gate voltages, the quantum capacitance dominates and at high gate voltages the interfacial capacitance is limited by the voltage-independent double layer capacitance.

In summary, the nextnano simulations with the extended Poisson-Boltzmann model for the electrolyte reproduces the experimentally observed results qualitatively, confirming the SGFET model presented in Section 3.1. The charge accumulation increases with increasing gate potential, as the Fermi level is pushed deeper into the valence band. Furthermore the simulations provide additional details such as the

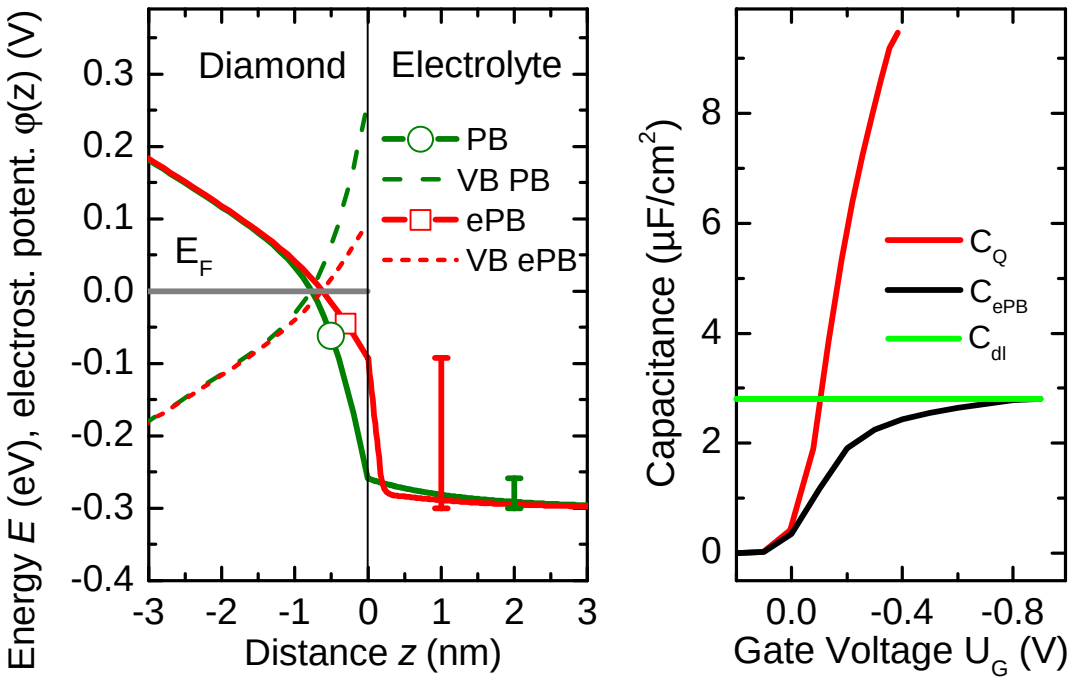

Figure 3.19: *left: Simulated potential drop across the diamond/electrolyte interface and the corresponding position of the valence band (VB) with respect to the Fermi level for the PB and the ePB models. The bars indicate the total potential drop in the electrolyte for the respective model. right: Simulated capacitance of the diamond/electrolyte interface (black). The interfacial capacitance is determined by the series combination of the quantum capacitance (red) and the double layer capacitance (green). The double layer capacitance in this figure is estimated as the maximum of the interfacial capacitance.*

subband occupation, help explain and confirm experimental findings and corresponding hypothesis such as the vanishing of the surface conductivity with increasing nitrogen content, and predict new phenomena like the switching of the charge state of nitrogen-vacancy centers. In the following the simulations are quantitatively compared with the experimental results, and yield an even deeper understanding of the charge accumulation at the diamond/electrolyte interface.

The simulations shown above were partly based on the isotropic effective mass assumption for greater calculation efficiency. The potential-dependent carrier density for the isotropic effective mass and the **k·p** calculations are compared in Figure 3.20, both for the Rauch and Willatzen parameter sets. For the Rauch parameters (left graph in Figure 3.20) the energy dispersion was very isotropic (see Figure 3.12) and

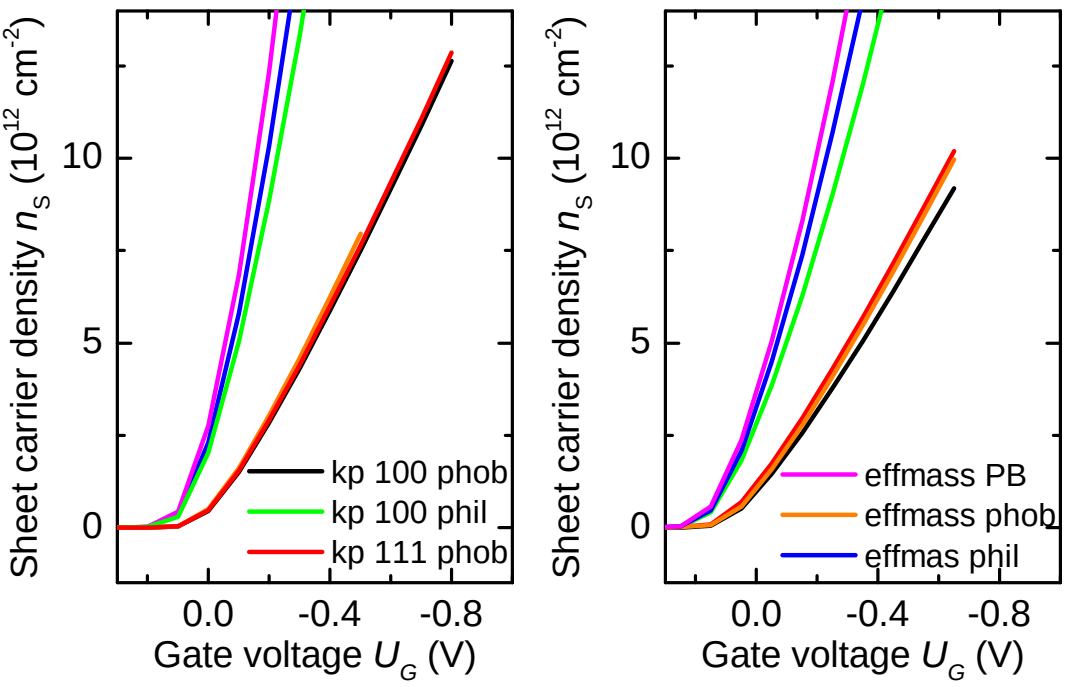

Figure 3.20: *Comparison between hole densities simulated with the isotropic effective mass approximation and with the effective masses calculated with the* ***k·p*** *method. left: for Rauch parameters and right: for Willatzen parameters. The results for each parameter set are compared for the hydrophobic and the hydrophilic case and the differences are compared to those that emerge for a (111) orientation or the conventional Poisson-Boltzmann model. Note, that the legends of the left and right figure are relevant for both.*

accordingly there is little difference between the (100) and the (111) **k·p** results for the hydrophobic case. Equally, the effective mass calculations yield the same result. For the hydrophilic case, the difference between the isotropic effective mass and the **k·p** calculations is more pronounced, with the **k·p** results yielding a weaker n_S-U_G dependence, i.e. a lower interfacial capacitance. In order to illustrate the difference between the hydrophobic and the hydrophilic case of the ePB model, the result for the conventional PB (assuming isotropic effective masses) is shown as well. The hydrophilic case, with its closer approach of the water and ions to the surface, shows a n_S-U_G dependence almost as high as for the PB model. The same comparisons are made for the parameters according to Willatzen. Here, the bigger anisotropy of the energy dispersion (see Figure 3.12) results in a more marked difference between the (100) and (111) **k·p** results for the hydrophobic case. However, the influence of the crystallographic orientation is much smaller than that of the hydrophobicity.

Comparing both parameter sets, the results are not only qualitatively but also quantitatively very similar. Obviously the differences in the energy dispersion between the parameter sets (see Figure 3.12) with their different effective masses does not show up as pronounced in the charge accumulation. The small difference between the **k·p** and isotropic effective mass calculations in turn justifies the use of this simplification for most cases.

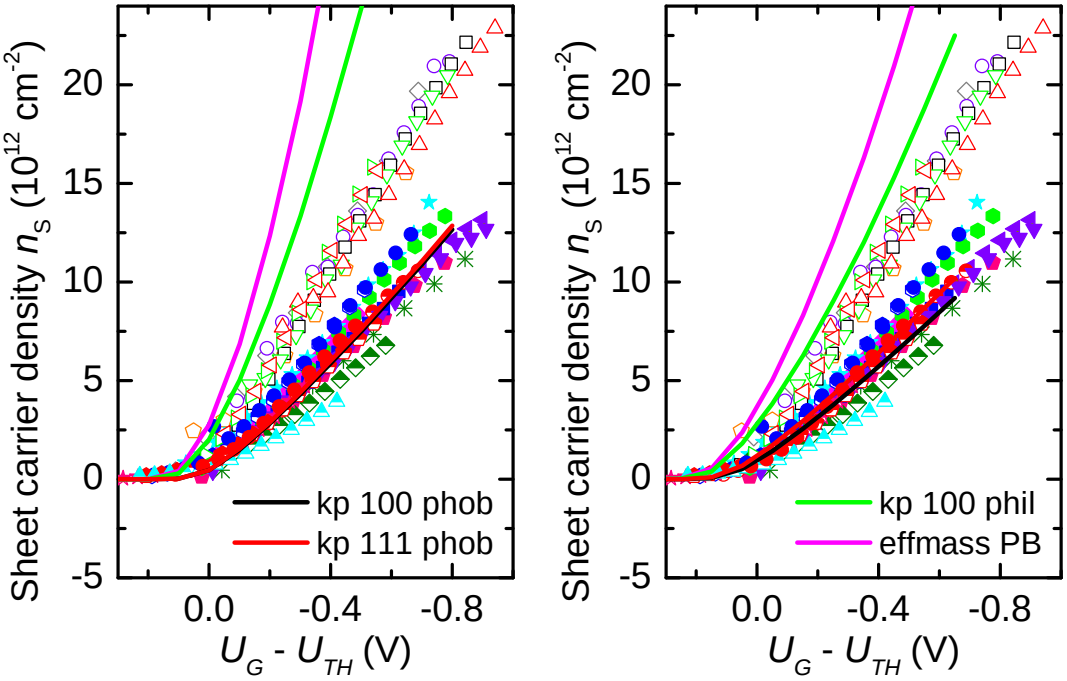

Figure 3.21: *Comparison between the simulated results and the experimentally obtained carrier concentrations for different gate potentials. All data sets are normalized with respect to their threshold voltage. The simulated results are based on* ***k·p*** *calculated effective masses and are shown for the (100) and the (111) orientation for the hydrophobic case, and the (100) orientation for the hydrophilic case (calculations based on left: Rauch parameters; right: Willatzen parameters). The result of the conventional Poisson-Boltzmann model based on isotropic effective masses is shown for reference.*

The nextnano simulations are compared to the experimental results for the charge accumulation versus the gate potential in Figure 3.21. The experimental results were normalized with respect to their threshold voltage, so that they differ only in the slope of the carrier concentration, which corresponds to the interfacial capacitance. The homogeneity of the interfacial capacitance and the difference for the (111) and the (100) surface orientations are very clear. Figure 3.21 encompasses the data

sets from Figure 3.7. Only those data sets are excluded whose slope of the carrier concentration is not linear enough to establish a threshold voltage. The nextnano simulations shown use the ePB model with **k·p** calculations for the (100) direction (hydrophobic and the hydrophilic case) and for the (111) direction (hydrophobic case only). The PB model for the (100) orientation with an isotropic effective mass approximation is shown as well for reference. The nextnano simulations were also normalized regarding their gate potential. The experimental data for the (100) surface orientation and the hydrophobic extended Poisson-Boltzmann model show a remarkable agreement for the parameter sets of both Rauch and Willatzen. The extended Poisson-Boltzmann model applied to the hydrophilic surface predicts an interfacial capacitance (i.e. the slope of the n_S-U_G curve) significantly higher than experimentally observed for the (100) surface orientation. The experimental data for the (111) surface orientation, however, can not be reproduced. For the Luttinger parameter set from Willatzen, the observed (111) versus (100) anisotropy qualitatively agrees with the experimental data, as the simulated results for the (111) orientation do show a higher capacitance than for the (100) orientation. But the simulated difference is much smaller than experimentally observed. This is of course even more the case for the largely isotropic parameters by Rauch. The experimentally observed difference in the interfacial capacitance between the (100) and (111) surface orientation, 2.45 μF cm^{-2} and 4.29 μF cm^{-2} respectively, can therefore not be explained with the crystallographic orientation of the diamond crystal according to the nextnano simulations. These simulations can only account for differences in the diamond itself, and thus only in the part of the interfacial capacitance that results from the quantum capacitance (see Figure 3.19). Therefore, the observed difference in the interfacial capacitance should result from a surface orientation dependent difference in the double layer capacitance. Possible mechanisms leading to different interfacial capacitances for the (100) and the (111) surface are discussed below.

According to the nextnano simulations, the surface hydrophobicity has a much larger impact on the interfacial capacitance than the crystal orientation. The contribution of the water density profile and the PMFs to the interfacial capacitance can be differentiated when shifting both profiles with respect to the surface. A shift of ± 0.5 Å with respect to the surface is a typical variation for different hydrophobic surfaces [Sed08, Sch10]. Figure 3.22 (*left*) shows the influence of the size of the water-depleted region (gray shaded region). The effect for an equivalent shift of the PMFs, in this case ± 1 Å , is shown in Figure 3.22 (*right*) using an enlarged x-axis, and is comparably insignificant.

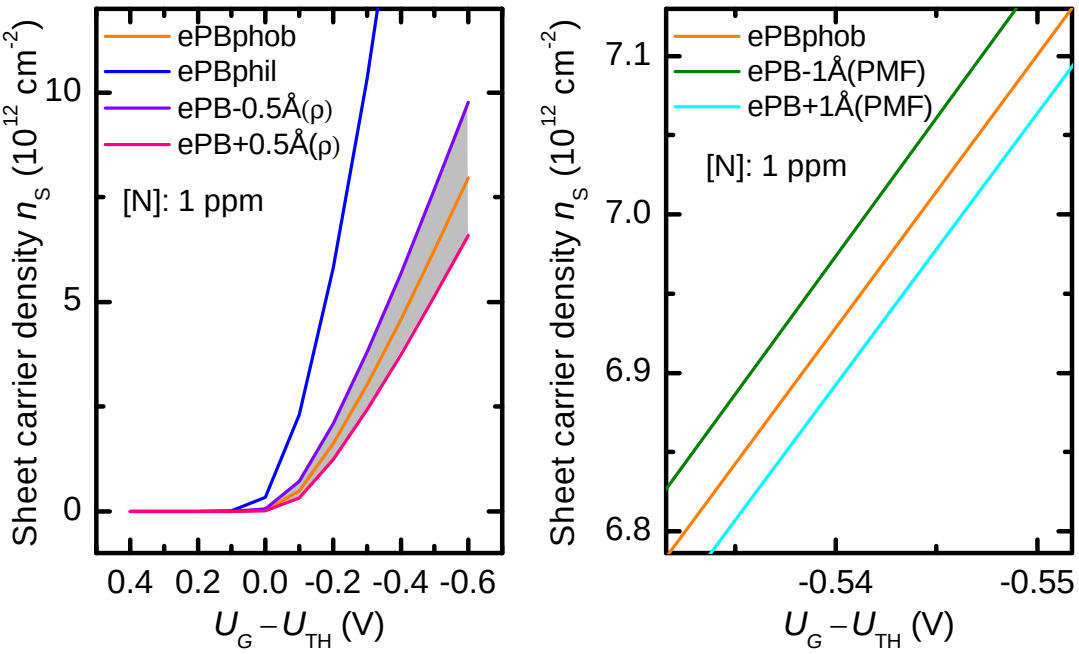

Figure 3.22: *left: Effect of a shift in the water density profile relative to the surface on the interfacial capacitance. For the hydrophobic case the water density profile is shifted ± 0.5 Å ("ePB ±0.5Å(ρ)") towards and away from the diamond surface (gray shaded region). The hydrophilic case is shown for comparison. right: Effect of a shift of the PMFs, and therefore the maximum of the ion density, relative to the sample surface. The PMFs are shifted ± 1 Å ("ePB±1Å(PMF)") towards and away from the diamond surface. The effect is too small to be visible on the scale of the figure on the left-hand side.*

The relative importance of the water density profiles as opposed to the PMFs can be explained with the simple model shown in Figure 3.23, where the interface is approximated using a plate capacitor model with three regions. The first being the region (size d_1= 0.5 nm) between the two-dimensional hole gas and the diamond surface with a diamond dielectric constant of 5.68; the second region (size d_2 = 0.34 nm) ranging from the diamond surface to the onset of the water density with a vacuum dielectric constant of 1; and the third region (size d_3 = 0.42 nm) with a water dielectric constant of 78 between the onset of the water density (neglecting any substructure of the water density) and the closest approach of the ionic countercharge. The distance d_3 is directly related to the PMFs and can be estimated from the maximum of the ion distribution shown in Figure 3.11. Effectively, these three regions correspond to three capacitors in series and the equation for the areal

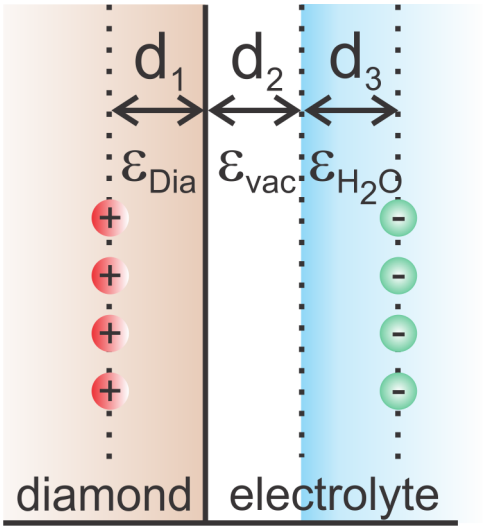

Figure 3.23: *Simple parallel plate capacitor model for the interfacial capacitance. The interface is modeled with three regions, corresponding to three capacitors in series. The first region extends from the maximum hole density to the surface (d_1), the second region extends from the surface to the onset of the water density (d_2), and the third region extends from the onset of the water density to the maximum ion density (d_3). The dielectric constants of these regions are the respective bulk constants of the materials diamond, vacuum, and water.*

capacitance is then:

$$\frac{C}{A} = \frac{78 \times 5.68 \times \epsilon_{vacuum}}{78 \times d_1 + 78 \times 5.68 \times d_2 + 5.68 \times d_3} \tag{3.16}$$

With the values for the extent of the regions given above (taken from the simulations), the areal capacitance calculates to 2.9 μF cm^{-2} - in excellent agreement to the capacitances found experimentally. As in any serial capacitor configuration, the smallest capacitance dominates the total capacitance and, in this case, the diamond/electrolyte interface is dominated by the capacitance of the water depletion region at the surface with its small dielectric constant. This crude model therefore succeeds in explaining the large effect of a shift in the water density profile (factor of 5.68×78 in the denominator) and the negligible effect of such a shift of the PMFs (effectively the approach of the ionic countercharge to the surface) with a factor of 5.68. As only the water density profile and its position are relevant, and the exact position of the ions much less so, the calculations for the PMFs are unnecessary for the charge accumulation. Any method that keeps the ions somewhat farther away from the surface than the water would be sufficient. Other methods to this effect, such as a generic soft ion repulsion, have been used when performing calculations

simulating solid/electrolyte surfaces [Bon11].

This hydrophobic gap with a low water density in the vicinity of the diamond surface is in agreement with studies of other hydrophobic systems where a water density depletion has been observed [Kun09] [Mez06] [Hua08] [Mez10] [Jen03]. The results shown in this thesis confirm the effect of the hydrophobicity of the hydrogen-terminated diamond surface on the charge accumulation at the electrolyte interface. More broadly, these results are relevant for any hydrophobic potentiometric biosensor, such as e.g. field effect transistor devices. The effect is negligible in Si/SiO_2-based field-effect transistor devices, not only due to their hydrophilic nature but also because the oxide acts as a dielectric spacer between the charges in the semiconductor and the water, thus masking the effect of an additional hydrophobic separation [Bir08]. However, new materials for biosensor devices, such as graphene, self-assembled monolayers, and some organic semiconductors are hydrophobic and are usually employed without an oxide layer [Dan10] [Sch10] [But11]. Accordingly, the discussed consequences of hydrophobicity and the resulting depletion layer are relevant there.

So far the accuracy, applicability, and shortcomings of the simulations have not yet been discussed. As is clear from Figure 3.21, the experimental results for the (111) surface orientation are not well replicated by the simulation. While the interfacial capacitance for (111) oriented samples is significantly lower than results for the hydrophilic ePB model, they are also significantly higher than for the (100) oriented samples and therefore higher than the results for the hydrophobic ePB model. Obviously even the simulations using the effective masses based on $\mathbf{k}\cdot\mathbf{p}$ calculations cannot account for this.

There are a number of other shortcomings of the presented simulations. For instance the parameters for the simulation of the electrolyte close to the hydrogen-terminated diamond surface were calculated for a model hydrophobic surface based on SAMs with hydrophobic and hydrophilic end groups respectively. As has been discussed before, a hydrophobic gap, meaning a water depletion layer in the vicinity of hydrophobic surfaces, has been postulated and observed for a wide range of hydrophobic surfaces. Therefore the general finding, that a hydrophobic gap influences the charge accumulation, or, more broadly, the potential drop at the surface remains relevant. However, the substructure of the water density profile is expected to change for different hydrophobic surfaces. Accordingly, the interfacial capacitance would change, e.g. representing the experimental results for the (100) surface less well. We

have tried to estimate the effects of such a change with the shift of the whole density profile as seen in the gray area of Figure 3.22. Likewise, the PMFs used were those for the Cl^- and Na^+ ions only, ignoring the other ions in the electrolyte. Given that the Cl^- and Na^+ ions constitute the mayor part of the electrolyte ions, and that the exact position of the ions has turned out to be almost irrelevant, this seems largely justified.

An additional simplification is the assumption that the water density is directly proportional to the dielectric constant according to Equation 3.10. However, it has been shown that water molecules may be oriented at surfaces and specifically at hydrophobic surfaces. Such an orientation would decrease the dielectric constant and potentially significantly alter the results. Water orientation at hydrophobic surfaces is attributed to a reduced density of hydrogen bonds between the water molecules and the surface, and the tendency of water molecules to maintain their hydrogen bond network [Sed08], and has been shown for different systems [Goh88] [Sca01]. This not only leads to a water dipole orientation, which would influence the dielectric constant, but also seems to change the reorientation time of these water dipoles and correlation of the dipoles, all affecting the dielectric permittivity, as suggested by studies on different systems [Des04] [Tie09] [Sha07]. Such changes in the dielectric constant were observed or calculated e.g. for biological systems ([Des04] [Tie09]) or at high electric fields [Yeh99]. However, these effects are still under study, and so far a quantitative dependence of the dielectric constant with respect to the distance of hydrophobic surfaces or, specifically the hydrophobic diamond surface, has not been presented. Furthermore, recent theoretical work [Bon11] suggested that the details of the dependence of the dielectric permittivity on water ordering at hydrophobic surfaces are not as straightforward as a permittivity decrease with increasing water ordering - though this is approximately the case. Moreover, even this study ([Bon11]) predicts the hydrophobic gap, which should be the more dominating effect, as discussed next.

Beyond the hydrophobic effect, the local electric field from the surface dipole moment of hydrogen terminated diamond could have an additional effect on the ordering of water molecules. The hydrogen-terminated diamond surface shows a surface dipole moment of 1.32×10^{-30} Asm (=0.08 eÅ) for the (100) orientation. Water molecules have been shown to be oriented in the electric field in the vicinity of charged surfaces for other systems [Hab86] [Ton94]. The polarity of the surface carbon-hydrogen bonds could also again affect the hydrophobicity of the surface in general and thereby

again influence the water depletion or orientation of water molecules [Gio07]. The effect of oriented water molecules can be roughly estimated with the simple plate capacitor model presented above. Assuming the most extreme case of completely oriented water molecules, the dielectric constant for the now oriented water layer of thickness d_3 is estimated to be 6 [Boc02]. The model would then predict an interfacial capacitance of 2.13 μF cm^{-2} instead of 2.86 μF cm^{-2} for water with a dielectric constant of 78. Obviously the total interfacial capacitance is still largely dominated by the hydrophobic gap with a dielectric constant of 1. Therefore, water ordering should be a secondary effect to the size of the hydrophobic gap. Yeh et al. found a 50 % decrease of the dielectric constant of water for an electric field of 50 mV/Å [Yeh99]. Considering that the potential drop is about 90 mV/Å in the water free region and only about 10 mV/Å at the onset of the water density (see Figure 3.19), the effect of water ordering is likely to be much less than the extreme case calculated by Yeh et al..

As shown above in Figure 3.21 the rather large difference in the interfacial capacitance between the (100) and the (111) surface orientation, 2.45 μF cm^{-2} versus 4.29 μF cm^{-2}, cannot be explained by the crystallographic orientation and the different energy dispersion. Considering that diamond is a highly symmetric crystal composed of only one element and therefore a neutral bond between the atoms, it is not surprising that the effect of accumulating charges with the potential along different directions leads in principle to the same results. However, the experimental values for the interfacial capacitances of the (100) and the (111) direction are significantly different. This in turn suggests, together with the fact that the electrolyte is the same for both orientations, that the difference in the interfacial capacitance between the (100) and the (111) oriented surface has to result from differences in the surface and interface itself. The primary difference between the (100) and the (111) orientation is the related to the density and orientation of the C-H bonds (see Section 2.2). The (100) surface has hydrogen bond density of 1.57 $\times$ 10^{15} cm^{-2}, 10 % less than for the (111) surface (1.81 $\times$ 10^{15} cm^{-2}). Additionally the C-H bonds are tilted by 25° versus the surface normal for the (100) surface, resulting in overal dipole moment of 1.32 $\times$ 10^{-30} Asm - 10% lower than for the (111) surface - when taking the dipole interactions into account [Mai01]. The greater dipole density of the (111) oriented surface could render the surface more polar, which in turn might decrease the hydrophobicity [Gio07]. A diminished hydrophobic gap would then result in a higher interfacial capacity. A systematic difference in the water con-

tact angle between (100) and (111) oriented samples could not be observed within the, admittedly high, margin of error for the measurements performed in this work. However, the macroscopic contact angle is not always in direct relationship to the nanoscopic hydrophobic gap [Mez10]. A higher dipole density might also lead to a local electric field, resulting in an enhanced orientation of water molecules and thus a smaller dielectric constant. This, however, would decrease the interfacial capacitance opposite to the observed results. The interplay between hydrophobicity of a surface and the dielectric constant in its vicinity, which largely determines the interfacial capacitance, is highly complex. On the one hand, the hydrophobicity represents the inability of the interfacial water to form hydrogen bonds, leading to the hydrophobic gap to preserve the hydrogen bond network of water. On the other hand, the interaction with the surface leads to orientation of water molecules, also diminishing the dielectric constant.
The average interfacial capacitance is 2.45 μF cm^{-2} for the (100) orientation and 4.29 μF cm^{-2} for the (111) orientation. If this difference were due solely to a difference in the hydrophobic gap, how large would that difference have to be? This shift in the water density profile can be established with the nextnano simulations. Here, a shift of 0.9 Å of the water density profile closer to the diamond surface is sufficient to increase the capacitance to the level corresponding to a (111) surface orientation. For comparison, the difference between a hydrophobic and a hydrophilic surface corresponds to a shift of 2.3 Å using Figure 3.10.

Finally, the higher interfacial capacitance for the (111) surface might also simply be a geometric effect due to a higher surface roughness. In principle the (111) surface is known to be harder to polish and might therefore indeed show a higher surface roughness. However, the surface roughness detected with an atomic force microscope (AFM) for (100) and (111) oriented, optical grade samples did not show any difference (see Figure 3.24). Of course, the resolution limit of the AFM still leaves the possibility of a different surface roughness on the nanometer scale for the (111) and (100) oriented samples, but the effect of such a difference is likely to be negligible.

In conclusion, the study on the charge accumulation at the diamond/electrolyte interface allows three major insights.

- The experimental data on the charge accumulation supports the SGFET model. The change in conductivity is primarily due to variations of the carrier concentration with the gate potential.

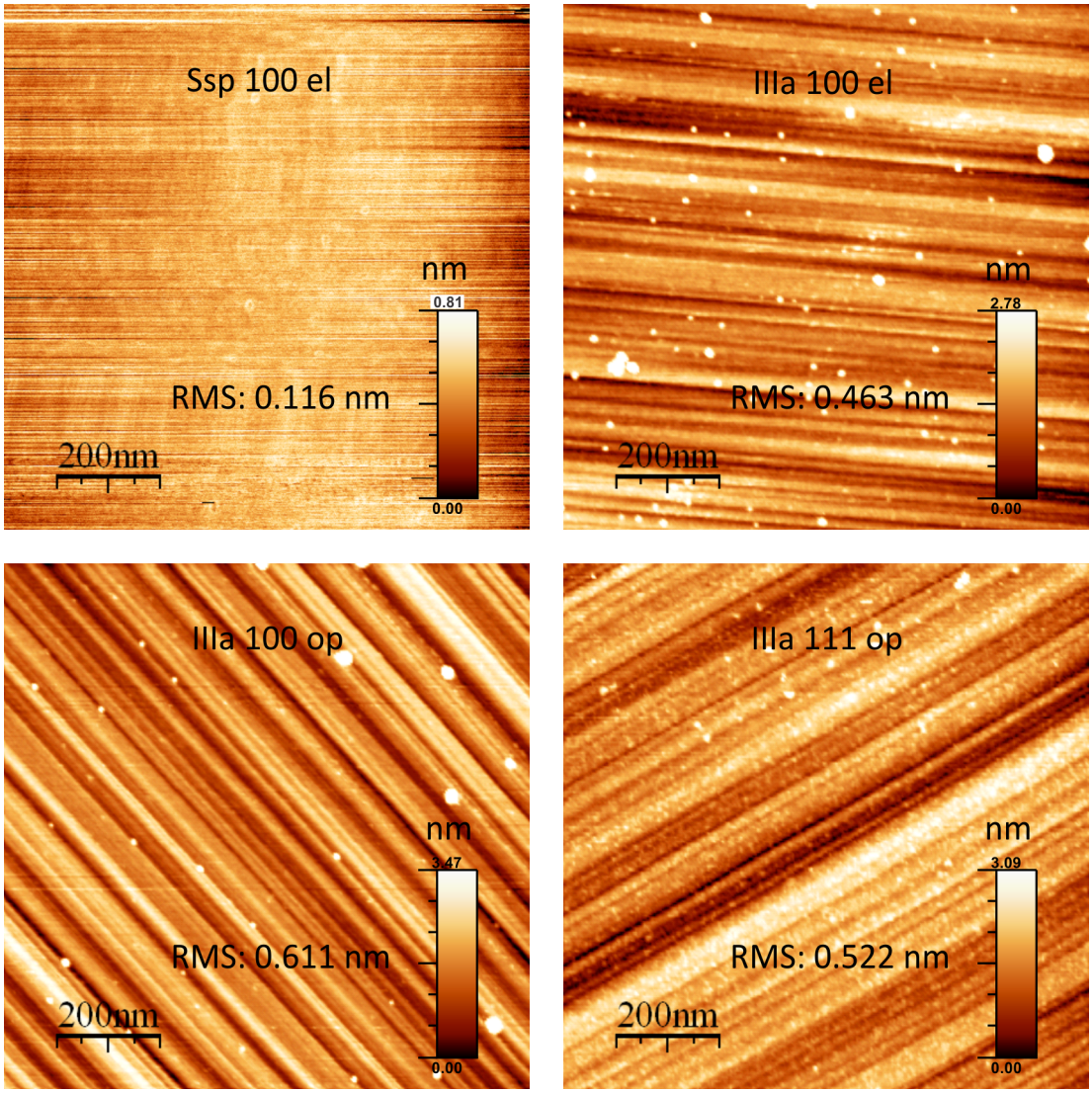

Figure 3.24: *AFM images for a set of samples representing various categories. top left: Electronic grade sample with "super" polishing. top right: Electronic grade sample with polishing lines revealing the surface roughness induced by the mechanic polishing. bottom left: Optical grade sample with a (100) orientation and polishing lines. bottom right: Optical grade sample with a (111) orientation and polishing lines.*

- The interfacial capacitance is dependent on the orientation of the diamond surface and independent of other factors.
- The interfacial capacitance can be explained quantitatively by assuming a hydrophobic gap in the vicinity of the diamond surface.

For the nextnano simulations, effective masses calculated with the **k·p** method as

well as the isotropic effective mass approximation were employed. Since the results do not differ significantly, the much faster isotropic effective mass approximation is sufficient to model the diamond/electrolyte interface for most purposes. The simulations based on **k·p** calculated effective masses do, however, allow a more realistic insight, e.g. into the subband structure of the hole channel. There is no agreement in literature on the effective masses or Luttinger parameters for the diamond valence band. Two parameter sets, one experimental, one theoretical, are tested against the experimental data of the interfacial capacitance. Both parameter sets agree with the experimental data. However, the experimentally obtained interfacial capacitances cannot be accounted for without assuming a hydrophobic gap. This hydrophobic gap consists of a region of diminished water density directly adjacent to the diamond surface. This gap, with its low dielectric constant, dominates the interfacial capacitance and explains the low capacitances found experimentally. The difference in the interfacial capacitance between the (100) and the (111) oriented surfaces, however, remains unresolved.

3.3 Electronic transport at the diamond/electrolyte interface

3.3.1 Experimental Hall mobility and influences on electronic transport

The electronic transport in the surface-conductive channel is of fundamental as well as practical interest, because an understanding of the mobility-limiting scattering mechanisms opens the possibility for improvement or reveals physical limits to device properties. In the course of this work, a range of potential influences and limitations of the hole mobility were investigated. The complete set of measurements for different diamond samples and the standard electrolyte are shown in Figure 3.25. While the wealth of data is confusing, a general conclusion can be drawn, which is supported by all measurements. Especially at high carrier concentration the mobility converges to values between 30 and 90 $cm^2\ V^{-1}s^{-1}$. This is in agreement with previous studies on the mobilities in surface-conductive diamond, all of which where actually performed not in electrolyte but with no gating [Jia99] [Neb01] [Neb04] [Rez06] or with a metallic gate [Hir10] [Hir08b] [Hir08a]. The mobility of the holes in surface conducting diamond is thus greatly reduced from that measured with the time-of-flight technique in bulk undoped samples [Isb02] [Nes08], which

report drift mobility values of up to 3800 $cm^2\ V^{-1}s^{-1}$ for holes at room temperature. These record measurements were taken at negligible carrier concentrations, as a consequence of the employed time-of-flight method. Nonetheless, the discrepancy between the actually obtained mobilities and the limit shown by the time-of-flight experiments motivates the search for the mechanisms limiting the mobility in the diamond SGFETs. Figure 3.25 also contains error bars for a selection of samples. These represent the statistical error of the measured and averaged data points only (for a discussion of systematic errors see Appendix A.2) and give an idea of the error, especially for low conductivities.

In order to separate different effects, subsets of the data in Figure 3.25 are discussed in the following. CVD grown electronic grade (nitrogen concentration $\leq$ 5 ppb; boron concentration $\leq$ 1 ppb) samples in comparison to CVD grown optical grade (nitrogen concentration $\leq$ 5 ppm) samples of (100) orientation are shown in Figure 3.26. For almost all samples at any concentration of holes, the mobility for the purer electronic grade samples is higher than that for the optical grade samples. The samples differ also in their mobility dependence on the hole concentration. While the optical grade samples show a mobility largely independent of the carrier concentration (in the range of 30 to 90 $cm^2\ V^{-1}s^{-1}$), the mobility of the electronic grade samples decreases with increasing carrier concentration. This leads to high mobility values at low carrier concentration for the electronic grade samples of up to approximately 400 $cm^2\ V^{-1}s^{-1}$.

A comparison between (100) and (111) oriented samples with a similar content of nitrogen impurities (optical grade and natural IIa samples) is shown in Figure 3.27. As a result of the higher interfacial capacity of the (111)-oriented samples, these data points start at a higher carrier concentration. At high carrier concentration, the mobilities for the (100) and the (111) surface orientation are in the same range of 30 to 90 $cm^2\ V^{-1}s^{-1}$. However, in contrast to the (100) oriented samples, the mobility decreases for the (111) oriented samples at low carrier concentrations. The decrease of mobility for the (111) surface with decreasing carrier concentrations depends on the individual sample.

Temperature dependent measurements

Temperature dependence is one of the most important characteristics usually employed to distinguish between different scattering mechanisms limiting electronic transport. However, temperature dependent measurements in aqueous electrolyte

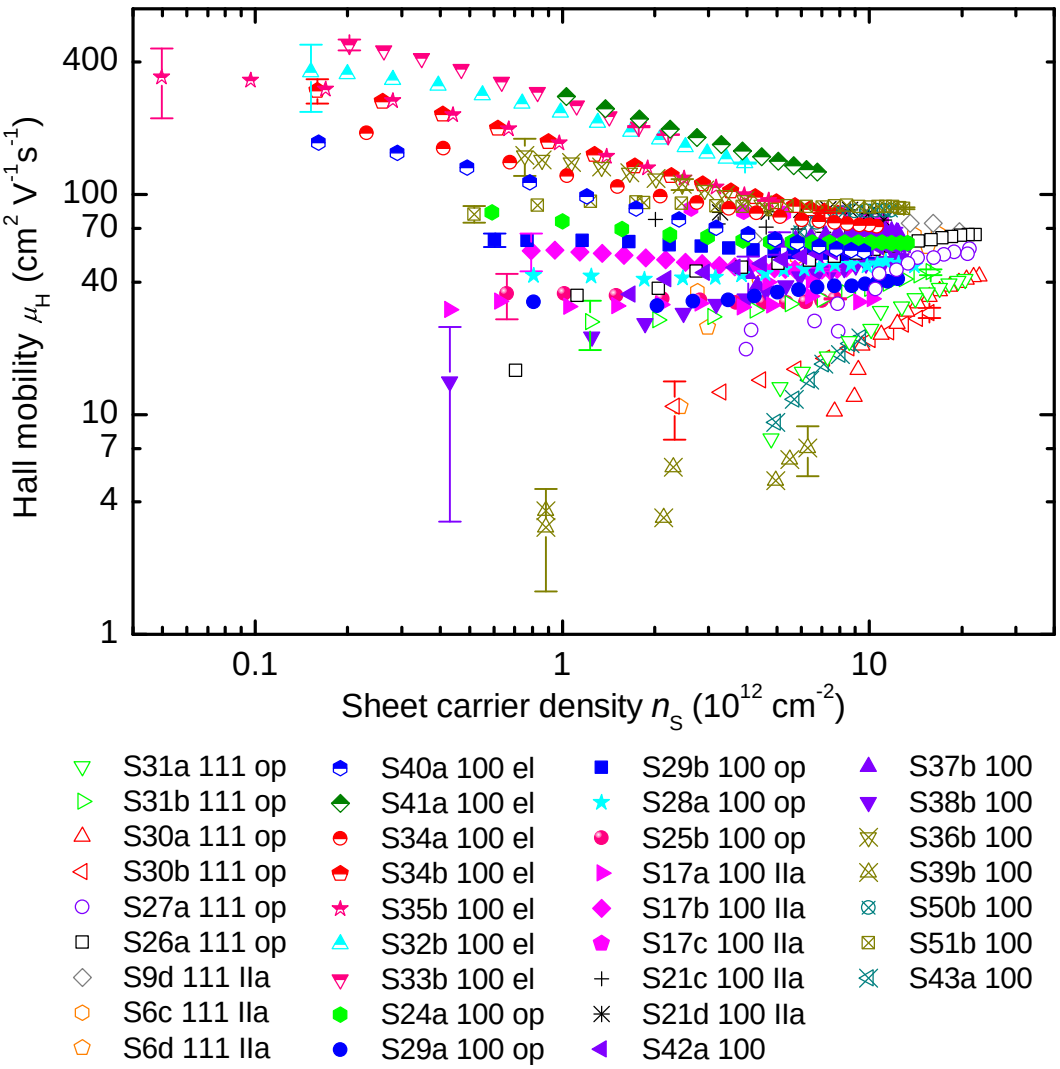

Figure 3.25: *Hall mobilities as a function of sheet carrier density for all samples investigated, calculated from the sheet resistance and the sheet carrier concentration (Figures 3.6 and 3.7). Solid symbols represent optical grade samples with a (100) orientation, open symbols depict optical grade samples with a (111) orientation. Half-solid symbols are for electronic grade samples, all of which have a (100) orientation. Open crossed symbols correspond to samples that fall in neither category.*

are naturally very limited in range. Figure 3.28 shows temperature dependent measurements in aqueous electrolyte for a number of samples at different hole densities. No clear temperature dependences for all samples or certain categories such as (100) or (111) oriented samples, or different concentration of nitrogen impurities, could be established. Specific transport mechanisms will be discussed in Sections 3.3.2 and 3.3.3.

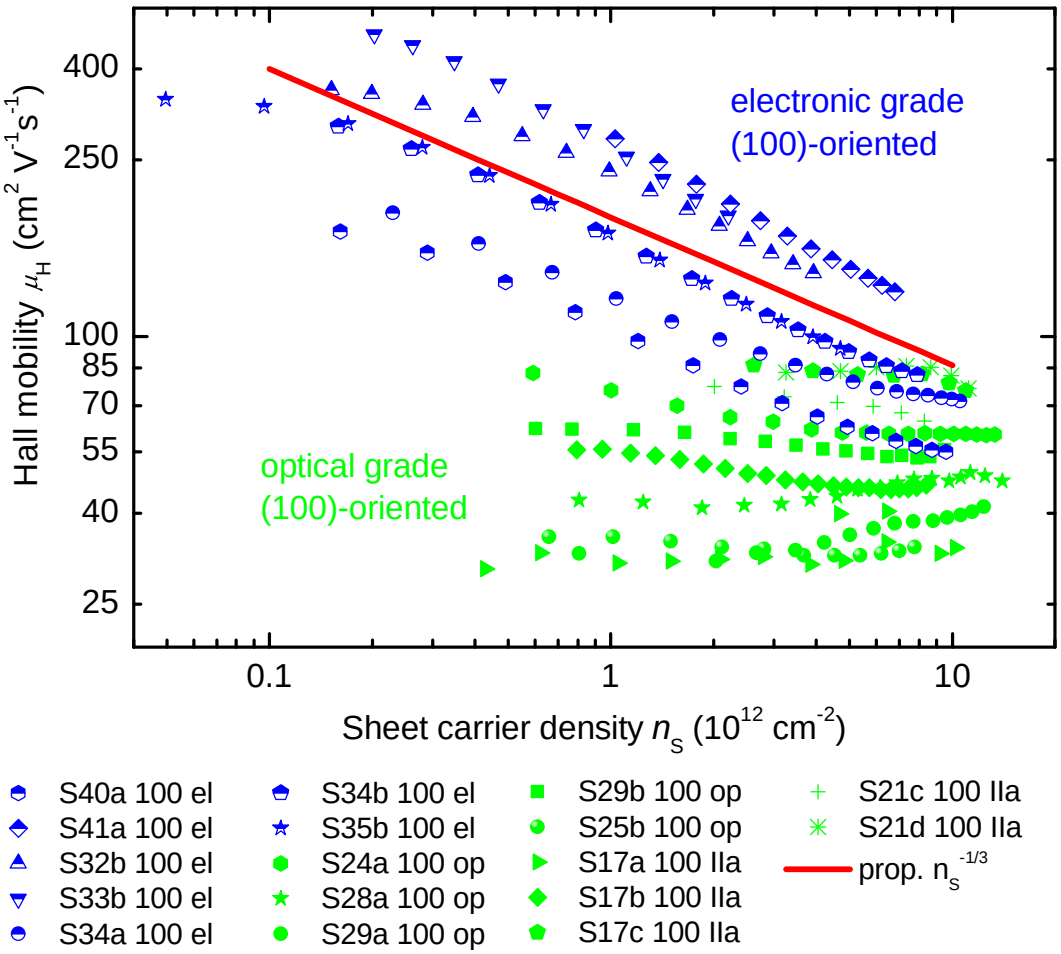

Figure 3.26: *Subset of the samples in Figure 3.25 showing only (100) oriented samples with different nitrogen impurity content: electronic grade (half-solid symbols; all blue) as well as optical grade and natural IIa (solid symbols; all green) diamond samples. The solid line, representing a mobility dependence of $n_S^{-1/3}$, is shown as a guide to the eye.*

pH dependence, ion sensitivity, and ion adsorption

The unique feature of the diamond SGFET is its electrolyte gate. Consequently, the influence the electrolyte gate has on the electronic transport is of particular interest. Previous studies have already shown that the surface conductivity is pH dependent and ion-sensitive [Har07]. The mechanism underlying both effects is a pH-dependent surface charge, which is partially screened by the electrolyte ions. The effect of this surface charge, as well as ion specific effects on the electronic transport have been investigated in this work.

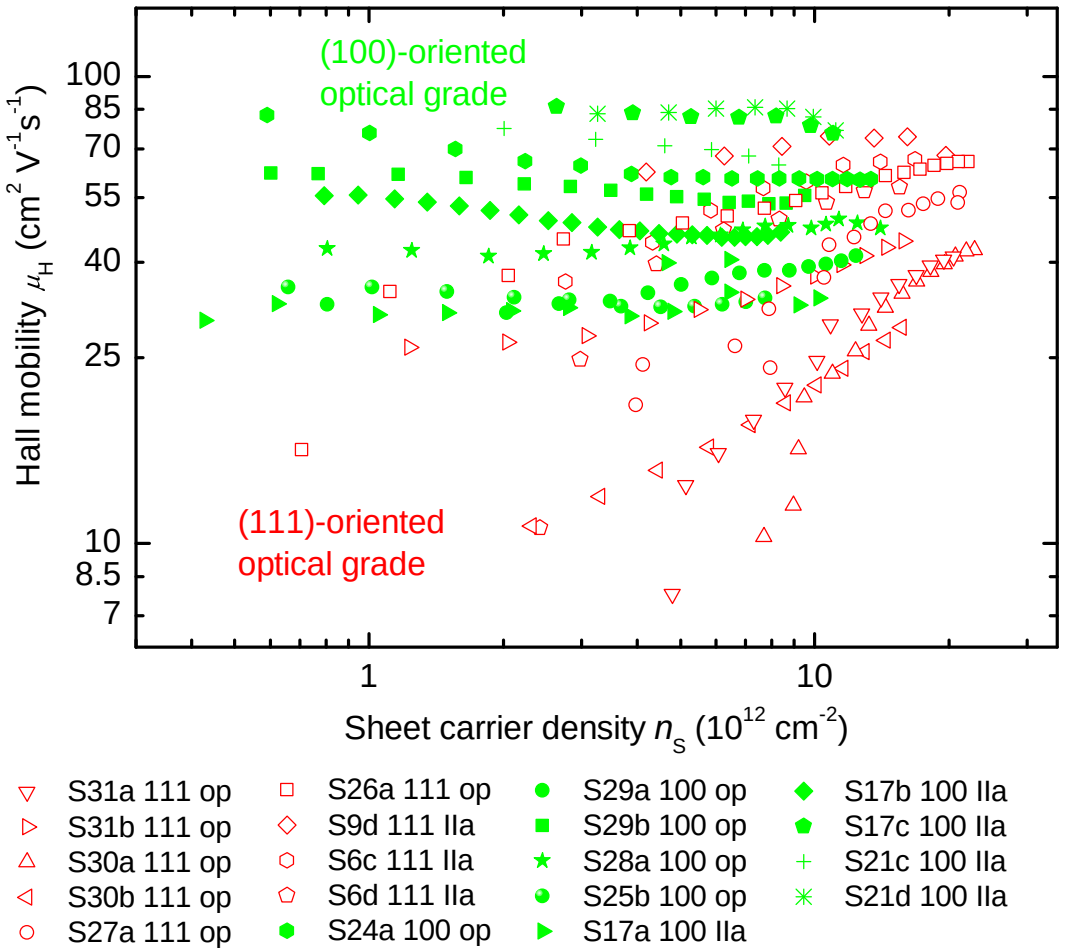

Figure 3.27: *Subset of the samples in Figure 3.25 showing only optical grade or natural IIa samples with different surface orientations: (100) (solid symbols; all green) and (111) (open symbols; all red) oriented diamond samples.*

The pH of the electrolyte was changed starting from low pH by adding KOH to the electrolyte solution, while keeping the ionic strength at 50 mM and the buffer concentration constant at 10 mM by adding appropriate amounts of water and H_3PO_4 to the solution (see Appendix A.4.1 for details). Figure 3.29 shows the effect of pH on the conductivity, carrier concentration and mobility. With increasing pH the negative surface charges increase, either by direct adsorption of hydroxide ions or via the site binding model [Här08]. The increase in negative surface charge is compensated by an increase in the hole accumulation. The pH dependence of the conductivity is 29 mV/pH at -0.4 V gate voltage, in agreement with previous studies [Här08]. The pH dependence of the conductivity can be understood as a result of a change in carrier concentration, as shown in Figure 3.29, which reveals that any change in

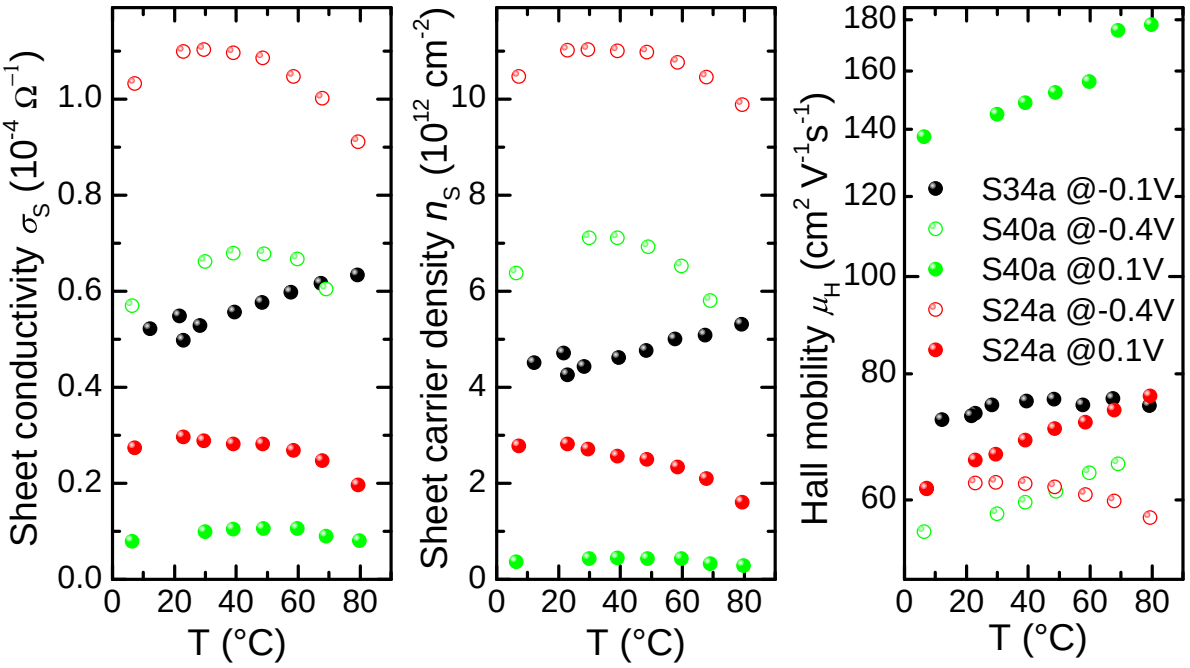

Figure 3.28: *Temperature dependent measurements of the sheet resistivity and the Hall effect for electronic (S34a, S40a) and optical (S24a) grade samples in different carrier concentration regimes (different gate voltages).*

mobility is solely based on the pH dependent change in carrier concentration. This is true for both the low and high carrier concentration regime investigated, where the mobility-carrier concentration curve of the pH-dependent measurements (see Figure 3.29 *right*: green and red curves respectively) follows that of the gate potential-dependent measurements of the same sample shown for comparison (see Figure 3.29 *right*: black curve). Two conclusions can be drawn from these results: Firstly, the proposed mechanism of the pH dependence as a change in surface charge, which is equivalent to an effective change in the gate potential, is supported. The carrier concentration increases with the pH, just as a change in the gate potential towards more negative values would. Secondly, the pH dependent change in surface charge seems to have no influence on the scattering mechanism limiting the hole mobility in the diamond. Independently of the pH value, and thus the surface charge, the mobility for a given carrier concentration stays the same.

The composition of the standard electrolyte was changed to look for any ion specific effects on the electronic transport or ion adsorption. For this, a trivalent cation, lanthanum La^{3+}, was used to replace the monovalent sodium or potassium ions. Ini-

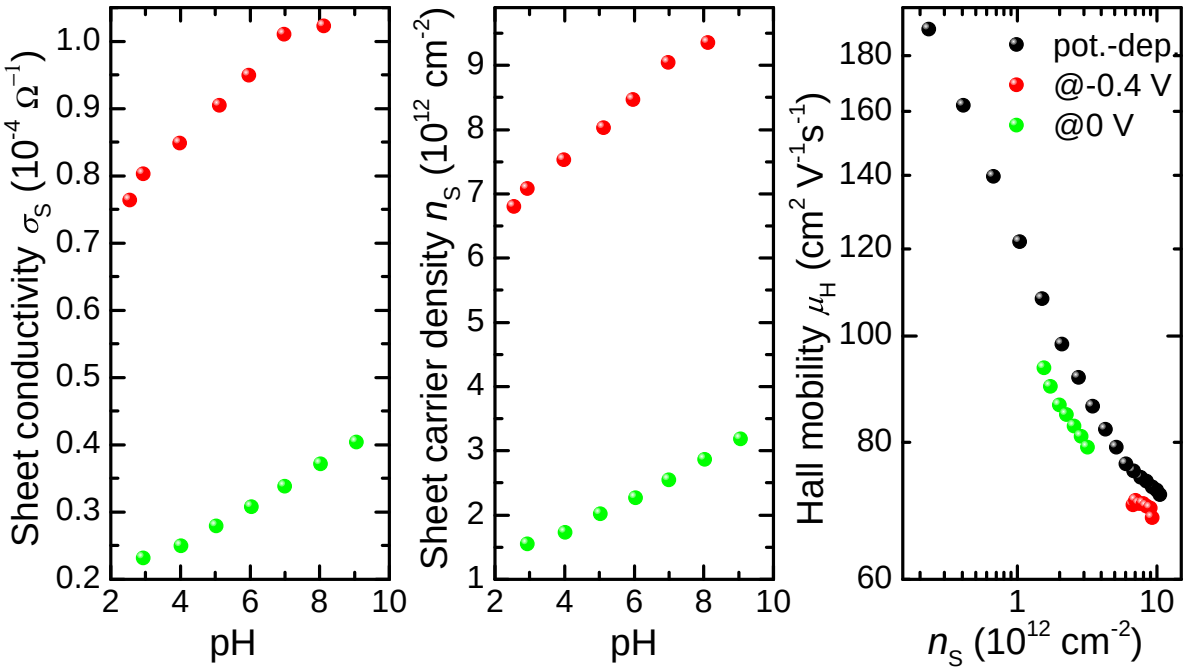

Figure 3.29: *pH-dependent measurements of the sheet resistivity, sheet carrier density, and Hall mobility at two different carrier concentration regimes (different gate potentials). The Hall mobility is shown as a function of the sheet carrier density for both gate potentials and compared to a potential dependent measurement of the same sample at pH 7 (black curve).*

tially, the ionic strength was doubled from 50 to 100 mM, followed by a replacement of the monovalent potassium cation with the trivalent lanthanum cation at equal ionic strength. The resulting effects on the charge accumulation and transport are presented in Figure 3.30. The increase of the ionic strength, as well as the increase of the cation valency both result in a negative shift of the threshold voltage towards an open channel visible both in the conductivity and carrier concentration graph (Figure 3.30). This can be explained with the Grahame equation [Har07].
To preserve charge neutrality, the sum of the charge in the diamond n_s, the charge at the diamond surface q_{surf}, and the diffuse counter charge in the electrolyte q_{dif}, must be zero: $n + q_{surf} + q_{dif} = 0$. The Grahame equation links the diffuse charge to the diffuse potential φ_{dif} [Har07]:

$$q_{dif} = -n_s - q_{surf} = \sqrt{2\epsilon_0 \epsilon RT} \left(\sum_i c_i exp \frac{-z_i F \varphi_{dif}}{RT} \right)^{1/2}, \tag{3.17}$$

where ϵ is the dielectric constant of the electrolyte and c_i is the concentration and z_i the valency of the ion species i. The Grahame equation describes the screening

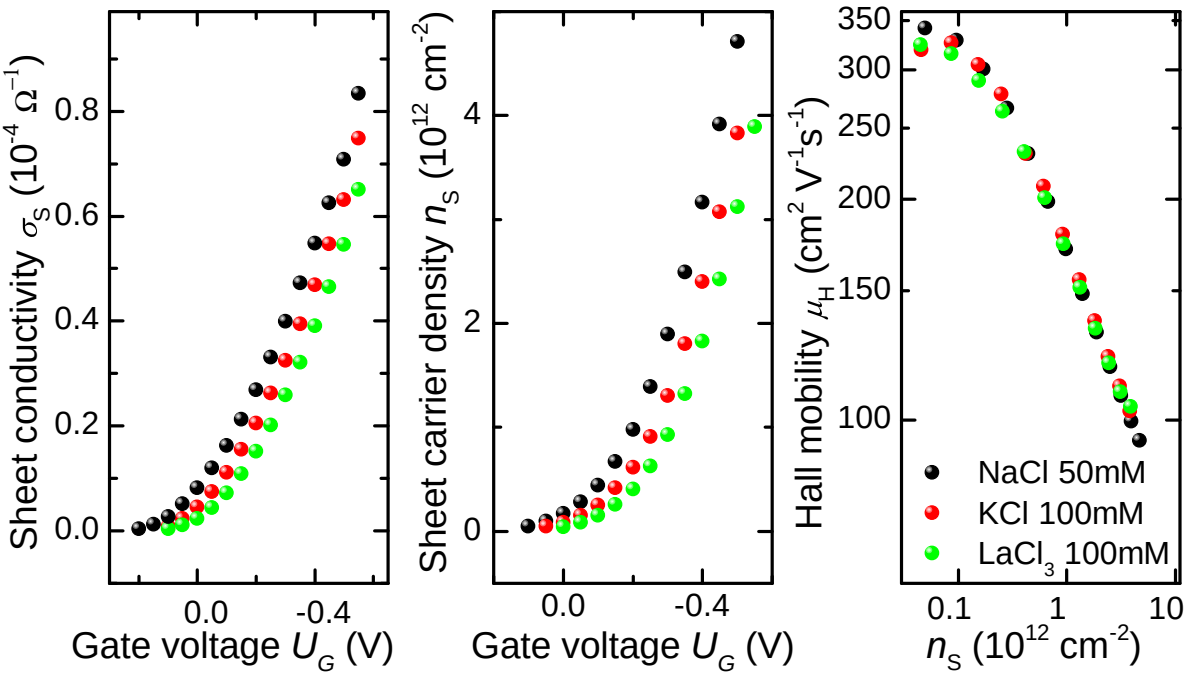

Figure 3.30: *Ion sensitivity measurements of the sheet resistivity, sheet carrier density, and Hall mobility for two different ionic strengths (50 and 100 mM) and two different ion valencies (K^+ and La^{3+}).*

effect from the electrolyte ions according to their concentration and valency. For the situation at pH 7, a negative surface charge has been deduced [Har07]. The increase in the ionic strength $I = \sum_i c_i z_i^2$ will therefore increase the diffuse charge, and thus screen the surface charge more effectively. As a result, the charge in the diamond hole channel decreases. This explains the observed shift in the threshold voltage for increasing ionic strength. The shift in the threshold voltage for the exchange of the cation is more complex. The exponential term in the Grahame Equation 3.17 is decreased, when increasing the (positive) valency. However, at the same time, the concentration of the anion is increased as well, and therefore it is not apparent whether the sum term in the Grahame equation increases or decreases overall. This depends on the salt concentration range investigated. In the concentration range investigated in Figure 3.30 (100 mM), it has been shown, that an increase in the cation valency leads to an increased screening [Har07] of the negative surface charge. The negative surface charge contributes to the hole concentration to preserve charge neutrality, thus the increase of the cation valency and the corresponding increase in screening leads to a decrease in the hole concentration. This then explains the shift in the threshold voltage for the exchange of the cation. As seen in the mobility

graph of Figure 3.30, neither the increase of the ion concentration, nor the increase in valency of the electrolyte has any effect on the electronic transport in the surface-conductive channel.

In order to further investigate the potential influence of charge centers at the diamond surface on the surface conductivity, poly-L-lysine (PLL) was used as an adsorbant. Poly-L-lysine is a polymer of the amino acid lysine that carries a positive charge at pH 7, and has been shown to adsorb on diamond surface [Kuc03]. A concentration of 0.01 mg/ml poly-L-lysine was added to the electrolyte. Subsequently the concentration was increased by a factor of ten to 0.1 mg/ml. The Hall effect measurements before and after each step are shown in Figure 3.31. The initial poly-L-lysine (concentration of 0.01 mg/ml) added leads to a clear shift in the threshold voltage of the sheet conductivity and carrier density graphs. This shift of 40 mV is in the negative direction, towards an open channel, as the positive charge of the PLL decreases the hole concentration. The observed threshold voltage shift corresponds to a change in surface charge of 0.11 μC cm^{-2}. A further increase in the PLL concentration to 0.1 mg/ml has no noticeable effect, indicating that the lower PLL concentration was sufficient to cover the diamond surface with adsorbed PLL. Beyond the shift in the threshold voltage a decrease in the interfacial capacitance from 2.7 to 2.2 μF cm^{-2} can be observed. The opposite would be expected from changes of the dielectric constant in the vicinity of the diamond surface, as the PLL is adsorbed at the diamond surface and therefore occupies the hydrophobic gap. A change of the dielectric constant in the hydrophobic gap from 1 for the vacuum dielectric constant, to the higher value of a PLL layer, would increase the overall interfacial capacitance. However, the transport properties with the adsorbed PLL at the diamond surface correspond to those of the clean surface (see Figure 3.31 *right*), and are thus not affected by the additional PLL charge.

Partially oxidized surfaces

In order to artificially induce surface potential fluctuations to the diamond surface and detect potential effects on the electronic transport, diamond samples were partially oxidized with ozone, as described in Section 2.2.3. The electron affinity changes drastically between hydrogen-terminated and oxygen-terminated diamond (see Section 2.2) and, accordingly, a partial oxidation of hydrogen-terminated diamond should create big surface potential fluctuations and coexisting conducting and

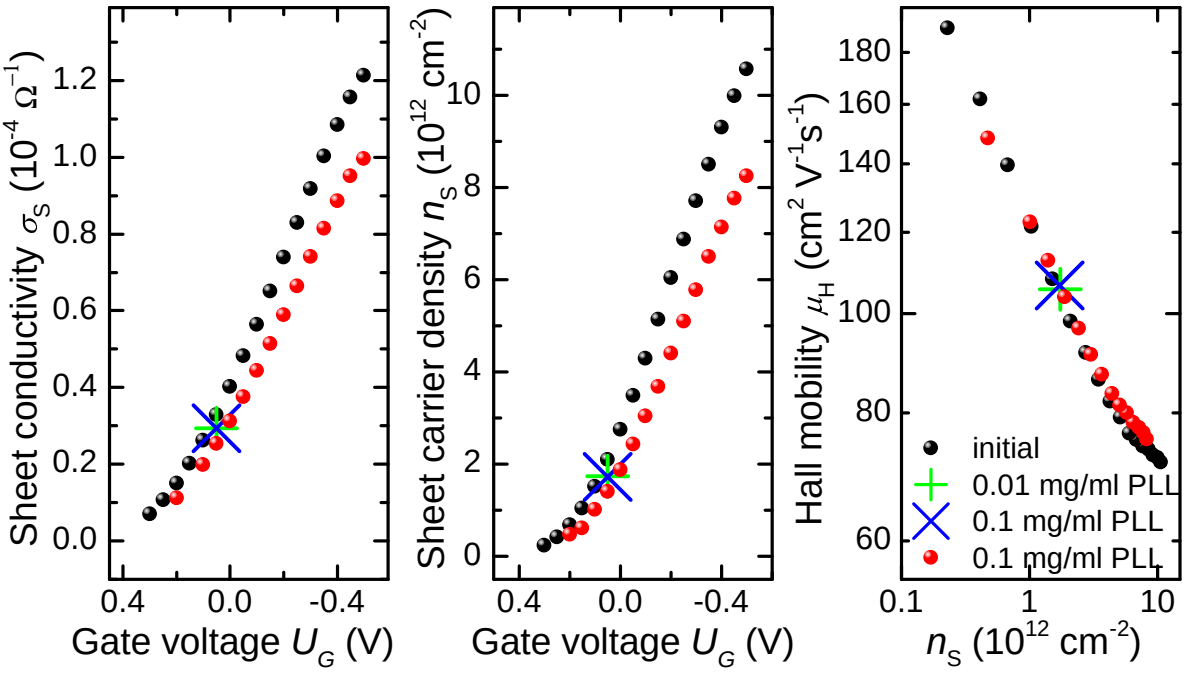

Figure 3.31: *Ion adsorption measurements of the sheet resistivity and the Hall effect for different concentrations of poly-L-lysine (PLL). Crosses indicate single data points taken directly after a concentration increase.*

non-conducting regions at small length scales.

The samples were oxidized in steps corresponding approximately to reductions in conductivity of about 10% to 20%. With a total of two to three steps the sample is thus still in a range representative of normal operation, that is in the linear range of the conductivity-gate potential dependence. A total of eight samples were investigated. All samples showed a shift in the threshold voltage toward an open channel. This is the expected behavior, as the partial oxidation should shift the band edges toward more positive values (see Section 3.1) and therefore shift the onset of charge accumulation and conduction. The behavior of the mobility is more complex. Some samples show a systematic decrease of mobility, some almost no effect on mobility, and some samples even show an initial increase of mobility. Categorizing the results according to either surface orientation or nitrogen impurity concentration does not lead to completely consistent results. However, those samples that do show a consistent decrease of mobility with each oxidation step also show a slight increase in the interfacial capacitance in addition to the shift in the threshold voltage (see e.g. Figure 3.32). Figure 3.33 shows a representative example of the second type of behavior observed. Here, the mobility exhibits an initial increase, which can

be either followed by a decrease (Figure 3.33), or a slight further increase, or no further effect on mobility. In this second type of sample no change in the interfacial capacitance can be observed.
The two (111) oriented samples measured, both show a systematic decrease of mobility with each consecutive oxidation step (first type of sample). One (100) oriented sample (S21, [Stü08]) also shows a decrease of mobility with each oxidation step, similar to the (111) oriented samples. Most of the (100) oriented samples show an unsystematic behavior for each individual sample, with the mobility increasing or showing no change with each consecutive oxidation step (second type of sample). A systematic difference between the (100) oriented electronic grade and optical grade or natural IIa samples could not be observed.
Beyond creating surface potential fluctuations by locally changing the electron affinity of the surface, the partial oxidation is also expected to introduce hydroxide groups at the surface. Such hydroxide groups are thought to be responsible for the pH sensitivity of the hydrogen-terminated diamond surface, as their charge is pH-dependent [Har07]. The surface charge thus introduced is negative at pH 7 and therefore increases the hole accumulation in the diamond. This surface charge and therefore the pH dependence does not continually increase with surface oxidation, but seems to reach a maximum [Här08]. Therefore, in principle, the partial oxidation of the hydrogen-terminated diamond surface can be expected to lead to both surface potential fluctuation based on the electron affinity and additional surface charge.
The experimentally observed change in the threshold voltage supports the model described in Section 3.1. While the experimental results are not completely systematic, the mobility in some samples (both (111) oriented samples and sample S21) seems to be limited by scattering mechanisms introduced or increased through partial oxidation. For this first type of samples it seems likely that this limitation does not start with the first oxidation effect, but is already limiting the mobility in the initial state.

3.3.2 Scattering mechanisms

An electric field accelerates the charge carriers and would do so infinitely, if these carriers would not experience scattering. The increase in current due to the electric field and the decay of that current due to scattering quickly reach a steady state situation reflected in the conductivity of the material. Any limit to the mobility is then only due to scattering, thus raising the question which mechanisms are responsible. There are a multitude of mechanisms resulting in the scattering of carriers

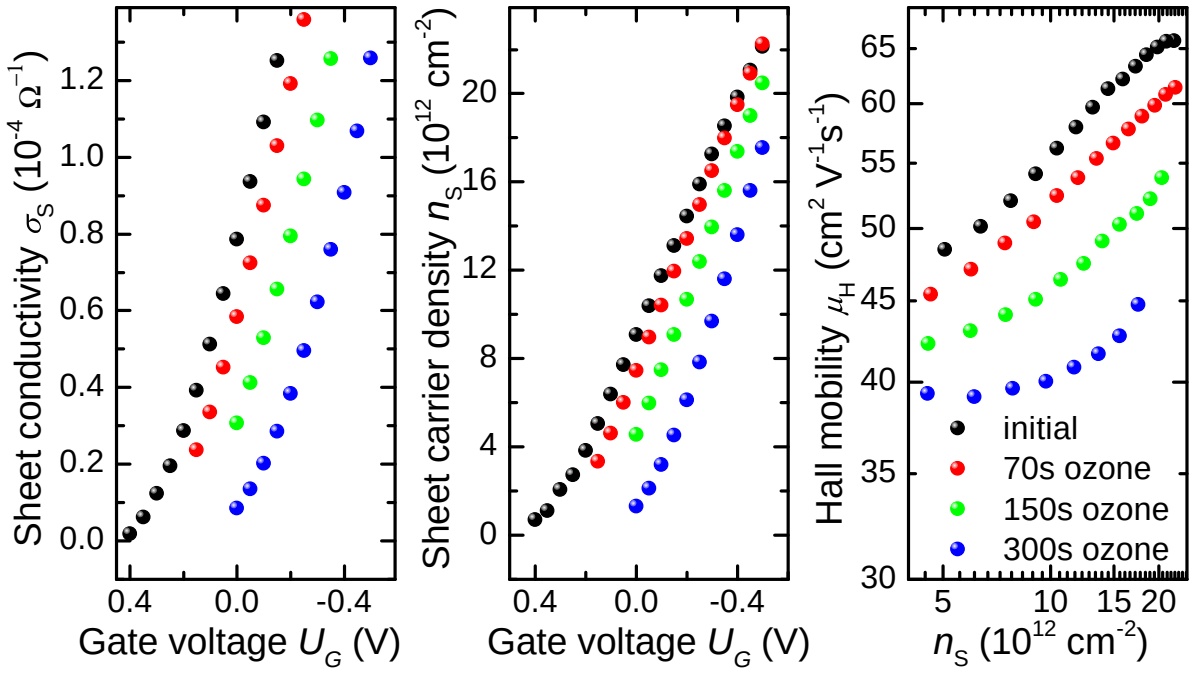

Figure 3.32: *Measurements of the sheet resistivity and the Hall effect of a (111) oriented, optical grade diamond sample (S26a 111 op) after consecutive partial oxidations of the hydrogen terminated diamond surface with ozone. The given oxidation times are the accumulated oxidation times.*

and usually more than one will be active in a given material. However, usually one mechanism will be mainly responsible for limiting the conductivity, dominating other mechanisms. As the mobility is dependent on the mean free time between scattering events,

$$\mu = \frac{e}{m}\tau \tag{3.18}$$

this is reflected in Mathiessen's rule [Böe02]:

$$\frac{1}{\tau} = \sum_i \frac{1}{\tau_i} \quad \text{leading to} \quad \frac{1}{\mu} = \sum_i \frac{1}{\mu_i} \tag{3.19}$$

So far the Hall mobility of the holes in the surface-conductive channel on hydrogen-terminated diamond has been only investigated in dry state (in vacuum or air) or with a metal gate, but not with an electrolyte gate. Beyond these contributions, we will also borrow from studies of the mobility in diamond not based on the surface conductivity but e.g. on doping with boron. Furthermore, many theoretical aspects of mobility in general and especially the mobilities of two-dimensional systems have been developed for silicon-based structures and especially the Si/SiO_2 system.

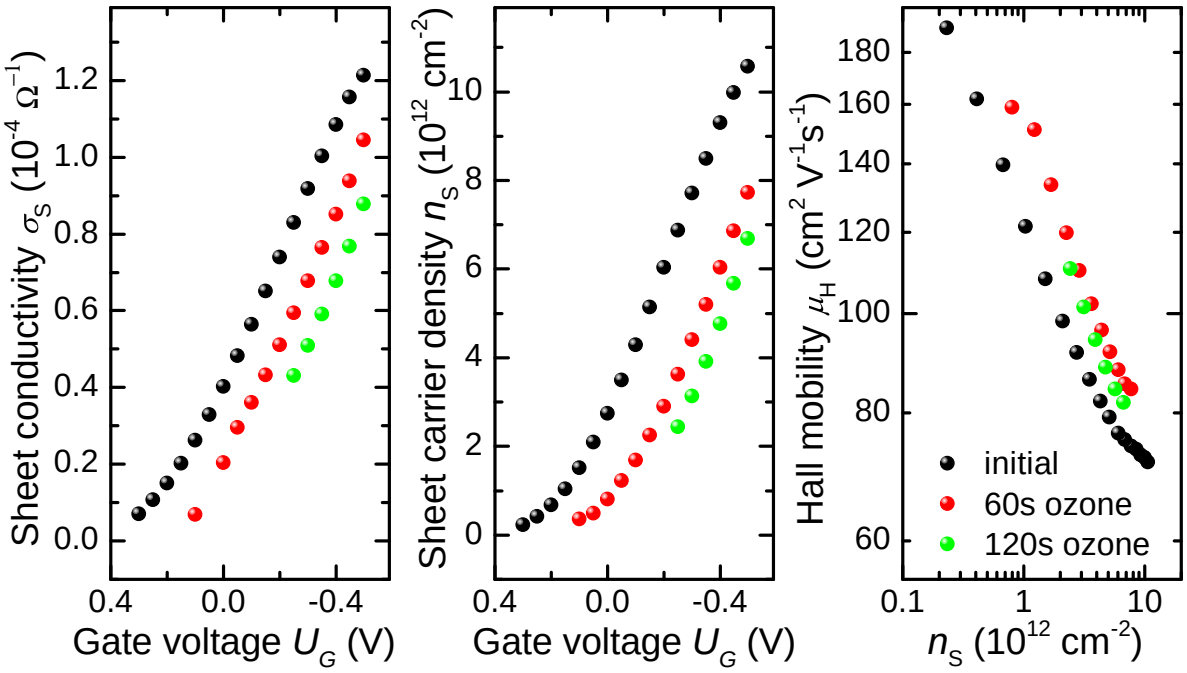

Figure 3.33: *Measurements of the sheet resistivity and the Hall effect of a (100) oriented, electronic grade diamond sample (S34a 100 el) after consecutive partial oxidations of the hydrogen terminated diamond surface with ozone. The given oxidation times are the accumulated oxidation times.*

In the following, we will discuss several scattering mechanisms to explain the transport in the quasi two-dimensional hole channel in diamond:
Acoustic phonon scattering is present in any conductor [Sho53] [Böe02]. With increasing temperature the number of lattice vibrations increase. At any given point in time this results locally in a slight increase or decrease of the lattice constant, which corresponds to a change in the band gap and thus the energy-band boundaries (see e.g. the "tight-binding method"). Consequently, these so-called deformation potentials influence the kinetic energy of a traveling electron wave and therefore give rise to reflections of the electron waves at these discontinuities. Calculations for two-dimensional charge accumulation as in the diamond surface conductivity yield the following proportionality for the mobility, in terms of sheet carrier density n_S and temperature T [And82, p.510] [Dav98, p.365]:

$$\mu \propto n_S^{-1/3} T^{-1} \tag{3.20}$$

This is in contrast to the more commonly used result for a three dimensional system, where the mobility is proportional to $T^{-3/2}$ and independent of the carrier density [Böe02]. Optical phonon scattering is not relevant for this work, as the Debye

temperature in diamond (2240 K) is far from the temperatures where diamond SGFETs can be operated, and the number of phonons decreases exponentially below approx. 30% of the Debye temperature (600K) [Isb09].

A second very common scattering mechanism arises from ionized impurities in the crystal [Sho53] [Böe02]. In a particle picture, the charge carriers are deflected by other charges within the conductor lattice. For the diamond SGFET we differentiate between three different sets of charges. First, there are the background ionized impurities within the diamond lattice. These are dominantly substitutional nitrogen impurities, which are ionized due to the band bending in the diamond SGFET. According to [Dav98, p.362] such a background impurity density $n^{3D}_{\mathrm{imp,i}}$ results in a mobility of:

$$\mu_{\mathrm{imp,i}} = \frac{e\tau_{\mathrm{imp,i}}}{m_{\mathrm{ds}}} \approx \frac{2\pi\hbar^3(2\pi n_S)^{3/2}}{m^2_{\mathrm{ds}} n^{3D}_{\mathrm{imp,i}}} \left(\frac{2\epsilon_0\epsilon_{\mathrm{sc}}}{e^2}\right)^2 \tag{3.21}$$

Hence, the mobility $\mu_{\mathrm{imp,i}}$ due to ionized impurity scattering centers varies with $n_S^{3/2}$. This is in contrast to the three dimensional case, where bulk ionized impurity scattering leads to a $T^{3/2}n^{-1}$ dependence [Böe02, p.118]. Secondly, the ions in the electrolyte form an idealized plane of charge, which compensates the hole charge in the diamond. Such a plane of charge at a distance d from the two-dimensional hole charge results in a scattering rate given by [Dav98, p.358]:

$$\frac{1}{\tau} = n_{charge}\frac{m_{\mathrm{ds}}}{2\pi\hbar^3 k_F^3}\left(\frac{e^2}{2\epsilon_0\epsilon_r}\right)^2 \int_0^{2k_F} \frac{e^{-2q|d|}}{(q+q_{\mathrm{TF}}G(q))^2}\left(\frac{b}{b+q}\right)^6 \frac{q^2\mathrm{d}q}{\sqrt{1-(q/2k_F)^2}} \tag{3.22}$$

$$\text{with}\quad G(q) = \frac{1}{8}\left[2\left(\frac{b}{b+q}\right)^3 + 3\left(\frac{b}{b+q}\right)^2 + 3\left(\frac{b}{b+q}\right)\right] \tag{3.23}$$

$$\text{and}\quad b = \left(\frac{33 m_{\mathrm{ds}} e^2 n_S}{8\hbar^2\epsilon_0\epsilon_r}\right)^{1/3}. \tag{3.24}$$

$q_{\mathrm{TF}} = \frac{m_{\mathrm{ds}}e^2}{2\pi\epsilon_0\epsilon_r\hbar^2}$ is the Thomas-Fermi wavenumber. $k_F = \sqrt{2\pi n_S}$ is the Fermi wavevector. The parameter b is part of a trial function used as a starting point to solve the coupled Schrödinger and Poisson equation discussed in Section 3.2.2 [Fan66] [Ste72] [Dav98, p.348]. For the scattering rate τ_{ion} for ions in the electrolyte, n_{charge} is given by the ion density $n^{2\mathrm{D}}_{\mathrm{ion}}$, $|d|$ is the distance of the ions from the interface, i.e. the separation of the Helmholtz plane, and in a first approximation, the dielectric constant ϵ_r amounts to the average between that of the semiconductor and that of the electrolyte $(\epsilon_{\mathrm{sc}} + \epsilon_{\mathrm{electrolyte}})/2$ [Fis93].

Thirdly, surface charges are believed to be present at the diamond surface, constituting a second plane of charges with a charge density $n^{2\mathrm{D}}_{\mathrm{int}}$. In this case, $n_{charge} = n^{2\mathrm{D}}_{\mathrm{int}}$,

$\epsilon_r \approx \epsilon_{\mathrm{sc}}$, and $d = 0$ for the calculation of the scattering rate τ_{int}. The difference with respect to the plane of charges formed by the electrolyte ions is not only a different distance from the hole channel but also that the amount of these charges remains constant, whereas the charges in the electrolyte vary with the charge density in the diamond (assuming a constant interface charge). With this modification, Equation 3.22 for the scattering rate can be applied. While, according to Equation 3.22, the exact dependence on the carrier concentration is complicated (see Figure 3.34 for the exact dependence), it can be approximated with a $n_S^{3/2}$ dependence given that the amount of impurity charges is fixed [Dav98, p. 359]. In both cases, with a fixed amount of impurity charge and with an amount of impurity charge dependent on the carrier concentration, the mobility is independent of temperature, according to Equation 3.22.

Dislocations are a frequent lattice defect in natural and CVD grown diamond [Fuj06]. In CVD grown diamond dislocation bundles are usually aligned with the direction of growth [Fri09]. Depending on the position of the Fermi level, these dislocations can introduce defect states that may become charged. These charges can then be screened by free carriers, thereby forming a cylinder along the dislocation with a radius equal to the Debye length. For the scattering at such a charged cylinder the mobility has been calculated to be proportional to the temperature and independent of the carrier density [Böe02, p.121]:

$$\mu \propto T \tag{3.25}$$

As the hole accumulation layer rests closely below the surface, surface roughness scattering needs to be considered as a limitation to electronic transport. The theory was originally developed for silicon inversion layers and yields a mobility proportional to the inverse squared of the carrier concentration [And82, p.505] [Böe02, p.360]:

$$\mu \propto n_S^{-2} \tag{3.26}$$

Scattering due to neutral lattice defects is one of the few mechanisms that results in a temperature and charge density independent scattering rate [Erg50]:

$$\mu_{\mathrm{imp,n}} = \frac{8\pi\epsilon_0 E_B}{20 n_{\mathrm{imp,n}}^{\mathrm{3D}} \hbar e} \tag{3.27}$$

where $n_{\mathrm{imp,n}}^{\mathrm{3D}}$ is the neutral impurity density, and E_B is the impurity ground state binding energy. The scattering rate has been calculated in analogy to the scattering of electrons by hydrogen atoms with a scattering cross section modeled with an equivalent Bohr radius for the impurity [Böe02, p.123]. Thus, a number of different

defects could potentially induce this scattering mechanism in diamond, such as vacancies, hydrogen atoms incorporated in the diamond lattice, point defects, or not ionized nitrogen related defects.

A more general mechanism leading to an increase of mobility with increasing carrier concentration was proposed by Arnold to explain data for certain samples in silicon inversion layers [Arn74] [Arn76] [And82, p.520]. According to this model, long-range potential fluctuations at the hydrogenated diamond surface lead to coexisting areas with the valence band below and areas with the valence band above the Fermi level. As there are no holes in the regions where the Fermi level E_F is above the valence band E_V, these regions are insulating. Conduction can then take place around the non-conducting regions, or with sufficient temperature activation over the non-conducting regions. Therefore the conductivity can be described as:

$$\sigma(E_F) = \begin{cases} \sigma_i(E_F) \approx \sigma_c(E_F) e^{\frac{E_V - E_F}{kT}} & \text{for } E_V < E_F \\ \sigma_c(E_F) & \text{for } E_V > E_F \end{cases} \tag{3.28}$$

where σ_i is the conductivity of the insulating regions, and $\sigma_c(E_F)$ is the average conductivity of the metallic regions. However, if the inhomogeneities are small with respect to the sample size, effective medium theory can be employed, to give an effective conductivity σ_s [Kir71] [Adk79]:

$$\sigma_s(E_F) = \frac{1}{2}(1-2p)(\sigma_c - \sigma_i) + \sqrt{\frac{1}{4}(1-2p)^2(\sigma_c - \sigma_i)^2 + \sigma_c \sigma_i}\ , \tag{3.29}$$

where p is the insulating fraction of the whole surface. If the conductivity of the conductive regions is much greater than that of the insulating regions, effective medium theory predicts the Hall mobility μ_H to be equal to the effective mobility μ_s:

$$\mu_H = \mu_s = \frac{\sigma_s(E_F)}{ne}. \tag{3.30}$$

The percolation mechanism therefore leads to a temperature activated conductivity and mobility, whereas the carrier concentration is not affected by the temperature. The activation energy decreases with increasing carrier concentration. As a consequence the conductivity and mobility increase with increasing carrier concentration at a given temperature [Arn76].

3.3.3 Discussion

The highest mobilities of surface conducting diamond are reached for electronic grade samples. In earlier reports on surface-conductive diamond, the highest mobilities

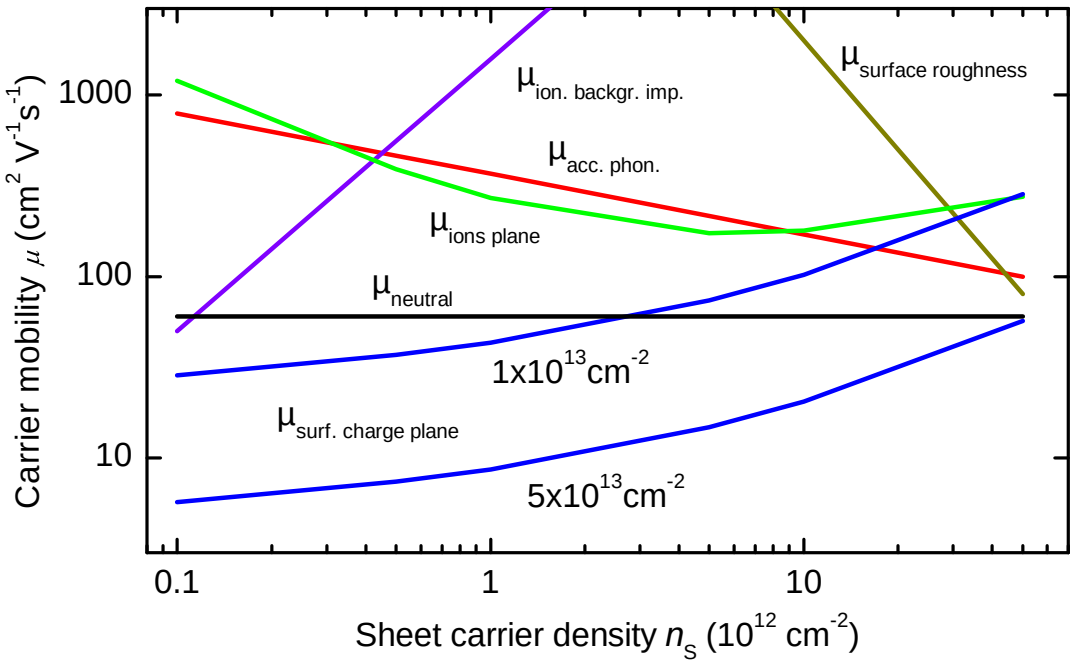

Figure 3.34: *Theoretical mobility dependences on the sheet carrier concentration for the different scattering mechanisms described in the text. Note that the dependences are given for a two-dimensional carrier accumulation and are different in the three-dimensional case.* $\mu_{surf.\ charge\ plane}$ *(blue) shows the dependence for ionized impurity scattering introduced by a plane of constant charge (1 and 5* $\times 10^{13}$ cm^{-2}*) at the diamond surface.* $\mu_{ions\ plane}$ *(green) illustrates the dependence for ionized impurity scattering induced by a plane of charge equal to the sheet carrier concentration at a distance of 0.75 nm from the surface, such as the electrolyte ionic charge compensating the holes in the diamond.* $\mu_{ion.\ backgr.\ imp.}$ *(purple) shows the dependence for ionized background impurity scattering, such as the charged nitrogen impurities in the diamond crystal.* $\mu_{acc.\ phon.}$ *(red) illustrates the dependence for acoustic phonon scattering.* $\mu_{surface\ roughness}$ *(dark yellow) shows the dependence for surface roughness scattering.* $\mu_{neutral}$ *(black) depicts a constant mobility, such as applicable for e.g. neutral lattice defects or dislocation scattering. The mobility dependence for the percolation model is not depicted, as it depends on temperature and details of the potential fluctuation profile.*

have usually been attributed to acoustic phonon scattering [Neb01] [Neb04] [Rez06] [Hir10] [Hir08b]. Though this has often been done without a clear dependence on temperature or carrier concentration.

The transport in boron doped samples has been studied more extensively and can be compared with some limitations to the surface-conductive transport in this work. Although the generation of carriers is achieved with a different mechanism, the holes in boron doped samples still have to travel through the same diamond lattice, and thus scattering induced by the diamond lattice can be compared. In order to properly compare these two systems, it is necessary to compare them at the same carrier concentration and in the same temperature range. In the surface-conductive channel the vast majority of carriers is located within a thickness of 1 nm. Taking this into account, sheet carrier densities between 1×10^{13} cm^{-2} and 5×10^{11} cm^{-2} correspond to volume densities of 1×10^{20} cm^{-3} to 5×10^{18} cm^{-3}, respectively. Studies showing a mobility dependence consistent with acoustic phonon scattering tend to have lower carrier concentrations [Hat99] [Ter06] at room temperature (of course the ionization of the boron donors is temperature activated), but can also reach into the carrier concentration regime [Tsu06] relevant for the surface-conductive channel. The absolute value of the mobility in these studies is higher (approx. 10^3 cm^2 V^{-1} s^{-1}) than that observed for the surface-conductive channel. However, since the mobility decreases with increasing carrier concentration, extrapolating this mobility dependence to carrier concentrations relevant for the surface-conductive channel leads to mobility values in the range to those experimentally observed [Isb09]. Some of this data, that has been attributed to acoustic phonon scattering shows a deviation from the theoretically predicted $T^{-3/2}$ dependence for the three dimensional case (e.g. [Ter06]).

In studies on the drift mobility of holes in diamond, acoustic phonon scattering has also been suggested to explain the mobility dependence on temperature around room temperature [Nav80] [Nes08]. Again, the mobility is higher than for the surface-conductive channel, most probably due to the much lower carrier concentration obtained in the time-of-flight experiments employed for these studies.

For two-dimensional conductive channels in general, the mobility is theoretically predicted to show a $\mu \propto n^{-1/3}T^{-1}$ dependence in case of acoustic phonon scattering (see Equation 3.20) [And82, p.510] [Dav98, p.365]. The line for $\mu \propto n^{-1/3}$ shown in Figure 3.26 corresponds well to the mobility dependence of the electronic grade

samples.

However, the temperature dependent mobility measurements (see Figure 3.28) show an increase of mobility with temperature especially at low carrier concentration and, thus, in the regime where acoustic phonon scattering should dominate. The increase for sample S40a at $U_G = -0.1$ V yields a temperature dependence of $\mu \propto T^{1.1}$ (see Figure 3.28), in clear contradiction to the predicted temperature dependence for acoustic phonon scattering. However, comparing the carrier concentration dependent mobility with literature data, the case for acoustic phonon scattering is strong and the temperature measurements need to be scrutinized. The temperature dependent measurements in electrolyte are statistically much less confirmed than the carrier concentration dependent ones. Systematic errors might lead to misleading results in the temperature dependent measurements in electrolyte as well. An increase in temperature for example, decreases the ordering of water molecules and could thus lead to an increase in the carrier concentration. Such changes would not affect the mobility directly, but result in a change of the dependence of carrier concentration and thus mobility on temperature. However, this should affect all samples equally and independently of the carrier concentration range, which is not the case, as some samples show a slight mobility decrease with temperature. Figure 3.35 supports this point by showing the temperature dependent mobility-carrier concentration data in comparison to the gate potential dependent data of the same samples. The mobility shows a steeper mobility dependence on the carrier concentration in the cases when the temperature was varied as opposed to the data acquired by a variation of the gate potential. This indicates that the mobility is affected independently of the carrier concentration by the temperature variation. Overall, the temperature dependent data contradicts acoustic phonon scattering, but is not conclusive. As the behavior of the interfacial water is not sufficiently understood, temperature based experiments based on non-aqueous and/or solid electrolytes might yield more useful results, as their temperature range is higher and their behavior with temperature less complex (see outlook in Chapter 7). Finally, it should be noted that the theoretical mobility values predicted for acoustic phonon scattering in the two dimensional case are about a factor ten higher than those experimentally observed. This has also been observed for measurements similar to ours at the interface between silicon and an acetonitrile based electrolyte [Tar85]. It was suggested that the approximations made fail at high carrier concentrations, and that the deformation potential for the phonon-scattering must be expanded one order higher [Ben90b]. This has a huge effect on the mobility values predicted, which are then up to a factor of ten lower

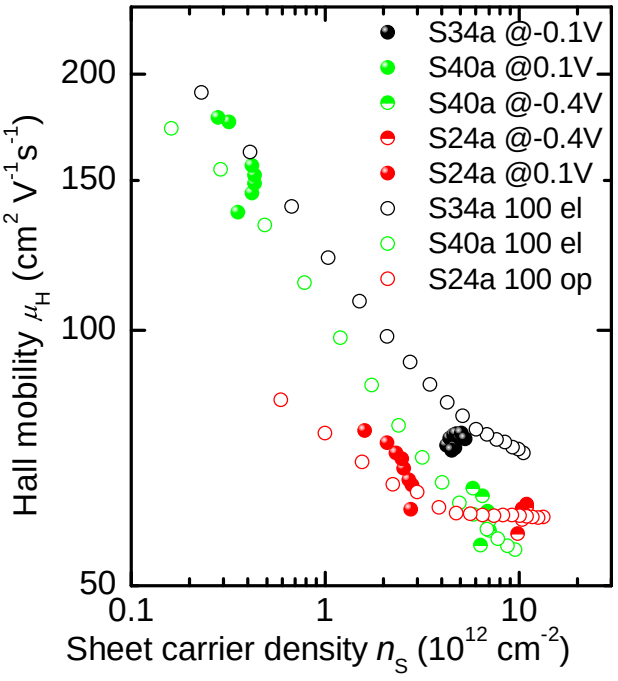

Figure 3.35: *Hall mobility as a function of sheet carrier density comparing data acquired by a variation of the gate potential (open symbols) with data acquired by a variation in temperature (solid and half-solid symbols) from Figure 3.28 for three samples.*

than formerly predicted [Ben90b].

Alternatively, the mobility dependence on carrier concentration observed for the electronic grade samples (Figure 3.26) could also be explained by ionized impurity scattering, in particular by considering the effect of the electrolyte ions. In a first approximation, the electrolyte ions form a charge plane some distance away from the surface-conductive channel. Neglecting the presence of any additional surface charge, the charge density from these ions corresponds to the charge density in the diamond, satisfying the charge neutrality condition. According to Equation 3.22 the combination of these remote ionized impurities results in a mobility dependence on the carrier concentration as shown in Figure 3.34. This mobility dependence is the result of two opposing trends: On the one hand, the scattering by the remote ionized impurities increases with increasing hole concentration. This dominates the behavior at low hole concentrations. On the other hand, the screening of the remote ionized impurities increases with an increasing hole concentration, dominating the behavior at higher hole concentrations. As opposed to the bulk ionized impurity [Böe02], the scattering from remote ionized impurities does not lead to any temperature de-

pendence. A different analysis [Shi76], however, building on work by [Ste67] does produce a temperature dependence predicting an increase of mobility with temperature [Böe02, p.360]. In this respect, the mobility dependence predicted by remote ionized scattering fits the experimental data better than that by acoustic phonon scattering. Furthermore, some of the electronic grade samples show a saturation of the mobility decrease with carrier concentration at high carrier concentrations. This can not be explained with acoustic phonon scattering, but could be indicative of the screening of remote ionized impurities becoming dominant, as predicted by the theoretically calculated mobility dependence for this case (see Figure 3.34).

While both acoustic phonon scattering and ionized impurity scattering can reproduce the carrier concentration dependence, the temperature dependent measurements supports ionized impurity scattering as the mobility limiting mechanism. Additionally, the saturation of the mobility decrease at high carrier concentration favors remote ionized impurity scattering as an explanation. The literature for diamond generally favors acoustic phonon scattering, but the studies on the surface conducting diamond are very limited and no studies investigate the electrolyte gated surface conductivity. In this situation we conclude, that the overall data is more supportive of ionized impurity scattering.

The mobility for (100) oriented optical grade samples in Figure 3.26 shows almost no dependence on the hole concentration. One of the few scattering mechanism which shows such a dependence is scattering by neutral lattice defects. Scattering by neutral impurities has been invoked to explain the behavior of some boron doped samples at room temperature [Isb09], however, it is generally deemed to be only relevant at very low temperature [Böe02] [See04]. The optical grade samples do contain a higher number of nitrogen impurities (ppm range) as opposed to the electronic grade samples, but as a result of the band bending these impurities are expected to be ionized. However, other neutral lattice effects such as point defects, hydrogen atoms incorporated during growth, or other not ionized nitrogen related defects might still be concentrated enough to dominate the scattering of optical grade (100) oriented samples. Especially in the absence of other explanations for the carrier concentration independent mobility, the prominence of such neutral lattice effects should be investigated. In order to explain the different mobility dependence between electronic grade and optical grade samples, such neutral lattice defects would have to be linked to the concentration of substitutional nitrogen impurities or to differences in the growth conditions.

Scattering at dislocations also yields a carrier density independent mobility, which is proportional to temperature (see Equation 3.25). The experimental data for example for sample S24a at $U_G = -0.4$ V for the high carrier concentration regime, where the mobility is constant with carrier concentration, does not show this temperature proportionality (see Figure 3.28). In CVD grown samples where the dislocations should predominantly be parallel to the growth direction [Fri09], one would expect a smaller effect for the (100) than the (111) surface orientation. The (111) oriented samples however do not show a carrier density independent mobility, although this could be masked by other scattering mechanisms. Finally the theory for dislocation scattering has not yet been adapted to the two-dimensional case, which might be necessary, as it effectively also involves scattering at the charges trapped at the dislocations. For an investigation of the relevance of dislocation scattering more information on the dislocation density in individual samples or sample groups need to obtained as well. One sample with a "low" dislocation density according to the supplier (Element Six Ltd.) showed no discernible difference in its transport properties, indicating that dislocations do not limit the mobility. However, the supplier did not provide any absolute or relative numbers as to the dislocation density.

The carrier density dependence of the mobility for (111) oriented samples is markedly different from that of the (100) oriented samples. Figure 3.27 shows an increase of the mobility with increasing carrier concentration for the (111) oriented samples. This trend is not equally strongly exhibited for all samples. A scattering mechanism that shows such as dependence is for example ionized impurity scattering, in this case with a constant density of ionized scatterers. Assuming a charge at the diamond surface of 9 μC cm^{-2} or 5 $\times 10^{13}$ cm^{-2}, the predicted mobility increase with increasing carrier concentration is similar to the experimental results (see Figure 3.27). Surface charges of such a value have been deduced from measurements of the ion sensitivity of hydrogen terminated diamond and the electrolyte screening [Har07]. However, this can not explain the differences in the dependence of the mobility on carrier concentration for the individual samples: different values for the surface charge will lead to a different range of mobility, but not to a more or less strong dependence on the carrier concentration. Furthermore, the studies that deduced the surface charge from the ion sensitivity did not differentiate between the surface orientation [Har07] [Dan08] [Hau08]. It is therefore not possible to confirm whether the (100) oriented surface shows a lower surface charge of e.g. 1 $\times 10^{13}$ cm^{-2}. This would be necessary to explain the higher mobilities for the (100) surfaces. Finally, we have

observed that a change in pH does not lead to a change in the mobility dependence (see Figure 3.29), although a change in pH changes the surface charge significantly [Har07]. Therefore, the data does not support impurity scattering resulting from the surface charge as a cause for the mobility dependence of the (111) oriented samples.

As discussed in Section 3.3.2, the percolation model of Arnold predicts an increase of mobility with carrier concentration [Arn76] [And82]. This model also predicts a temperature activated mobility as carriers are excited over the prohibited regions. Some of the (111) oriented samples indeed show a temperature activation of the mobility - e.g. sample S6d shows a $\mu \propto T^{1.5}$ dependence and a conductivity dependence in this range (see [Stü08, p.62]). Although this temperature dependence does not quantitatively match the one predicted by Arnold (see Equations 3.30 and 3.29). For the percolation mechanism to lead to an increase of mobility with carrier concentration, one has to assume large potential fluctuations, as the potential range over which the carrier concentration is changed in the diamond samples is in the range of several 100 meV. In such a case, however, the predicted temperature dependence should be marginal compared to the effect when the carrier concentration is controlled with the gate bias. In the temperature range available for investigation in electrolyte (7-80 °C), the change in kT is equal to 6.4 meV, which is orders of magnitude smaller than the potential change induced with the gate bias. Therefore, the basic theory should still be valid with a negligible temperature dependence. A non-perfect hydrogen termination, as well as surface damage induced for instance by surface polishing could all give rise to the surface potential fluctuations that are required in the percolation theory of Arnold. Different surface potential fluctuations could explain the experimentally observed difference in mobility dependence between the (100) and the (111) surface orientation. In case for an imperfect hydrogen-termination this seems unlikely, as one would expect a corresponding systematic difference in threshold voltage, which is not observed in (111) versus (100) samples. However, the partial oxidation with ozone leads to a distinct behavior of the (111) oriented samples, whose mobility systematically decreases with each oxidation step (see Figure 3.32). This indicates, that the mobility of the (111) oriented samples might indeed be limited by surface potential fluctuations. Surface damage could well be dependent on the surface orientation, e.g. in the form of higher surface roughness. Atomic force microscopy measurements have not revealed any difference in the surface roughness between (111) and (100) samples, but the resolution of this technique only allows to investigate effects on a scale of several nanometers. In conclusion, the percolation model based on surface potential fluctuations is not contradicted by the

experimental data, and can explain the increase of mobility with carrier concentration. However, further experimental evidence would be necessary to verify that this mechanism is indeed responsible for the mobility dependence of the (111) oriented samples.

Other scattering mechanisms could in principle be applicable to the transport in surface-conductive diamond.
Scattering from ionized background impurities, such as nitrogen, is certainly contributing to the hole transport, but should not be the dominant scattering mechanism considering its predicted mobility dependence and range. As a result of band bending, all substitutional nitrogen impurities should be ionized in the vicinity of the surface, where the conducting holes are confined, resulting in a maximum concentration of 5 ppm for optical grade samples. To investigate the influence of ionized impurity scattering, one sample of Ib grade with a very high nitrogen impurity concentration of 200 ppm was investigated. The mobility of this sample is significantly lowered with a maximum of about 10 $cm^2\ V^{-1}\ s^{-1}$ (see sample S39b 100 in Figure 3.25). While the scattering of the data is too high to derive any clear mobility dependence, this dramatically lowered mobility should be a result of ionized background impurity scattering.

Considering that the conductive channel rests only about a nanometer beneath the surface, surface roughness scattering needs to be considered. A surface roughness scattering limited mobility is predicted to depend on the carrier concentration following $\mu \propto n_s^{-2}$ [Böe02], a dependence which is not observed for the samples investigated in this work. However, surface roughness scattering is often invoked to explain the limitation of mobilities at high carrier concentrations [Hir10] [Hir08b]. The surface roughness of the samples investigated was studied with atomic force microscopy measurements. Two categories can be distinguished, polished samples with polishing lines and a rms roughness of 0.2 to 0.8 nm, and so called super-polished samples that show a rms roughness of 0.1 nm and no polishing lines. The polishing has been provided by the "Element Six Ltd." and "Diamond Detectors Ltd." (for the super-polished samples) and both companies do not reveal their polishing methods in detail. However, it can be assumed that the polishing lines result from purely mechanical surface treatment, leading to subsurface damage, while the super-polished samples might involve additional dry etching with an inductively coupled Ar/Cl plasma, removing this subsurface damage [Fri09]. Electronic grade samples with

both polishing methods have been investigated and no difference in their mobility dependence could be observed. S33b and S32b are normal polished electronic grade samples, while S34b/S34a, S35b, S40a, and S41a are super-polished electronic grade samples (see Figures 3.26 for the mobility dependence and 3.24 for representative AFM images, respectively). Additionally, differences in conductivity parallel and perpendicular to the polishing lines have been investigated at carrier concentrations of around 1 $\times 10^{13}$ cm^{-2} in a greek cross configuration. However, the anisotropy in conductivity was less than 5% even when taking out measurements which showed a larger difference in both directions, which can be attributed to differences in the contact resistance. In van der Pauw Hall effect measurements any anisotropy in mobility would not prevent a quantitatively correct result for a homogeneous carrier concentration [Bie04] [Bie08]. The measured resistivity would correspond to the average resistivity. Hall measurements would therefore not reveal any difference in mobility. While surface roughness scattering due to the polishing lines of the sample surfaces can be excluded, surface roughness on a smaller scale (1 nm) could still become the limiting scattering mechanism at very high carrier concentration. To properly investigate this, much higher carrier concentrations need to be reached at which surface roughness scattering is expected to dominate. This could be done, for example, by employing non-aqueous electrolytes as gates (see outlook in Chapter 7).

In conclusion, the surface orientation and the nitrogen impurity concentration both influence the electronic transport in the hole accumulation layer at the diamond/ electrolyte interface. The mobility as a function of the sheet carrier concentration shows three distinct characteristics, depending on the sample category:

- (100) oriented, electronic grade samples show a decrease of the mobility with increasing carrier concentration, exhibiting a $n_s^{1/3}$ dependence. Either acoustic phonon scattering or remote ionized impurity scattering from the electrolyte ions could explain such a dependence. The experimental data, notably the temperature dependent measurements, is more supportive of remote ionized impurity scattering, although it is far from conclusive. Additional measurements with a greater temperature range seem best suited to test the different scattering mechanisms.

- (100) oriented, optical grade samples show a largely constant mobility with carrier concentration. Scattering by neutral lattice defects or dislocations shows such a dependence. There are a number of potential sources of neutral lattice

effects, e.g. neutral nitrogen impurity-related defects, hydrogen incorporated in the diamond lattice, or vacancies. However, the concentration of these scattering sources in optical grade samples has yet to be shown to be sufficient for the mobility ranges observed and much smaller in electronic grade samples. Alternatively, dislocation scattering should be tested, employing samples of different surface orientations, whose dislocation density has been determined.

- (111) oriented, optical grade samples show an increase of the mobility with increasing carrier concentration, whereby the rate depends on the individual sample. A model based on a percolation mechanism is best suited to explain the currently available data, though it is not conclusive. The percolation model is based on the assumption of surface potential fluctuations. In order to be consistent with the data, these fluctuations have to be more prevalent or pronounced on the (111) oriented surface, as opposed to the (100) oriented surface. The data from partially oxidized samples supports the model in that respect. A more controlled surface chemistry and surface morphology ("super polishing") of the (111) oriented samples would be required to confirm this model.

The variations in the electrolyte composition, such as pH, ionic strength and valency, and ion adsorption, left the mobility behavior largely undisturbed. This is noteworthy, as the electrolyte gate is in direct contact with the diamond surface in the SGFET configuration. We conclude that the mobility is therefore determined by the quality of the diamond crystal and its surface.

Chapter 4

Applications of solution-gated field effect transistors

This chapter presents several applications of the SGFET principle. Initially, the pH sensitivity of the diamond SGFET transistor will be introduced as a basic application and an illustration of the SGFET concept [Dan08]. This concept is then transfered to non-aqueous electrolytes in the second section [Dan12]. Finally, the diamond is replaced by an alternative carbon based material, the much-hyped graphene, to form graphene based SGFETs [Dan10].

4.1 The pH sensitivity of diamond SGFETs

The pH sensitivity of diamond SGFETs has been studied by several groups [Gar05, Son06, Neb06, Rez07]. However, there had been no agreement about the value or even the sign of the pH sensitivity of the surface conductivity of hydrogen-terminated diamond. Initially, Kawarada et al. have reported that hydrogen-terminated diamond surfaces are not pH sensitive [Kaw01]. Later on, it was shown that the introduction of certain groups at the surface of hydrogen-terminated diamond resulted in a pH sensitivity, and that a decrease of the pH resulted in a decrease of the surface conductivity [Gar05] [Son06]. Several models have been suggested to account for this pH sensitivity. These reports initiated some controversy, as the sign of the reported pH sensitivity was opposite to the prediction of the transfer doping model [Mai00] [Zha08]. The confusion further increased with several publications reporting that the surface conductivity increased with decreasing pH [Neb06] [Rez07]. Therefore, differences in the experimental conditions were expected as the origin of the discrepancy. As a matter of fact, while the Nebel group reported the use of a Pt wire as

a reference electrode (RE), others have used Ag/AgCl reference electrodes. As will be shown below, the choice of the reference electrode, Pt or Ag/AgCl, determines the pH sensitivity of the system.

To demonstrate this effect, the pH sensitivity of diamond SGFETs has been investigated with a Pt wire and a Ag/AgCl reference electrode. The diamond SGFETs were operated in a three-electrode electrochemical cell controlled by a potentiostat. The electrolyte used was a 10 mM phosphate buffer solution with the ionic strength adjusted to 100 mM with NaCl. The devices were operated in a transistor configuration in which the electrolyte acts as the gate (see Section 3.1). The sensitivity of the surface conductivity to the pH of the solution was measured in the following way: the device was biased with a constant drain-source voltage of -100 mV. A constant gate-source voltage of -500 mV vs. Ag/AgCl or 0 mV vs. the Pt RE was applied with the potentiostat, while the drain source current was monitored versus time. The difference in the gate bias for both electrodes stems from the different electrode potential of Pt and Ag/AgCl; thus, the gate voltage has been selected to have the same drain-source current in both configurations. Small aliquots of HCl or KOH were added in order to modify the pH of the electrolyte, and the effect on the drain-source current was recorded. Figure 4.1 shows the effect of changing the pH on the drain-source current in the case of using a Ag/AgCl RE or a Pt RE. When the Ag/AgCl RE is used, a decrease of the pH results in a current decrease; the opposite is observed if a Pt wire is used as a reference electrode. In addition to the different sign of the pH sensitivity, the value of the sensitivity differs in both cases (higher sensitivity for the Pt RE). A more detailed evaluation of the pH sensitivity, is summarized in Figure 4.2, in which the pH was varied between pH 4 and 8, and the gate voltage required to offset the effect of pH and keep a constant drain-source current was calculated with respect to the Ag/AgCl RE or the Pt electrode. In the case of the Ag/AgCl RE, the pH sensitivity is about +15 mV/pH, whereas when using the Pt RE the sensitivity is about -56 mV/pH. These values are in very good agreement with previous results (about +15 mV/pH measured with Ag/AgCl RE in [Gar05] [Son06] versus -56 mV/pH with Pt RE in [Neb06] [Rez07]. The apparent contradiction of pH sensitivities observed in Figure 4.1 and Figure 4.2 can be resolved if the pH dependence of the Pt electrode potential is considered. While the potential of a Ag/AgCl RE with respect to the vacuum level is independent of the solution pH, Pt electrodes are well known to have a pH dependent electrode potential [Ive61] [Che83]. This is illustrated in Figure 4.3, which shows the variation of the open circuit potential (U_{OCP}) of Pt with respect to the Ag/AgCl RE. The U_{OCP}

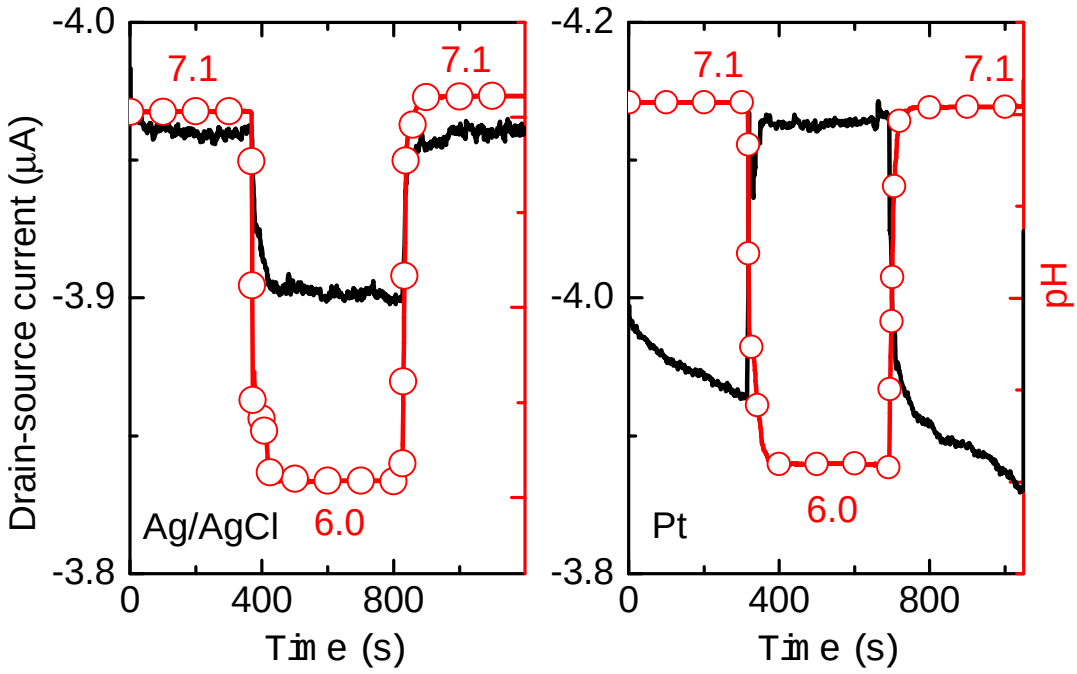

Figure 4.1: *Effect of pH on the surface conductivity of hydrogen-terminated diamond when either a Ag/AgCl reference electrode (left), or a Pt wire reference electrode (right), is used to control the applied gate voltage.*

is the potential difference between two electrodes measured with a high-impedance voltmeter. For increasing pH, the U_{OCP} of the Pt RE decreases, with a variation of about -50 mV/pH. This pH dependence of the Pt electrode potential follows from the catalysis of the oxidation/reduction of H_2 to H^+ and vice versa by the Pt. The reaction can therefore reach thermodynamic equilibrium, using the Pt electrode as a sink or source of electrons, thereby determining its potential. The potential value adjusts itself according to Nernst' equation for the redox potential in equilibrium:

$$U = U_0 + \frac{RT}{F} \ln \frac{[a(H_3O^+)]}{\sqrt{p_{H_2}}} \tag{4.1}$$

Where R and F are the gas and Faraday constant respectively and U_0 is the potential for standard conditions. p_{H_2} is the partial pressure of hydrogen dissolved in the electrolyte, which is usually constant. $a(H_3O^+)$ is the activity of the hydronium ion determined by pH. The expected sensitivity to pH of the Pt electrode according to the Nernst equation is -59 mV/pH. However, the Pt electrode can be poisoned and its potential can be further influenced by e.g. adsorption of ions, leading to a deviation from the expected value of the sensitivity [Ye92]. After recognizing the influence of pH on the potential of the Pt RE, the apparently contradictory results

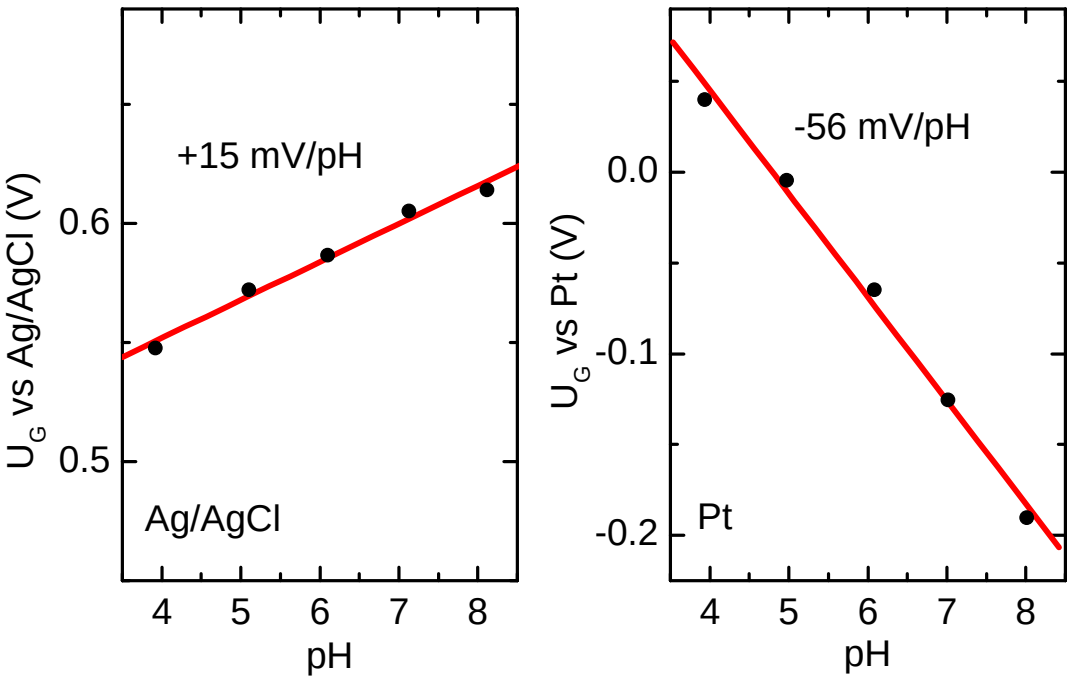

Figure 4.2: *Evaluation of the pH sensitivity as equivalent changes in gate voltage, using a Ag/AgCl reference electrode (left), and a Pt wire as reference electrode (right).*

published in the literature can be reconciled using the diagram in Figure 4.3, where the positions of the conduction and valence band of a hydrogen-terminated diamond surface are shown with respect to the vacuum level. A negative electron affinity of about 1.0 V is assumed for the surface in contact with water. The position of the Ag/AgCl RE potential is fixed at about 4.7 eV below the vacuum level [Ive61], and is independent of pH. On the other hand, the potential of the Pt RE depends on the pH, as discussed above. The values of the Pt electrode potential at pH 2 and pH 10 are represented in Figure 4.3.

It is evident that the potential variation of Pt with pH must be considered for a correct interpretation of the pH sensitivity results. For instance, if one assumes that the diamond surface is not pH sensitive, and a Pt wire is used as a reference electrode, a pH decrease will result in a lower position of the Pt electrode potential with respect to the vacuum reference. This will induce an increase of the surface conductivity as the Fermi level is driven further below the valence band maximum (Figure 4.3). Thus, neglecting the effect of pH on the Pt reference will result in an incorrect estimation of the pH sensitivity of the diamond surface, of about -59 mV/pH. For a correct evaluation of the pH sensitivity of the hydrogen-terminated

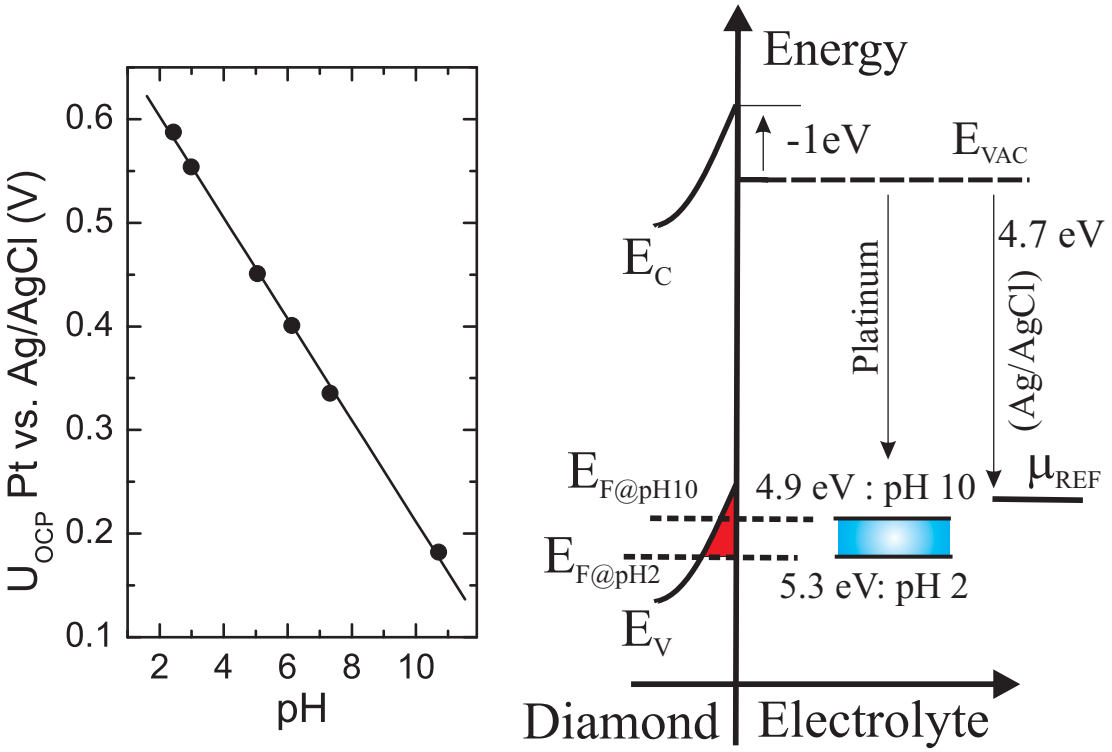

Figure 4.3: *left: Influence of pH on the open circuit potential (U_{OCP}) of the Pt wire with respect to the Ag/AgCl reference electrode. right: Band diagram showing the positions of conduction and valence band of diamond, as well as the position of the electrode potentials of Ag/AgCl and Pt for two different pH values.*

diamond surface when a Pt reference electrode is used in the experimental setup, the measured pH sensitivity must be calculated as,

$$S_{pH}^{surf} = S_{pH}^{meas} - S_{pH}^{ref} \ , \tag{4.2}$$

where the three terms correspond to the real pH sensitivity of the surface S_{pH}^{surf}, the measured pH sensitivity S_{pH}^{meas}, and the pH sensitivity of the reference electrode S_{pH}^{ref}. Thus, the pH sensitivity calculated from Figure 4.2 (*right*), -56 mV/pH must be corrected by the pH sensitivity of the Pt electrode. Ideally, this sensitivity would be -59 mV/pH, although we have measured a slightly smaller value, -50 mV/pH (Figure 4.3). Therefore, the real sensitivity of the hydrogen-terminated diamond surface would be around +5 mV/pH. We attribute the disagreement with the +15 mV/pH estimated in Figure 4.2 to the drift of the drain source current observed when a Pt reference electrode was used (see Figure 4.1 *right*).

In summary, it has been demonstrated, that the discrepancy of the pH sensitivities of the surface conductivity of hydrogen-terminated diamond, is a result of the

pH sensitivity of the Pt wire used as reference electrode in some studies [Neb06] [Rez07]. A correct account of the effect of pH on the potential of the Pt wire reference electrode resolves the associated controversy. Thus, we conclude that, in agreement with previous reports [Kaw01] [Gar05] [Son06], the pH sensitivity of the H-terminated diamond surface conductivity does not follow the prediction of the transfer doping model, as has been suggested [Neb06] [Rez07]. Instead, we confirm that hydrogen-terminated diamond surfaces, if ideally perfectly hydrogenated, show a very weak pH sensitivity.

Two explanations have been suggested to explain the origin of this pH sensitivity. Both mechanisms lead to a pH-dependent change in the surface charge, and thus an effective change in the gate potential which corresponds to the observed pH sensitivity as the preceding discussion has shown. On the one hand, a pH-dependent change of the charge state of surface groups such as hydroxyl groups has been suggested [Son06, Här08] - a mechanism referred to as the site binding model [Yat74]. Obviously, this explanation requires an imperfect hydrogenation and, indeed, an increase of the pH sensitivity has been observed with a partial oxidation of the surface [Gar05]. On the other hand, a pH-dependent, preferential adsorption of OH^- groups on hydrophobic surfaces such as hydrogen-terminated diamond was proposed to explain the pH sensitivity [Har07]. This second explanation could explain a pH sensitivity even when assuming a perfectly hydrogen-terminated surface. However, so far, neither explanation could be experimentally verified and it is unclear if either one or both of these mechanisms are responsible for the pH sensitivity of hydrogen-terminated diamond surfaces.

4.2 Solid polyelectrolyte-gated surface conductive diamond field effect transistors

Surface-conductive diamond field effect transistors can be gated with aqueous electrolytes, as required for applications in bioelectronics and biosensing [Ber03, Kaw01]. Generally, gating with electrolytes, where the gate charge is ionic as opposed to electronic, has great potential for achieving high carrier concentrations at low gate voltages [Pan05, Lu10]. In these devices, usually no insulating dielectric is necessary, and therefore the separation of charges in the electric double layer formed between the gate and the conductive channel is small, leading to a high interfacial capacitance [Yua09, Ye10, Uen11]. However, liquid electrolyte gates and the electrochemical setup necessary for their control are cumbersome or even prohibitive

for many applications. Solid polyelectrolytes can provide both the high capacitance that electrolytes inherently offer and the convenience of a solid gate. Recently, electric double layer transistors with and without solid gate have attracted considerable attention, mostly due to their ability to achieve high carrier accumulation (10^{13} carriers/cm^2) [Ono08] [Uen08] [Yua09] [Lu10] [Pan05] [But11]. Previously, metals have been used as solid gate materials for diamond transistors [Hir06]. However, the insulator required between the gate metal and the channel for carrier accumulation inherently reduces the interfacial capacitance.

Consequently, a solid electrolyte was used to fabricate a FET based on surface-conductive diamond [Dan12]. Polyethylene oxide (PEO) is employed as the gate material, leading to transistor characteristics that are comparable to those of diamond SGFETs with an aqueous gate. The standard diamond SGFETs were fabricated, including the passivation with SU8 and silicone glue (see Appendix A.5.1). Polyethylene oxide (100 000 M.W., Alfa Aesar) together with $LiClO_4$ (Sigma Aldrich) in a 16:1 ether oxygen : lithium ion ratio was dissolved in acetonitrile to form a 10 % (weight) solution and filtered through a 0.45 μm syringe filter. The solution was drop-casted onto the transistor gate area, dried in air for 1 hour and then in vacuum over night. Finally, the dried PEO layer was contacted with an evaporated gold layer (100 nm) used as gate electrode (see Figure 4.4 for a schematic of the device). The aqueous electrolyte-gated samples, whose data is compared with that of the polyelectrolyte-gated samples, are operated in a standard pH 7 phosphate-based buffer solution with an ionic strength of 0.1 M from KCl.

In principle, the fabricated polyelectrolyte-gated FETs behave similarly as the solution gate field effect transistors: the number of free carriers accumulated at the diamond surface is controlled by the potential drop across the diamond/polyelectrolyte interface. The potential drop in the hydrogen-terminated diamond determines the position of the Fermi level at the diamond surface, which can be adjusted beneath the valence band edge, thereby inducing the accumulation of positive charge carriers on the diamond side. In the polyelectrolyte, these charges are mirrored by a net surplus of ions of opposite (here negative) charge close to the interface. As opposed to an aqueous electrolyte, the mobile ions (here Li^+ and ClO_4^-) are incorporated in the solid polymeric structure (here PEO), which allows net charge accumulation of the ions, but still gives the polyelectrolyte the characteristics of a solid.

The PEO/diamond interface was characterized with cyclic voltammetry (CV) and electrochemical impedance spectroscopy (EIS) (see Figure 4.5). The CV experiments revealed that, within a gate voltage ranging between -0.2 and 0.4 V, the behavior

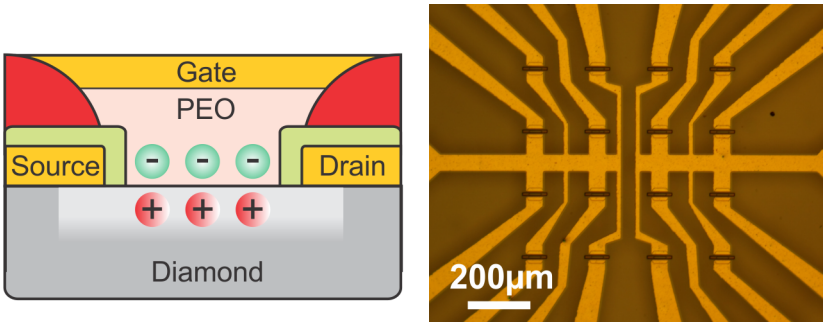

Figure 4.4: *left: Schematic layout of the PEO-gated surface-conductive diamond transistor. Drain and source contact are passivated with SU8 (light green) and silicone glue (red). The solid PEO (light pink) rests directly on the diamond surface and is contacted with the gate electrode. The conductivity of the p-type conductive channel in the diamond can be modulated by applying a gate voltage across the PEO/diamond interface. right: Image of a 4x4 transistor array with common source and individual drain contacts. The transistor dimensions are 20x40 μm^2.*

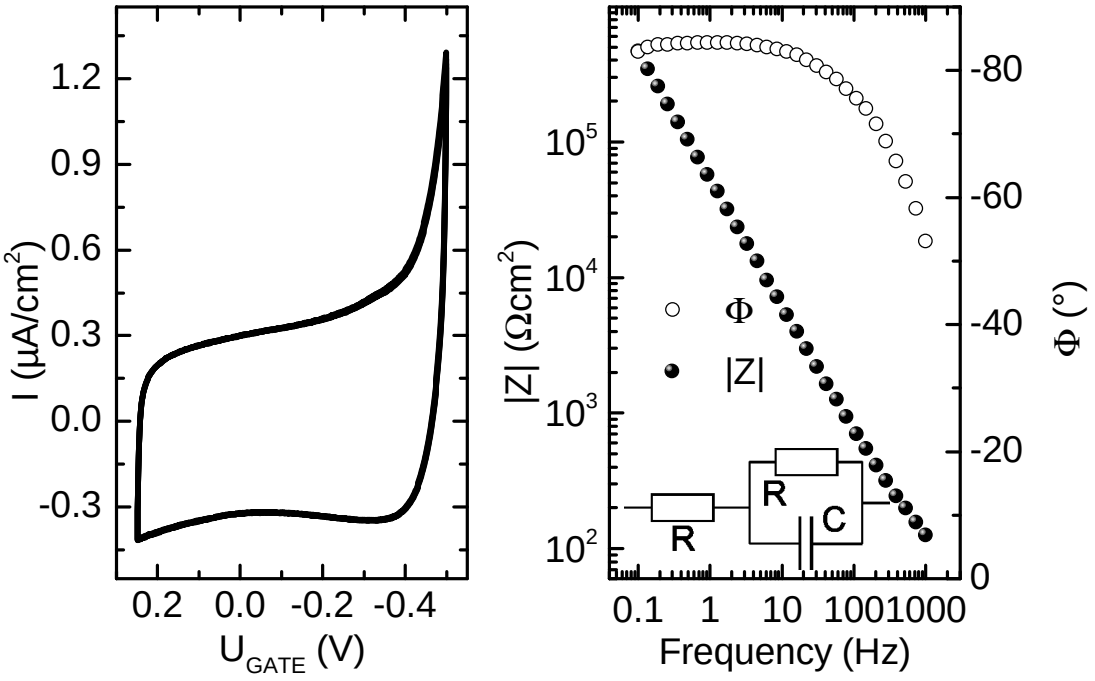

Figure 4.5: *left: Cyclic voltammetry of the diamond/PEO interface recorded at 10 mV/s. right: Phase Φ and absolute impedance value $|Z|$ of the diamond/PEO interface versus frequency taken at a gate voltage of 0.3 V. The equivalent circuit used to calculate the interfacial capacitance is shown as an inset.*

is almost exclusively capacitive with no faradaic components to the current. The reproducibility of the scans confirms the stability of the surface. Electrochemical

impedance spectroscopy has been used to probe the interface over a range of frequencies. The experimentally acquired data can be fitted with an R(CR) equivalent circuit (see Figure 4.5 inset; resistance and capacitance in parallel representing the interfacial charge transfer resistance and capacitance, respectively, and another resistance in series representing the electrolyte resistance). The resulting capacitance of 3 ± 1 μF/cm^2 is in agreement with the values derived from Hall effect measurements (see Figure 4.7). Furthermore, the phase stays close to -90° for frequencies up to about 100 Hz, indicating purely capacitive behavior without diffusive elements. This suggests that the charging of the interface is not limited by the mobility of the electrolyte ions in this frequency regime.

Field effect transistors (20x40 μm^2) were successfully fabricated (see optical micrograph in Figure 4.4) as described before. As seen in Figure 4.6, the p-type surface conductivity of the diamond can be modulated nicely with the PEO gate. The drain-source current can be varied over 4-5 orders of magnitude within a gate voltage range of 0.8 V to −0.5 V. Analyzing the transistor characteristics further, the

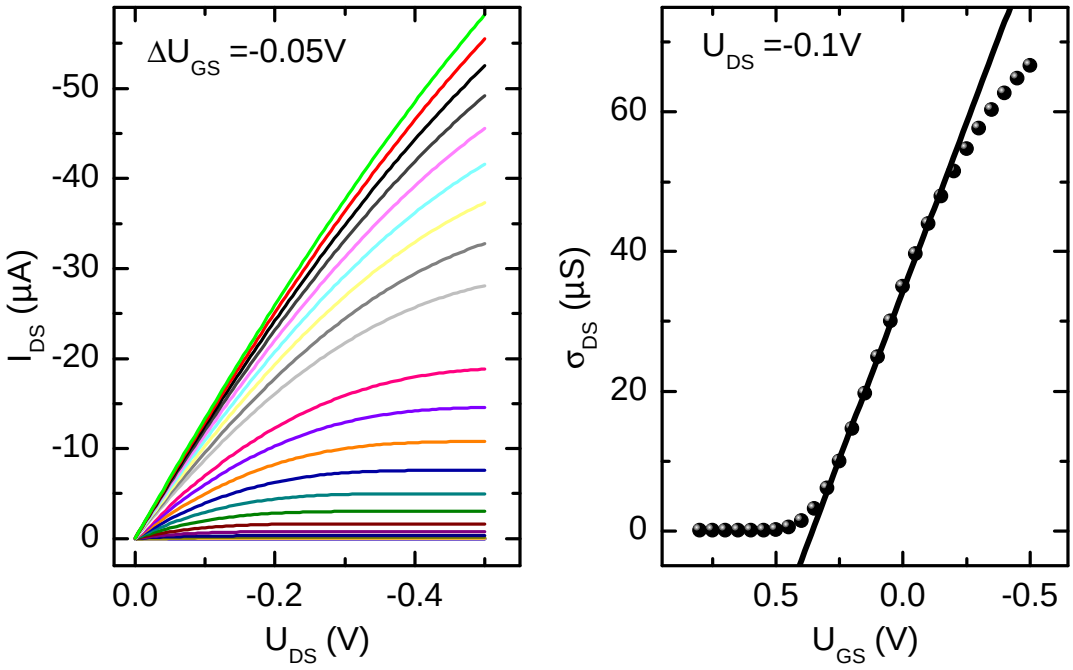

Figure 4.6: *left: Drain-source current (I_{DS}) versus drain-source voltage (U_{DS}) at different gate potentials, showing transistor-typical behavior with linear and saturation regions. right: Sheet conductivity in the linear region. The slope above the threshold voltage is 0.1 $\mu S\ mV^{-1}$. The transistor dimensions are 1x1 mm^2.*

gate-dependent drain-source conductivity (Figure 4.6) is linear above the threshold voltage over a large gate range with a slope of 0.1 μS mV^{-1}. The transconductance

shows its maximum at U_{gate}=−0.1 V, which is the gate bias at which the sensitivity of the drain-source current towards changes in the gate potential is highest. These results are very similar to those from hydrogen-terminated diamond FETs operated in an aqueous electrolyte (see Section 3.1 and [Dan09]).

Complementing the transistor characterization, Hall effect measurements were performed as a function of the gate voltage in a van-der-Pauw configuration. These results are compared to those of diamond solution gate field effect transistors (SGFET) of the same samples operated in an aqueous electrolyte. The hole concentration derived from the Hall effect measurements at different gate potentials shows a linear slope above the threshold voltage. This gate-dependent carrier accumulation corresponds to a capacitance of 2.3 μF/cm^2, which is close to the value calculated from the EIS experiment (3 ± 1 μF/cm^2). As shown in Figure 4.7, the charge modulation obtained with the polyelectrolyte gate is equal to that obtained using the aqueous electrolyte gate, suggesting that the gate material has no or little influence on the carrier concentration. Together with the conductivity, the Hall

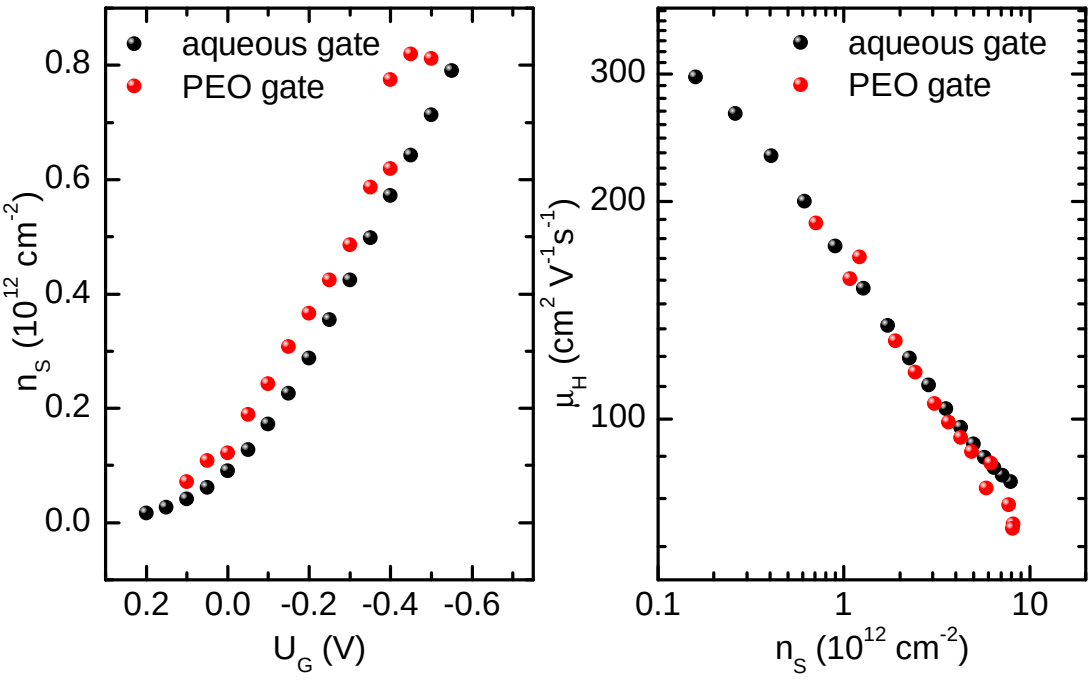

Figure 4.7: *left: Sheet carrier (hole) concentration versus gate voltage as derived from Hall effect measurements for an electronic grade sample with a PEO gate configuration as well as an aqueous electrolyte gate configuration. right: Corresponding Hall mobility as calculated from the sheet conductivity and carrier concentration.*

mobility can be derived from the carrier concentration. As can be seen in Figure 4.7, the gate dependence of the mobility of the diamond PEO-FET corresponds to

the behavior observed with the aqueous electrolyte gate, suggesting that the same scattering mechanisms govern transport in both types of devices. As discussed in Section 3.3.3, the mobility would be limited by acoustic phonon scattering or ionized impurity scattering from the electrolyte ions which has emerged as the more likely mobility limiting mechanism. This is not necessarily a contradiction to the results observed here: Firstly, as discussed in the following, the PEO-gated devices are likely to have a thin water layer adsorbed at the diamond surface resulting in the equivalent mobility behavior to the aqueous electrolyte-gated devices. Secondly, even when assuming no adsorbed water layer between the diamond surface and the PEO, the ion charge density in the PEO-gated devices would be the same as in the aqueous electrolyte-gated devices. Thus, a scattering mechanism dependent on these charges would lead to the same mobility behavior as in the aqueous electrolyte-gated devices.

Considering the almost identical behavior between the PEO-gated and the aqueous electrolyte-gated samples with regard to the charge accumulation, we propose that a thin water layer remains between the diamond surface and the PEO. This water layer, that is thought to be responsible for the diamond surface conductivity (see Section 2.2.1), would then lead to the same interfacial capacitance for the polyelectrolyte-gated devices as discussed in Section 3.2.3. Furthermore, this water layer has been shown to be surprisingly stable - though it remains unclear whether the water itself or adsorbed ions are responsible for the stability of the surface conductivity at elevated temperatures [Mai00] (see also Section 2.2.1). The presence of an interfacial water layer could explain why the observed interfacial capacitance does not vary for devices with a PEO gate as opposed to an aqueous electrolyte gate (see Figure 4.7), as we would expect when exchanging the electrolyte.

Replacing the aqueous electrolyte with a non-aqueous polyelectrolyte based on polyethylene oxide, which does not form hydrogen bonds, should diminish any effect based on hydrophobicity (see Section 3.2.3). Accordingly, no depletion of the electrolyte in the vicinity of the surface would be expected, increasing the dielectric constant in this region from the vacuum permittivity to that of polyethylene oxide and therefore increasing the capacitance of this region. In a series-capacitor model, where the overall interfacial capacitance is limited by the smallest capacitance, the overall interfacial capacitance should increase in this case. Based on the simple model for the aqueous electrolyte (see Equation 3.16) and using a dielectric constant of 14 for the polyethylene oxide monomer [Dav63], an interfacial capacitance in the range of 8 μF cm^{-2} would be expected, in contrast to the measured 2 μF cm^{-2}. To inves-

tigate this hypothesis, further experiments are needed, e.g. by removing the water layer on the diamond surface before depositing the polyelectrolyte. This could lead to higher capacitances, as the polyelectrolyte/diamond interface might not show a hydrophobic gap.

The main advantage of the polyelectrolyte-gated surface-conductive diamond-based transistor device is its solid gate. Additionally, the device is relatively easy to process and the PEO based electrolyte is transparent for wavelengths longer than approx. 350 nm (data not shown), making the whole device transparent in the visible spectrum.

We see potential applications of this technology in e.g. studies of the electronic properties of diamond crystals. As discussed in Section 3.3.3, the aqueous electrolyte offers only a very limited temperature range and the interfacial properties (e.g. water ordering) could change with temperature. Therefore, solid electrolytes offer the possibility of Hall measurements in a wider temperature range, thus allowing a better judgment of the various scattering mechanisms which potentially limit the mobility. Of course, the solid electrolyte could influence these transport properties, but it should at least be possible to rule out some scattering mechanisms. The studies by Chazalviel and coworkers, who employed PEO and methanol based electrolytes to explain data for silicon inversion layers at the interface with acetonitrile can work as an example [Ben90a] [Tar85] for such an approach. Finally, another application that can benefit from a solid, and transparent gate is the recently discovered switching of the charge state of diamond NV centers for quantum computing [Hau11].

4.3 Graphene SGFETs

In 2004 a new allotrope was added to the carbon family: graphene [Nov04]. The subsequent hype about this new material is at least partly founded in its extraordinary properties, and its widespread investigation testifies also to the ease with which the material processing can be mastered and results can be achieved. In addition to various other fields of application, biosensors and bioelectronic devices could benefit from graphene. Graphene combines the chemical stability and biocompatibility of other carbon materials with its extraordinary electronic properties such as a high carrier mobility, that make graphene FETs superior to those based on other materials. On top of this, the material is flexible, which facilitates a combination with living tissue. Further, the fabrication of devices for operation in electrolytes is rather easier compared to e.g. the silicon.

As it turns out, much of the technology employed and developed for diamond surface-conductive SGFETs can be applied to graphene, and thus the fabrication of graphene SGFETs [Dan10] [Hes11a]. This is true for a large part of the processing technology, which can be applied to epitaxial graphene as well as to chemical vapor deposited (CVD) graphene. Obviously, all of the characterization techniques used for diamond SGFETs can also be applied to graphene SGFET. And even some of the physical concepts that govern the device behavior can be transferred to graphene SGFETs. This has allowed our group to rapidly adopt graphene as a new material for SGFETs and their applications in bioelectronics [Dan10] [Hes11a] [Hes11b]. In this section, the principles of device fabrication of graphene SGFETs are presented together with their electronic characterization in electrolyte.

The results shown here are based on epitaxial graphene, which was prepared from SiC by graphitization of the Si face at 1200°C [Dan10]. The graphene SGFET device array was fabricated on this graphene layer using optical lithography. A Ti/Au layer stack (10 nm/100 nm) was evaporated to form bond pads and leads to the active area. Prior to the metal evaporation, the open areas were defined by selective etching in an oxygen plasma. In this way, the graphene layer was fully removed from the contact area, improving the adhesion of the Ti/Au layer to the SiC substrate. The active graphene areas of the transistors were defined by etching the surrounding graphene regions using an oxygen plasma. In order to contact the active area of the FETs and form drain and source contacts, an additional Au layer (100 nm) was deposited on the leads, partly overlapping the graphene active region. This step involves the evaporation of Au on the whole device and then selective etching with a KI/I_2 solution with the Au contacts protected by a standard photoresist layer. To prevent the direct contact between the electrolyte and the metal contacts, the entire sample was covered with two subsequent layers (1.5 μm each) of a chemically stable photoresist (SU-8), which were opened at the gate area by optical lithography. Transistors with two different gate areas (width x length: 40x10 μm^2 and 40x20 μm^2) were processed around the sample center, where a van der Pauw structure of 700x700 μm^2 was fabricated for Hall-effect measurements (see Figure 4.8). For CVD grown graphene, which offers various advantages with respect to epitaxial graphene, the process involves principally the same steps [Hes11b]. While the Ti/Au contacts are processed on the substrate and the graphene sheet transfered on top, the contact is still provided by an extra Au layer, selectively etched by a KI/I_2 solution. The active area is also defined by selectively etching the graphene sheet with an oxygen plasma and the insulation of the contacts is also achieved with a SU-8 layer. The

resulting device looks much the same as the diamond SGFETs with the hydrogen-terminated diamond part replaced with graphene (see Figure 4.8 for a micrograph of a finished device). The measurements of sheet resistivity and Hall effect were performed analogue to those of the diamond SGFET (see Section A.2).

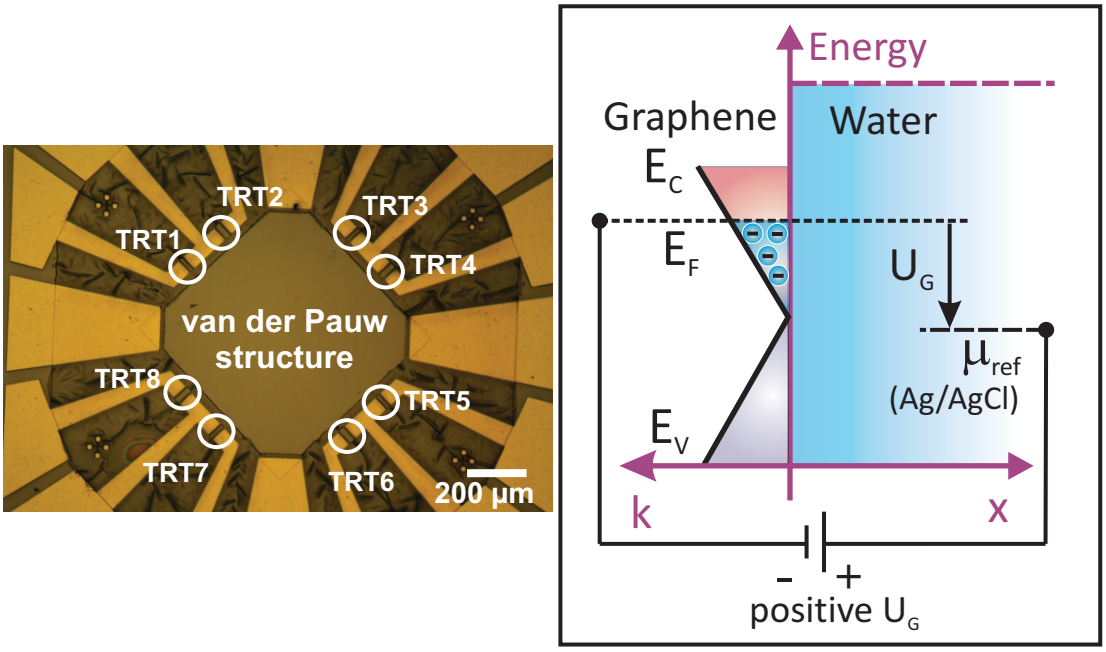

Figure 4.8: *Fabrication and operation of graphene solution-gated field effect transistors. left: Optical micrograph of graphene SGFETs. The Ti/Au structures (yellow) represent drain and source contacts for the transistors (gate areas of 40x10 μm^2 and 40x20 μm^2) and contacts for the van der Pauw structure in the center. right: Schematic drawing representing the modulation of the carrier density in the graphene film: the applied gate voltage (with respect to the reference electrode) shifts the Fermi level in graphene above (shown) or below the Dirac point, thus modulating the number of free carriers.*

The operating principle of graphene SGFETs is the same as that of the diamond SGFETs described in Section 3.1. A gate potential U_G is applied across the interface between the graphene and a reference electrode in the electrolyte. By changing the electrical potential of graphene, its electrochemical potential, the Fermi level E_F can be adjusted. The particular electronic band structure of graphene does not exhibit a band gap, but the valence and conduction band touch each other at the so-called Dirac point U_D, giving graphene its semimetal nature. As a result, both p-type and n-type charge can be accumulated by shifting the Fermi level position accordingly. This is shown schematically in Figure 4.8.

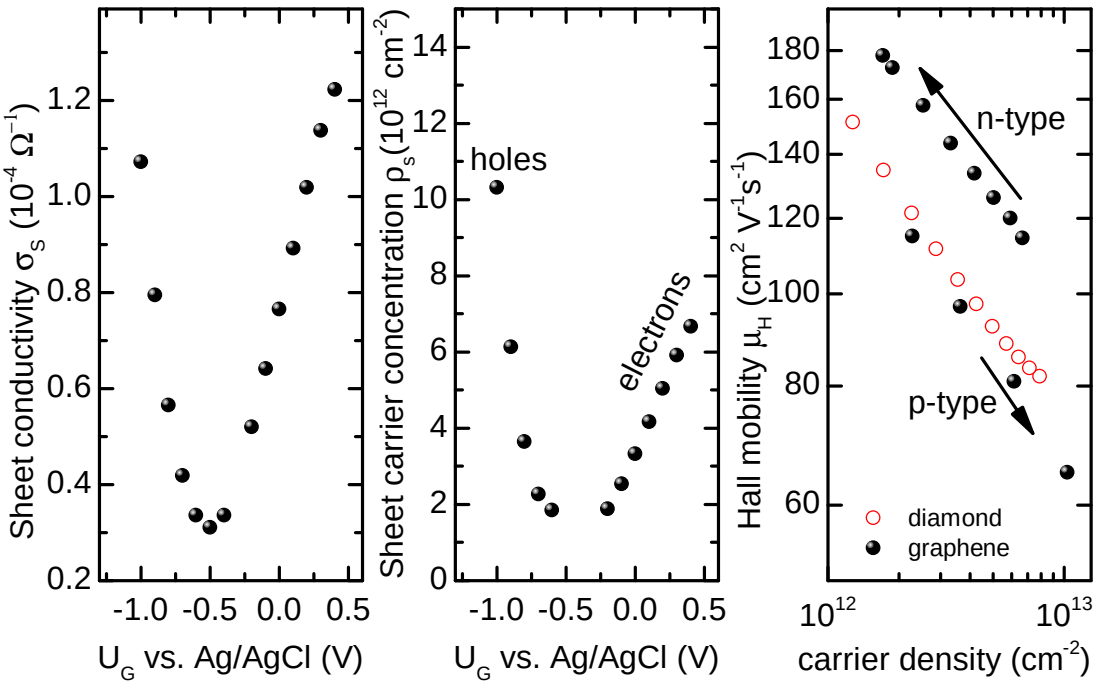

Figure 4.9: *left: Sheet conductivity derived from the 4-point resistivity measurements performed using the van der Pauw structure. The minimum of the conductivity occurs at a gate potential of -0.5 V versus the Ag/AgCl reference electrode. middle: Carrier concentration versus gate voltage calculated from the 4-point Hall-effect experiments. Close to the Dirac point, it is not possible to estimate the number of carriers. The curve exhibits a clear asymmetry around the Dirac point. right: Hall mobility versus carrier concentration. For comparison the mobility for a surface conductive, electronic grade diamond sample is shown. A clear asymmetry around the Dirac point is revealed, with electrons showing a higher mobility than holes. For both electrons and holes, the Hall mobility decreases with increasing carrier concentration, following a power law in which* $\mu \propto n^{-0.3}$.

The effect of this peculiar electronic structure of graphene can be seen in Figure 4.9, which depicts the results from sheet conductivity and Hall effect measurements in electrolyte under gate potential control. The conductivity shows a V-shape with the lowest conductivity at the Dirac point U_D. Figure 4.9 also shows the variation of the sheet carrier concentration as a function of U_G, where three regions should be considered: for $U_G > U_D$ a quasi-linear relationship between the electron density and U_G is observed; for $U_G < U_D$, on the other hand, a supra-linear dependence between the hole density and U_G is observed. The estimation of the carrier concentration becomes difficult near the Dirac point, since the Hall voltage goes to zero when the number of holes and electrons is similar. In any case, the estimated carrier

density near the Dirac point, which is about 10^{12} cm^{-2}, can be considered an upper limit. Ideally, for single layer graphene, a concentration of about 10^{11} cm^{-2} holes and electrons is expected at the Dirac point at room temperature [CN09]. We note that the presence of charged impurities can induce chemical doping, increasing significantly the number of carriers and shifting the Fermi level away from the Dirac point in the absence of a gate potential. Furthermore, it has been shown that the built-in electric field at the graphene/SiC interface can result in electron doping of the graphene layers [Emt09] [Hee07] [Oht07] [Ked08].

In order to fully understand the modulation of the carrier density in graphene with the electrolyte potential, we have to consider the charge distribution at the graphene/electrolyte interface. An electrical double layer is expected to form at an ideally polarizable electrode/electrolyte interface, as has been discussed in Section 3.2.2. In the case of graphene, in addition to the double layer capacitance, the so-called quantum capacitance must be considered. The quantum capacitance is defined as $\partial Q/\partial U_{gr}$, where $Q = e(p - n)$ corresponds to the total charge in graphene and U_{gr} represents the electrostatic potential in graphene, i.e. the position of the Fermi level in graphene with respect to the Dirac point [Lur88] [Fan07] [Xia09]. Both the quantum capacitance and the double layer capacitance contribute to the total interfacial capacitance. Thus, the applied gate voltage cannot be directly assigned to the electrostatic potential in graphene, since part of the applied voltage drops in the electrolyte close to the graphene surface.

The potential drop at the graphene/electrolyte interface and the resulting charge accumulation were simulated using the nextnano software. In the simulations, as done previously for diamond, we have used the conventional PB model with a static bulk dielectric constant of water of 78 as well as the ePB model for the hydrophobic case with PMFs for the electrolyte ions. It should be noted, that the parameters for the dielectric constant and the PMFs as for diamond in Section 3.2.2 have been used [Sch10]. It is worth recalling, that graphene, as hydrogen-terminated diamond, exhibits a good hydrophobicity. In graphene, the sheet charge density is calculated according to Fang et al., assuming a linear energy dispersion E(k) for isolated graphene [Fan07]. This leads to electron densities n and hole densities p given by

$$n = \frac{2}{\pi}\left(\frac{k_B T}{\hbar \nu_F}\right)^2 F_1(+\eta) \quad \text{and} \quad p = \frac{2}{\pi}\left(\frac{k_B T}{\hbar \nu_F}\right)^2 F_1(-\eta)\,, \tag{4.3}$$

where the Fermi velocity ν_F of the charge carriers in graphene is chosen to be 0.98 $\times 10^6$ m/s. F_1 is the Fermi-Dirac integral of the order 1 with $\eta = (E_F - E_D)/k_B T$ as its argument, whereby the relative position of the Fermi level E_F to the Dirac

point E_D determines the charge density.

Using this model, we have evaluated the carrier densities in graphene and the ion densities in the electrolyte at the graphene/electrolyte interface [Dan10]. When comparing the potential profiles at the interface as resulting from the PB and the ePB model, the ePB shows a much steeper potential drop on the electrolyte side, just as in the diamond case (see Section 3.2.3). This is a result of the vanishing of the water density and corresponding dielectric constant in the vicinity of the graphene surface, which is assumed in the hydrophobic ePB model. Therefore, while in the PB model any change in the gate potential is changing the Fermi level in the graphene by almost the same amount, in the ePB a part of the potential change is "lost" in this interfacial region. Thus the interfacial capacitance is lowered for the hydrophobic ePB model. The carrier density calculated based on the discussed

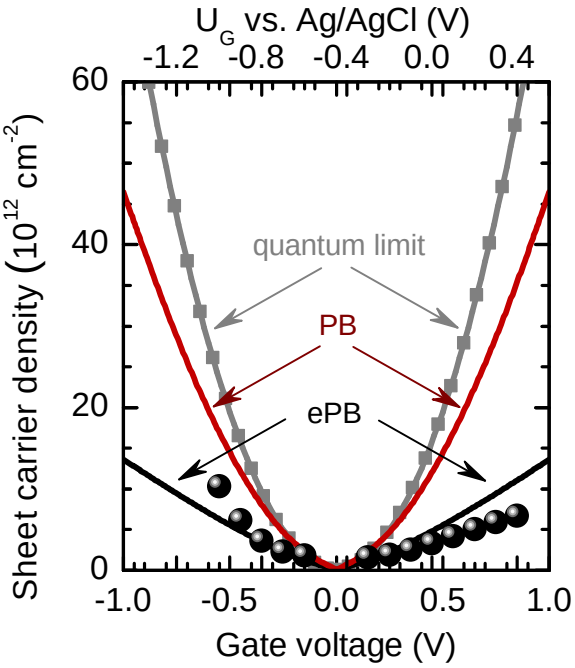

Figure 4.10: *Carrier density versus applied gate voltage for graphene solution-gated FETs. The experimental results (normalized so that U_D=0 V) are compared to the nextnano simulations. The experimental data is best represented by the ePB model, where an important potential drop occurs in the electrolyte strongly reducing the electrostatic potential in the graphene film. In the case of the PB model, the potential drop in the electrolyte is almost negligible, i.e. the electrostatic potential in graphene approximately equals U_G, resembling the "quantum limit" situation, in which $E_F = eU_G$.*

models is shown in Figure 4.10; the carrier density expected from the so-called

quantum limit in graphene ($U_{gr} = E_F/e$) is shown for comparison, together with the experimental results obtained from the Hall measurements. This comparison confirms that the graphene/electrolyte interface cannot be solely described by the quantum capacitance, since the experimental carrier density is much smaller than predicted by the quantum limit. Furthermore, the PB model cannot describe the experimental results; the double layer capacitance predicted by this model is too high, and therefore the situation is similar to the quantum limit. Finally, the carrier density predicted by the ePB model, which accounts for the microscopic structure of water near the interface with no fitting parameters, is in reasonable agreement with the experimental results.

However, the electron-hole asymmetry found experimentally (Figure 4.9 and Figure 4.10) cannot be understood with this model. It has been proposed, that the access region beneath the SU-8, where there is no gate control via the electrolyte, will be slightly doped, either n- or p-type, and thus forming a p-n junction with the gated graphene region, if the respectively opposite carrier type is accumulated [Hes11a]. For the data presented here, this would necessitate a p-type doping in the access region beneath the SU-8, in order to form a p-n junction with the gated region in an electron accumulation state, and therefore result in an earlier leveling off of the sheet conductivity. However, such an additional resistance, which is in effect a contact resistance, should not affect the results of the four-point van-der-Pauw measurements. Equally, the Hall effect measurements should not be affected by such an additional resistance and in the results for the carrier concentration the asymmetry is apparent as well. Other considerations, such as bilayer graphene with its different effective mass for electrons and holes [Cas07], or chemical doping by ion adsorption [Ang08], could possibly explain this effect.

Using the resistivity and carrier density determined directly from in-solution Hall-effect measurements, the dependence of the carrier mobility on the electrolyte gate potential and thus the carrier density can be evaluated (Figure 4.9). It is observed that the Hall mobility decreases with increasing carrier density. The magnitude of the mobility is in good agreement with values for epitaxial graphene prepared on the Si-face of SiC, where low carrier mobilities are typically reported [Ber04] [Ted09]. However, more recent measurements point to higher mobilities, even for epitaxial graphene [Hes11a]. There is also a clear asymmetry for hole and electron mobilities: at the same carrier concentration, the electron mobility is noticeably higher than the hole mobility. Although the influence of charged impurities on transport in graphene is widely acknowledged, the limiting scattering mechanism is still a matter

of discussion [Che08] [Ada07] [Kat08]. It has been suggested that Coulomb scatterers present at the graphene/substrate interface, or even adsorbed on the graphene surface limit the carrier mobility. Theory predicts that long-range Coulomb scattering, such as that due to charged impurities in the vicinity of graphene, will lead to carrier mobilities which are independent of the carrier density [Che08] [Ada07]. On the other hand, short-range scattering, such as that due to point defects or ripples in the film, is predicted to decrease the mobility with increasing carrier density [Che08] [Kat08] [Sta07]. Recently, Tedesco et al. have reviewed the dependence of the Hall mobility on the carrier density in epitaxial graphene on SiC [Ted09]. For graphene grown on the Si-face of SiC, the mobility strongly decreases with increasing carrier concentration (both electrons and holes), almost following a $\mu \propto n^{-1}$ dependence. It was suggested that the relationship between carrier mobility and carrier concentration may result from the stepped morphology of graphene due to the underlying SiC substrate, and is an intrinsic characteristic of epitaxial graphene synthesized by the sublimation method [Ted09]. As can be seen in Figure 4.9, our experiments do not reproduce such a trend; instead, the mobility exhibits a weaker dependence on the carrier concentration, following $\mu \propto n^{-0.3}$. We note, however, that the exact dependence of the mobility on the carrier density, as theoretically predicted for ripple-induced scattering, strongly depends on the surface morphology, and it has been shown to vary from an almost constant value to a $\mu \approx n^{-1}$ dependence [Che08] [Kat08]. In our specific case, in which the graphene film is in contact with an aqueous electrolyte, additional Coulomb scattering is expected due to the double layer formed at the graphene/electrolyte interface. As in the case of diamond SGFETs, the ion density in the vicinity of the graphene depends on the carrier density, due to the charge neutrality requirement. Therefore, even if the ions are treated as long-range Coulomb scatterers, the mobility is expected to decrease with increasing carrier density, due to the correspondingly increased density of ionic scattering centers. Additional scattering mechanisms related to the graphene/aqueous electrolyte interface could also be relevant, such as interface dipole scattering introduced by structuring of water in contact with the hydrophobic surface of graphene.

With regard to applications as biosensor or in bioelectronics, graphene is in many ways the "better diamond". It appears to combine the big strengths of diamond in its stability in electrolyte environments [Tan09] and its biocompatibility [Lee11] [Hes11b] with a number of other advantages over diamond and specifically hydrogen-terminated diamond. The remarkable electronic properties of graphene, notably its high carrier mobilities, are also exhibited in electrolyte [Hes11a]. The high mobilities

and a similar interfacial capacitance to diamond lead to a higher transconductance, i.e. a higher sensitivity, of the devices [Hes11a]. The fact that these superior properties could not be observed in initial experimental results [Dan10] can be probably attributed to not-yet optimized graphene sheets. Among other things the graphene had to endure a short Pt etching in aqua regia ($HCl + HNO_3$) - further testament to the chemical stability of the material. The higher sensitivity of graphene SGFETs combined with low noise leads to very competitive signal-to-noise ratios [Hes11b]. Furthermore, the mechanical flexibility that graphene sheets offer is certainly advantageous for the combination with living tissue, which is of particular interest for neuroprosthetic devices. Starting from epitaxial or CVD graphene, the processing technology for graphene SGFET could be adapted straight from diamond SGFET. Finally the availability of graphene is surpassing that of diamond, judging from the numerous scientific groups that have mastered the production of graphene.

Chapter 5

Detection of cell signals with diamond SGFETs

The development of neuroprostheses, and, to a lesser extent, biosensors, has been one of the main drivers for the investigation of diamond in electrolytes and thus, this thesis.[1] In order to understand the electrical synapse at the cell/transistor interface, we will briefly review the fundamental aspects of the electrical activity in electrogenic cells.

The membrane that encloses every cell not only forms a mechanical barrier but also an electrical barrier that gives rise to an inner cell potential that differs from the surrounding potential. The membrane potential ΔV is defined as the difference between the inner cell potential V_M and the potential of the extracellular solution V_E. The cell membrane contains specialized proteins, the ion channels, that selectively transport ions across the cell membrane. This leads to different concentrations for a number of ion species inside and outside the cell (see Table 5.1). As a result of these concentration gradients, a potential difference arises between the inside and the outside of the cell. Since the membrane is permeable only selectively to one ion species, a diminishing of the concentration gradient by diffusion, would lead to a charging of the cell, and thus increase the potential inside the cell. The situation therefore reaches a steady state between the concentration gradient driven diffusion and the potential driven diffusion. In this situation, the ion species i with valency z_i is generating the Nernst potential V_i for the cell [Nel04]:

$$V_i = -\frac{RT}{z_i F} \ln \frac{c_i^{in}}{c_i^{out}} \tag{5.1}$$

[1] This thesis has been carried out in the frame of a EU project, DREAMS, aiming at developing diamond-based retinal prosthetic devices.

Table 5.1: *Typical ion concentrations inside c_{in}, and outside c_{out} a squid giant axon, as well as the Nernst potential resulting from the concentration gradient for Na^+, K^+, and Cl^- ions [Nel04].*

ion	c_{in}	c_{out}	V_{Nernst}
Na^+	50	440	54 mV
K^+	400	20	-75 mV
Cl^-	52	560	-59 mV

As will be shown in the following, the permeability, that is the conductance, of the membrane for each ion species determines the contribution of its Nernst potential to the total membrane potential.
From an electrical point of view, the cell can be represented by an equivalent circuit, the so-called Hodgkin-Huxley element [Kan95]. The Hodgkin-Huxley element consists of parallel current pathways I_i for each ion species across the cell membrane. Along its pathway, each ion experiences the potential drop provided by the Nernst potential and the resistance (specific conductivity g_i) from the ion channel specific to this ion species. Additionally, a capacitance C_M is used to account for the capacitive behavior of the membrane. In the steady state situation, according to Kirchhoff's law, the membrane potential ΔV is then [Nel04]:

$$\Delta V = V_M - V_E = V_i + \frac{I_i}{g_i} \text{ and therefore } I_i = g_i(\Delta V - V_i) \tag{5.2}$$

The sum of all ion currents $\sum_i I_i$ is zero in the case of the steady state situation, where the membrane potential is not changing. Therefore, considering the ion species potassium, sodium and chloride [Nel04]:

$$g_{Na}(\Delta V - V_{Na}) + g_K(\Delta V - V_K) + g_{Cl}(\Delta V - V_{Cl}) = 0 \ , \tag{5.3}$$

which then leads to the membrane potential

$$\Delta V = \frac{g_{Na}V_{Na} + g_K V_K + g_{Cl}V_{Cl}}{g_{Na} + g_K + g_{Cl}} = \frac{g_{Na}}{g_{tot}}V_{Na} + \frac{g_K}{g_{tot}}V_K + \frac{g_{Cl}}{g_{tot}}V_{Cl} \ , \tag{5.4}$$

where g_{tot} is the sum of the specific conductances. If the extracellular potential V_E is used as a reference and set to zero, the inner cell potential V_M is then known.
By opening and closing the ion channels for the specific ions, the cell can then change its potential. The conductivity for each ion species determines to what extent its Nernst potential contributes to the whole membrane potential. In this way, neurons

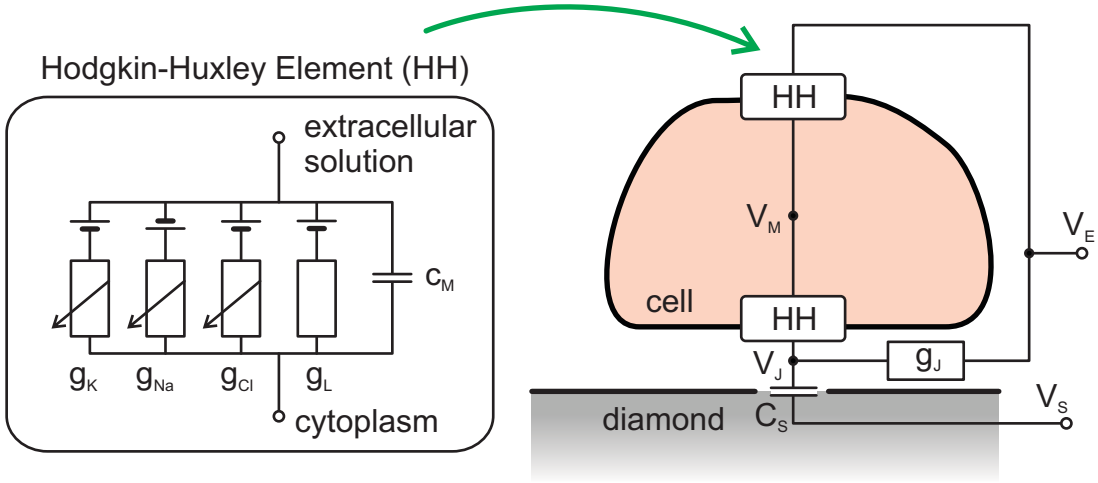

Figure 5.1: *left: The electrical behavior of the cell membrane is represented by a Hodgkin-Huxley element. It is composed of the potassium, sodium, and chloride ion channels with their specific conductances g_K, g_{Na}, and g_{Cl}, plus a potential independent leakage channel g_L, and the membrane capacitance C_M. right: Graphical representation of the point-contact model for a cell/transistor junction, with the transductive extracellular potential V_J, the electrical potential of the cell V_M, the potential in the bulk electrolyte V_E, the potential of the diamond substrate V_S, the capacitance of the diamond/electrolyte interface C_S, and the conductance g_J of the cleft between cell and transistor.*

can generate action potentials, that is transitory variations of their membrane potential, that can travel from cell to cell and thus facilitate communication [Alb02]. For an action potential to be generated, the membrane potential needs to reach a certain threshold. Once this threshold is reached, both the sodium and potassium channels open with different time constants. The faster sodium channels open first producing an inflow of Na^+ ions which raise the inner potential, causing a positive feedback loop in which yet more sodium channels open. The sodium channels then close and the slower potassium channels become dominant, resulting in an outflow of K^+ ions, which pushes the potential in the opposite direction. This transitory variation of the membrane potential is the action potential. Both sodium and potassium channels open only for a certain time after the threshold is reached and after returning to the resting state they need a refractory period to become active again. This mechanism generates the potential pulses and prevents changes to the membrane potential for longer time periods.

One of the goals of bioelectronics is to couple the electrogenic cells to electronic devices in order to detect and possibly excite these action potentials. Cells however, do not form a tight contact with surfaces. Instead, membrane proteins bind the cell to the surface leaving a cleft of 60-100 nm in between [Bra98]. The cell-transistor coupling that allows the signal transduction between cell and sensor via this cleft has been described with the point-contact model (see Figure 5.1) [Reg89] [Fro03]. The point-contact model describes the potential changes in the cleft above the active area of the transistor by assuming all ionic and capacitive currents passing through one point in the cleft and thus canceling each other according to Kirchhoff's law. The potential of the node, where all the current paths meet, is called the junction potential V_J or transductive extracellular potential, and is equivalent to the effective gate potential the transistor responds to. The cleft between the cell and the transistor surface is small enough to provide a significant resistance between the junction region and the extracellular solution depending on the cleft size. This is a condition for the potential in the cleft to differ from the potential in the extracellular solution determined by the reference electrode. Upon opening of ion channels in the cell membrane, induced either by an action potential or by externally forcing the membrane potential via patch-clamp, ions flow into and out of the space between cell and transistor. The additional charge and the concentration change in the cleft lead to a potential change in the junction, that can then be detected by the transistor [Reg89] [Fro03].

Frequency response of diamond SGFETs

There are several preconditions that must be met in order to successfully record action potentials from cells. As cells usually need to be grown on the sensors, the devices need to be stable in cell culture media for a certain time, usually of the order of several days. Diamond SGFETs easily fulfill this criteria, as shown in Section 2.2.7. Equally fundamental is a sufficient signal to noise ratio for successful signal detection. Diamond SGFETs have been shown to exhibit low noise compared to, e.g. silicon FET used for cell signal detection [Hau10]. Combined with their transconductance, which is higher [Hes11a] than for comparable silicon devices, this results in a higher signal-to-noise ratio.

Furthermore, the device needs to be capable of responding sufficiently fast in order to resolve the action potentials of cells, i.e. the bandwidth of the whole recording setup needs to be high enough not to attenuate important frequency components

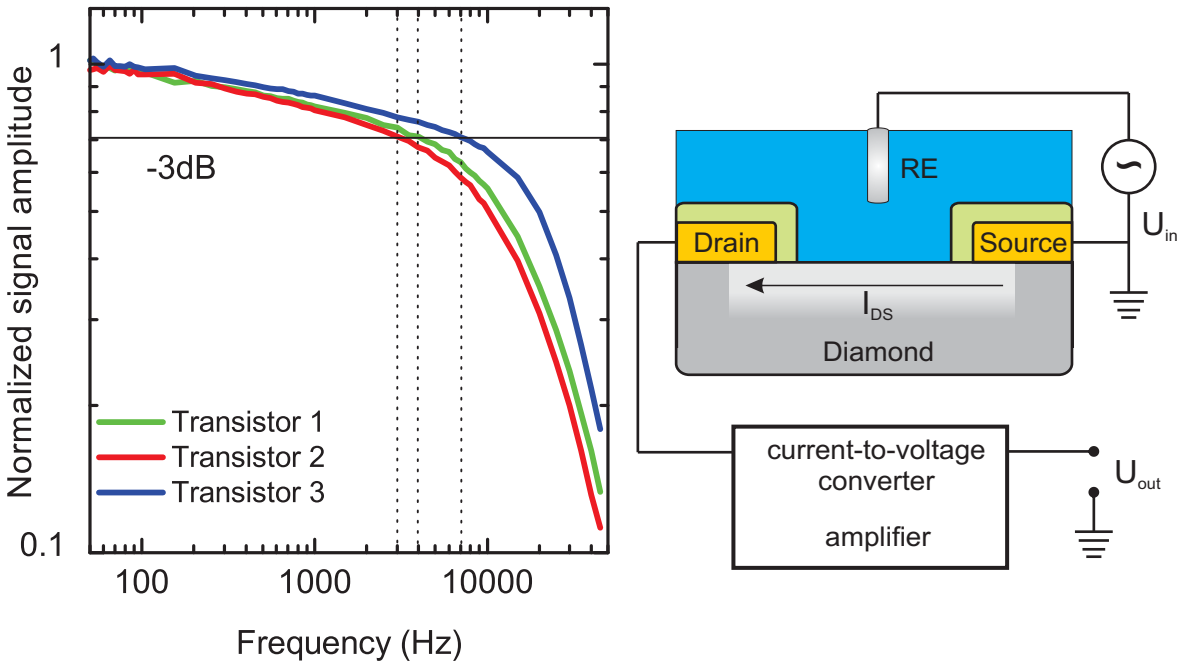

Figure 5.2: *left: Bandpass behavior of the signal amplitude measured for three diamond SGFETs in one sample. The recorded signal is normalized by the input signal amplitude. The cut-off frequencies, defined as a signal attenuation of 3dB, are indicated by the dashed vertical lines. right: Experimental setup for the bandwidth measurements. The reference electrode potential is modulated by the input voltage U_{in}. The corresponding drain-source current signal is converted to a voltage and amplified to give the output voltage U_{out}. The output voltage is compared to the input voltage, taking the transconductance of the respective transistor into account.*

of the signal. The recording setup includes a current-to-voltage converter and an amplifier. The interfacial capacitance of the diamond SGFETs in combination with the electrolyte resistance forms a low pass filter. Therefore, higher frequencies suffer a higher attenuation. Measurements of the systems bandwidth show a cut-off frequency (3dB attenuation) of the devices, including the setup, between 3 and 7 kHz (see Figure 5.2). At frequencies above the cut-off, the attenuation increases drastically, suppressing any signal component at higher frequencies. However, the frequencies of cell action potentials are below this range, typically less than 1000 Hz. At this frequency, the device plus amplifier transmits 80 to 90% of the signal amplitude. Therefore, the cell signals are expected to be well resolved using diamond SGFETs.

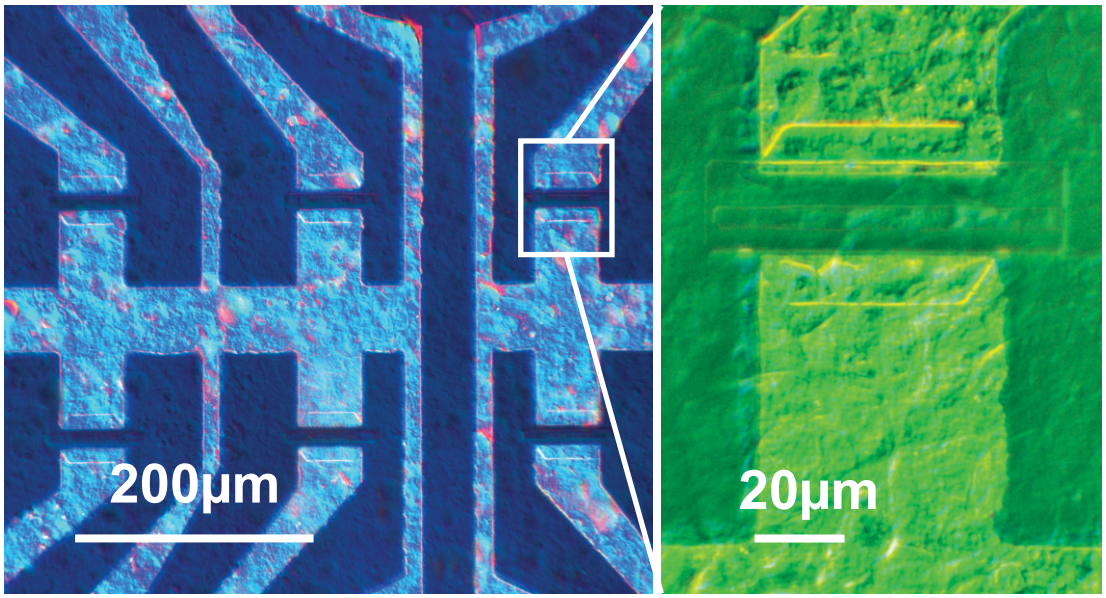

Figure 5.3: *Differential interference contrast image of HL-1 cells growing in a confluent layer on the diamond SGFET array after three days in vitro. Bright regions indicate metalized areas underneath the SU-8 passivation. Individual cells cannot be resolved due to their dense growth.*

Extracellular recording of HL-1 action potentials

Cardiomyocyte-like HL-1 cells were seeded on the 4x4 transistor arrays and cultured [Hau08, Dan09]. After three days, the cells were confluent enough to form a densely packed layer covering the active areas of the transistors as well as the SU-8 passivated space in between, as shown in Figure 5.3. The devices below this cell carpet were still fully functional, as revealed by measurements of the transistor characteristics [Hau08, Dan09]. The simultaneous recording of the drain-source current of all 16 transistors at a common operation point shows almost concurrent and repeated spikes on all working transistors, as can be seen in Figure 5.4. We attribute these events to the action potentials of the cells, which are known to be spontaneously generated and automatically propagate across the whole syncytium [Cla98]. The fact that almost all transistors of the array show clearly visible signals is an indication for the healthy growth of cells and, more significantly, for the close attachment of the cells to the active area of each individual transistor. Figure 5.4 also shows the same measurement with a higher time resolution, where the time delay between the events recorded by different transistors becomes visible. Due to the propagation of the action potentials through the cell culture, there exists a time delay between the

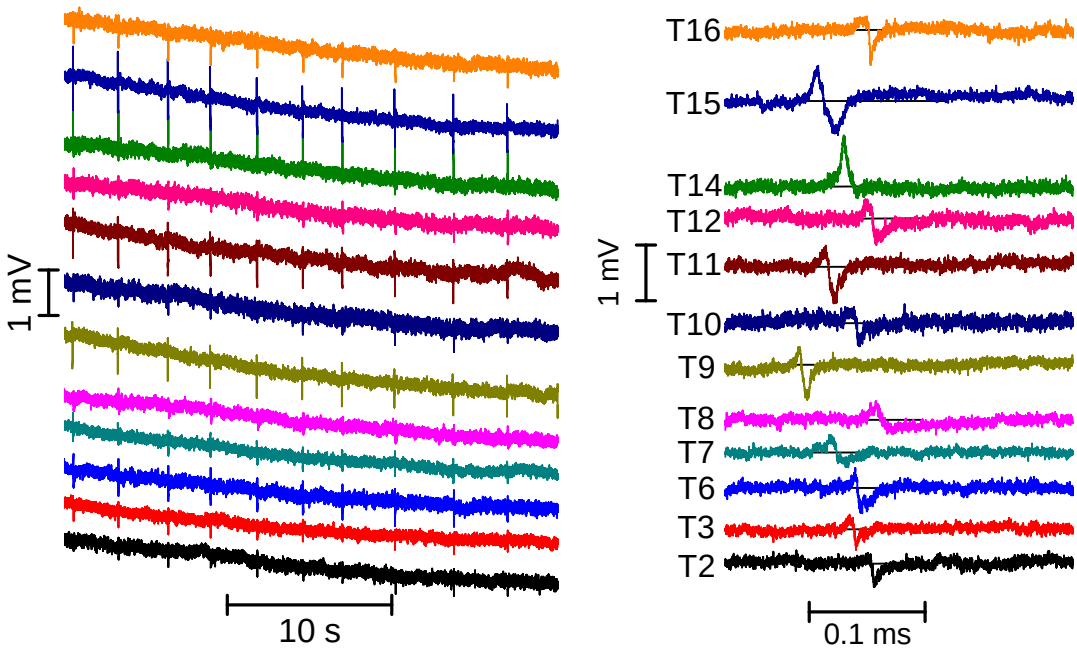

Figure 5.4: *left: Simultaneous recording of the gate voltage modulation of 12 channels of a diamond SGFET array. All transistors record repeated action potentials produced simultaneously from HL-1 cells on their respective gates. The HL-1 cells formed a continuous layer after three days of culture. right: Same recordings with an enlarged time axis. The measured action potential signals show different time delays for different transistors on this time scale. Most transistors record a signal shape similar to the one most clearly visible for transistor 15 with a positive peak followed by a negative peak typical of a capacitive response [Fro99].*

occurrences of the action potentials from one cell to another. As a consequence, the measured signals will propagate through the cell layer and arrive at different times at each of the transistors. However, as can be derived from Figure 5.4, the speed of propagation is not homogeneous. In young cultures the interconnection between the cells may not be fully developed, and a lack of connections requires the signal to take a longer path around this area. Nevertheless, the time delay between the recorded events rules out other possible sources for the recorded spikes, like a spike of the reference electrode potential or other distortions which would occur at all transistors simultaneously. The distribution of the time delays between the different transistors is constant for the duration of this and other measurements. Besides the time delay between the individual transistors, there is also a distribution of different signal shapes recorded by the transistors. Generally, the signal transduction from

the cell to the transistor can be explained by the so-called point-contact model introduced before [Fro03] [Fro08]. According to this model, an action potential of the cell, i.e. a spike of the inner cell potential caused by ionic flux across the membrane, translates into various signals recorded by the transistors depending on the conductivity of the cleft, the capacitance of the transistor/electrolyte interface, and the ionic and capacitive currents through the parts of the cell membrane attached to the transistor [Fro08]. The most frequent kind of signal transduction is dominated by capacitive currents through the attached cell membrane [Fro99], as exemplary shown by transistor 15 (Tr15) in Figure 5.4. Other signal shapes are more dominated by currents of various ions through the attached membrane into the cleft [Ing05]. The signal shape also depends on the distance of the cell to the transistor, and therefore the cleft size, or on the distribution of ion channels between the attached and the free part of the cell membrane [Fro03]. While the shape of the signal stays the same during the measurement, in a few cases we observed a change in the signal shape between two different days of measurement of the same transistor. As the cells are alive and continue to grow, this is probably caused by changes in the cell/transistor attachment.

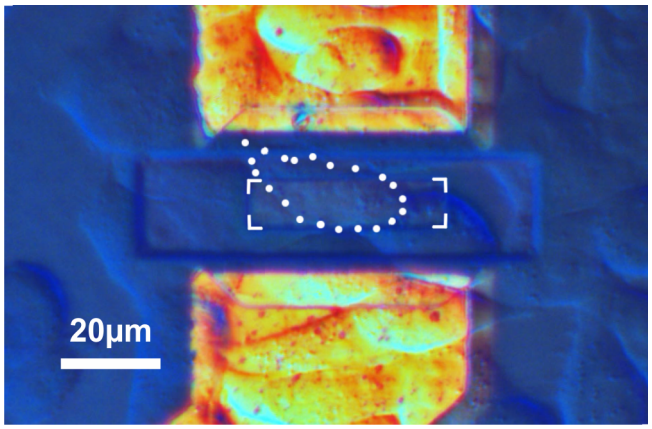

Figure 5.5: *Differential interference contrast image of HEK293 cells growing in the vicinity of the gate area of a transistor after 3 days in cell culture. The bright areas correspond to the source and drain Au contacts. In addition, the opening of the SU-8 passivation layer to the transistor gate (marked) is also visible. The outline of a cell covering the largest part of the gate is indicated by the dotted line.*

Extracellular recording of HEK293-EAG cells:

In order to observe the signals of individual cells and to do so in a controlled fashion, HEK293 cells (human embryo kidney cell line) were seeded and grown on the transistor array [Hau08, Dan09]. Figure 5.5 shows a representative example of a transistor with a number of HEK293 cells in close vicinity, and one cell on top of the active area of the transistor. The spindle like shape of the cells indicates good attachment to the substrate and a healthy cell growth. The hydrogen-terminated diamond constituting the active area of the transistor therefore also shows good biocompatibility with this second type of cells. HEK293-EAG cells are genetically modified to express potassium ion channels in the cell membrane, which lead to a release of potassium ions from the cell interior if a certain threshold for the membrane potential is exceeded. Cells on top of transistors were contacted with the patch-clamp method, where an electrode is attached to the cell with a glass pipette. Using this electrode, the cell's membrane potential can be controlled. Figure 5.6 shows the applied membrane potential V_M (top curve), the resulting ionic current I_M through the cell membrane (middle curve) and the response of the transistor beneath the cell (bottom curve). For HEK293 cells, the depolarization of the cell membrane to +90 mV is sufficient to induce the opening of the ion channels. A hyper-polarization pre-pulse (at 75 ms in Figure 5.6) shorty before the depolarization re-sets the voltage-gated channels to ensure that they are not in a refractory state. The channels close again when the membrane is repolarized to the resting potential of -50 mV. As a result, the membrane current I_M increases after the polarization until approaching a saturation value, as more and more potassium channels open [Sch02] [Wro05]. The quick change in potential from -50 to +90 mV and vice versa, additionally causes a capacitive current. In the membrane current graph of Figure 5.6 this contribution cannot be observed, since for usual patch-clamp recordings this signal part is compensated for by the patch-clamp amplifier electronics (20.8 pF membrane capacitance for this experiment). The effect of the change in conductance of the cell membrane on the gate potential of the transistor can be seen in the third part of Figure 5.6. Like the transduction of the action potentials of the HL-1 cells, this recorded response can be explained in a first approximation by the point-contact model [Wro05]. As mentioned above, the transductive extracellular potential above the transistor gate is determined by the conductance of the current paths leading to it. During the opening of the potassium channels, the conductance of the cell membrane changes, as it becomes permeable to the potassium ions. As a result, the junction potential V_J and thus the effective gate potential of the transistors are affected, leading to an

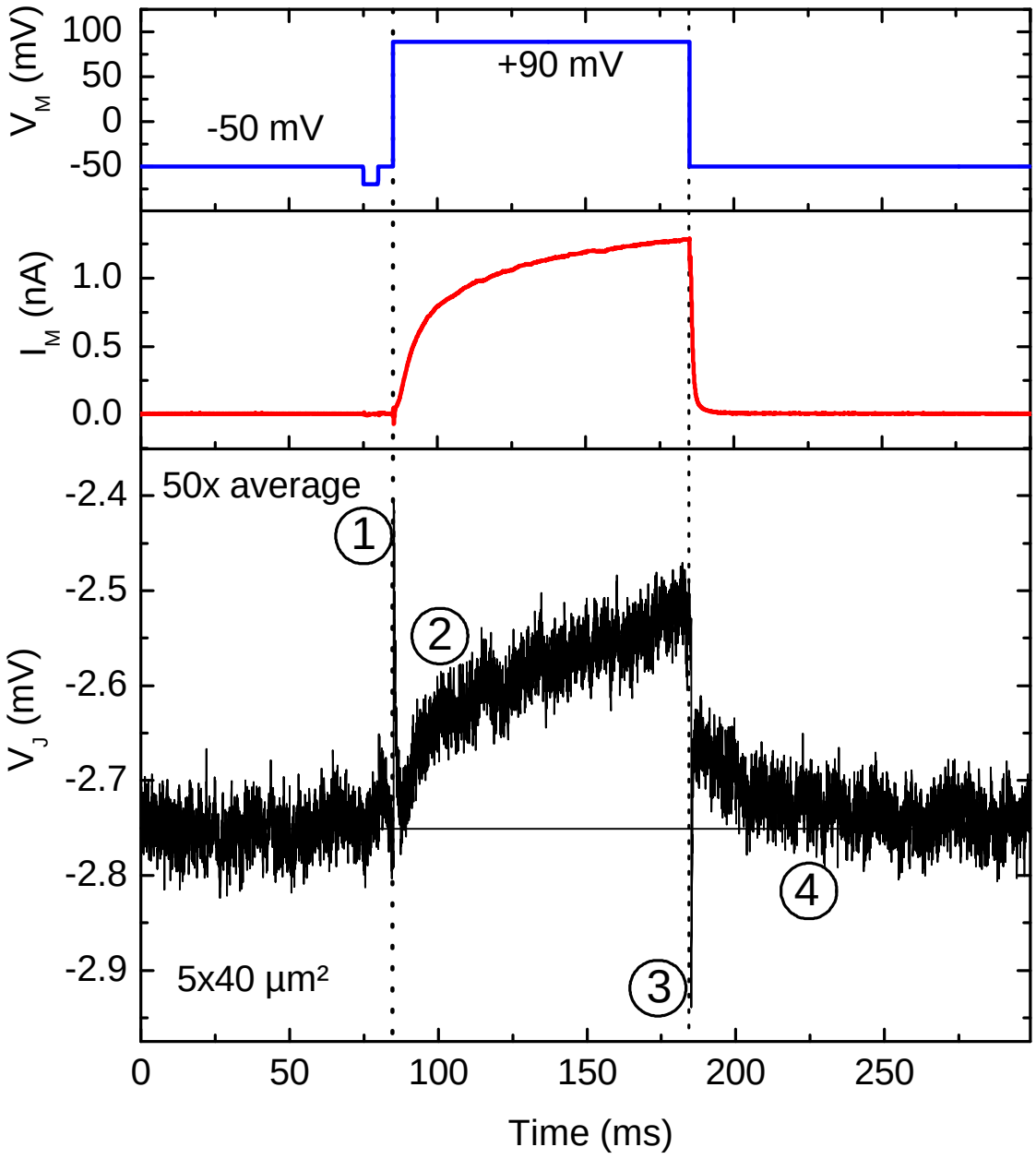

Figure 5.6: *Patch-clamp recording (top and middle) and corresponding transistor response (bottom) of a HEK293 cell located on the gate area of the transistor. The cell potential V_M as applied with the patch electrode is shown on top (blue), together with the current across the membrane I_M (red), and the transductive extracellular potential V_J (black) as recorded with the diamond transistor. The curves are averages of 50 recordings to improve the signal-to-noise ratio. The membrane current graph (red) does not show the sharp capacitive membrane current resulting from the change in membrane potential (dashed line at 85 and 185 ms) as this is compensated for by the amplifier electronics.*

increase of the recorded potential towards more positive values with an increase of the membrane conductance [Fro08]. Hence, changes in the membrane conductance of the cell, capacitive currents across the attached cell membrane, and changes of the cleft conductance will all contribute to modify the gate potential, influencing in turn the drain-source current of the transistor. The transistor recording shown in Figure 5.6 shows capacitive contributions from both the depolarization (marked "1") and repolarization (marked "3") of the cell membrane, as they are not compensated by the FET recording system. After the depolarization of the membrane to +90 mV, the gate potential increases following the increase of the membrane current (marked "2"). Upon repolarization of the membrane, the gate potential reaches again its initial value (marked "4"). This transistor response can be well explained by the change in conductance of the attached cell membrane according to the point-contact model discussed above. However, in contrast to the membrane current, the gate potential shows a less pronounced saturation trend after the initial increase following the polarization. Additionally, after the repolarization, the initial fast decrease of the gate potential is followed by a much slower return to the initial value. Both effects can be understood considering the ion sensitivity of the hydrogen terminated diamond SGFETs. During the depolarization of the cell membrane, potassium channels open and release potassium ions into the cleft. Depending on the thickness and the size of the cleft, diffusion of the potassium ions from the cleft into the bulk electrolyte will be limited, such that potassium ions accumulate in the cleft resulting in a steady state situation with a local increase of the ion concentration. After the closure of the potassium channels, the concentration of potassium ions in the cleft slowly returns to the bulk value of the electrolyte [Bri05] [Pab07] [Sch07]. Such a change of the ion concentration and therefore the ionic strength will lead to a change in the drain-source current of the transistor, resulting from the screening of the charge present at the hydrogen-terminated diamond surface [Har07]. In order to calculate this effect, the ion sensitivity of a diamond SGFET to KCl was evaluated by recording the drain-source current dependence on the KCl concentration. As shown in Figure 5.7, below 10 mM KCl concentration the concentration of the buffer ions dominates the transistor response. Above 10 mM KCl the drain-source current decreases linearly with the logarithmic increase of the KCl concentration [Har07]. In order to roughly estimate the effect of potassium ions accumulation in the cleft between cell and transistor during depolarization, one needs to consider that only a small part of the membrane is closely attached to the substrate and seals the cleft from the bulk electrolyte. We assume that 10 % of the potassium

ions released as membrane current (approx. 1 nA) during 100 ms of polarization pass through the attached membrane into the cleft with a thickness of 100 nm and a radius of 10 μm, and do not diffuse to the bulk electrolyte [Fro99]. This results in an increase of the concentration of potassium ions by 3 mM. The relevant ion concentration of the extracellular solution and the additional potassium ions for our experiments is 145 and 148 mM respectively, and therefore in the linear section (black line) of the graph. Taking the transconductance g_m for this transistor into account, the resulting decrease in drain-source current corresponds to an increase of 60 μV in the gate potential for each 1 mM of ion concentration change at this ion concentration. Accordingly, the estimated effect corresponds to a 180 μV increase of the gate potential. The observed effect on the gate potential of around 150 μV is of comparable magnitude. Close adhesion between cell and transistor gate leads to a high resistance of the cleft, which is favourable for high signal amplitudes. The accumulation of ions in the cleft due to decelerated diffusion of ions to the bulk electrolyte attests to this.

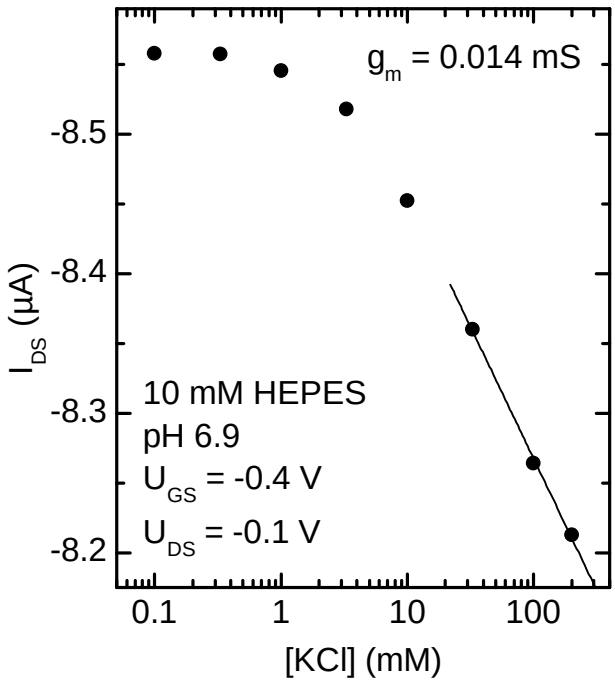

Figure 5.7: *Ion sensitivity of the drain-source current of a transistor recorded at a constant operating point and constant pH. The x-axis displays the concentration of KCl added to the buffer solution (10 mM HEPES).*

The transistor measurements shown in Figure 5.6 are the average of 50 recordings, which is necessary for this type of experiment in order to improve the signal-to-

noise ratio. Although the signal is visible on each single recording, a detailed shape analysis is only possible with the averaged signal. The fact that such averaging is possible emphasizes the reproducibility of both the cell and the transistor response. Such artificial cell signals produced as controlled events, where membrane potential, membrane current, and the response of the sensing element are known, enable a thorough analysis of the mechanisms governing the signal detection.

In conclusion, the results in this last section show that diamond is a suitable material for bioelectronics. Its biocompatibility allows the growth of cells and a close enough attachment to the transistor surface so as to enable transduction of the cell signals. The device performance could be further improved by functionalizing the gate area of the transistor in order to enhance directed growth of cells on the sensitive areas. In addition to the read-out of cells, capacitive stimulation of cells using the advantage of the high specific interfacial capacitance of the diamond/electrolyte interface appears feasible.

Chapter 6

Summary

In the course of this PhD project, hydrogen-terminated diamond SGFETs have been investigated with a focus on their interfacial properties and applications in the field of bioelectronics. The apparent limitations of silicon as an electronic material in aqueous electrolytes has motivated the search for alternative materials and diamond has emerged as a promising candidate. The development of diamond SGFETs spawned interest in using these devices for the signal transduction of living cells. This goal required a thorough understanding of the hydrogen-terminated diamond/electrolyte interface, as well as technological advancements in the application of these devices.

For the study of the charge accumulation at the diamond/electrolyte interface, in-liquid Hall effect measurements were employed, allowing us to correlate relevant properties of this interface to various sample parameters. The necessary setup was specifically developed for this purpose and allows measurements under potential control in electrolyte in a fully automatic mode. Simulations were then employed to quantitatively reproduce the experimental values. These simulations with the nextnano^3 software allowed us to calculate the charge accumulation at the diamond/electrolyte interface using a spatially dependent dielectric constant on the electrolyte side. We found that the measured capacitance of the hydrogen-terminated diamond/electrolyte interface could be understood by assuming a hydrophobic gap in the direct vicinity of the diamond surface, consisting of a vanishing water density and consequently diminished dielectric constant. A simple analysis of the contributions to the interfacial capacitance finds the dominant effect to be from the water density fluctuations at the hydrophobic surface as opposed to the finite approach of the ions. Furthermore, a systematic difference in the interfacial capacitance between the (100) and the (111) surface orientation was experimentally observed. Simulations based on effective valence band masses calculated with the

kp method showed only a negligible comparable effect. Potential causes for this orientation dependence of the capacitance are discussed, but none can be substantiated with the available experimental data. Aside from the comparison to available experimental data, the simulations further illustrate the electronic situation in the potential well beneath the diamond surface and the effects of parameters such as the nitrogen impurity concentration. The experimental study of the electronic transport in the hole channel revealed a clear dependence on the nitrogen impurity content and on the surface orientation, though less pronounced. Electronic grade, (100)-oriented samples exhibit the highest mobilities, and optical grade, (111)-oriented samples the lowest mobilities. The mobility dependences of the different sample categories are compared to those theoretically predicted for relevant scattering mechanisms. These are in turn tested by Hall effect experiments that vary parameters such as temperature, or surface potential fluctuations. While the mobility dependence of no sample category could be unambiguously attributed to a certain scattering mechanism, potential candidates have been singled out for further investigations.

The stability of diamond is a key motivation for its study as a material for bioelectronics, and consequently the electrochemical stability of the hydrogen-termination was confirmed. The all-important termination of the diamond surface was studied with XPS and the results on the composition of the hydrogen-terminated diamond surface suggest the presence of an adsorbed water layer. Some advancements of technological capabilities will aid the application of diamond SGFETs in bioelectronics and where necessary to carry out the research in this work, such as the partial oxidation of the surface.

The diamond SGFET principle was used in three applications. Firstly, as a pH sensor for which the long-standing controversy on the pH sensitivity of the diamond surface conductivity could be resolved. Secondly, a polyelectrolyte was employed to produce solid gate diamond SGFETs. Thirdly, the SGFET principle was applied to graphene. The graphene SGFETs show very promising characteristics and seem likely to surpass diamond in their applicability in bioelectronics. Finally, signals from single living cells could be successfully detected with diamond SGFETs for the first time. Cell culture studies confirmed the diamond SGFETs to be compatible with cell growth. The cell signals could then be detected with sufficient resolution to differentiate signal shapes. The correct signal transduction could be shown with single cells excited with the patch-clamp technique and thus correlated to the measured signal.

Chapter 7

Outlook

This thesis set out to advance the development of diamond as a material for biosensing and bioelectronics, as well as to explore those material properties that are fundamental in this field. Some progress has been made and some questions answered on this broad front, but many more remain.

The largest part of this thesis deals with the charge accumulation and the electronic transport at the diamond/electrolyte interface. Here, the difference in the interfacial capacitance between the (100) and the (111) surface orientation remains largely unexplained. The first step towards a better understanding of this effect could be molecular dynamics simulations properly including the charge separation in the C-H surface dipoles and thus test their effect on either the interfacial water density or its orientation. Experimentally, analogue measurements for the (110) surface as those presented here could provide an additional data point against which to test possible explanations. Studies on the morphology of the surface with atomic resolution, e.g. with STM, could check for systematic differences in surface morphology between the orientations.

Non-aqueous electrolytes can replace the aqueous electrolyte gate of diamond SGFETs and potentially increase the charge accumulation, either by increasing the interfacial capacitance, or by increasing the potential window of the diamond devices. This has been already tried in this thesis, but the data suggests it is necessary to remove the adsorbed water layer on the diamond surface before depositing the gate material. The procedure would probably involve annealing in vacuum or oxygen-free atmosphere and deposition of the gate material in situ. The exchange of the electrolyte could help to elucidate the crystal orientation dependent interfacial capacitance, or lead to new physical phenomena such as superconductivity through the high charge accumulation as in other materials [Uen08, Ye10].

The investigation of the electronic transport in the p-type surface conductive channel of diamond has established a basis on which specific scattering mechanisms can be tested. To this effect, a wider range for temperature dependent Hall effect measurements would be highly advantageous. Non-aqueous electrolytes, such as solids or liquids with a lower freezing or boiling point, used as gate materials can facilitate this wide temperature range. A higher carrier accumulation would also shed light on the mobility dependence beyond the region of uniform mobility values at high carrier concentrations.

The nextnano simulations that contributed so much to the understanding of the charge accumulation and the electronic properties of the diamond SGFETs are based on the description of the band structure by Luttinger parameters or effective masses. As has been discussed, there is no agreement in literature on the values of these parameters. This unsatisfactory situation should be addressed with a thorough experimental study, with credible statistics e.g. with cyclotron resonance on the effective masses in intrinsic diamond for the main crystallographic directions. Such a study could clarify the controversy and serve as an anchor point for theoretical studies and thus greatly aid further calculations on the charge accumulation in diamond.

The hydrophobic interaction has been studied on a number of material systems, but, at least experimentally, very rarely on diamond [Jen03, Ost05, Mez06, Poy06, Poy08, Kun09]. We believe that the diamond surface could provide a model system in this field, as it can be both hydrophobic and hydrophilic, depending on the surface termination. As both terminations are stable in aqueous environments this should provide a suitable platform for studies on the hydrophobic effect.

The proposed water layer on the diamond surface should be studied again. For this, a repetition of the ambient pressure XPS experiments should be performed. An improved hydrogen termination of the samples and better statistics should enable reliable results and provide a clearer difference between the clean surface and that with adsorbed water or oxygen. The source of the adsorbed oxygen could then be clarified with e.g. sum-frequency generation measurements on diamond surfaces with the adsorbed water layer [She06].

The signal transduction from neurons would be the next logical step in the development of diamond bioelectronics. To make such an attempt successful, the neuron growth should be directed. To this end, the functionalization of the diamond surface with a monolayer of linker molecules which can then bind to growth promoting proteins would be advantageous. The combination of areas with growth promot-

ing proteins and growth inhibiting proteins should maximize the selectivity of the neuron growth.

The controversy around the pH sensitivity of the diamond surface conductivity could be resolved in this work. However, the mechanism of the pH sensitivity is still not fully understood. A combination of XPS measurements to detail the residual oxygen content on the surface in combination with pH measurements could possibly reveal the source of the pH dependent surface charge.

Considering the rise of graphene, the outlook for diamond as a material for biosensing and bioelectronics is bleak. In these areas graphene seems to combine the strengths of diamond with superior electronic properties. The fabrication of graphene SGFETs in this work has greatly benefited from the technologies and the expertize developed for diamond SGFETs. The remarkable stability of diamond in electrolytes could still lead to applications of diamond as an electrode material for demanding electrochemical applications.

Appendix A

Appendix

A.1 Monolayer calculation from XPS spectra

From XPS spectra the coverage of an adsorbate layer over an underlying substrate can be calculated. When photoelectrons are generated in a material not all escape, as those photoelectrons generated deeper in the sample are recaptured or trapped, resulting in an exponential decay of the generated intensity from deeper layers. This intensity attenuation depending on the material-specific exponential escape probability can be used to calculate the thickness of an adsorbate layer. The intensity I (e.g. of the O1s electrons) for a layer with the thickness d is therefore obtained by integrating over the exponential escape probability [Den08] (supplementary information).

$$I = n_A \sigma_A \int_0^d \exp\left(\frac{-z}{l_A}\right) dz = n_A \sigma_A l_A \left[1 - \exp\left(\frac{-d}{l_A}\right)\right] \tag{A.1}$$

- n_A: density of the atom A (e.g. oxygen) in the matrix (e.g. H_2O)
- σ_A: atomic photoionization cross-section of the atom A - e.g. oxygen
- l_A: photoelectron escape depth in the matrix (e.g. H_2O)

If the adsorbate layer A is now covering a material B of thickness d', the intensity of the photoelectrons that escape from that material is now attenuated again when passing through the adsorbate layer A:

$$I = n_B \sigma_B l_B \exp\left(\frac{-d}{l_A}\right) \left[1 - \exp\left(\frac{-d'}{l_B}\right)\right] \tag{A.2}$$

For a bulk material the depth d' goes to infinity and the intensity is (without the adsorbate layer):

$$I = n_B \sigma_B l_B \tag{A.3}$$

If the coverage of the adsorbate layer is one monolayer or less, with X being the fraction of the substrate surface covered, we write [Sea79] for the intensity of the adsorbate layer

$$I = X n_A \sigma_A \lambda_{m,A} \cos\Theta \left[1 - \exp\left(\frac{-1}{\lambda_{m,A}\cos\Theta}\right)\right] \tag{A.4}$$

And the intensity of the bulk substrate layer:

$$I = n_B \sigma_B \lambda_{m,B} \cos\Theta \left[1 - X + X\exp\left(\frac{-1}{\lambda_{m,A}\cos\Theta}\right)\right] \tag{A.5}$$

Here, the escape depth l is replaced with the product of the inelastic mean free path λ and a geometric factor.

$$l = \lambda_m \cos\Theta \tag{A.6}$$

Θ denotes the angle between the surface normal and the detector. λ_m is given in units of monolayers and related to the inelastic mean free path via the thickness a of one monolayer: $\lambda = a\lambda_m$.

Ideally, spectra from an adsorbate-free as well as a covered substrate are available and compared to calculate the thickness of the adsorbate layer. In our case, the goal is to estimate the coverage of the oxygen-terminated part of the diamond surface. However, data from perfectly hydrogenated samples with no oxygen content was not available. It can be safely assumed that the oxygen-terminated part constitutes less than a monolayer of the diamond surface. Accordingly, the oxygen coverage is estimated as follows:

$$\frac{I_{O1s}}{I_{C1s}} = \frac{X n_O \sigma_O \lambda_{m,O} \cos\Theta \left[1 - \exp\left(\frac{-1}{\lambda_{m,O}\cos\Theta}\right)\right]}{n_C \sigma_C \lambda_{m,C} \cos\Theta \left[1 - X + X\exp\left(\frac{-1}{\lambda_{m,O}\cos\Theta}\right)\right]} \tag{A.7}$$

As the detector is oriented parallel to the surface normal, $\cos\Theta$ is unity. Furthermore, we use λ instead of λ_m. We then simplify:

$$\underbrace{\frac{I_{O1s}}{I_{C1s}}\frac{n_C\sigma_C\lambda_C}{n_O\sigma_O\lambda_O}}_{Z} = \frac{X - X\exp\left(\frac{-a}{\lambda_O}\right)}{1 - X + X\exp\underbrace{\left(\frac{-a}{\lambda_O}\right)}_{\alpha}} \tag{A.8}$$

Normal calculus gives us the fraction of the surface covered by the oxygen-termination:

$$X = \frac{Z}{1+Z}\frac{1}{1-\exp\alpha} \tag{A.9}$$

The intensities can be directly taken from the areas of the fitted XPS peaks.

The density of the carbon atoms can be simply calculated from the volume density of $\rho = 3.515$ g/cm^3 with the Avogadro constant N_A and the molar mass of carbon M_C with $\frac{\rho N_A}{M_C}$ and is 1.76×10^{23} cm^{-3}. The reciprocal value is the volume of one atom and therefore the cube of the monolayer thickness a, which is then 0.18 nm. In order to estimate the density of the oxygen atoms of the oxygen termination, it is not sensible to take e.g. the liquid or solid oxygen density, as each oxygen atom rests at a carbon atom or between two carbon atoms. We therefore roughly estimate the density by assuming that it is equal to the surface density of the carbon atoms. Taking the mean of the (100) and (111) surface that is 1.7×10^{15} cm^{-2}. We then multiply with the monolayer thickness for diamond to get a volume density to reach 0.94×10^{23} cm^{-3}. For the monolayer thickness we again take the diamond value of 0.18 nm.

The atomic photoionization cross-section can be taken from literature databases [Yeh85]. The X-ray energy for the oxygen spectra was 730 eV and for the carbon spectra 480 eV, resulting in a photoelectron energy of roughly 200 eV in both cases. The inelastic mean free path are also taken from a literature database [Rol11] based on equations from Seah and Dench [Sea79]. Here, the photoelectron energy is the relevant energy, which is 200 eV for both the diamond and the oxygen case. For diamond the inelastic mean free path is 0.43 nm using the equations suitable for elements from Seah and Dench (for comparison: Tanuma et al. give a value of 0.57 nm [Tan05]). The inelastic mean free path for the oxygen is 0.57 nm, again from the same database and using the equation for elements as a surface monolayer (the density was given at 2.7 g/cm^3 according to the above considerations). All values are summed up in Table A.1.

According to these calculations, the overall value for the coverage of the oxygen-terminated part of the diamond surface is 3% for the best sample. While this discussion is educational with respect to the imprecisions involved in estimating a monolayer coverage from such XPS data, it shows that the final value can indeed only be taken as a rough estimate. Halving the surface density of oxygen, for example, doubles the final monolayer coverage value.

A.2 In-liquid Hall effect measurements under potential control

The Hall effect was first observed by E.H. Hall in 1879 [Hal79], who discovered that charge carriers in a conductor are deflected by a magnetic field perpendicular to the

thickness of monolayer a, oxygen	0.18	nm	estimate
thickness of monolayer, diamond	0.18	nm	calculated
surface density oxygen	0.94 $\times 10^{22}$	atoms/cm^3	estimate
surface density diamond	1.76 $\times 10^{23}$	atoms/cm^3	calculated
photoion. cross-section oxygen at 730 eV	2.5 $\times 10^5$	barns	[Yeh85]
photoion. cross-section carbon at 480 eV	3.0 $\times 10^5$	barns	[Yeh85]
IMFP oxygen (density 2.7 g/cm^3)	0.57	nm	[Rol11]
IMFP diamond (density 3.5 g/cm^3)	0.43	nm	[Rol11]
intensity ratio O1s to C1s peak	0.005		experimental
overall surface coverage ratio	3%		

Table A.1: *Parameters used for the calculation of the fraction of oxidized surface of hydrogenated diamond.*

direction of the current. As a result of the carrier deflection, a Hall voltage that is in turn perpendicular to the current and the magnetic field is induced. Figure A.1 illustrates the situation schematically. The Hall voltage U_H generates an electric

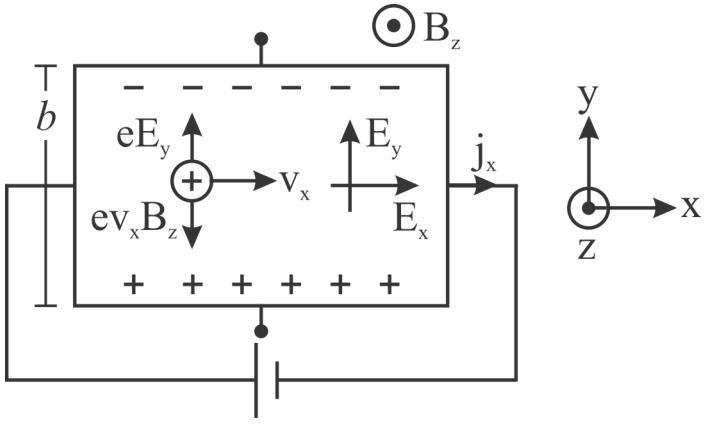

Figure A.1: *Schematic of the Hall effect represented for positive charge carriers. The two forces in y-direction acting on the charge carrier, eE_y and ev_xB_z, are opposite and equal.*

field E_y in the y-direction that exactly counteracts the Lorentz force on the charge carriers in a steady state situation.

$$F_y = 0 = -e(\vec{v} \times \vec{B})_y - eE_y = ev_xB_z - eE_y \ , \tag{A.10}$$

whereby $E_y = U_H/b$ is the so-called Hall field and b the width of the conductor. Assuming positive charge carriers, the current density is $j_x = \frac{I}{bd} = pev_x$, with d the thickness of the conductor, and p the hole density. Therefore,

$$E_y = \frac{U_H}{b} = \frac{1}{pe} j_x B = \frac{1}{pe} \frac{IB}{bd} \quad \text{or} \tag{A.11}$$

$$U_H = R_H \frac{IB}{d} \,, \tag{A.12}$$

where $R_H = 1/pe$ is called the Hall coefficient. If both holes and electrons contribute to the conductivity, the Hall coefficient is defined as:

$$R_H = \frac{p\mu_p^2 - n\mu_n^2}{e(p\mu_p + n\mu_n)^2} \,, \tag{A.13}$$

where μ_p and μ_n are the hole and electron mobility, respectively [Sho53, Yu05].
The conduction of carriers is hindered by scattering, where the time between two scattering events is named τ. When the charge carriers have a distribution in energy (which is the case in real systems), the scattering time τ also has an energy distribution. Additionally, different scattering mechanisms have different energy dependences [Sho53] [See04] [Yu05]. Taking this scattering into account, the Hall coefficient (for the sake of simplicity, here only considered for hole conduction) is

$$R_H = \frac{r_H}{ep} \tag{A.14}$$

where r_H represents the Hall factor

$$r_H = \frac{\langle \tau^2 \rangle}{\langle \tau \rangle^2} \tag{A.15}$$

$\langle \tau^2 \rangle$ denotes the mean squared scattering time, and $\langle \tau \rangle^2$ the square of the mean scattering time, which is always smaller. Here, the assumption is of spherical energy surfaces in the Brillouin zone and a scattering time only dependent on energy [Sho53]. With the conductivity $\sigma = e\mu p$ and the carrier concentration known from Hall effect measurements, the mobility μ can be calculated as $\mu = R_H \sigma$. However, the mobility derived from Hall effect measurements μ_{Hall} differs from the drift mobility μ_{drift} by the Hall factor:

$$\mu_{Hall} = r_H \mu_{drift} \tag{A.16}$$

The value of the Hall factor depends on the scattering mechanisms affecting the carrier transport and other factors, such as the shape of the energy surfaces in the Brillouin zone [Sho53]. Its value is usually not known, and is generally approximated by one. Despite these approximations, the Hall effect is an important technique to

determine both the concentration and the sign of the charge carriers in a sample as well as the mobility of the charge carriers.

As the surface-conductive channel of hydrogen-terminated diamond is two-dimensional, the sheet conductivity and the areal charge carrier concentration are the relevant quantities for this work. The sheet carrier density is therefore defined as $n_s = nd$, and the sheet resistance ρ_s is defined as $\rho_s = \rho/d$, when using equation A.12 as for the three-dimensional case. Alternatively, d needs to be set to 1 in equation A.12. The sheet resistivity has the unit [Ω], which is normally written as Ω/□ to differentiate it from the resistance - for this work however just Ω is used.

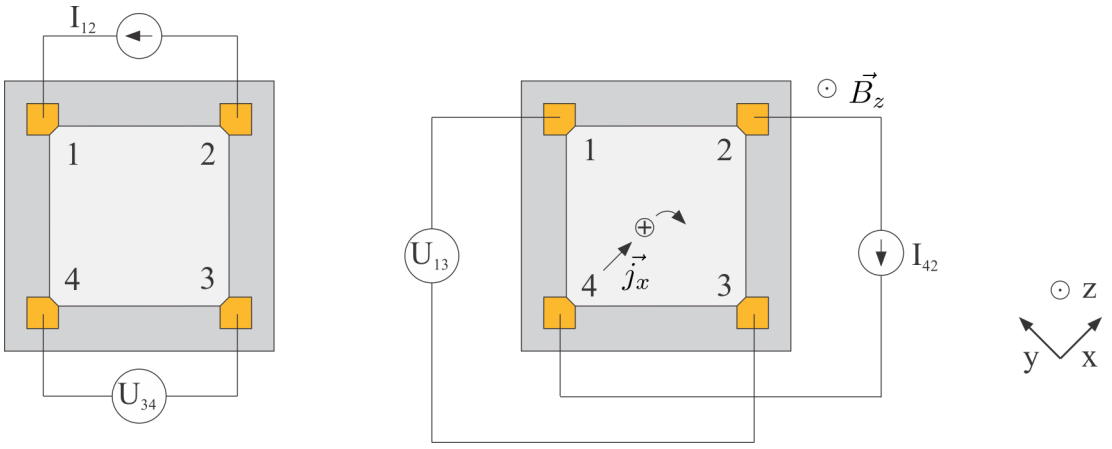

Figure A.2: *Van der Pauw configuration for measurements of the sheet conductivity (left) and the Hall effect (right). Only one of several configurations necessary for a complete measurement according to the van der Pauw theorem is shown.*

Besides the bar structure shown in Figure A.1, on flat samples, the Hall effect can also be measured in a van der Pauw configuration [Pau58]. Here, four contacts on the edge of the arbitrarily shaped sample are necessary, which are labeled clockwise as illustrated in Figure A.2. According to van der Pauw, the resistivity can be obtained by setting a current between two adjacent contacts and measuring the corresponding voltage across the remaining contacts. Thus, a resistance

$$R_{12,34} = \frac{I_{12}}{U_{34}} \tag{A.17}$$

can be evaluated. The first contact number is defined as the positive pole for the set current as well as the measured voltage. This procedure is repeated for $R_{23,41} = \frac{I_{23}}{U_{41}}$. These two measurements would suffice, but for added accuracy the measurement is permuted over all contacts with an additional polarity reversal. The resistivity can

then be calculated according to van der Pauw from [Pau58]:

$$exp\left(-\pi\frac{d}{\rho}\frac{R_{12,34}+R_{21,43}}{2}\right)+exp\left(-\pi\frac{d}{\rho}\frac{R_{23,41}+R_{32,14}}{2}\right) = 1 \quad (A.18)$$

$$\Leftrightarrow \rho=\frac{\pi d}{\ln 2}\frac{R_{12,34}+R_{23,41}}{2}f\left(\frac{R_{12,34}}{R_{23,41}}\right), \quad (A.19)$$

which leads to

$$\rho_s^A=\frac{\pi}{\ln 2}\frac{R_{12,34}+R_{21,43}+R_{23,41}+R_{32,14}}{4}f\left(Q\right)\ and \quad (A.20)$$

$$\rho_s^B=\frac{\pi}{\ln 2}\frac{R_{34,12}+R_{43,21}+R_{41,23}+R_{14,32}}{4}f\left(Q\right) \quad (A.21)$$

for the reciprocal resistances respectively (case A and B). The resistivity is replaced here with the sheet resistivity ρ_s. The function f is the solution to the equation

$$\cosh\left(\frac{\ln 2}{f}\frac{R_{12,34}-R_{23,41}}{R_{12,34}+R_{23,41}}\right)=\frac{1}{2}exp\left(\frac{\ln 2}{f}\right), \quad (A.22)$$

which cannot be solved analytically, but is approximated by a Taylor series:

$$f(Q)\approx 1-\frac{\ln 2}{2}\left(\frac{Q-1}{Q+1}\right)^2-\left(\frac{(\ln 2)^2}{4}-\frac{(\ln 2)^3}{12}\right)\left(\frac{Q-1}{Q+1}\right)^4 \quad (A.23)$$

where $Q=\frac{R_{12,34}+R_{21,43}}{R_{23,41}+R_{32,14}}$ for case A. For the samples used in this work, the error of this approximation is around 1%. In the case of samples with inhomogenous contacts and low resistivities the expected error is less than 5%. Finally, ρ_s^A and ρ_s^B are averaged, yielding the sheet resistance ρ_s of the sample.

For the Hall effect measurement according to van der Pauw, the current is applied diagonally across the sample and the Hall voltage measured via the remaining two contacts. In order to cancel out inhomogeneities, this configuration is permuted and the direction of the current reversed. Furthermore, to eliminate offset voltages, the Hall voltage U_H is obtained from measurements performed with and without magnetic field.

The van der Pauw theorem assumes point contacts located at the circumference of the sample [Pau58]. While photolithography allows us to place the contacts indeed at the circumference of the hydrogen-terminated and therefore conducting area of the sample (see Figure A.2), the contacts have a finite size. The minimum size of the contacts is also limited, as the conductivity decreases with the contact size and therefore limits the maximum current for a given voltage. For the sheet resistivity measurements, with a contact length of 0.1 mm and the length of the conducting

area of 2 mm, the calculated error is $\leq 0.1\%$ [Chw74]. The measured conductivity is enlarged by this value. Similarly, the Hall effect measurements are affected by the finite contact size and the error thus introduced is about 3 % for the geometry used [Chw74]. The measured Hall voltage is reduced by this value, which increases the calculated carrier concentration. As the error of the resistivity measurement is negligible in comparison, the Hall mobility is therefore reduced by approximately 3 %.

For Hall bar structures the geometry and the contacts also result in errors, just as for van der Pauw structures. The end contacts of the bar are limited in size, as they can short the Hall voltage for small length to width ratios of the bar [Ise48] [Kai06]. Additionally, the voltage-measuring contacts ideally need to be infinitesimally small. To reduce errors, the voltage contacts are put at the end of contact arms [Lak12]. The Hall voltage contacts also need to be placed opposite each other as accurately as possible.

Beyond these systematic geometric errors, there are also statistical errors caused by noise. The diamond samples measured for this work show a Hall voltage of roughly 50-150 μV with significant noise. Therefore, lock-in amplifiers were used for the measurements. Lock-in amplifiers have a greatly reduced bandwidth for recording and therefore reduce the noise significantly. The use of lock-in amplifiers is based on the fact that the noise of a signal is usually spread over a wide spectrum. By cross-correlating a known AC reference signal with the measured signal of the same frequency, and integrating over a long period of time, the contribution from other frequencies is strongly attenuated. Thus, when using the lock-in technique, an AC signal has to be used for the measurements.

A Hall effect and resistivity setup was developed to measure the charge accumulation, resistivity, and thereby the transport properties of the hydrogen-terminated diamond samples under electrolytic gate control. Figure A.3 illustrates this fully automated setup, which enables the characterization of the diamond solution gate field effect structures in normal operating conditions. Additionally, the gate control allows the measurement of charge accumulation and mobility over a range of carrier concentrations, yielding a much richer dataset in that respect than in ”dry” conditions. This can be used to understand the scattering mechanism limiting transport in diamond surface-conductive channels.

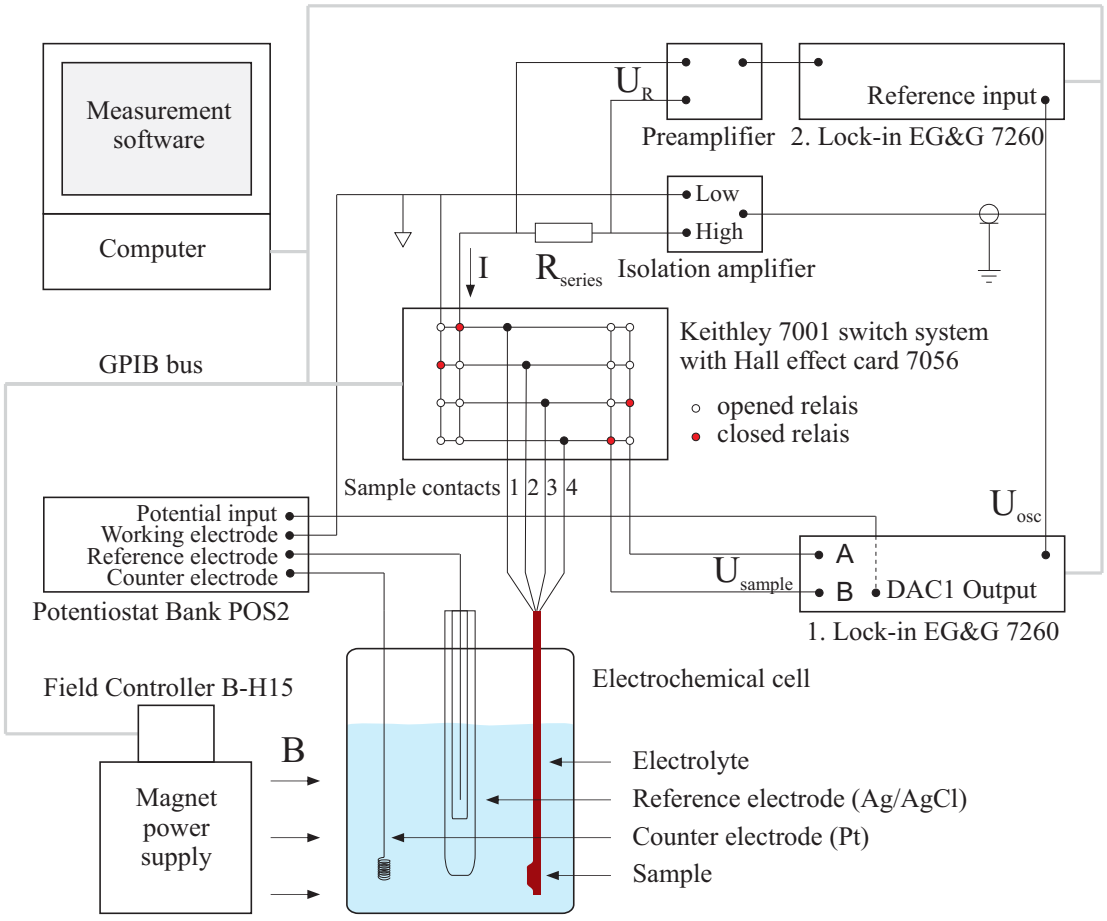

Figure A.3: *Schematic of the fully automated in-electrolyte Hall effect measurement setup with potential control. An example configuration is shown, with a current applied between contacts 1 and 2, and a voltage measurement between contacts 3 and 4. See text for details to the setup.*

The requirement for potential-controlled measurements in electrolyte causes a number of problems which need to be addressed. Initially, the potential control is implemented with a potentiostat and the sample in an electrochemical cell. The reference and counter electrode in the electrochemical cell are directly connected to the potentiostat, which also needs to be connected to one of the four contacts of the diamond sample, which functions as a working electrode. However, the resistivity and Hall measurement using the lock-in technique obviously require an AC current to be applied to the sample. The *low* contact of this AC current source, which is provided by the lock-in amplifier, shall be connected to ground. This would in effect put the working electrode, i.e. the diamond surface, on earth ground, preventing any effec-

tive control of its potential by the potentiostat. Therefore, an isolation amplifier (gain = 1) is employed to transmit the AC current provided by the oscillator output of the lock-in, at the same time galvanically separating the circuit from the earth ground of the lock-in. The *low* contact after the isolation amplifier is then a virtual ground and it can be connected to the working electrode input of the potentiostat and to one of the sample contacts. The *low* and the *high* contact of the isolation amplifier relay the AC current via a commercial switch system with an integrated Hall effect card to the four contacts of the diamond sample. The fully automated switch system applies the AC current according to the different configurations required by the van der Pauw technique described above. The remaining two contacts are used for the voltage measurements and directly relayed to the A and B input of the lock-in (these inputs are used in a A-B configuration and therefore floating with respect to earth ground). Finally, to actually determine the AC current, a resistor of known value is used after the *high* contact of the isolation amplifier. The voltage drop across this resistor is measured with a second lock-in amplifier, which gets its reference AC signal from the first lock-in amplifier. In order to enhance the input resistance of this second lock-in, a preamplifier (gain = 1) is used. This is not necessary for the first lock-in since the voltage is applied through the Hall effect card, which has a high input resistance. Both lock-in amplifiers and the switch system with Hall effect card are controlled via a GPIB bus from a computer with a measurement software [Lip10]. The magnet providing the electric field has a field controller, which is also controlled via the GPIB bus and the software. The gate potential is applied through the potentiostat, which receives the potential to apply from a DAC output of the first lock-in and is therefore also software controlled.

The in-electrolyte operation imposes further restrictions on the measurements. The gate potential of the sample is controlled via the working electrode contact. This contact is always made the *low* current leading contact for the Hall measurements so as not to influence the Hall voltage measurements. The working electrode therefore permutes over the four sample contacts for the different van der Pauw configurations. However, this in turn means, that the *high* current leading contact is on a potential different from the working electrode potential by the amount of voltage necessary to induce the set current in the sample. In order to measure a sample, which is approximately homogeneous, i.e. at the same potential and therefore the same carrier concentration over the whole sample area, the applied voltage needs to be limited. This limit was set to 50 mV, and no voltage applied to the sample exceeds this value. For high sample resistances this leads to small applied currents

(e.g. down to 50 nA) and is a further reason for the small Hall voltage signals and the need for the lock-in technique. Another requirement concerns the prevention of voltages capable of oxidizing the hydrogen-termination. It was observed, that besides user errors, these can occur e.g. during switching. In order to avoid these, all applied voltages are set to zero before the switch system changes the contact configuration. Furthermore, the magnet especially has been shown to cause massive (several volts) potential peaks when turning on or switching the direction of the current. Consequently, the magnet is turned on to a negligible field (0.01 T) before the sample is installed between the pole shoes of the magnet. From then on, the magnet field is only varied from this initial value to the maximum value (0.01 T to 1.8 T). Efforts to prevent these voltage peaks with a low pass filter (capacitance parallel to the lead to the sample) have been proved futile.

The application of the lock-in technique and an AC setup generally allows for more accurate measurements. However, additional effects from AC currents and voltages have to be taken into account. The electric circuit contains a number of capacitances and resistances, which form low pass filters. Capacitances include e.g. the capacitance of BNC cables, but especially the capacitance of the diamond / electrolyte interface, which also gets charged and discharged by the AC voltages applied. Figure A.4 shows the frequency dependence of the resistance across the sample in a van der Pauw configuration. As the actual Hall voltage is measured as a difference between the voltage at the Hall contacts at two different magnetic fields, the dependence on the frequency of the Hall voltage is much weaker. The low pass behavior illustrated in Figure A.4 can be calculated from the equivalent circuit also shown. The values of the resistances for the calculation are taken from experimental electrochemical impedance spectroscopy data.

$$Z_{sample}^{\mathrm{Theory}}(f) = \left| \left(\frac{1}{0.5R_{sample}} + \left(R_{\mathrm{el}} + \frac{1}{1/R_{\mathrm{ct}} + i2\pi f C_{\mathrm{dl}}} \right)^{-1} \right)^{-1} + 0.5R_{sample} \right| \tag{A.24}$$

Considering this data, a frequency of 1 Hz or lower eliminates the low pass effects from the AC measurements. However, the isolation amplifier needs a minimal frequency to have its intended gain of 1 (gain 0.99 at 1 Hz). Therefore a measuring frequency of 1 Hz is chosen.

A further problem of measuring in electrolyte is caused by drift of the interfacial potential. When the gate voltage of the sample is set by the potentiostat, the actual potential of the sample takes some time to reach an equilibrium value. Possible explanations for this effect are e.g. changes in the surface charge. The sample resis-

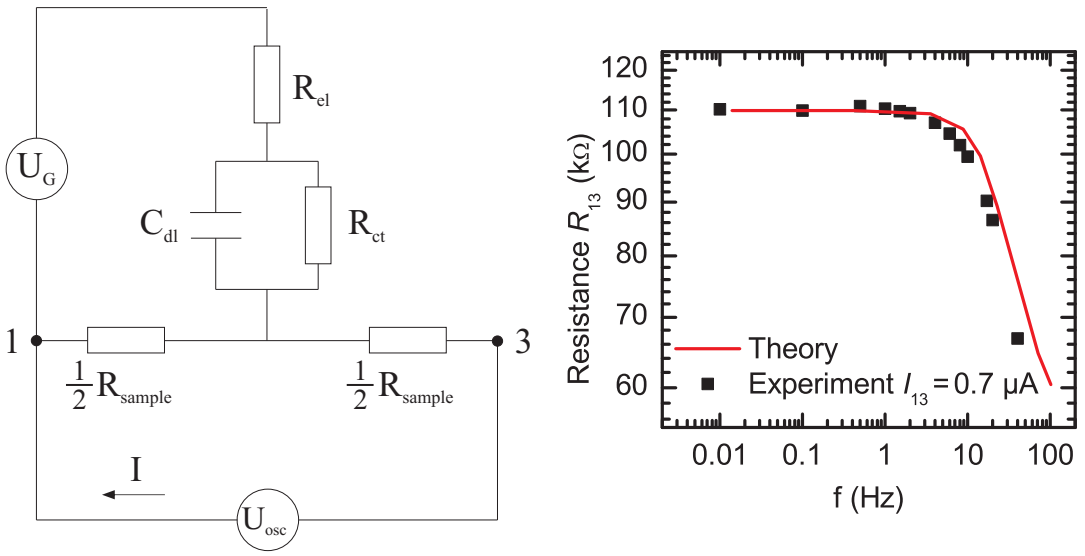

Figure A.4: *left: Equivalent circuit of the diamond/electrolyte interface and the sample resistance R_{sample} with an applied gate voltage U_G and a potential U_{OSC} applied between contacts 1 and 3. The double layer capacitance C_{dl} of the interface, the charge transfer resistance R_{ct} across the interface, and the resistance of the electrolyte R_{el} are shown. The interface acts as a low pass filter. right: Frequency dependence of the resistance measured between contacts 1 and 3 with the sample in electrolyte. The red curve represents a calculation assuming the equivalent circuit shown on the left, obtained from equation A.24.*

tance, which is dependent on the actual potential, thus changes over time [Lip10]. Accordingly, after setting a new potential, a waiting time of 5 min was implemented, after which the resistance value changes less than 2 %.

Some transport mechanisms are temperature dependent [Arn76], therefore the in-liquid Hall effect setup was equipped with a temperature control. This was achieved with a heating coil in the electrochemical cell, operated with a thermostat. Obviously the temperature range for an aqueous electrolyte is limited and the effective range of this setup is from 7°C to 80°C.

Beyond the intended change of the sample temperature, that of the electrolyte and the other electrodes is changed as well. The reference electrode is slightly temperature dependent, with a change of 6.5 mV in the reference electrode potential between 7 and 80°C [Stü08]. This has been investigated by measuring the potential difference between two identical reference electrodes in two separate electrolyte baths connected by a salt bridge. While one of the baths is kept at room temperature, the temperature of the other bath can be varied while detecting a change in the

potential difference of the two electrodes in an open circuit mode [Stü08] [Bar87].

The electrolyte is affected by the temperature through its effect on the acid dissociation constant (pK_a), which determines the pH at given concentrations (see Appendix A.4.1) [Bey96]. The pK_a value is affected by temperature and also by the ionic strength. A change of pH in turn affects the ionic strength as an acid and its conjugate base have different valency. Overall, for the temperature range between 7°C and 80°C, the ionic strength changes by approximately 10% and the pH changes from pH 6.9 to pH 7.1. These small changes of pH and ionic strength due to the temperature change have an negligible effect on the effective potential of the diamond samples [Har07].

The software controlling the resistivity and Hall effect measurements is fully automatic. After installing the sample and setting the measurement parameters, the software executes the resistivity measurement, followed by the Hall measurement, and repeats this for a given series of gate potentials. Not only does this add to the reproducibility of the measurements and avoids user errors during the multitude of singular measurements and configuration changes. It also allows a more efficient time allocation on behalf of the user - at least after the completion of the setup itself. While this might appear to be a mere convenience, it qualitatively affects the research. In a situation, where a complex system is under investigation with a high number and variation of parameters, automation brings measurements within reach, that would be deemed unrealistic otherwise - just as the advent of broadband internet has not only made things faster, but by doing so also spawned new applications such as video streaming.

For this work the van der Pauw structure has been used exclusively. However, the measurement software and the setup in general also allow the use of an 8-contact Hall bar. While not used in this work, as this option became available only late, it has been tested and is operational. The main advantages of a van der Pauw configuration is the possibility to measure flat samples of *arbitrary* shape, and the need of only four contacts [Lak12]. For the Hall bar at least six, and better eight, contacts are necessary and obviously the sample has to be brought into a Hall bar shape. Since some form of photolithographic processing is necessary for the surface conducting diamond samples in any event, a Hall bar structure is little additional effort. While the accuracy might not be greater than with a van der Pauw structure, the analysis is more straightforward, which should be especially helpful when investigating unknown and possibly inhomogeneous materials. An additional advantage is that the Hall bar requires less measurements and thus is faster than

the van der Pauw measurement.

A.3 Interfacial capacitance and threshold voltage

Table A.2: *Interfacial capacitance and threshold voltage of a subset of the investigated diamond samples in Figure 3.7. For a few samples the measured data does not allow a sensible calculation for each value as the carrier concentration-gate voltage dependence is not linear.*

sample name	surface orientation	impurity grade	$C_{interface}$ [μF cm^{-2}]	U_{th} [mV]
S29a	(100)	op	3.00	165
S28a	(100)	op	2.95	223
S24a	(100)	op	2.78	282
S29b	(100)	op	2.41	125
S25b	(100)	op	2.69	-23
S42a	(100)	op	2.43	399
S38b	(100)	op	2.35	512
S17a	(100)	IIa	3.39	-44
S17b	(100)	IIa	2.75	-64
S21d	(100)	IIa	2.15	241
S17c	(100)	IIa	2.31	175
S50b	(100)	-	2.42	393
S43a	(100)	op	2.40	132
S39b	(100)	200 ppm	3.69	-166
S36b	(100)	-	1.68	-286
S34a	(100)	el	2.51	189
S40a	(100)	el	3.02	12
S41a	(100)	el	1.88	81
S35b	(100)	el	2.37	-184
S34b	(100)	el	2.32	-7
S33b	(100)	el	1.26	-265
S32b	(100)	el	1.48	-79
S27a	(111)	op	4.37	291

continued on next page

continued from previous page				
S26a	(111)	op	4.23	347
S31a	(111)	op	4.19	285
S30a	(111)	op	3.92	442
S31b	(111)	op	4.74	37
S30b	(111)	op	4.53	55
S9d	(111)	IIa	4.47	89
S6d	(111)	IIa	3.83	49

A.4 Electrochemical cell

In order to set the potential of an electrode in an electrolyte on an absolute scale (e.g. vs. vacuum potential), a second electrode is necessary as a reference point versus which to apply the potential (see e.g. [Bar01] or [Boc98] for details). This second electrode is called reference electrode in electrochemistry. The electrode whose potential is set is called the working electrode. The reference electrode potential is established by a chemical reaction at defined reaction conditions delivering a reproducible electrochemical potential. An example is the silver/silver-chloride (Ag/AgCl) reference electrode employed in this work, which uses the solvation of Ag^+ and Cl^- ions from AgCl into a solution with defined Cl^- concentration to establish its potential. On a physical scale the electrochemical potential of the 3M Ag/AgCl electrode is approximately at -4.7 eV versus the vacuum potential [Ive61]. Any current through the reference electrode will influence its potential. Therefore, the electrochemical equivalent of a four point measurement is often used to set the working electrode potential. A device called potentiostat measures the potential between the reference and the working electrode via a high impedance input and therefore with minimal current. In order to then adjust the working electrode potential to the desired value, a potential is applied via the working electrode and a third electrode, the so-called counter electrode. Figure A.5 shows the operating mechanism of a potentiostat. In case the reference and counter electrode are not separated, but one and the same, the potentiostat just acts as any normal voltage source and the configuration is called a two electrode configuration.

In this work, the investigated hydrogen-terminated diamond sample is the working electrode. With the setup described above, their electrochemical potential can be set to the desired value. This can either be used to explore the electrochemical properties at different electrode potentials or to change the surface conductivity as

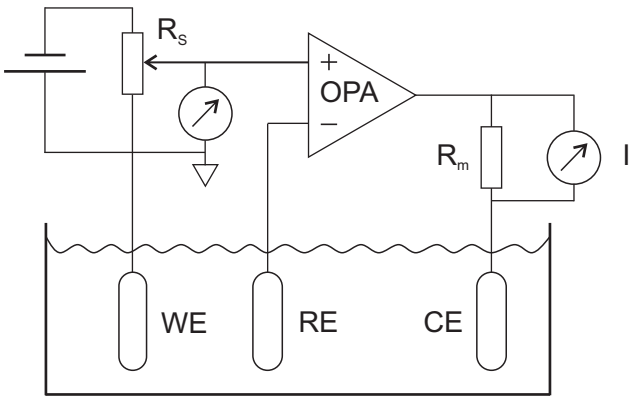

Figure A.5: *Schematic of a potentiostat with an adjustable target potential and current measurement. The desired potential difference between the working electrode (WE) and the reference electrode (RE) is obtained by the operational amplifier (OPA) applying an appropriate potential between the working and the counter electrode (CE).*

for the SGFETs (see Section 3.1), thereby effectively using the reference electrode and the electrolyte as a gate.

A.4.1 Electrolyte

The standard electrolyte used for most experiments in this work was a phosphate based buffer solution with potassium or sodium chloride added. The pH was usually 7, with an ionic strength of 0.05 M, and a buffer concentration of 0.01 M.

The pH of a buffer solution is determined by the concentration ratio between the buffer acid $[HA]$ and its conjugate base $[A^-]$ according to the Henderson-Hasselbalch equation [Bey96]:

$$pH = pK_a + \log_{10} \frac{[A^-]}{[HA]} \tag{A.25}$$

The pK_a of the protonation/deprotonation reaction of the buffer is dependent on temperature and ionic strength I [Bey96]:

$$pK_a^{'} = pK_a + (2z_{acid} - 1) \left[\frac{A\sqrt{I}}{1 + \sqrt{I}} - 0.1I \right] , \tag{A.26}$$

where z_{acid} is the valency of the conjugate buffer acid and A is a correction factor dependent on temperature. $A = 0.507$ at 20°C [Bey96].

The phosphate buffer has three pK_a points corresponding to the stepwise deproto-

nation of the phosphoric acid [Bey96]:

$$pK_{a1} = 2.15 \ \ for \ \ [H_3PO_4] \rightarrow [H_2PO_4]^- \tag{A.27}$$

$$pK_{a2} = 7.2 \ \ for \ \ [H_2PO_4]^- \rightarrow [HPO_4]^{2-} \tag{A.28}$$

$$pK_{a3} = 12.33 \ \ for \ \ [HPO_4]^{2-} \rightarrow [PO_4]^{3-} \tag{A.29}$$

A variation in pH changes the ratio between two of these conjugate acid/base pairs. It changes the valency of the buffer and therefore the ionic strength. As the pK_a of the buffer reaction is itself influenced by the ionic strength, the pH and ionic strength are interdependent. For accurate measurements it is necessary that the ionic strength is controlled and adjusted for changes in the pH. Additions of base salt (e.g. potassium chloride) or water keep the ionic strength constant in experiments varying the pH.

In order to prepare an electrolyte buffer solution, four steps are necessary making use of the equations given above:

1. Determine the temperature of use, the ionic strength and type base salt, the type of buffer and the buffer concentration, and the desired pH for the electrolyte.
2. Calculate the corrected pKa (for the appropriate pH range).
3. Calculate the amount of base needed.
4. Calculate the amount of base salt needed to reach the desired ionic strength.

A.4.2 "Soft" turn on/off of equipment

The on/off switching of the potentiostat has been shown to lead to voltage peaks, that can oxidize the hydrogen-terminated diamond working electrode (see Section 2.2.7). The following procedure was developed for the soft on/off switching of the potentiostat, thereby avoiding said potential peaks.

switch on:

1. The WE potential of the potentiostat is set to zero.
2. The RE, WE, and CE are all connected to the (floating) dummy cell.
3. The potentiostat is now turned on (cell active).
4. The RE connector is connected additionally to the real RE. The input impedance of the RE is very high, and no voltage is applied. However, the potential of the RE input is already brought closer to the real RE potential of the cell.
5. The WE connector is connected additionally to the real WE.
6. The CE connector is connected additionally to the real CE.

7. The WE connector is disconnected from the dummy WE.
8. The CE connector is disconnected from the dummy CE.
9. The RE connector is disconnected from the dummy RE.
10. Finally, the WE potential of the potentiostat can be set to the desired value.

switch off:

1. The WE potential of the potentiostat is set to zero.
2. The RE connector is connected additionally to the dummy RE.
3. The WE connector is connected additionally to the dummy WE.
4. The CE connector is connected additionally to the dummy CE.
5. The WE connector is disconnected from the real WE.
6. The CE connector is disconnected from the real CE.
7. The RE connector is disconnected from the real RE.
8. The potentiostat can now be turned off.

A.5 Sample fabrication

A.5.1 SGFET fabrication

Starting from a hydrogenated sample (see Section 2.2.2), the following processing steps are performed:

1) **Photolithography for metal evaporation:** The samples are placed on a spinner and rinsed first with acetone and subsequently with isopropanol. Finally, they are tried with nitrogen to remove surface contaminations. A standard photoresist (S1818; Rohm and Haas Company) is spin-coated on the sample (9000 revolutions per minute, 30 s). As the diamond samples are very small (e.g. 3x3 mm^2) compared to wafers usually used for spin-coating, photoresist accumulates in the corners of the sample surface, forming edge-beads. As these edge-beads are higher than the rest of the photoresist-covered sample surface, they prevent a close approach of the photomask during exposure, resulting in an inaccurate transfer of the pattern to the photoresist on the sample. Thus, the edge-beads are best removed with a razor-blade, while the sample is still on the spinner. After spin-coating, a pre-expose bake follows for 10 min in a 90°C oven. The photoresist is exposed for 5 s with a 365 nm wavelength mercury lamp in a commercial mask aligner to transfer the pattern of the photomask onto the photoresist. Subsequently, the samples

are developed by immersion in diluted potassium hydroxide for 20 s. The development is stopped by immersing and rinsing the samples with DI water.

2) **Evaporation of bond pads and leads:** After the development of the photoresist, the samples are oxidized in an oxygen plasma reactor (300 s, 1.4 mbar oxygen, 200 W). This significantly increases the adhesion of the metal to the diamond surface. After oxidation, the samples are mounted in a metal evaporation system (base pressure 1×10^{-6} mbar). 100 Å of titanium is evaporated on the sample surface as an adhesion layer, followed by 1000 Å gold. For lift-off, the samples are immersed in acetone to dissolve the photoresist underneath. Ultrasound (at least up to 140 V) may be used to aid the lift-off process. Samples should not be allowed to dry while the lift-off process is not complete, to avoid metal flakes sticking to the diamond surface.

3) **Definition of the conductive area:** In a second photolithography step, the conductive regions are defined by covering them with photoresist and oxidizing the rest of the exposed surface. The same parameters apply for the coating with photoresist as previously. The samples are subsequently oxidized in the oxygen plasma reactor (300 s, 1.4 mbar oxygen, 200 W). All sides of the sample need to be oxygen terminated to avoid short-circuits (depending on the layout of the final structure). It is necessary for each side to face upwards and be subjected to the oxidation procedure separately. After oxidation, the photoresist protection is removed from the samples with acetone.

4) **Contacting the conductive areas:** The conductive regions need to be separately contacted by a gold overlap from the previously evaporated metal leads onto the conductive areas. This two step procedure is necessary as the metal does not adhere well to the hydrogen-terminated regions. For this step, the samples are best mounted in a metal evaporation system immediately after removing the photoresist from the previous step with the acetone/isopropanol/nitrogen rinsing. 1000 Å of gold are evaporated on the whole sample surface. This is followed by standard photolithography as in the previous steps to protect the metal contacts that should remain on the surface with photoresist. The sample is then immersed in a KI/I_2 solution (20 ml H_2O, 2 g KI, 0.5 g I_2) for 45 - 60 s and constantly agitated. The KI/I_2 solution dissolves the gold from the areas not protected by photoresist - the etching rate depends on the concentration of the solution. However, underetching beneath the photoresist from the edges can be a problem; it is around

2 μm for the specified concentration and time. The etching process is terminated by immersing the sample in DI water and rinsing with DI water. The protective photoresist layer is removed by immersing the sample and carefully rinsing it with acetone, followed by isopropanol, and drying with nitrogen. As soon as the protective photoresist layer is dissolved, the metal overlap onto the conductive areas is very vulnerable to mechanical damage!

5) **SU-8 passivation of metal areas:** As the samples will be immersed in electrolyte, the metal contacts need to be passivated in order to avoid faradaic reactions at the metal areas. This passivation is accomplished with the negative SU-8 photoresist (SU-8 2002 MicroChem Corp.). The samples are mounted on the spinner after the previous step and a small drop of SU-8 is placed on the sample. To dose the SU-8, a syringe with a 0.4 mm needle has proved useful (storing it in upright position for some minutes minimizes bubbles). Immediately after placing the SU-8 on the sample, the sample is spun at 6000 revolutions per minute for 40 s. As the SU-8 cannot be removed with acetone, proper removal of the edge-beads is critical to ensure a perfect transfer of the pattern of the photomask onto the resist. The SU-8 requires a pre-expose bake on a hotplate for a total of 4 minutes on a glass slide - 2 min ramping to 95°C and 2 min heating at 95°C. During this heating, the sample is covered with a hood and flooded with nitrogen as a precaution against oxidation - though the necessity of this is unproven. After the pre-expose bake, the SU-8 covered samples are exposed for 6 s (365 nm). This is followed by a post-expose bake, analogue to the pre-expose bake. The sample is then developed with a SU-8 developer for 60 s, and the developing process is stopped with isopropanol. The whole process is repeated to form a second SU-8 layer in order to avoid pin-holes. No acetone should be applied to the sample after the first layer! Finally, the SU-8 is cured with a hard bake to give it its stability. The hard bake requires baking at 150°C for 30 minutes and should be performed in an oxygen-free environment to avoid oxidation ($p < 1 \times 10^{-6}$ mbar). Especially for delicate structures with small openings in the SU-8 for small gates, the SU-8 process causes difficulties. A sufficient exposure of the SU-8 is necessary, so as not to remove it during developing. However, scattering of light during exposure might expose areas, that are meant to be free of SU-8 and thus, e.g. cover gate areas. This necessitates a careful choice of the exposure time. The resolution limit for this process are gate areas with a width of 10 μm, though reproducible success could only be achieved with a 20 μm width. As the dia-

mond is transparent, backscattering from the back of the diamond sample or the surface beneath the sample can also contribute to unwanted exposure.

6) **Packaging and bonding:** The processed sample is placed onto the sample holder with double-sided adhesive tape. Bonding to connect the bond pads on the sample with the sample holder contacts should start with the first bond on the bond pad and the second on the sample holder contact. Two bonds per bond pad serve as backup. The bonds may be mechanically strengthened by silver glue.

7) **Passivation of metal leads with silicone glue:** The sample can now be sealed with silicone glue (Scrintec 901) to passivate all leads to the sample and the sample holder. The silicone glue is applied manually under a microscope with a fine wire and a toothpick as tools.

A.5.2 Sample recycling

1) **Mechanical cleaning:** Initially, scrintec silicone glue, SU-8, bond wires, and double sided adhesive tape are macroscopically removed from the sample with a razor blade and tweezers. In a second step, the samples are thoroughly cleaned with Q-tips, while being immersed in acetone, until all visible residues are completely removed.

2) **Chemical removal of SU-8 and other residues:** The samples are immersed in a covered acetone bath with ultrasound (US) for 60 minutes at 50°C to remove residues of photoresist. The acetone is removed by rinsing the samples with isopropanol. For SU-8 removal, the samples are cooked at 70°C plus US for 60 minutes in commercially available SU-8 remover (MicroChem), followed by rinsing with isopropanol and drying with nitrogen. Cooking at 80°C plus US for 60 minutes in a highly concentrated aqueous hydroxide solution dissolved residues of SU-8. Finally samples are rinsed with DI water.

3) **Chemical removal of metal contacts:** Aqua regia (3/4 hydrochloric acid 37 % and 1/4 nitric acid 65 %) at 80°C for 60 minutes disolves the Ti/Au contacts and other metal contaminations. Subsequently, the samples are rinsed in DI water.

4) **Wet chemical oxidation:** The samples are immersed in sulphuric acid with a small quantity of KNO_3 ($\approx$ 0.5 g per 20 ml H_2SO_4) at 225°C for 60 minutes, in

order to remove graphitic carbon and chemically oxidize the diamond surface. The samples are again rinsed repeatedly in DI water to remove any ionic contaminations and dried with nitrogen.

5) **Plasma oxidation:** Directly before hydrogen termination, the samples are oxidized in a microwave oxygen plasma reactor for 300 s at 1.4 mbar and 200 W. This step leaves the surface in a defined oxidized state and removes any adsorbed organic contaminations.

A.5.3 Oxidation with ozone

Procedure for oxidation with UV-generated ozone:

1. Mount the sample in the reaction chamber and close the reaction chamber while leaving open an exhaust. The reaction chamber should be situated in a fume hood to dispose the generated ozone gas.
2. The reaction chamber is flushed with oxygen for two minutes.
3. While still flushing the chamber with oxygen, seal it as good as possible, and then turn off the oxygen flow.
4. Turn on the UV lamp (check whether the lamp is working through an inspection window).
5. After the desired process time, turn off the UV lamp, immediately flush with nitrogen and open the chamber. Be aware of the ozone flushed out from the chamber!
6. Unmount the sample. Flush it with nitrogen to remove any ozone residues.

A.5.4 Functionalization of diamond surfaces

Hydrogen-terminated diamond surfaces can be functionalized with trifluoroacetamide-protected 10-aminodec-1-ene (TFAAD) (see Figure A.6). The hydrogen-terminated diamond sample is covered with TFAAD and illumination with UV-light induces electron transfer from the diamond valence band that activates the double bond of the molecule and enables the bond to the diamond surface. The TFA-protected end is deprotected with tetramethylammonium hydroxide solution leaving an amine end-group, that can be used for further functionalization.
The functionalization of oxygen-terminated diamond surfaces with 3-aminopropyl-triethoxysilane (APTES) requires no special activation. The silanes react to silanols with hydroxyl groups on the oxygen-terminated diamond surface in the presence of adsorbed water (see Figure A.7).

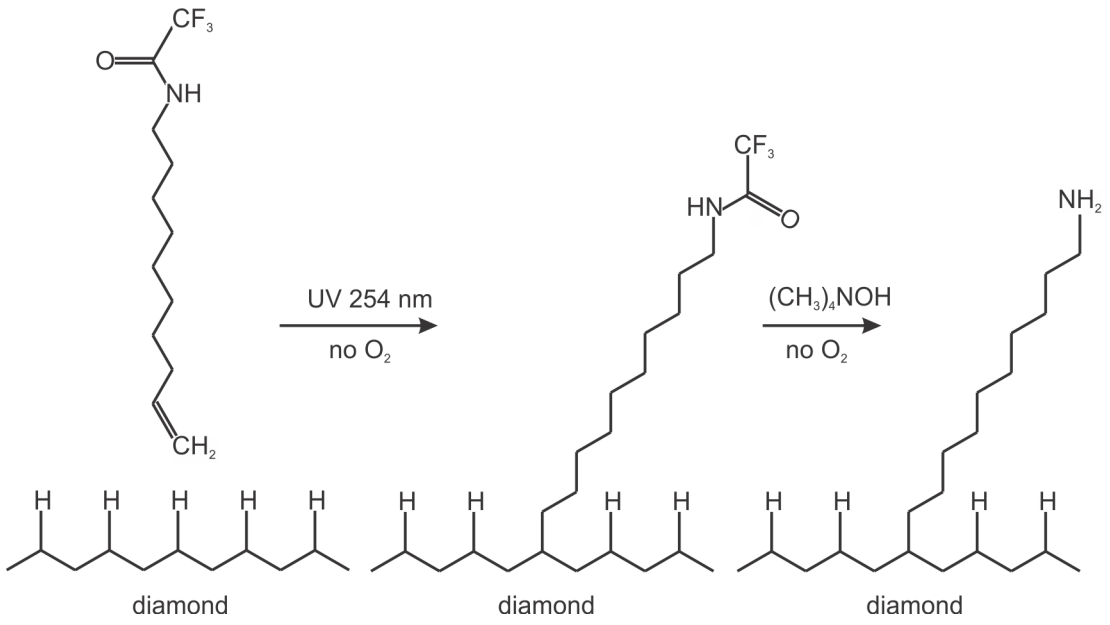

Figure A.6: *The UV light induces electron transfer from the diamond surface into the TFAAD molecule and thus activates the double bond of TFAAD. The attached TFAAD is deprotected with a tetramethylammonium hydroxide solution, leaving a terminal amine group.*

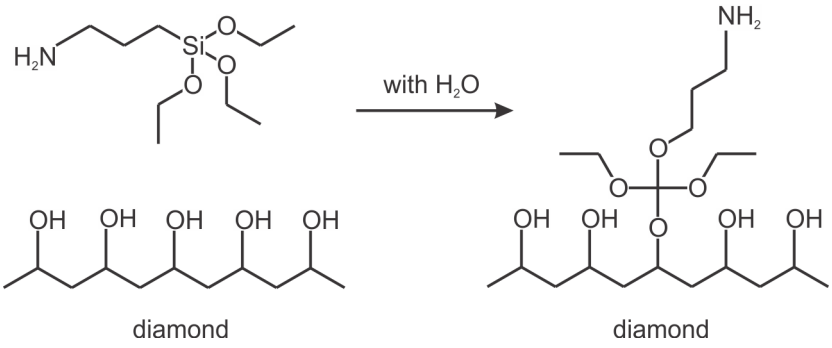

Figure A.7: *The ethoxy groups of the APTES molecule react to silanols with the water adsorbed on the oxygen-terminated diamond surface and subsequently bond to the hydroxyl groups at the diamond surface.*

Protocol for the functionalization of hydrogen-terminated diamond surfaces with TFAAD:

1. Put the hydrogen-terminated diamond sample into the UV reaction chamber and cover it with TFAAD.
2. Place a UV-transparent quartz glass slide on top of the sample. This generates a thin film of TFAAD between sample and glass slide.

3. Close the UV reaction chamber and flood it with nitrogen.
4. Turn on the UV lamp (254 nm). Use a filter to cut off shorter wavelengths.
5. After 2 hours the process is finished. Clean the sample (and the glass slide) with chloroform in an US bath for 15 min, followed by a methanol cleaning in an US bath for further 15 min. Dry with nitrogen.
6. Clean the sample in dilute acetic acid in an US bath for 15 min to remove adsorbed contaminations.

Protocol for the functionalization of oxygen-terminated diamond surfaces with APTES:

1. Place the oxygen-terminated diamond sample into a beaker with a mixture of 20 ml toluene and 95 μl of APTES.
2. Place the beaker for 90 min in a cooled US bath.
3. Clean the sample with toluene for 15 min in an US bath, followed by cleaning with isopropanol for a further 15 min.
4. Dry the sample with nitrogen.
5. Clean the sample in dilute acetic acid in an US bath for 15 min to remove adsorbed contaminations.

A.6 Sample specification

A vast number of diamond samples has been used in this work, 24 of which are identified in the data presented in this work and listed in Table A.3. The sample labels include a number differentiating between the samples, followed by a letter differentiating between devices processed and measured on one and the same sample, with the sample undergoing the recycling procedure (see Section A.5.2) in between the measurements. The measurements on the samples with letters "b", "c", and "d" have been discussed previously [Stü08, Lip10] and their historic label is given for easy reference. The samples include natural diamond samples of IIa quality with a nitrogen impurity content of < 50 ppm. All other samples are CVD grown. Optical grade samples have less than 5 ppm nitrogen impurities, electronic grade samples have less than 5 ppb nitrogen impurities and less than 1 ppb boron impurities. In this work natural IIa and optical grade samples are usually put in one category, as their nitrogen impurity concentrations are of a similar order. Samples "S37", "S38", and "S42" are of optical grade impurity quality, but contain significant surface damage in the form of cavities in the micrometer range. "S39" contains an especially

high amount of nitrogen, 200 ppm. "S36" is supposed to contain comparatively less dislocations according to the manufacturer (Element Six Ltd.). "S50" and "S51" are high quality, very pure homoepitaxial layers on top of a HPHT diamond substrate grown at CEA LIST, France. "S43" is a sample grown in the "AIST" institute in Japan. Samples "S34", "S35", "S40", and "S41" are "super polished" samples polished by "Diamond Detectors Ltd.", that do not show any polishing lines in the AFM. All natural IIa, optical and electronic grade samples are polished conventionally and do show polishing lines. All samples are 3x3 mm^2 in size, except the "super polished" samples, which are 4.5x4.5 mm^2 in size.

Table A.3: *Diamond samples with specifications used in this work.*

sample name	historic sample label	surface orientation	nitrogen impurity grade	specifications
S6c	6v3 [Stü08]	(111)	IIa	[N]<50 ppm
S6d	6v4 [Stü08]	(111)	IIa	[N]<50 ppm
S9d	9v4 [Stü08]	(111)	IIa	[N]<50 ppm
S17a	-	(100)	IIa	[N]<50 ppm
S17b	S17 [Lip10]	(100)	IIa	[N]<50 ppm
S17c	17v3 [Stü08]	(100)	IIa	[N]<50 ppm
S21c	21v3 [Stü08]	(100)	IIa	[N]<50 ppm
S21d	21v4 [Stü08]	(100)	IIa	[N]<50 ppm
S24a	-	(100)	op	[N]<5 ppm
S25a	-	(100)	op	[N]<5 ppm
S26a	-	(111)	op	[N]<5 ppm
S27a	-	(111)	op	[N]<5 ppm
S28a	-	(100)	op	[N]<5 ppm
S29a	-	(100)	op	[N]<5 ppm
S29b	S29 [Lip10]	(100)	op	[N]<5 ppm
S30a	-	(111)	op	[N]<5 ppm

continued on next page

continued from previous page				
S30b	S30 [Lip10]	(111)	op	[N]<5 ppm
S31a	-	(111)	op	[N]<5 ppm
S31b	S31 [Lip10]	(111)	op	[N]<5 ppm
S32b	S32 [Lip10]	(100)	el	[N]<5 ppb; [B]<1 ppb
S33b	S33 [Lip10]	(100)	el	[N]<5 ppb; [B]<1 ppb
S34a	-	(100)	el	"super" polished; [N]<5 ppb; [B]<1 ppb
S34b	S34 [Lip10]	(100)	el	"super" polished; [N]<5 ppb; [B]<1 ppb
S35b	S35 [Lip10]	(100)	el	"super" polished; [N]<5 ppb; [B]<1 ppb
S36b	S36 [Lip10]	(100)	-	low dislocation density
S37b	S37 [Lip10]	(100)	op	[N]<1 ppm; [B]<0.05 ppm
S38b	S38 [Lip10]	(100)	op	[N]<1 ppm; [B]<0.05 ppm
S39b	S39 [Lip10]	(100)	Ib	[N]<200 ppm; [B]<0.1 ppm
S40a	-	(100)	el	"super" polished; [N]<5 ppb; [B]<1 ppb
S41a	-	(100)	el	"super" polished; [N]<5 ppb; [B]<1 ppb
S42a	-	(100)	op	[N]<1 ppm; [B]<0.05 ppm
S43a	-	(100)	op	no polishing; similar to op. grade
S50b	S50 [Lip10]	(100)	-	homoepi1 no polishing; similar to el. grade
S51b	S51 [Lip10]	(100)	-	homoepi2 no polishing; similar to el. grade

The graphene samples used in this work were epitaxial graphene prepared on the Si face of SiC substrates using annealing in an UHV setup [Dan10].

Bibliography

[Ada07] S. Adam, E. H. Hwang, V. M. Galitski and S. Das Sarma: *A self-consistent theory for graphene transport*, Proc. Natl. Acad. Sci. U. S. A. **104**, 18392 (2007).

[Adk79] C. J. Adkins: *Effective-medium theory of conductivity and Hall-effect in 2 dimensions*, J. Phys. C Solid State **12**, 3389 (1979).

[Akh10] R. Akhvlediani, S. Michaelson and A. Hoffman: *Interaction of water molecules with bare and deuterated polycrystalline diamond surface studied by high resolution electron energy loss and X-ray photoelectron spectroscopies*, Surf. Sci. **604**, 2129 (2010).

[Alb02] B. Alberts, A. Johnson, L. Lewis, M. Raff, K. Roberts and P. Walter: *Molecular Biology of the Cell*, Garland Science, 2002.

[And82] T. Ando, A. B. Fowler and F. Stern: *Electronic properties of two-dimensional systems*, Rev. Mod. Phys. **54**, 437 (1982).

[Ang08] P. K. Ang, W. Chen, A. T. S. Wee and K. P. Loh: *Solution-gated epitaxial graphene as pH sensor*, J. Am. Chem. Soc. **130**, 14392 (2008).

[Arn74] E. Arnold: *Disorder-induced carrier localization in silicon surface inversion layers*, Appl. Phys. Lett. **25**, 705 (1974).

[Arn76] E. Arnold: *Conduction mechanisms in bandtails at the Si-SiO_2 interface*, Surf. Sci. **58**, 60 (1976).

[Bar87] P. Barabash, R. Cobbold and W. Wlodarski: *Analysis of the threshold voltage and its temperature-dependence in electrolyte-insulator-semiconductor field-effect transistors (EISFETs)*, IEEE T. Electron Dev. **34**, 1271 (1987).

[Bar01] A. Bard and L. Faulkner: *Electrochemical Methods: Fundamentals and Applications*, John Wiley & Sons, 2001, Second edn..

[Bas81] V. K. Bashenov, A. G. Gontar and A. G. Petukhov: *Excited-states of a shallow acceptor in semiconducting diamond from photoconductivity spectra*, Phys. Status Solidi B **108**, K139 (1981).

[Böe02] K. W. Böer: *Survey of Semiconductor Physics-Volume II: Electronic Transport in Semiconductors*, vol. II, John Wiley & Sons, 2002, Second edn..

[Ben90a] H. Benisty and J. N. Chazalviel: *Extended phonon-scattering mechanism as an explanation for low mobility in highly concentrated electron layers at silicon interfaces*, Phys. Rev. B **41**, 12568 (1990).

[Ben90b] H. Benisty and J. N. Chazalviel: *Very high density, electrochemically induced, 2-dimensional electron gases at a chemically stabilized silicon surface*, J. Electrochem. Soc. **137**, 1209 (1990).

[Ber70] P. Bergveld: *Development of an ion-sensitive solid-state device for neurophysiological measurements*, IEEE T. Bio-Med. Eng. **BM17**, 70 (1970).

[Ber03] P. Bergveld: *Thirty years of isfetology - what happened in the past 30 years and what may happen in the next 30 years*, Sensor. Actuat. B-Chem. **88**, 1 (2003).

[Ber04] C. Berger, Z. M. Song, T. B. Li, X. B. Li, A. Y. Ogbazghi, R. Feng, Z. T. Dai, A. N. Marchenkov, E. H. Conrad, P. N. First and W. A. de Heer: *Ultrathin epitaxial graphite: 2D electron gas properties and a route toward graphene-based nanoelectronics*, J. Phys. Chem. B **108**, 19912 (2004).

[Bey96] R. Beynon and J. Easterby: *Buffer Solutions*, The Basics, IRL Press at Oxford University Press, 1996.

[Bie04] O. Bierwagen, R. Pomraenke, S. Eilers and W. Masselink: *Mobility and carrier density in materials with anisotropic conductivity revealed by van der Pauw measurements*, Phys. Rev. B **70**, 165307 (2004).

[Bie08] O. Bierwagen, T. Ive, C. G. Van de Walle and J. S. Speck: *Causes of incorrect carrier-type identification in van der Pauw-Hall measurements*, Appl. Phys. Lett. **93**, 242108 (2008).

[Bir] S. Birner: *nextnano3*, http://www.nextnano.de/.

[Bir07] S. Birner, T. Zibold, T. Andlauer, T. Kubis, M. Sabathil, A. Trellakis and P. Vogl: *nextnano: General purpose 3-D simulations*, IEEE T. Electron Dev. **54**, 2137 (2007).

[Bir08] S. Birner, C. Uhl, M. Bayer and P. Vogl: *Theoretical model for the detection of charged proteins with a silicon-on-insulator sensor*, J. Phys.: Conf. Ser. **107**, 012002 (2008).

[Bir11] S. Birner: *Modeling of semiconductor nanostructures and semiconductor-electrolyte interfaces*, PhD thesis, Technische Universität München, Physik-Department (2011).

[Blu10] H. Bluhm: *Photoelectron spectroscopy of surfaces under humid conditions*, J. Electron Spectrosc. Relat. Phenom. **177**, 71 (2010).

[Boc98] J. O. Bockris and A. Reddy: *Modern Electrochemistry 1 - ionics*, Plenum Press, 1998.

[Boc02] J. O. Bockris, A. Reddy and M. Gamboa-Aldeco: *Modern Electrochemistry 2A - Fundamentals of Electrodics*, Plenum Press, 2002.

[Bon11] D. J. Bonthuis, S. Gekle and R. R. Netz: *Dielectric profile of interfacial water and its effect on double-layer capacitance*, Phys. Rev. Lett. **107**, 166102 (2011).

[Bra98] D. Braun and P. Fromherz: *Fluorescence interferometry of neuronal cell adhesion on microstructured silicon*, Phys. Rev. Lett. **81**, 5241 (1998).

[Bri05] M. Brittinger and P. Fromherz: *Field-effect transistor with recombinant potassium channels: fast and slow response by electrical and chemical interactions*, Appl Phys A-Mater **81**, 439 (2005).

[Bro91] F. Brochardwyart, J. M. Dimeglio, D. Quere and P. G. DeGennes: *Spreading of nonvolatile liquids in a continuum picture*, Langmuir **7**, 335 (1991).

[But11] F. Buth, D. Kumar, M. Stutzmann and J. A. Garrido: *Electrolyte-gated organic field-effect transistors for sensing applications*, Appl. Phys. Lett. **98**, 153302 (2011).

[Cas07] E. V. Castro, K. S. Novoselov, S. V. Morozov, N. M. R. Peres, J. M. B. L. Dos Santos, J. Nilsson, F. Guinea, A. K. Geim and A. H. C. Neto: *Biased*

bilayer graphene: Semiconductor with a gap tunable by the electric field effect, Phys. Rev. Lett. **99**, 216802 (2007).

[Cha05] D. Chandler: *Interfaces and the driving force of hydrophobic assembly*, Nature **437**, 640 (2005).

[Cha07] V. Chakrapani, J. C. Angus, A. B. Anderson, S. D. Wolter, B. R. Stoner and G. U. Sumanasekera: *Charge transfer equilibria between diamond and an aqueous oxygen electrochemical redox couple*, Science **318**, 1424 (2007).

[Che83] G. Cheek, C. P. Wales and R. J. Nowak: *pH response of platinum and vitreous carbon electrodes modified by electropolymerized films*, Anal. Chem. **55**, 380 (1983).

[Che08] J. H. Chen, C. Jang, S. Adam, M. S. Fuhrer, E. D. Williams and M. Ishigami: *Charged-impurity scattering in graphene*, Nat. Phys. **4**, 377 (2008).

[Chw74] R. Chwang, B. Smith and C. Crowell: *Contact size effects on the van der Pauw method for resistivity and Hall-coefficient measurement*, Solid-State Electron. **17**, 1217 (1974).

[Cla98] W. C. Claycomb, N. A. Lanson, B. S. Stallworth, D. B. Egeland, J. B. Delcarpio, A. Bahinski and N. J. Izzo: *Hl-1 cells: A cardiac muscle cell line that contracts and retains phenotypic characteristics of the adult cardiomyocyte*, Proc. Natl. Acad. Sci. U. S. A. **95**, 2979 (1998).

[Cla09] J. Clausen: *Man, machine and in between*, Nature **457**, 1080 (2009).

[CN09] A. H. Castro Neto, F. Guinea, N. M. R. Peres, K. S. Novoselov and A. K. Geim: *The electronic properties of graphene*, Rev. Mod. Phys. **81**, 109 (2009).

[Cui98] J. B. Cui, J. Ristein and L. Ley: *Electron affinity of the bare and hydrogen covered single crystal diamond (111) surface*, Phys. Rev. Lett. **81**, 429 (1998).

[Dan08] M. Dankerl, A. Reitinger, M. Stutzmann and J. A. Garrido: *Resolving the controversy on the pH sensitivity of diamond surfaces*, Phys. Status Solidi-R **2**, 31 (2008).

[Dan09] M. Dankerl, S. Eick, B. Hofmann, M. Hauf, S. Ingebrandt, A. Offenhausser, M. Stutzmann and J. A. Garrido: *Diamond transistor array for extracellular recording from electrogenic cells*, Adv. Funct. Mater. **19**, 2915 (2009).

[Dan10] M. Dankerl, M. V. Hauf, A. Lippert, L. H. Hess, S. Birner, I. D. Sharp, A. Mahmood, P. Mallet, J. Y. Veuillen, M. Stutzmann and J. A. Garrido: *Graphene solution-gated field-effect transistor array for sensing applications*, Adv. Funct. Mater. **20**, 3117 (2010).

[Dan12] M. Dankerl, M. Tosun, M. Stutzmann and J. A. Garrido: *Solid polyelectrolyte-gated surface conductive diamond field effect transistors*, Appl. Phys. Lett. **100**, 023510 (2012).

[Dav63] D. Davidson and G. Wilson: *Low-frequency dielectric properties of ethylene oxide and ethylene oxide hydrate*, Can. J. Chem. **41**, 1424 (1963).

[Dav78] J. Davis, R. James and J. Leckie: *Surface ionization and complexation at oxide/water interface 1. Computation of electrical double-layer properties in simple electrolytes*, J. Colloid Interf. Sci. **63**, 480 (1978).

[Dav98] J. H. Davies: *The physics of low-dimensional semiconductors*, Cambridge University Press, 1998.

[Dav09] G. Davies: *CVD Diamond for Electronic Devices and Sensors*, chap. Basic Properties of Diamond: Phonon Spectra, Thermal Properties, Band structure, John Wiley & Sons, 2009, 3–28.

[Den08] X. Deng, T. Herranz, C. Weis, H. Bluhm and M. Salmeron: *Adsorption of water on Cu_2O and Al_2O_3 thin films*, J. Phys. Chem. C **112**, 9668 (2008).

[Des04] F. Despa, A. Fernandez and R. Berry: *Dielectric modulation of biological water*, Phys. Rev. Lett. **93** (2004).

[Dow08] R. Dowden: *Africa - altered states, ordinary miracles*, Portobello Books Ltd., 2008.

[Emt09] K. V. Emtsev, A. Bostwick, K. Horn, J. Jobst, G. L. Kellogg, L. Ley, J. L. McChesney, T. Ohta, S. A. Reshanov, J. Rohrl, E. Rotenberg, A. K. Schmid, D. Waldmann, H. B. Weber and T. Seyller: *Towards wafer-size graphene layers by atmospheric pressure graphitization of silicon carbide*, Nat. Mater. **8**, 203 (2009).

[Ere91] M. I. Eremets: *Semiconducting diamond*, Semicond. Sci. Technol. **6**, 439 (1991).

[Erg50] C. Erginsoy: *Neutral impurity scattering in semiconductors*, Phys. Rev. **79**, 1013 (1950).

[Fan66] F. Fang and W. Howard: *Negative field-effect mobility on (100) Si surfaces*, Phys. Rev. Lett. **16**, 797 (1966).

[Fan07] T. Fang, A. Konar, H. Xing and D. Jena: *Carrier statistics and quantum capacitance of graphene sheets and ribbons*, Appl. Phys. Lett. **91**, 092109 (2007).

[Far69] R. Farrer: *On substitutional nitrogen donor in diamond*, Solid State Commun. **7**, 685 (1969).

[Fis93] M. V. Fischetti and S. E. Laux: *Monte-carlo study of electron-transport in silicon inversion-layers*, Phys. Rev. B **48**, 2244 (1993).

[Foo09] J. S. Foord: *CVD Diamond for Electronic Devices and Sensors*, chap. Diamond Electrochemical Sensors, John Wiley & Sons, 2009, 440–465.

[Fra95] G. Francz and P. Oelhafen: *Photoelectron-spectroscopy of the annealed and deuterium-exposed natural diamond (100) surface*, Surf. Sci. **329**, 193 (1995).

[Fre90] A. Freedman and C. D. Stinespring: *Fluorination of diamond (100) by atomic and molecular-beams*, Appl. Phys. Lett. **57**, 1194 (1990).

[Fre94] A. Freedman: *Halogenation of diamond (100) and (111) surfaces by atomic-beams*, J. Appl. Phys. **75**, 3112 (1994).

[Fri09] I. Friel, S. L. Clewes, H. K. Dhillon, N. Perkins, D. J. Twitchen and G. A. Scarsbrook: *Control of surface and bulk crystalline quality in single crystal diamond grown by chemical vapour deposition*, Diamond Relat. Mater. **18**, 808 (2009).

[Fro91] P. Fromherz, A. Offenhausser, T. Vetter and J. Weis: *A neuron-silicon junction: a Retzius cell of the leech on an insulated-gate field-effect transistor*, Science **252**, 1290 (1991).

[Fro99] P. Fromherz: *Extracellular recording with transistors and the distribution of ionic conductances in a cell membrane*, Eur. Biophys. J. Biophy. **28**, 254 (1999).

[Fro03] P. Fromherz: *Nanoelectronics and Information Technology*, chap. Neuroelectronic Interfacing: Semiconductor Chips with Ion Channels, Nerve Cells, and Brain, Wiley-VCH Verlag, 2003, 781–810.

[Fro08] P. Fromherz: *Joining microelectronics and microionics: Nerve cells and brain tissue on semiconductor chips*, Solid-State Electron. **52**, 1364 (2008).

[Fuj06] N. Fujita, A. T. Blumenau, R. Jones, S. Oberg and P. R. Briddon: *Theoretical studies on 100 dislocations in single crystal CVD diamond*, Phys. Status Solidi A **203**, 3070 (2006).

[Fur96] J. Furthmuller, J. Hafner and G. Kresse: *Dimer reconstruction and electronic surface states on clean and hydrogenated diamond (100) surfaces*, Phys. Rev. B **53**, 7334 (1996).

[Gar05] J. Garrido, A. Hardl, S. Kuch, M. Stutzmann, O. Williams and R. Jackmann: *pH sensors based on hydrogenated diamond surfaces*, Appl. Phys. Lett. **86**, 073504 (2005).

[Gar08] J. A. Garrido, S. Nowy, A. Hartl and M. Stutzmann: *The diamond/aqueous electrolyte interface: An impedance investigation*, Langmuir **24**, 3897 (2008).

[Gar09] J. Garrido: *CVD Diamond for Electronic Devices and Sensors*, chap. Biofunctionalisation of Diamond Surfaces: Fundamentals and Applications, John Wiley & Sons, 2009, 401–437.

[Ghe99] E. Gheeraert, S. Kozumi, T. Teraji, H. Kanda and M. Nesladek: *Electronic states of boron and phosphorus in diamond*, Phys. Status Solidi A **174**, 39 (1999).

[Gho10] S. Ghodbane, D. Ballutaud, F. Omnes and C. Agnes: *Comparison of the XPS spectra from homoepitaxial 111, 100 and polycrystalline boron-doped diamond films*, Diamond Relat. Mater. **19**, 630 (2010).

[Gi95] R. S. Gi, T. Mizumasa, Y. Akiba, Y. Hirose, T. Kurosu and M. Iida: *Formation mechanism of p-type surface conductive layer on deposited diamond films*, Jpn. J. Appl. Phys. 1 **34**, 5550 (1995).

[Gi99] R. S. Gi, K. Tashiro, S. Tanaka, T. Fujisawa, H. Kimura, T. Kurosu and M. Iida: *Hall effect measurements of surface conductive layer on undoped diamond films in NO_2 and NH_3 atmospheres*, Jpn. J. Appl. Phys. 1 **38**, 3492 (1999).

[Gio07] N. Giovambattista, P. G. Debenedetti and P. J. Rossky: *Effect of surface polarity on water contact angle and interfacial hydration structure*, J. Phys. Chem. B **111**, 9581 (2007).

[Goh88] M. Goh, J. Hicks, K. Kemnitz, G. Pinto, K. Bhattacharyya, T. Heinz and K. Eisenthal: *Absolute orientation of water-molecules at the neat water-surface*, J. Phys. Chem. **92**, 5074 (1988).

[Gra94] R. Graupner, J. Ristein and L. Ley: *Photoelectron-spectroscopy of clean and hydrogen-exposed diamond (111)surfaces*, Surf. Sci. **320**, 201 (1994).

[Gra98] R. Graupner, F. Maier, J. Ristein, L. Ley and C. Jung: *High-resolution surface-sensitive C1s core-level spectra of clean and hydrogen-terminated diamond (100) and (111) surfaces*, Phys. Rev. B **57**, 12397 (1998).

[Gra99] M. C. Granger, J. S. Xu, J. W. Strojek and G. M. Swain: *Polycrystalline diamond electrodes: basic properties and applications as amperometric detectors in flow injection analysis and liquid chromatography*, Anal. Chim. Acta **397**, 145 (1999).

[Gra00] M. C. Granger, M. Witek, J. S. Xu, J. Wang, M. Hupert, A. Hanks, M. D. Koppang, J. E. Butler, G. Lucazeau, M. Mermoux, J. W. Strojek and G. M. Swain: *Standard electrochemical behavior of high-quality, boron-doped polycrystalline diamond thin-film electrodes*, Anal. Chem. **72**, 3793 (2000).

[Hab86] M. Habib and J. Bockris: *Potential-dependent water orientation - an insitu spectroscopic study*, Langmuir **2**, 388 (1986).

[Hal79] E. H. Hall: *On a new action of the magnet on electric currents*, Am. J. Math. **2**, 287 (1879).

[Ham98] C. Hamann and W. Vielstich: *Elektrochemie*, Wiley-VCH Verlag, 1998, Third edn..

[Har04] A. Hartl, E. Schmich, J. A. Garrido, J. Hernando, S. C. R. Catharino, S. Walter, P. Feulner, A. Kromka, D. Steinmuller and M. Stutzmann:

Protein-modified nanocrystalline diamond thin films for biosensor applications, Nat. Mater. **3**, 736 (2004).

[Har07] A. Hartl, J. A. Garrido, S. Nowy, R. Zimmermann, C. Werner, D. Horinek, R. Netz and M. Stutzmann: *The ion sensitivity of surface conductive single crystalline diamond*, J. Am. Chem. Soc. **129**, 1287 (2007).

[Hat99] A. Hatta, S. Sonoda and T. Ito: *Electrical Properties of B-doped homoepitaxial diamond films grown from UHP gas sources*, Diamond Relat. Mater. **8**, 1470 (1999).

[Hau08] M. V. Hauf: *Diamond SGFETs for the Detection of Cell Signals*, diploma thesis, Technische Universität München (2008).

[Hau10] M. V. Hauf, L. H. Hess, J. Howgate, M. Dankerl, M. Stutzmann and J. A. Garrido: *Low-frequency noise in diamond solution-gated field effect transistors*, Appl. Phys. Lett. **97**, 093504 (2010).

[Hau11] M. V. Hauf, B. Grotz, B. Naydenov, M. Dankerl, S. Pezzagna, J. Meijer, F. Jelezko, J. Wrachtrup, M. Stutzmann, F. Reinhard and J. A. Garrido: *Chemical control of the charge state of nitrogen-vacancy centers in diamond*, Phys. Rev. B **83**, 081304 (2011).

[Hee07] W. A. de Heer, C. Berger, X. S. Wu, P. N. First, E. H. Conrad, X. B. Li, T. B. Li, M. Sprinkle, J. Hass, M. L. Sadowski, M. Potemski and G. Martinez: *Epitaxial graphene*, Solid State Commun. **143**, 92 (2007).

[Hei04] T. Heimbeck: *Electronic properties of hydrogen-terminated diamond surfaces*, Master's thesis, Technische Universität München (2004).

[Her08] G. T. Hermanson: *Bioconjugate Techniques*, Elsevier, 2008, Second edn..

[Hes11a] L. H. Hess, M. V. Hauf, M. Seifert, F. Speck, T. Seyller, M. Stutzmann, I. D. Sharp and J. A. Garrido: *High-transconductance graphene solution-gated field effect transistors*, Appl. Phys. Lett. **99**, 033503 (2011).

[Hes11b] L. H. Hess, M. Jansen, V. Maybeck, M. V. Hauf, M. Seifert, M. Stutzmann, I. D. Sharp, A. Offenhausser and J. A. Garrido: *Graphene transistor arrays for recording action potentials from electrogenic cells*, Adv. Mater. **23**, 5045 (2011).

[Hir06] K. Hirama, S. Miyamoto, H. Matsudaira, K. Yamada, H. Kawarada, T. Chikyo, H. Koinuma, K. Hasegawa and H. Umezawa: *Characterization of diamond metal-insulator-semiconductor field-effect transistors with aluminum oxide gate insulator*, Appl. Phys. Lett. **88**, 112117 (2006).

[Hir08a] K. Hirama, H. Takayanagi, S. Yamauchi, J. H. Yang, H. Kawarada and H. Umezawa: *Spontaneous polarization model for surface orientation dependence of diamond hole accumulation layer and its transistor performance*, Appl. Phys. Lett. **92**, 112107 (2008).

[Hir08b] K. Hirama, H. Takayanagi, S. Yamauchi, J. H. Yang, H. Umezawa and H. Kawarada: *Channel mobility evaluation for diamond mosfets using gate-to-channel capacitance measurement*, Diamond Relat. Mater. **17**, 1256 (2008).

[Hir10] K. Hirama, K. Tsuge, S. Sato, T. Tsuno, Y. Jingu, S. Yamauchi and H. Kawarada: *High-performance p-channel diamond metal-oxide-semiconductor field-effect transistors on H-terminated (111) surface*, Appl. Phys. Express **3**, 044001 (2010).

[Hof10] R. Hoffmann, A. Kriele, H. Obloh, J. Hees, M. Wolfer, W. Smirnov, N. Yang and C. E. Nebel: *Electrochemical hydrogen termination of boron-doped diamond*, Appl. Phys. Lett. **97**, 052103 (2010).

[Här08] A. Härtl: *Novel concepts for biosensors using diamond-based field effect transistors*, PhD thesis, Technischen Universität München Walter Schottky Institut (2008).

[Hua08] D. M. Huang, C. Sendner, D. Horinek, R. R. Netz and L. Bocquet: *Water slippage versus contact angle: A quasiuniversal relationship*, Phys. Rev. Lett. **101**, 226101 (2008).

[Hum98] G. Hummer, S. Garde, A. Garcia, M. Paulaitis and L. Pratt: *Hydrophobic effects on a molecular scale*, J. Phys. Chem. B **102**, 10469 (1998).

[Ing05] S. Ingebrandt, C. Yeung, M. Krause and A. Offenhausser: *Neuron-transistor coupling: interpretation of individual extracellular recorded signals*, Eur Biophys J Biophy **34**, 144 (2005).

[Iof11] Ioffe Physico-Technical Institute: http://www.ioffe.ru/SVA/NSM/Semicond /Diamond/index.html (2011).

[Isb02] J. Isberg, J. Hammersberg, E. Johansson, T. Wikstrom, D. J. Twitchen, A. J. Whitehead, S. E. Coe and G. A. Scarsbrook: *High carrier mobility in single-crystal plasma-deposited diamond*, Science **297**, 1670 (2002).

[Isb09] J. Isberg: *CVD Diamond for Electronic Devices and Sensors*, chap. Transport properties of electrons and holes in diamond, John Wiley & Sons, 2009, 29–48.

[Ise48] I. Isenberg, B. Russell and R. Greene: *Improved method for measuring Hall coefficients*, Rev. Sci. Instrum. **19**, 685 (1948).

[Ive61] D. J. G. Ives and G. J. Janz: *Reference Electrodes*, Academic Press, New York, 1961.

[Jen03] T. R. Jensen, M. O. Jensen, N. Reitzel, K. Balashev, G. H. Peters, K. Kjaer and T. Bjornholm: *Water in contact with extended hydrophobic surfaces: Direct evidence of weak dewetting*, Phys. Rev. Lett. **90**, 086101 (2003).

[Jia99] N. Jiang and T. Ito: *Electrical properties of surface conductive layers of homoepitaxial diamond films*, J. Appl. Phys. **85**, 8267 (1999).

[Kai06] W. Kaiser: *Spinabhängiger Transport in Magnetit*, diplomathesis, Technische Universität München (2006).

[Kal08] M. Kalbacova, L. Michalikova, V. Baresova, A. Kromka, B. Rezek and S. Kmoch: *Adhesion of osteoblasts on chemically patterned nanocrystalline diamonds*, Phys. Status Solidi B **245**, 2124 (2008).

[Kan95] E. Kandel, J. Schwartz and T. Jessel: *Essentials of Neural Science and Behavior*, Appleton & Lange, 1995.

[Kat08] M. I. Katsnelson and A. K. Geim: *Electron scattering on microscopic corrugations in graphene*, Philos. T. R. Soc. A **366**, 195 (2008).

[Kau04] R. A. Kaul, N. I. Syed and P. Fromherz: *Neuron-semiconductor chip with chemical synapse between identified neurons*, Phys. Rev. Lett. **92**, 038102 (2004).

[Kaw94] H. Kawarada, M. Aoki and M. Ito: *Enhancement-mode metal-semiconductor field-effect transistors using homoepitaxial diamonds*, Appl. Phys. Lett. **65**, 1563 (1994).

[Kaw01] H. Kawarada, Y. Araki, T. Sakai, T. Ogawa and H. Umezawa: *Electrolyte-solution-gate FETs using diamond surface for biocompatible ion sensors*, Phys. Status Solidi A **185**, 79 (2001).

[Ked08] J. Kedzierski, P. L. Hsu, P. Healey, P. W. Wyatt, C. L. Keast, M. Sprinkle, C. Berger and W. A. de Heer: *Epitaxial graphene transistors on SiC substrates*, IEEE T. Electron. Dev. **55**, 2078 (2008).

[Kir71] S. Kirkpatrick: *Classical transport in disordered media - scaling and effective-medium theories*, Phys. Rev. Lett. **27**, 1722 (1971).

[Kla10] F. Klauser, S. Ghodbane, R. Boukherroub, S. Szunerits, D. Steinmuller-Nethl, E. Bertel and N. Memmel: *Comparison of different oxidation techniques on single-crystal and nanocrystalline diamond surfaces*, Diamond Relat. Mater. **19**, 474 (2010).

[Kon93] J. Kono, S. Takeyama, T. Takamasu, N. Miura, N. Fujimori, Y. Nishibayashi, T. Nakajima and K. Tsuji: *High-field cyclotron-resonance and valence-band structure in semiconducting diamond*, Phys. Rev. B **48**, 10917 (1993).

[Kuc03] S. Kuch: *Functionalization of Diamond Surfaces for Biosensor Applications*, Master's thesis, Walter Schottky Institut, Technische Universität München (2003).

[Kun09] J. J. Kuna, K. Voitchovsky, C. Singh, H. Jiang, S. Mwenifumbo, P. K. Ghorai, M. M. Stevens, S. C. Glotzer and F. Stellacci: *The effect of nanometre-scale structure on interfacial energy*, Nat. Mater. **8**, 837 (2009).

[Lai04] A. Laikhtman, A. Lafosse, Y. Le Coat, R. Azria and A. Hoffman: *Interaction of water vapor with bare and hydrogenated diamond film surfaces*, Surf. Sci. **551**, 99 (2004).

[Lak12] Lake Shore: *Appendix a Hall effect measurements: 7500/9500 series Hall system user's manual*, Lake Shore (2012).

[Lan89] M. I. Landstrass and K. V. Ravi: *Hydrogen passivation of electrically active defects in diamond*, Appl. Phys. Lett. **55**, 1391 (1989).

[Law71] P. Lawaetz: *Valence-band parameters in cubic semiconductors*, Phys. Rev. B **4**, 3460 (1971).

[Lee11] W. C. Lee, C. H. Y. X. Lim, H. Shi, L. A. L. Tang, Y. Wang, C. T. Lim and K. P. Loh: *Origin of enhanced stem cell growth and differentiation on graphene and graphene oxide*, ACS NANO **5**, 7334 (2011).

[Ley09] L. Ley: *CVD Diamond for Electronic Devices and Sensors*, chap. Surface Conductivity of Diamond, John Wiley & Sons, 2009, 69–102.

[Lip10] A. Lippert: *Electronic transport at the hydrogen-terminated diamond/electrolyte interface*, diploma thesis, Technische Universität München (2010).

[Lu10] A. X. Lu, J. Sun, J. Jiang and Q. Wan: *Low-voltage transparent electric-double-layer ZnO-based thin-film transistors for portable transparent electronics*, Appl. Phys. Lett. **96**, 043114 (2010).

[Lur88] S. Luryi: *Quantum capacitance devices*, Appl. Phys. Lett. **52**, 501 (1988).

[Mai00] F. Maier, M. Riedel, B. Mantel, J. Ristein and L. Ley: *Origin of surface conductivity in diamond*, Phys. Rev. Lett. **85**, 3472 (2000).

[Mai01] F. Maier, J. Ristein and L. Ley: *Electron affinity of plasma-hydrogenated and chemically oxidized diamond (100) surfaces*, Phys. Rev. B **64**, 165411 (2001).

[Mak03] N. W. Makau and T. E. Derry: *Study of oxygen on the three low index diamond surfaces by XPS*, Surf. Rev. Lett. **10**, 295 (2003).

[Mez06] M. Mezger, H. Reichert, S. Schoder, J. Okasinski, H. Schroder, H. Dosch, D. Palms, J. Ralston and V. Honkimaki: *High-resolution in situ X-ray study of the hydrophobic gap at the water-octadecyl-trichlorosilane interface*, Proc. Natl. Acad. Sci. U. S. A. **103**, 18401 (2006).

[Mez10] M. Mezger, F. Sedlmeier, D. Horinek, H. Reichert, D. Pontoni and H. Dosch: *On the origin of the hydrophobic water gap: an X-ray reflectivity and MD simulation study*, J. Am. Chem. Soc. **132**, 6735 (2010).

[Mil96] J. B. Miller and D. W. Brown: *Photochemical modification of diamond surfaces*, Langmuir **12**, 5809 (1996).

[Nav80] F. Nava, C. Canali, C. Jacoboni, L. Reggiani and S. Kozlov: *Electron effective masses and lattice scattering in natural diamond*, Solid State Commun. **33**, 475 (1980).

[Neb01] C. E. Nebel, C. Sauerer, F. Ertl, M. Stutzmann, C. F. O. Graeff, P. Bergonzo, O. A. Williams and R. Jackman: *Hydrogen-induced transport properties of holes in diamond surface layers*, Appl. Phys. Lett. **79**, 4541 (2001).

[Neb04] C. E. Nebel, B. Rezek and A. Zrenner: *Electronic properties of the 2D-hole accumulation layer on hydrogen terminated diamond*, Diamond Relat. Mater. **13**, 2031 (2004).

[Neb06] C. E. Nebel, B. Rezek, D. Shin and H. Watanabe: *Surface electronic properties of H-terminated diamond in contact with adsorbates and electrolytes*, Phys. Status Solidi A **203**, 3273 (2006).

[Neb07] C. E. Nebel, B. Rezek, D. Shin, H. Uetsuka and N. Yang: *Diamond for bio-sensor applications*, J. Phys. D Appl. Phys. **40**, 6443 (2007).

[Nel04] M. Nelson, P. Radosavljevic and S. Bromberg: *Biological Physics*, WH Freeman and Co., 2004.

[Nes08] M. Nesladek, A. Bogdan, W. Deferme, N. Tranchant and P. Bergonzo: *Charge transport in high mobility single crystal diamond*, Diamond Relat. Mater. **17**, 1235 (2008).

[Nic06] B. M. Nichols, K. M. Metz, K. Y. Tse, J. E. Butler, J. N. Russell and R. J. Hamers: *Electrical bias dependent photochemical functionalization of diamond surfaces*, J. Phys. Chem. B **110**, 16535 (2006).

[Nov04] K. S. Novoselov, A. K. Geim, S. V. Morozov, D. Jiang, Y. Zhang, S. V. Dubonos, I. V. Grigorieva and A. A. Firsov: *Electric field effect in atomically thin carbon films*, Science **306**, 666 (2004).

[Oht07] T. Ohta, A. Bostwick, J. L. McChesney, T. Seyller, K. Horn and E. Rotenberg: *Interlayer interaction and electronic screening in multilayer graphene investigated with angle-resolved photoemission spectroscopy*, Phys. Rev. Lett. **98**, 206802 (2007).

[Ono08] S. Ono, S. Seki, R. Hirahara, Y. Tominari and J. Takeya: *High-mobility, low-power, and fast-switching organic field-effect transistors with ionic liquids*, Appl. Phys. Lett. **92** (2008).

[Ost05] V. Ostroverkhov, G. A. Waychunas and Y. R. Shen: *New information on water interfacial structure revealed by phase-sensitive surface spectroscopy*, Phys. Rev. Lett. **94**, 046102 (2005).

[Pab07] M. Pabst, G. Wrobel, S. Ingebrandt, F. Sommerhage and A. Offenhausser: *Solution of the Poisson-Nernst-Planck equations in the cell-substrate interface*, Eur. Phys. J. E **24**, 1 (2007).

[Pan05] M. Panzer, C. Newman and C. Frisbie: *Low-voltage operation of a pentacene field-effect transistor with a polymer electrolyte gate dielectric*, Appl. Phys. Lett. **86**, 103503 (2005).

[Pau58] L. van der Pauw: *A method of measuring specific resistivity and Hall effect of discs of arbitrary shape*, Philips Research Reports **13**, 1 (1958).

[Poy06] A. Poynor, L. Hong, I. K. Robinson, S. Granick, Z. Zhang and P. A. Fenter: *How water meets a hydrophobic surface*, Phys. Rev. Lett. **97**, 266101 (2006).

[Poy08] A. Poynor, L. Hong, I. K. Robinson, S. Granick, P. A. Fenter and Z. Zhang: *Comment on "How water meets a hydrophobic surface" Reply*, Phys. Rev. Lett. **101**, 039602 (2008).

[Pra77] L. Pratt and D. Chandler: *Theory of hydrophobic effect*, J. Chem. Phys. **67**, 3683 (1977).

[Rau61] C. J. Rauch: *Millimeter cyclotron resonance experiments in diamond*, Phys. Rev. Lett. **7**, 83 (1961).

[Rau62] C. Rauch: *Millimeter cyclotron resonance in diamond*, in A. Stickland (ed.), *Proceedings of the International Conference on the Physics of Semiconductors*, 1962, 276.

[Reg83] L. Reggiani, D. Waechter and S. Zukotynski: *Hall-coefficient factor and inverse valence-band parameters of holes in natural diamond*, Phys. Rev. B **28**, 3550 (1983).

[Reg89] W. G. Regehr, J. Pine, C. S. Cohan, M. D. Mischke and D. W. Tank: *Sealing cultured invertebrate neurons to embedded dish electrodes facilitates long-term stimulation and recording*, J Neurosci Meth **30**, 91 (1989).

[Rei08] A. Reitinger: *Towards the Detection of Neurotransmitters with Diamond ENFETs*, diploma thesis, Technische Universität München (2008).

[Rez06] B. Rezek, H. Watanabe and C. E. Nebel: *High carrier mobility on hydrogen terminated (100) diamond surfaces*, Appl. Phys. Lett. **88**, 042110 (2006).

[Rez07] B. Rezek, D. Shin, H. Watanabe and C. E. Nebel: *Intrinsic hydrogen-terminated diamond as ion-sensitive field effect transistor*, Sensor. Actuat. B-Chem. **122**, 596 (2007).

[Rie04] M. Riedel, J. Ristein and L. Ley: *The impact of ozone on the surface conductivity of single crystal diamond*, Diamond Relat. Mater. **13**, 746 (2004).

[Ris02] J. Ristein, M. Riedel, M. Stammler, B. Mantel and L. Ley: *Surface conductivity of nitrogen-doped diamond*, Diamond Relat. Mater. **11**, 359 (2002).

[Ris06] J. Ristein: *Surface science of diamond: Familiar and amazing*, Surf. Sci. **600**, 3677 (2006).

[Rob08] M. E. Roberts, S. C. B. Mannsfeld, N. Queralto, C. Reese, J. Locklin, W. Knoll and Z. N. Bao: *Water-stable organic transistors and their application in chemical and biological sensors*, Proc. Natl. Acad. Sci. U. S. A. **105**, 12134 (2008).

[Rol11] Roland Benoit CNRS Orléans: *Lasurface.com*, http://www.lasurface.com/xps/imfpgrapher.php (2011).

[Rös02] U. Rössler (ed.): *Landolt-Börnstein. Added t.p.: Numerical data and functional relationships in science and technology Semiconductors A1: Group IV Elements, IV-IV and III-V Compounds Part Beta: Electronic, Transport, Optical and Other Properties*, vol. III of *Landolt-Börnstein*, Springer, 2002, new series edn..

[Sak03] T. Sakai, K. S. Song, H. Kanazawa, Y. Nakamura, H. Umezawa, M. Tachiki and H. Kawarada: *Ozone-treated channel diamond field-effect transistors*, Diamond Relat. Mater. **12**, 1971 (2003).

[Sca01] L. F. Scatena, M. G. Brown and G. L. Richmond: *Water at hydrophobic surfaces: Weak hydrogen bonding and strong orientation effects*, Science **292**, 908 (2001).

[Sch02] R. Schonherr, L. Mannuzzu, E. Isacoff and S. Heinemann: *Conformational switch between slow and fast gating modes: allosteric regulation of voltage sensor mobility in the EAG K+ channel*, Neuron **35**, 935 (2002).

[Sch07] I. Schoen and P. Fromherz: *The mechanism of extracellular stimulation of nerve cells on an electrolyte-oxide-semiconductor capacitor*, Biophys. J. **92**, 1096 (2007).

[Sch09] M. Schreck: *CVD Diamond for Electronic Devices and Sensors*, chap. Heteroepitaxial Growth, John Wiley & Sons, 2009, 125–161.

[Sch10] N. Schwierz, D. Horinek and R. R. Netz: *Reversed anionic Hofmeister series: the interplay of surface charge and surface polarity*, Langmuir **26**, 7370 (2010).

[Sea79] M. P. Seah and W. A. Dench: *Quantitative electron spectroscopy of surfaces: A standard data base for electron inelastic mean free paths in solids*, Surf. Interface Anal. **1**, 2 (1979).

[Sed08] F. Sedlmeier, J. Janecek, C. Sendner, L. Bocquet, R. R. Netz and D. Horinek: *Water at polar and nonpolar solid walls*, Biointerphases **3**, FC23 (2008).

[See04] K. Seeger: *Semiconductor Physics*, Springer, 2004, 9th edn..

[Sha07] M. Sharma, R. Resta and R. Car: *Dipolar correlations and the dielectric permittivity of water*, Phys. Rev. Lett. **98** (2007).

[She06] Y. Shen and V. Ostroverkhov: *Sum-frequency vibrational spectroscopy on water interfaces: Polar orientation of water molecules at interfaces*, Chem Rev **106**, 1140 (2006).

[Shi76] C. Shiue and C. Sah: *Studies of electron screening effects on electron-mobility in silicon surface inversion layers*, Surf. Sci. **58**, 153 (1976).

[Shi05] D. C. Shin, H. Watanabe and C. E. Nebel: *Insulator-metal transition of intrinsic diamond*, J. Am. Chem. Soc. **127**, 11236 (2005).

[Sho53] W. Shockley: *Electrons and Holes in Semiconductors with applications to transistor electronics*, D. van Nostrand Company Inc., 1953.

[Son06] K.-S. Song, Y. Nakamura, Y. Sasaki, M. Degawa, J.-H. Yang and H. Kawarada: *pH-sensitive diamond field-effect transistors (FETs) with directly aminated channel surface*, Anal. Chim. Acta **573**, 3 (2006).

[Stü08] E. U. Stützel: *Surface conductivity at the diamond/electrolyte interface*, diploma thesis, Technische Universität München (2008).

[Sta07] T. Stauber, N. M. R. Peres and F. Guinea: *Electronic transport in graphene: A semiclassical approach including midgap states*, Phys. Rev. B **76**, 205423 (2007).

[Ste67] F. Stern and W. E. Howard: *Properties of semiconductor surface inversion layers in electric quantum limit*, Phys. Rev. **163**, 816 (1967).

[Ste72] F. Stern: *Self-consistent results for n-type Si inversion layers*, Phys. Rev. B **5**, 4891 (1972).

[Ste05] G. Steinhoff, B. Baur, G. Wrobel, S. Ingebrandt, A. Offenhausser, A. Dadgar, A. Krost, M. Stutzmann and M. Eickhoff: *Recording of cell action potentials with AlGaN/GaN field-effect transistors*, Appl. Phys. Lett. **86**, 033901 (2005).

[Str04] P. Strobel, M. Riedel, J. Ristein and L. Ley: *Surface transfer doping of diamond*, Nature **430**, 439 (2004).

[Stu06] M. Stutzmann, J. A. Garrido, M. Eickhoff and M. S. Brandt: *Direct biofunctionalization of semiconductors: A survey*, Phys. Status Solidi A **203**, 3424 (2006).

[Sus09] R. Sussmann: *CVD Diamond for electronic devices and sensors*, John Wiley & Sons, 2009.

[Sze07] M. Sze and K. Ng: *Physics of Semiconductor Devices*, John Wiley & Sons, Inc., 2007, Third edn..

[Tan05] S. Tanuma, C. J. Powell and D. R. Penn: *Calculations of electron inelastic mean free paths. VIII. Data for 15 elemental solids over the 50-2000 eV range*, Surf. Interface Anal. **37**, 1 (2005).

[Tan09] L. Tang, Y. Wang, Y. Li, H. Feng, J. Lu and J. Li: *Preparation, structure, and electrochemical properties of reduced graphene sheet films*, Adv. Funct. Mater. **19**, 2782 (2009).

[Tar85] A. Tardella and J. N. Chazalviel: *Highly accumulated electron layer at a semiconductor electrolyte interface*, Phys. Rev. B **32**, 2439 (1985).

[Ted09] J. L. Tedesco, B. L. VanMil, R. L. Myers-Ward, J. M. McCrate, S. A. Kitt, P. M. Campbell, G. G. Jernigan, J. C. Culbertson, C. R. Eddy and D. K. Gaskill: *Hall effect mobility of epitaxial graphene grown on silicon carbide*, Appl. Phys. Lett. **95**, 122102 (2009).

[Ter06] T. Teraji, H. Wada, M. Yamamoto, K. Arima and T. Ito: *Highly efficient doping of boron into high-quality homoepitaxial diamond films*, Diamond Relat. Mater. **15**, 602 (2006).

[Tie09] K. J. Tielrooij, D. Paparo, L. Piatkowski, H. J. Bakker and M. Bonn: *Dielectric relaxation dynamics of water in model membranes probed by terahertz spectroscopy*, Biophys. J. **97**, 2484 (2009).

[Ton94] M. F. Toney, J. N. Howard, J. Richer, G. L. Borges, J. G. Gordon, O. R. Melroy, D. G. Wiesler, D. Yee and L. B. Sorensen: *Voltage-dependent ordering of water-molecules at an electrode-electrolyte interface*, Nature **368**, 444 (1994).

[Tsu99] K. Tsugawa, K. Kitatani, H. Noda, A. Hokazono, K. Hirose, M. Tajima and H. Kawarada: *High-performance diamond surface-channel field-effect transistors and their operation mechanism*, Diamond Relat. Mater. **8**, 927 (1999).

[Tsu06] K. Tsukioka and H. Okushi: *Hall mobility and scattering mechanism of holes in boron-doped homoepitaxial chemical vapor deposition diamond thin films*, Jpn. J. Appl. Phys. 1 **45**, 8571 (2006).

[Uch01] K. Uchida, A. Izumi and H. Matsumura: *Novel chamber cleaning method using atomic hydrogen generated by hot catalyzer*, Thin Solid Films **395**, 75 (2001).

[Uen08] K. Ueno, S. Nakamura, H. Shimotani, A. Ohtomo, N. Kimura, T. Nojima, H. Aoki, Y. Iwasa and M. Kawasaki: *Electric-field-induced superconductivity in an insulator*, Nat. Mater. **7**, 855 (2008).

[Uen11] K. Ueno, S. Nakamura, H. Shimotani, H. T. Yuan, N. Kimura, T. Nojima, H. Aoki, Y. Iwasa and M. Kawasaki: *Discovery of superconductivity in KTaO(3) by electrostatic carrier doping*, Nat. Nanotechnol. **6**, 408 (2011).

[Ulm96] A. Ulman: *Formation and structure of self-assembled monolayers*, Chem. Rev. **96**, 1533 (1996).

[Vel08] M. Velliste, S. Perel, M. C. Spalding, A. S. Whitford and A. B. Schwartz: *Cortical control of a prosthetic arm for self-feeding*, Nature **453**, 1098 (2008).

[Ver07] A. Verdaguer, C. Weis, G. Oncins, G. Ketteler, H. Bluhm and M. Salmeron: *Growth and structure of water on SiO_2 films on Si investigated by Kelvin probe microscopy and in situ X-ray spectroscopies*, Langmuir **23**, 9699 (2007).

[Wil94] M. Willatzen, M. Cardona and N. Christensen: *Linear muffin-tin-orbital and kp calculations of effective masses and band-structure of semiconducting diamond*, Phys. Rev. B **50**, 18054 (1994).

[Wro05] G. Wrobel, R. Seifert, S. Ingebrandt, J. Enderlein, H. Ecken, A. Baumann, U. B. Kaupp and A. Offenhausser: *Cell-transistor coupling: Investigation of potassium currents recorded with p- and n-channel FETs*, Biophys. J. **89**, 3628 (2005).

[Wu93] J. Wu, R. Cao, X. Yang, P. Pianetta and I. Lindau: *Photoemission-study of diamond (100) surface*, J. Vac. Sci. Technol. A **11**, 1048 (1993).

[Xia09] J. Xia, F. Chen, J. Li and N. Tao: *Measurement of the quantum capacitance of graphene*, Nat. Nanotechnol. **4**, 505 (2009).

[Yan02] W. S. Yang, O. Auciello, J. E. Butler, W. Cai, J. A. Carlisle, J. Gerbi, D. M. Gruen, T. Knickerbocker, T. L. Lasseter, J. N. Russell, L. M. Smith and R. J. Hamers: *DNA-modified nanocrystalline diamond thin-films as stable, biologically active substrates*, Nat. Mater. **1**, 253 (2002).

[Yat74] D. Yates, S. Levine and T. Healy: *Site-binding model of electrical double-layer at oxide-water interface*, J. Chem. Soc. Farad. T. 1 **70**, 1807 (1974).

[Ye92] S. Ye, H. Kita and A. Aramata: *Hydrogen and anion adsorption at platinum single-crystal electrodes in phosphate solutions over a wide-range of pH*, J. Electroanal. Chem. **333**, 299 (1992).

[Ye10] J. T. Ye, S. Inoue, K. Kobayashi, Y. Kasahara, H. T. Yuan, H. Shimotani and Y. Iwasa: *Liquid-gated interface superconductivity on an atomically flat film*, Nat. Mater. **9**, 125 (2010).

[Yeh85] J. J. Yeh and I. Lindau: *Atomic subshell photoionization cross-sections and asymmetry parameters: $1 \leq Z \leq 103$*, Atomic Data and Nuclear Data Tables **32**, 1 (1985).

[Yeh99] I. Yeh and M. Berkowitz: *Dielectric constant of water at high electric fields: Molecular dynamics study*, J. Chem. Phys. **110**, 7935 (1999).

[Yu05] P. Yu and M. Cardona: *Fundamentals of Semiconductors*, Springer, 2005, Third edn..

[Yua09] H. T. Yuan, H. Shimotani, A. Tsukazaki, A. Ohtomo, M. Kawasaki and Y. Iwasa: *High-density carrier accumulation in ZnO field-effect transistors gated by electric double layers of ionic liquids*, Adv. Funct. Mater. **19**, 1046 (2009).

[Zha08] W. Y. Zhang, J. Ristein and L. Ley: *Hydrogen-terminated diamond electrodes. II. Redox activity*, Phys. Rev. E **78**, 041603 (2008).

[Zho07] Y. L. Zhong, K. F. Chong, P. W. May, Z. K. Chen and K. P. Loh: *Optimizing biosensing properties on undecylenic acid-functionalized diamond*, Langmuir **23**, 5824 (2007).

List of Publications

- M. Dankerl, A. Reitinger, M. Stutzmann and J. A. Garrido: *Resolving the controversy on the pH sensitivity of diamond surfaces*, Phys. Status Solidi-R **2**, 31 (2008).

- J. A. Garrido, A. Hartl, M. Dankerl, A. Reitinger, M. Eickhoff, A. Helwig, G. Muller and M. Stutzmann: *The surface conductivity at the diamond/aqueous electrolyte interface*, J. Am. Chem. Soc. **130**, 4177 (2008).

- M. Dankerl, S. Eick, B. Hofmann, M. Hauf, S. Ingebrandt, A. Offenhausser, M. Stutzmann and J. A. Garrido: *Diamond transistor array for extracellular recording from electrogenic cells*, Adv. Funct. Mater. **19**, 2915 (2009).

- M. V. Hauf, L. H. Hess, J. Howgate, M. Dankerl, M. Stutzmann and J. A. Garrido: *Low-frequency noise in diamond solution-gated field effect transistors*, Appl. Phys. Lett. **97**, 093504 (2010).

- M. Dankerl, M. V. Hauf, A. Lippert, L. H. Hess, S. Birner, I. D. Sharp, A. Mahmood, P. Mallet, J. Y. Veuillen, M. Stutzmann and J. A. Garrido: *Graphene solution-gated field-effect transistor array for sensing applications*, Adv. Funct. Mater. **20**, 3117 (2010).

- M. V. Hauf, B. Grotz, B. Naydenov, M. Dankerl, S. Pezzagna, J. Meijer, F. Jelezko, J. Wrachtrup, M. Stutzmann, F. Reinhard and J. A. Garrido: *Chemical control of the charge state of nitrogen-vacancy centers in diamond*, Phys. Rev. B **83**, 081304 (2011).

- M. Dankerl, A. Lippert, S. Birner, E. U. Stuetzel, M. Stutzmann and J. A. Garrido: *Hydrophobic interaction and charge accumulation at the diamond-electrolyte interface*, Phys. Rev. Lett. **106**, 196103 (2011).

- M. Dankerl, M. Tosun, M. Stutzmann and J. A. Garrido: *Solid polyelectrolyte-gated surface conductive diamond field effect transistors*, Appl. Phys. Lett.

100, 023510 (2012).

- B. Grotz, M. V. Hauf, M. Dankerl, B. Naydenov, S. Pezzagna, J. Meijer, F. Jelezko, J. Wrachtrup, M. Stutzmann, F. Reinhard and J. A. Garrido: *Charge state manipulation of qubits in diamond*, Nat Commun **3**, 729 (2012).

- M. Dankerl, M. V. Hauf, M. Stutzmann, and J. A. Garrido: *Diamond solution-gated field effect transistors: Properties and bioelectronic applications*, Phys. Status Solidi A **209**, 1631 (2012).

Acknowledgment

The form this thesis took - the present text and the years of research it is based on - owes a lot to the people listed here. It has been a very pleasant time in my life and I can honestly say that I enjoyed the work, and, again, this is thanks to the people I had the privilege and joy to work with.

- **Jose A. Garrido**, who thought up this broad and interdisciplinary topic which sustained my interest until the very end. The innumerable discussions we had were a constant source of new ideas and motivation. Your leadership through your own motivation and unfailing good mood made working a pleasure. Your ability to see the good in people was an inspiration. Thank you for being a mentor and sparring partner in physics - and beyond. Muchas gracias, Jose!

- **Martin Stutzmann**, who initially accepted me as his PhD student at his chair. Thank you for our physical discussions, which provided new perspectives and included the right to disagree. Your critical reading of various manuscripts and your relentless hunt for errors helped to keep up the standards. I especially appreciated (and made liberal use of) the freedom you gave me to pursue all my scientific and non-scientific goals. Vielen Dank, Martin!

- My four diploma students **Andreas Reitinger**, **Moritz Hauf**, **Ulrich Stützel**, and **Andreas Lippert**: Thank you for your much appreciated and valuable contributions to this thesis. Your motivation to achieve something kept me busy in a very positive sense. I really enjoyed our excellent atmosphere at work and sometimes beyond. Good luck and great success with your current endeavors!

- **Michael Gruber**, **Mahmut Tosun**, **Mete Karagözlü**, and **Edgar Albert**, my working students: Thank you for your independent work style and the rigor necessary to achieve anything in science. All the best for your future!

- **Stefan Birner**, who provided us with the nextnano^3 software. Thank you for a very fruitful collaboration between theory and experiment! Thank you for your introduction to nextnano^3 and your patient willingness to adapt the program to my requirements to make its results even more relevant and useful to me as an experimentalist.

- **Stefan Eick**, **Boris Hofmann**, **Vanessa Maybeck**, and **Andreas Offenhäusser** at the Forschungszentrum Jülich: Thanks to your mastery of cell culture and electrophysiology we married cells and diamond. Thank you for your friendship and hospitality during my stays in Jülich and our time together sharing the benefits of the DREAMS project.

- **Miquel Salmeron**, **Hendrik Bluhm**, **Allard Katan**, **Ferenc Borondics**, and **Ed Wong** at the Lawrence Berkeley National Laboratory: Thank you for synchrotron beamtime and the AFM measurements as well as your patience and especially your good will towards me and my research project. I learned a lot from this stay. Thank you also for your very warm hospitality outside the lab.

- **Romain Caplette**, **Bogdan Kolomiets**, and **Serge Picaud** at the Institut De La Vision in Paris: Thank you for your help with the electrophysiological retina experiments and your hospitality.

- I want to thank **Veronika Enter** and **Joana Figueiredo** for their uncomplicated and always friendly support with secretarial work. I thank **Michi Fischer**, **Claudia Paulus**, **Wolfgang Bendack** for their technical help.

- I'm very thankful to the current and past members of the E25 chair and especially the carbon group for a highly collaborative and pleasant working atmosphere. I would particularly like to thank **Felix Buth** and **Roberta Caterino** for keeping me in shape and in very pleasant company outside the WSI; **Moritz Hauf** for throwing excellent parties which have become a social melting pot and for very successful collaborations in the lab; **Lucas Hess**, **Andreas Reitinger**, **Alda Cavallini**, **Sabrina Niesar**, **Naima Hutter**, **Felix Hoehne**, **Susanne Schäfer**, **Max Seifert**, **Andreas Härtl**, and **Wojciech Gajewski** for help on various occasions and/or good company. I greatly enjoyed our time inside and outside the WSI.

- My friends and the Debating Club Munich for a good life outside of physics.

- Meine **Eltern** und mein **Bruder Matthias**, die für mich ein gutes Basislager sind, und die irgendwie das aus mir gemacht haben was ich bin und deshalb großen Anteil an allem haben. Vielen lieben Dank!

- Meine Liebe **Simone**, Danke für Deine Liebe, Deine Geduld, Deine Hilfe und die willkommene Ablenkung von der Arbeit!